EXPLORATION OF THE MYSTERY OF POLAR WAVE DYNAMICS WITH LIDAR/RADAR OBSERVATIONS AND GENERAL CIRCULATION MODELS & DEVELOPMENT OF NEW WAVE ANALYSIS METHODS

by

CAO CHEN

B.Sc., University of Science and Technology of China, 2008

M.Sc., University of Science and Technology of China, 2010

A thesis submitted to the

Faculty of the Graduate School of the

University of Colorado in partial fulfillment

of the requirement for the degree of

Doctor of Philosophy

Department of Aerospace Engineering Sciences

2016

This thesis entitled:

EXPLORATION OF THE MYSTERY OF POLAR WAVE DYNAMICS WITH LIDAR/RADAR OBSERVATIONS AND GENERAL CIRCULATION MODELS & DEVELOPMENT OF NEW WAVE ANALYSIS METHODS

written by Cao Chen

has been approved for the Department of Aerospace Engineering Sciences

_____

Prof. Xinzhao Chu (Chair)

_____

Prof. Jeffrey M. Forbes

Date: _____

The final copy of this thesis has been examined by the signatories, and we find that both the content and the form meet acceptable presentation standards of scholarly work in the above mentioned discipline.

Chen, Cao (Ph.D., Aerospace Engineering Sciences)

Exploration of the Mystery of Polar Wave Dynamics with Lidar/Radar Observations and General Circulation Models & Development of New Wave Analysis Methods

Thesis directed by Professor Xinzhao Chu

The Space-atmosphere interaction region (SAIR) between ~50 and 200 km is one of the key factors enabling our Earth to harbor life. Its fundamental processes are believed to be universal and applicable to the atmospheres of Earth-like planets throughout our galaxy. However, the SAIR remains one of the least observed and understood regions. This thesis aims to advance the observations and characterizations of atmospheric waves that are fundamental to shaping the SAIR, especially exploring the mystery of persistent inertia-gravity waves, discovered by our Fe Boltzmann lidar measurements of temperatures at McMurdo (77.8°S, 166.7°E), Antarctica.

This thesis discovers a new wave phenomenon in the Antarctic middle and upper atmosphere, namely the persistent inertia-gravity waves with periods of 3-10 h. This group of large-amplitude waves dominates the temperature perturbations from the stratosphere to the lower thermosphere (about 30–115 km). They occur so frequently as to appear endless and uninterrupted, impacting the composition, chemistry and thermodynamics of the SAIR. This thesis reports the first simultaneous lidar/radar observations of inertia-gravity waves in Antarctica. Utilizing the lidar data in June from 2011 to 2015, this thesis characterizes the persistent gravity wave properties for the first time. These waves exhibit a uniform dominant vertical wavelength of 20–30 km across periods of 3.5–10 h and vertical phase speeds of 0.8–2 m/s. They possess more than half of the spectral energy for ~93% of the time. An analysis of the

65-h lidar data on 28–30 June 2014 demonstrates multiple wave packets spanning as long as 60 h. Further analysis of May and July data confirms the persistency and dominancy of these waves but reveal a month-to-month variability.

This thesis develops a system of wave analysis methods, including extracting gravity waves from ~30–155 km in the neutral atmosphere for the first time. Our methodologies also include the temporal hodograph methods for simultaneous lidar/radar data; improved 1-D Morlet wavelet transform methods; rigorous pre-whitening and post-coloring spectral analysis techniques; and automated 2-D Morlet wavelet analysis and synthesis methods. Successful application of these methodologies provides new insights into gravity waves, their sources and impacts on the whole atmosphere and space.

Dedication

Dedicated to my parents Chen, Meiyuan and Cao, Hua, and to my fiancée Zhang, Wei.

Acknowledgments

I owe my deepest gratitude to my advisor Professor Xinzhao Chu for guiding me through the PhD research on both science discoveries and lidar adventures and providing me the opportunity to work in Antarctica. I sincerely acknowledge the invaluable discussions and comments from Dr. Sharon Vadas, Dr. Adrian McDonald, Dr. Jeffrey Forbes, Dr. Hanli Liu, Dr. Takuji Nakamura, Dr. Kaoru Sato, Dr. Mike Taylor, Dr. Elsayed Talaat, and Dr. Ian Grooms. I am also grateful to my colleagues Dr. Xian Lu, Dr. John A. Smith, Dr. Weichun Fong, Dr. Zhibin Yu, Dr. Chihoko Yamashita Cullens, Dr. Wentao Huang, Dr. Zhangjun Wang, Dr. Cyrus Abari, Mr. Jian Zhao, Mr. Ian F. Barry, Mr. Brendan Roberts, and Dr. Bo Tan. I am indebted to Dr. Adrian McDonald for providing the Scott Base MF radar data, Dr. Andreas Dörnbrack for the high-resolution ECMWF data, Dr. Dominique Pautet for the South Pole imager data, Dr. Kaoru Sato for KANTO and JAGUAR GCM data, and Dr. Hanli Liu for WACCM GCM data used in this dissertation. I sincerely acknowledge Dr. Vladimir Papitashvili, Dr. Julie Palais, Mr. Richard Dean, and Ms. Judy Shiple for their guidance and support of the McMurdo lidar campaign. We appreciate the staff of the United States Antarctic Program, McMurdo station, Antarctica New Zealand, and Scott Base for their superb support. This dissertation was supported by the NSF grants ANT-0839091, PLR-1246405, AGS-1136272, and CIRES Graduate Student Research Award.

CONTENTS

Chapter

List of Tables

List of Figures

CHAPTER 1

Introduction

Our planet Earth orbits around a variable magnetic star, the Sun, which is constantly emitting varying rates and magnitudes of solar radiations, magnetized solar winds and energetic particles. Throughout the 3.5 billion years during which our planet Earth has harbored life, the Sun's output energy increased by more than 20%. In spite of this large change in solar activities, Earth has remained habitable because of the effects of a set of key universal processes that govern the evolution of planetary atmospheres everywhere [*OASIS*, 2014]. For example, the Earth's magnetic field shields our atmosphere from the energetic particles in the solar wind that are partially responsible for stripping Mars of its primordial atmosphere [see review by *Moore and Horwitz*, 2007]. The significant modification of Earth's atmosphere by life itself prevents the runaway greenhouse effect that is responsible for the high temperatures on Venus today [*Rasool and De Bergh*, 1970]. However, there are many coupled mechanisms and feedback processes that are unknown and cannot be addressed without a complete description of the whole atmosphere, from its lower boundary to its upper region that interacts with space. Because of the relative inaccessibility of the near-space environment, the upper region between about 50 and 200 km, also called the space-atmosphere-interaction region (SAIR) is the least known region in our atmosphere. However, the SAIR is essential for sustaining life on Earth by absorbing extreme solar radiation, ablating meteoric material, regulating gaseous escape, dissipating energetic particles and fields from space, while balancing influences from the planet itself in the form of tsunami-like atmospheric waves propagating from below, hurricane-speed winds

exceeding several hundred mph and temperatures four times that of the surface [*OASIS*, 2014]. Studying the properties of SAIR and the processes that govern them can significantly advance our understanding of the fundamental, universal processes that shape the atmospheres of habitable Earth-like planets throughout our galaxy. The McMurdo lidar campaign provides a unique opportunity to study the SAIR via providing unprecedented measurements, which enable new science discoveries. This thesis is one of the outcomes of the McMurdo lidar campaign, aiming to advance the observations and characterizations of the atmospheric waves that are fundamental to shaping the SAIR.

1.1 Atmospheric Waves and Their Roles in the Whole Atmosphere and Space

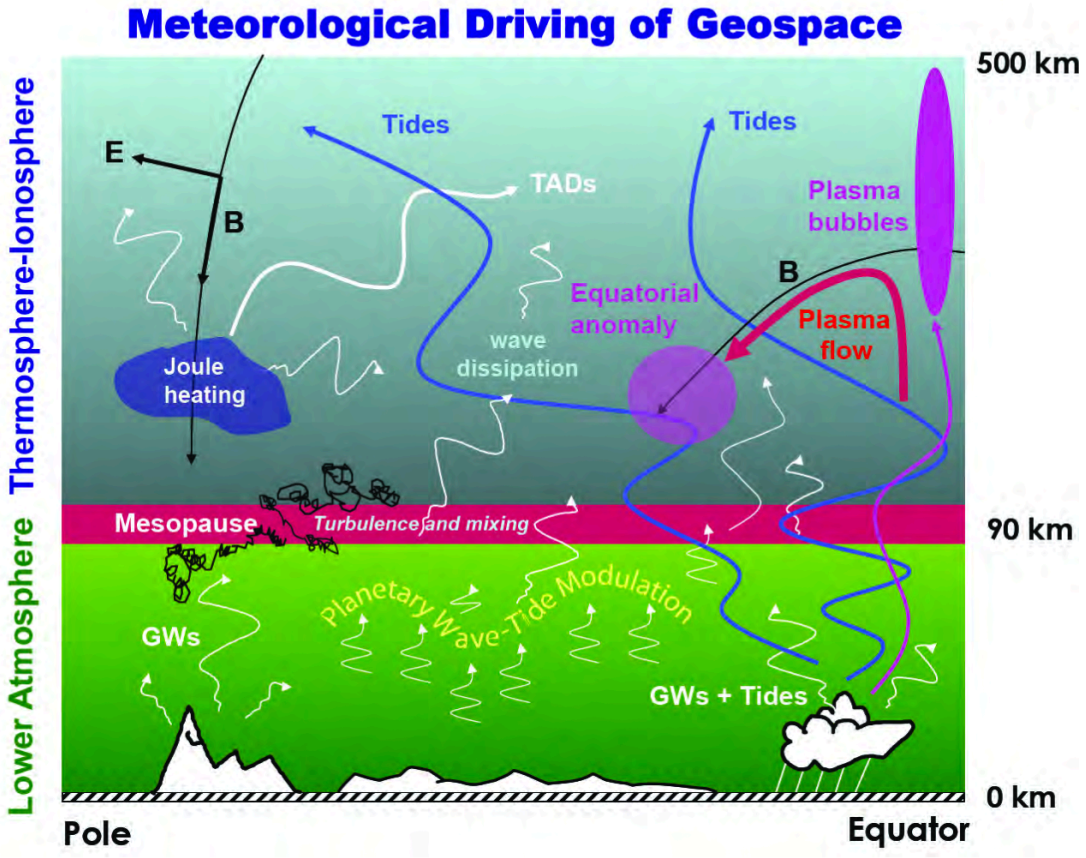

Figure 1.1. Schematic of the various mechanisms through which lower-atmosphere processes influence the ionosphere and thermosphere. Graphic from *National Research Council*, [2013].

The SAIR is strongly driven by waves, as waves are the primary mechanisms through which fluxes of mass, momentum and energy are transported and exchanged between neutral gasses and the dynamic plasma of space as illustrated in Figure 1.1 [*National Research Council*, 2013]. For example, gravity wave forcing drives the mesosphere and lower thermosphere (MLT) circulation so much that this region is not in radiative equilibrium. Consequently, the stratospheric jets in both hemispheres close and reverse directions, and the summer to winter meridional circulation is significantly enhanced [*Holton*, 1983]. Gravity wave induced strong disturbances to the electron densities in the ionosphere (often called "traveling ionospheric disturbances (TID)") can affect the refraction of radio waves and degrade directional finders [see review by *Hocke and Schlegel*, 1996]. Tidal waves excited by the absorption of solar radiation (e.g., by tropospheric H_2O and stratospheric O_3) propagate to the ionosphere causing the redistribution of ionospheric plasma, either through the dynamo mechanism, or directly by moving plasma along magnetic field lines. Planetary waves can cause remarkable wind, temperature and constituent variability of the middle and upper atmosphere with planetary spatial scales and periods of several days. Since Earth's atmosphere acts as a resonant cavity for mechanical waves, resonant modes of such a cavity are spontaneously excited. These waves are called "normal modes" or "Lamb waves" when their periods are short. They have been reported to cause variations in the thermospheric densities [*Forbes et al.*, 1999]. It is likely that similar processes of these waves occur at other planets as well. The dissipation of vertically propagating gravity waves in the thermosphere is thought to also occur at Mars [*Yiğit and Medvedev*, 2010]. The vertical propagation of tides, their dissipation, and their driving of the mean flow also have similarities at Earth and Mars [*Moudden and Forbes*, 2009].

Currently, the dynamical processes induced by large-scale waves such as tides and planetary waves are reasonably well understood, and have been incorporated into global circulation models (GCMs) by directly resolving the processes. However, for small-scale waves, such as gravity waves, many of the wave generation, propagation and dissipation processes are sub-grid processes in GCMs, so their effects need to be parameterized in such models before the influences can be determined. Unfortunately, such crude representation of gravity waves remains the largest uncertainty in middle and upper atmosphere model predictions and the parameterizations used in these models have not been thoroughly validated by observations, due to the observational challenges of gravity waves. Therefore, long-duration, large-altitude-range and high-resolution measurements of temperature and wind are essential to characterize the properties of the gravity waves, examine their propagation and infer the probable sources, and thus are critical to provide constraints for gravity wave parameterizations in GCMs.

In the Polar Regions, gravity waves play an important role in many dynamical and chemical processes in the atmosphere. For example, the meridional circulation driven by the dissipation of gravity waves in the polar MLT causes a strong adiabatic cooling of the summer MLT region, making it the coldest place on Earth [*Theon et al*., 1967; *Andrews et al*., 1987]. Gravity waves have been observed to induce the formation of polar stratospheric clouds (PSC), which can lead to enhanced ozone depletion in the polar regions [*Dörnbrack et al*., 2002; *Shibata et al*., 2003; *McDonald et al*., 2009]. Recently, studies have shown that underestimated gravity wave drag, in the polar regions, may be responsible for the long-standing 'cold pole' problem in many general circulation and chemistry climate models [e.g., *Tan et al*., 2011; *McLandress et al*., 2012]. While there are many observational studies of gravity waves at mid- and low-latitudes [e.g., *Cot and Barat*, 1986; *Sato*, 1994; *Sato et al*., 1997; *Thomas et al*., 1999; *Guest et al*., 2000;

Vincent and Alexander, 2000; *Hoffmann et al*., 2006; *Nastrom and Eaton*, 2006; *Vaughan and Worthington*, 2007; *Nakamura et al*., 1993; *Hall et al*., 1995; *Li et al*., 2007; *Lu et al*., 2009], the observations of gravity waves in polar regions especially in the Antarctica MLT region are still limited by very few observations of range-resolved temperature measurements. There have been observations using MF or meteor radar wind data of diurnal and semidiurnal tides [e.g., *Forbes et al*., 1995; *Baumgaertner et al*., 2005; *Murphy et al*., 2006], planetary waves [e.g., *Dowdy*, 2004; *Espy et al*., 2005; *Lu et al*., 2013], gravity waves [e.g., *Vincent*, 1994; *Hibbins et al*., 2007], and lamb waves [e.g., *Forbes et al*., 1999; *Portnyagin et al*., 2000; *Kovalam and Vincent*, 2003]. There have been observational studies of gravity waves, tides and planetary waves using OH intensities by OH all sky imagers [e.g., *Nielsen et al*., 2012], wind and temperature measured by Michelson [e.g., *Sivjee and Walterscheid*, 1994; *Azeem and Sivjee*, 2009] or Fabry-Perot interferometers [e.g., *Hernandez et al*., 1992; *Wu et al*., 2005]. These instruments do not have range-resolve ability. Sodium density broadband lidar system has also been used to observe the wave dynamics in the sodium density layers [*Collins and Gardner*, 1995]. Large-scale global waves such as tides and planetary waves in the Antarctic MLT are studied by satellite observations [e.g., *Iimura et al*., 2009; *Morris et al*., 2009]. Unfortunately, most of the above studies do not have range-resolved temperature observations about the waves in Antarctic MLT. Range-resolved temperature observations provide vertical information such as the vertical wavelengths of the waves, which is very crucial to the identification of waves. It will help resolve the ambiguity in wave propagation direction if only one single station wind measurement is available in the wave analysis.

Advances in remote sensing technologies in the last several decades have significantly improved observing capabilities, providing volumes of data with unprecedented coverage,

precision, and temporal and spatial resolution. New whole atmosphere models are under fast development towards predicting the system-level response of the atmosphere. However, the developments of data analysis methods in the middle and upper atmosphere research have not advanced as much in the same time but are greatly needed. In particular, developments on automated pattern analysis, detection, recognition, tracking, and reconstruction techniques for application to observational and model data have been identified as one of the priorities by the community [*CEDAR: Strategic Vision*, 2011]. For example, a new development in wave analysis method is to implement the wavelet transform and reconstruction to automatically detect and reconstruct wave packets. The advantage of the wavelet spectral analyses lies in the ability to adapt its window's temporal width to the wave spectrum, i.e., automatically narrowing at high frequencies and widening at low frequencies [*Chui*, 1992]. Therefore, wavelet analysis methods are more suitable than Fourier transform methods for localization of the real atmospheric waves since many waves are inherently intermittent [*Teitelbaum and Vial*, 1991; *Sato and Yamada*, 1994; *Forbes et al*., 1995; *Alexander and Dunkerton*, 1999], i.e., wave properties such as amplitude, frequency and vertical wavenumber vary with both time and space as the wave propagates. Many remote sensing instruments deliver two-dimensional (2-D) data. For example, ground-based lidars and radars record range-resolved atmospheric data over time at a fix location, thus 2-D data in the range-time domains. Ground-based imagers, and many satellite sensors, obtain 2-D spatial images. Unfortunately, extracting intermittent/localized two-dimensional wave packets is still a common technical challenge in analyzing atmospheric and space data. Therefore, the 2-D wavelet transform is recognized as an important tool for the autonomous processing of atmospheric data.

1.2 McMurdo Lidar Campaign and My Antarctic Winter-Over Experience in 2014

To fill a critical data gap in observations of the middle and upper atmosphere between the South Pole and the Antarctic Circle, the University of Colorado lidar group deployed an Fe Boltzmann lidar to McMurdo Station (77.83°S, 166.67°E) in December 2010 and has been collecting data since then [*Chu et al*., 2011a, 2011b]. McMurdo is located on Ross Island (see Figure 1.2), and this lidar campaign is a collaboration between the United States Antarctic Program (USAP) and Antarctica New Zealand (AntNZ). The lidar was successfully installed in the AntNZ facility at Arrival Heights near McMurdo, and the first Fe signals were obtained on 16 December 2010. Since then, the University of Colorado lidar researchers have operated the lidar around the clock, weather permitting, through all 12 months of the year to acquire as many observations as possible. Developed at the University of Illinois more than a decade ago [*Chu et al*., 2002], the lidar system consists of two independent channels operating at two neutral Fe absorption lines, 372 nm and 374 nm, respectively. Thus, the lidar measures the Fe layers in two different wavelengths, and the ratio between these two channels is used to derive temperature in the MLT region [*Gelbwachs*, 1994; *Chu et al*., 2002]. Owing to the narrowband interference filters and Fabry-Perot etalons employed in the lidar receivers and the high-power pulsed Alexandria lasers employed in the lidar transmitters, this Fe Boltzmann lidar is capable of full-diurnal measurements of Fe density and temperature, along with Rayleigh temperature in the altitude range of 30 to 70 km. Principles, capabilities and error analysis of the lidar can be found in [*Chu et al*., 2002]. Before its deployment to McMurdo, this Fe Boltzmann lidar was refurbished and upgraded at the University of Colorado to restore its specifications and to further enhance spectral stability temporal resolution and daytime capability [*Chu et al*., 2011a; *Wang et*

al., 2012]. Such full-diurnal capabilities facilitate both the atmosphere temperature measurements and observations of dominant waves in this region with various time-scales.

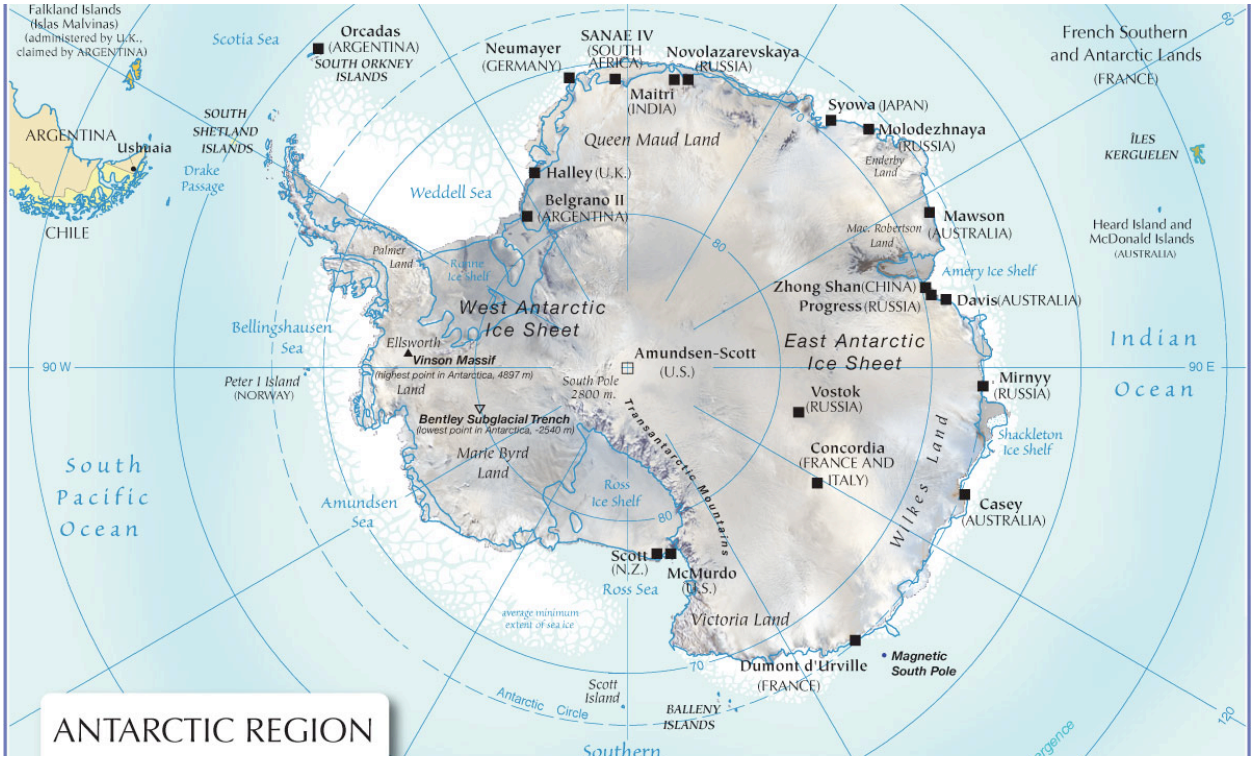

Figure 1.2. The map of Antarctica. Source: National Online Projects (http://www.nationsonline.org).

Since the start of the McMurdo lidar campaign in 2010, the raw temperature data from the stratosphere to the lower thermosphere (about 30–115 km) exhibited persistent, dominant, large-amplitude waves with non-tidal periods of ~3–10 h and vertical wavelengths of ~20–30 km. This is shown in Figure 1.3 with four typical MLT temperature observations in 2014. Here, the word "persistent" is used to describe the fact that these waves continue for a prolonged period, e.g., a single wave event may last at least 10 h, and sometimes over 50 h, in the small field of view (FOV, 1 mrad) of the lidar beams. If we do not separate the observed wave variations into individual wave events with individual periods, but regard these waves as a group of waves with periods ranging between 3 and 10 h, then this wave group is perpetual. That is,

these waves occur on every lidar run spanning sufficient duration, and occur frequently enough as to appear endless and uninterrupted. There has not been any single lidar run that does not show the signature of this 3–10 h wave group during 5 years of lidar observations at McMurdo, and so far we have not seen any inactive wave gap epoch in observed temperature data. It is surprising that these waves are so dominant and so strong in the Antarctic MLT, which suggests a significant gap in our understanding of the wave sources and the generation mechanisms in the SAIR. Their implications on GCMs are also significant, particularly with regard to the "cold pole" problem. The persistent occurrence of 3–10 h waves in the Antarctic mesopause region implies that these waves are unlikely to severely dissipate in the stratosphere, so they may not produce sufficient wave drag in the stratosphere to be responsible for the "cold pole" problem. However, we cannot investigate the above intriguing questions of these 3–10 h waves before characterizing their properties through observations.

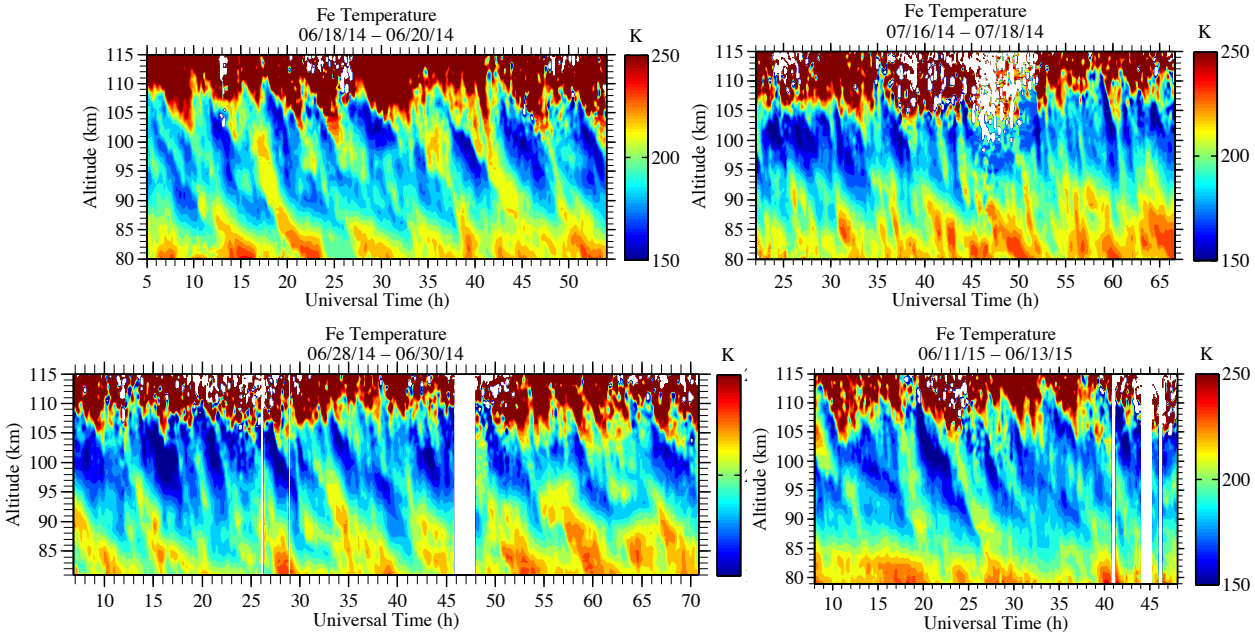

Figure 1.3. Examples of strong 3–10 h waves observed in the Antarctic MLT temperatures in 2014. The original Fe temperatures in the MLT are derived in resolutions of 0.25 h and 0.5 km, with the sampling window shifted at steps of 0.1 h and 0.1 km.

With the motivation to gather more information on these 3–10 h waves through more observations, from October of 2013 to October of 2014, I worked at McMurdo station as the winter-over lidar scientist for the Fe Boltzmann temperature lidar campaign. The work that I performed, which involved diagnosing and resolving various technical issues, led to many record-breaking long lidar runs with some of the highest signal levels of all five years of our campaign. In particular, I was motivated to take nearly three days of continuous lidar data in 2014 to investigate whether these waves ever paused. Figures 1.3 clearly shows that the 3–10 h waves were persistent for three entire days during 28–30 June 2014. The long datasets also made studies such as wave-tide interactions and planetary waves possible in the Antarctic MLT for the first time.

Overall, a total of ~1350 hours of data was collected from October 2013 to the end of October 2014. It is worth mentioning that the 64.5 hours of continuous lidar run by myself from June 28-30, 2014 was the longest winter records of lidar observations from 2010 to 2015. I was also one of the key members in the 3-person lidar team who made the historic record of continuous lidar run for 174 hours from Dec. 29, 2013 to Jan. 6, 2014 in Antarctica. All these data have been used in the study of the newly observed thermospheric Fe layers events [*Chu et al*., 2016], gravity wave potential energy [*Lu et al*., 2015b], the 3–10 h waves [*Chen et al*., 2016b], temperature tides [*Fong et al*., 2014, 2015] and temperature structures [*Fong et al*., 2016].

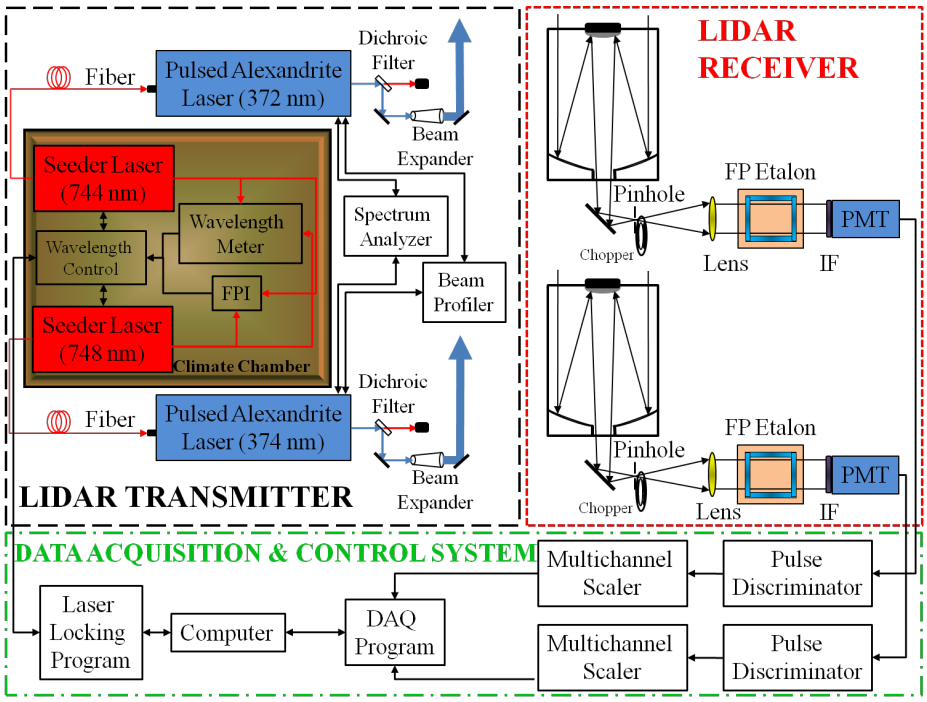

Figure 1.4. Diagram of the upgraded Fe Boltzmann and Rayleigh temperature lidar system [*Wang et al.*, 2012].

The upgraded lidar system diagram is shown in Figure 1.4. The transmitter consists of two lasers operating at 372 and 374 nm, corresponding to resonance lines of the two sublevels of iron atom's ground state. Each transmitter channel consists of an injection-seeded, frequency-doubled, flash lamp-pumped, pulsed alexandrite laser (PAL) and a seed laser. The seed lasers were packaged in a sealed climate chamber that keeps the air temperature and humidity stable. In addition, a Bristol wavelength meter and a scanning Fabry-Perot Interferometer (FPI) are used to control and monitor the seed lasers via a laser-locking program. The output of the seed laser is fiber coupled for injection into the PAL cavity. A dichroic filter was used to separate the fundamental and second harmonic pulses. The outgoing laser beam is expanded by a 6×beam expander to reduce the divergence below 0.35 mrad, and then directed into the sky via a steering

mirror. The pulsed output of the alexandrite laser is monitored with a pulsed laser spectrum analyzer and a beam profiler.

Each receiver channel, which is aligned to look in a fixed zenith direction, consists of a 40-cm Schmidt-Cassegrain telescope with enhanced UV dielectric coating. The return signal collected by the telescope is reflected by a 45º high reflection mirror, focused through a field-stop pinhole, collimated by lenses passes through a daytime etalon filter and an interference filter, and then detected by a PMT running in photon counting mode. The field of view of the telescope is controlled via the pinhole size at the focal plane and is set to match the divergence of the outgoing laser beam. To prevent PMT saturation by the strong low-altitude returns, a mechanical chopper is placed just behind the field stop in the receiver chain. The output signal from PMT is then thresholded by a discriminator, and the acquisition of two channels' data is handled by the data acquisition system via two multi-channel scalers (SR430s).

Unlike the Doppler technique that relies on the temperature dependence of the Doppler broadening of atomic resonance absorption lines, the Boltzmann technique relies on the temperature dependence of the Maxwell–Boltzmann distribution of atomic populations on different atomic energy levels in thermodynamic equilibrium. More detailed information on the operation principle can be found in *Gelbwachs* [1994] and *Chu et al*., [2002].

1.3 Polar Intradiurnal Atmospheric waves

Atmospheric waves with periods shorten than 12 h are often referred as "intradiurnal" waves. At Polar Regions, intradiurnal waves have been observed with various measurement techniques and many interpretations have been put forth to explain the observed waves. The observation techniques used in these previous studies of intradiurnal waves are MF or meteor radars, OH all-sky imagers, Michelson or Fabry-Perot interferometers and incoherent scatter

radars (ISRs). Except for the ISR observations that provide simultaneous temperature and wind measurements, the other observation techniques either provide only temperature or only wind measurements, and some of the instruments do not have vertical resolution. The interpretations put forth to explain the observed intradiurnal waves are: Lamb waves, quartra-diurnal and terdiurnal tides, wave-wave interactions and inertia-gravity waves. Each theory is summarized and discussed.as follows.

1.3.1 Lamb Waves

Hernandez et al. [1992] observed a pronounced westward propagating wave in the wind field with a period of 10.1 h near the South Pole and concluded that they observed an zonal wavenumber s = 1 Lamb wave. The vertical wavelength of the wave was derived from an MF radar at McMurdo (Scott Base), and was near 100 km. *Forbes et al*. [1999] also observed westward propagating wind oscillations for s = 1 using meteor radar measurements near the South Pole during the winter months. These oscillations have periods between 7.5 and 10.5 h and amplitudes ±5–15 m/s. Two modes appear to be dominant in their analysis, i.e., the second symmetric mode with period ~8.6 h and the first asymmetric mode with period ~10.4 h [*Portnyagin et al*., 2000]. The observations were interpreted in terms of atmospheric manifestations of normal modes or Lamb waves. *Kovalam* and *Vincent* [2003] used MF radar observations at Adelaide (35°S, 138°E) and Davis (68°S, 78°E) and identified the intradiurnal wind variations as Lamb waves with vertical wavelengths ~80 km.

A Lamb wave is the free oscillation solution of the atmosphere under isothermal and non-dissipation condition [*Forbes*, 1995]. Under these conditions, horizontal wave velocities of the Lamb wave grow with height z as $\exp(\varkappa z/H)$ where $\varkappa = 2/7$ and H is scale height ~8 km. First, this suggests that Lamb wave has no phase change with height under ideal conditions. Second,

the growth rate of this wave amplitude is associated with an actual decay of energy so that most of the free wave's energy is concentrated within a few scale heights of the ground. This means that Lamb wave has no vertical flux of energy out of the atmosphere. However, after the effects of the nonisothermality, surface friction, eddy and molecular dissipation and ion drag are considered, *Lindzen and Blake* [1972] found that Lamb waves can have internal wave behavior, i.e., phase progression with height and finite lifetime (~4 days). Simulation of such wave is also performed in the study by *Forbes et al*. [1999] (see Figure 1.5), which further confirms the theoretical base of the probable occurrence of Lamb wave in the real atmosphere.

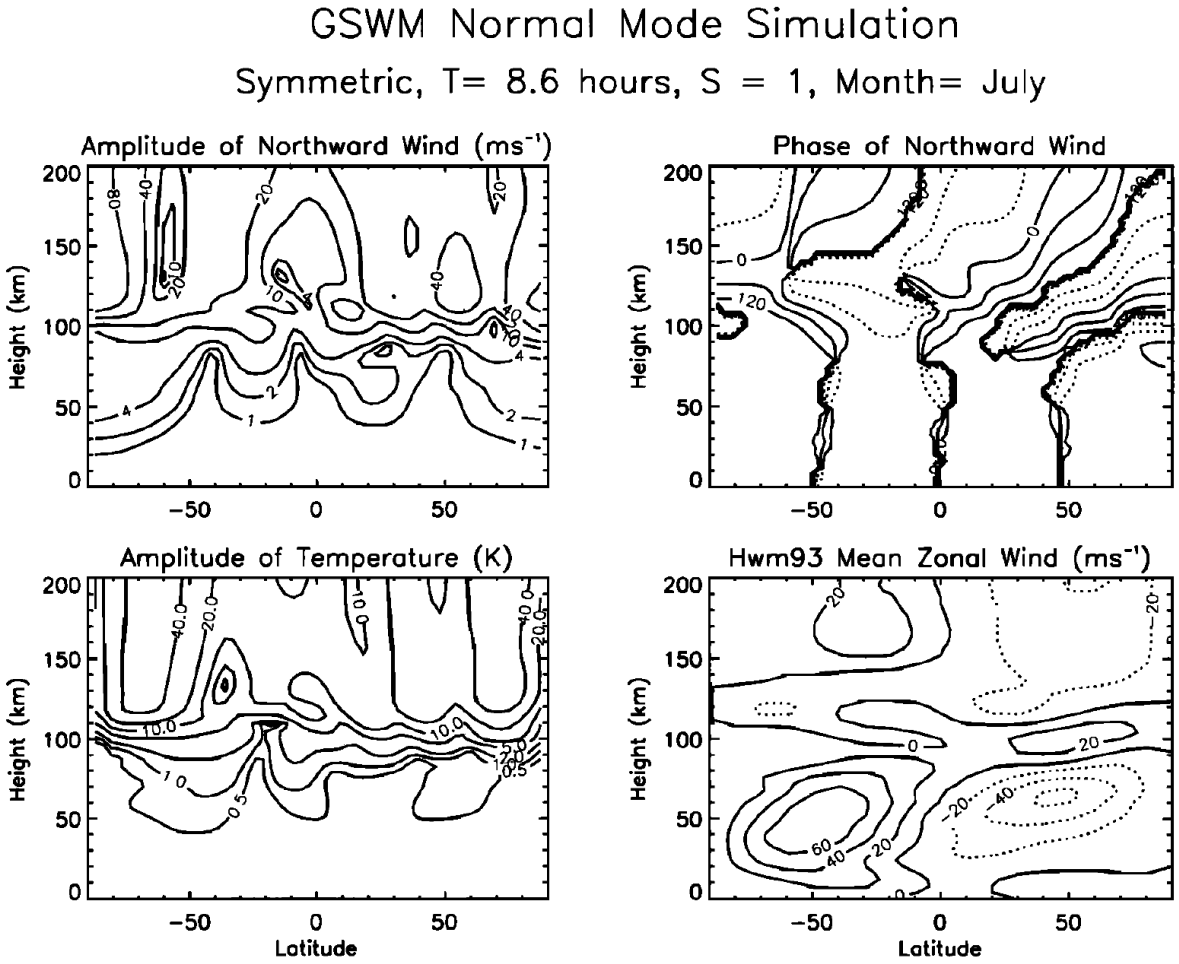

Figure 1.5. GSWM simulation of the 8.6 h, first symmetric mode of Lamb waves by *Forbes et al*. [1999]. As can bees seen from the phase of the north wind, Lamb wave does not show phase progression until reaching ~100 km.

1.3.2 Quartra-Diurnal Tides and Terdiurnal Tides

Atmospheric tides are global scale oscillations with periods that are sub-harmonics of 24 hours, and are typically forced by direct solar heating of the Earth's atmosphere. In the Antarctic MLT, there are a few observations of quartra-diurnal (6-hour period) or terdiurnal (8-hour period) tides based on OH temperature measurements, which complement most MLT radars that only give provide wind measurements. *Azeem and Sivjee* [2009] analyzed 8-h tidal signatures in the OH temperatures measured by a Michelson interferometer at South Pole from 1994 to 2007. They found the existence of an 8-h wave but with great variability in amplitude and determined the zonal wavenumber $s = 0$ from the zero phase difference between different azimuth angles. However, they found the diurnal tides are the strongest and most persistent and coherent tidal component at South Pole. *Sivjee and Walterscheid*, [1994] reported the occurrence of a 6-h zonaly symmetric ($s = 0$) in the OH temperature data at South Pole. Compared with the Antarctic, there are a few more but still very limited studies of terdiurnal tides in the northern hemisphere high latitudes [*Virdi and Williams*, 1993; *Oznovich et al*., 1997; *Hall et al*., 1998; *van Eyken et al*., 2000; *Younger*, 2002]. These studies revealed that 8-h tide could be a significant component of the polar MLT region but with significant day-to-day variability. It is anticipated from classical tidal theory that the solar driven global terdiurnal tide has basically long vertical wavelength (>80 km) [*Aso*, 2003]. Consequently, shorter vertical wavelengths (25-35 km) observed by *Younger* [2002] are explained by nonlinear interaction between 12- and 24-h tides. However, none of the above studies have information of zonal wavenumber, which is quite critical to the interpretation of the generation mechanism of 6-h and 8-h tide. For example, if an $s = 0$ terdiurnal tide is observed, the nonlinear interaction of migrating 12-h ($s = 2$) and 24-h ($s = 1$)

tide will not be a plausible explanation, since migrating 12-h and 24-h tides will only generate an 8-h tide with $s = 3$ or $s = -1$ through non-linear interaction. However, note that nonlinear interaction between non-migrating tides can generate such $s = 0$ terdiurnal tides (see *Moudden and Forbes* [2013]). To investigate whether an observed wave has tidal origin, we need to analyze more data from various station rather than single station or to make use of global circulation models.

1.3.3 Planetary Wave-Tide or Gravity Wave-Tide Interactions

Planetary wave could modulate a tide through nonlinear interactions and give rise to sideband waves with frequencies and wavenumbers equal to the sum and difference of those of the two interacting wave components [*Manson et al*., 1982; *Teitelbaum et al*., 1989]. Note that such nonlinear interaction is a consequence of the nonlinearities inherent in the governing primitive equations [*Andrews et al*., 1987]. When observed from a single ground-based location, such nonlinear interaction results in a new "child wave" or an apparent modulation of the tidal amplitudes by the planetary wave period [e.g., *Teitelbaum and Vial*, 1991]. At northern high latitudes, based on the measurements from an array of instruments, *Wu et al*., [2002] presented comprehensive observations of a 10-h oscillation in the temperature and wind fields of the mesosphere and lower thermosphere. By comparing the phase of the wave at different stations, a zonal wave number $m = 5$ was inferred, and the vertical wavelength was estimated to be about 53 km. These wave properties led to the conclusion that nonlinear coupling between the semidiurnal tide and the 2-day planetary wave was the likely excitation mechanism.

Superimposed on the mean winds, the different local mean wind profiles induced by tides imply very different background environments that affect the propagation and dissipation of gravity waves [*Fritts and Vincent*, 1987]. Since the amplitudes of the diurnal tide are very large,

saturation and momentum deposition of the gravity waves are greatly affected and thereby modulated by the tidal winds. When observed from a single ground-based location, such interaction results in oscillations with tidal periods. A gravity wave/tidal interaction model proposed by *Fritts and Vincent* [1987] suggests that the wind background induced by tides put a limit on the gravity wave amplitude while gravity waves induce accelerations to the mean flow and thereby affect tidal waves. Pseudo-tides, generated by gravity wave momentum fluxes modulated by the solar-driven tide, were proposed by *Walterscheid et al*. [1986] to explain the large tidal oscillations observed in polar MLT temperature variation. These oscillations depend upon the intensities, phase velocities and coherence of the gravity waves and thus can be quite variable from day-to-day [*Vial and Forbes*, 1989]. So far, this mechanism has been used to explain 12-h and 24-h tides. However, in principal, gravity waves will modulate/generate any other tidal period oscillations with considerable amplitude.

1.3.4 Inertia-Gravity Waves

Inertia-gravity waves (IGWs) have frequencies in the vicinity of the inertial frequency (or Coriolis frequency, $2\Omega\sin\phi$, where Ω is Earth's rotation rate, ϕ is the latitude) and are strongly affected by the rotation of the Earth. Note that American Meteorological Society (AMS) currently adopts the term "inertio-gravity waves" for such waves in its glossary of meteorology. But historically, many of the earliest and most cited literatures in the field of aeronomy used the term "inertia-gravity waves" instead [e.g., *Cadet and Teitelbaum*, 1979; *Hirota and Niki*, 1985; *Cornish et al.*, 1988; *Sato et al.*, 1997; *Vincent and Alexander*, 2000; *Fritts and Alexander*, 2003]. Although there are no differences between the two terms, we prefer the usage of the term "inertia-gravity waves" throughout this thesis to be consistent with the previous studies. At Polar Regions, due to the short inertial period (12.24 h at McMurdo), a large fraction of gravity waves

with periods longer than 3 h are classified as IGWs. *Hernandez et al.*, [1993] hinted that some 12-h oscillations at South Pole in the optical measurements of the Doppler shift of the OH emission might be manifestations of IGWs. IGWs have been observed by *Nicolls et al*. [2010] using an ISR in the Arctic with a long period of ~10.5 h, and a short vertical wavelength of ~4–10 km. *Nicolls et al*., [2010] continued to use ray tracing to find that a possible mechanism for IGW generation is geostrophic adjustment of the jet stream. Some model studies by *Mayr* [2003] and *Mayr et al*. [2004] reported horizontal wind and temperature oscillations with periods around 10 h in their Numerical Spectral Model (NSM) in the upper mesosphere. The oscillations were identified as planetary-scale inertio-gravity waves, generated by instabilities in the atmosphere. Inertia-gravity waves should follow the gravity wave dispersion and polarization [see reviews in *Fritts and Alexander*, 2003, 2012]. By examining whether the observed temperature and wind perturbations satisfy the polarization relationship, we can identify whether these perturbations are caused by inertia-gravity waves. Dispersion relationship will help us determine the horizontal wavelengths and intrinsic periods of the waves.

1.4 Research Objectives of This Dissertation

This dissertation is aimed to explore the wave dynamics in the polar SAIR by providing observations and quantitative characterizations of the gravity wave properties derived from the range-resolved temperature measurements. Such characterizations are essential to understanding the generation mechanisms of these waves and their potential impacts on the Earth's atmosphere. During the characterization process, many new wave analysis methods that facilitate the process are developed. For example, the 2-D wavelet analysis and synthesis methods are recognized as an important tool for the autonomous processing of 2-D atmospheric data.

The specific research objectives of this thesis are:

1) Derive the properties of the fast thermospheric gravity waves in the thermospheric Fe densities and separate them from the long-period neutral temperature variations in the stratosphere through MLT.
2) Derive the intrinsic properties of inertia-gravity waves during three events, incorporating temperature and wind data from simultaneous lidar and radar observations.
3) Perform a statistical study on the wave properties of the persistent 3–10 h waves in lidar temperature data in June by applying 1-D wavelet analysis and parametric spectral methods.
4) Develop automated 2-D wave packets detection, reconstruction and wave property analysis techniques using 2-D Morlet wavelet analysis. Establish the mathematical formalism of the 2-D Morlet wavelet analysis and synthesis with a detailed mathematical derivation. Demonstrate the utility of 2-D Morlet wavelet methods by applying them to lidar temperature data observed in May to July.
5) Explore the possible wave sources with a statistical study of GCM and reanalysis data.

1.5 Structure of This Dissertation

The organization of the dissertation is as follows:

1. Chapter 1 is the introduction.
2. Chapter 2 focuses on the derivation of the properties of the thermospheric gravity waves from the stratosphere to the lower thermosphere in Fe densities and neutral temperatures observed by lidar. The is my contribution to *Chu et al.*, [2011b].
3. Chapter 3 provides details on the discovery of the inertia-gravity waves and the derivation of their intrinsic properties based on three case studies from simultaneous lidar and radar observations. This is published in *Chen et al*. [2013].

4. Chapter 4 describes the persistent 3–10 h gravity waves and provides the statistical results on their wave properties such as life spans, periods, vertical wavelengths and vertical phase speeds. This is published in *Chen et al*. [2016b].
5. Chapter 5 introduces a new automated 2-D wave packets detection and reconstruction technique based on 2-D Morlet wavelet analysis with detailed mathematical formalism and applications to 2-D (time and vertical) lidar data. This work has been submitted and is under review [*Chen and Chu*, 2016].
6. Chapter 6 discusses the mystery of the wave identities in the framework of classical tidal theory and then explores the possible wave sources using ECMWF reanalysis data.
7. Chapter 7 contains the conclusions and outlook for our future research.
8. Appendix A includes another case study of an IGW event on 11 July 2011 observed with lidar and radar at McMurdo, which is originally published in [*Chen et al.*, 2012]. Appendix B gives the detailed derivations of the 2-D Morlet wavelet transforms that are not shown in Chapter 5.

Journal papers and conference proceedings published and submitted for this dissertation:

[1] Chen, C., X. Chu, Z. Yu, W. Fong, A. J. McDonald, X. Lu, and W. Huang (2012), Lidar and radar investigation of inertia gravity wave intrinsic properties at McMurdo, Antarctica, in *Proceedings of the 26th International Laser Radar Conference*, pp. 1057–1060, Porto Heli, Greece.

[2] Chen, C., X. Chu, A. J. McDonald, S. L. Vadas, Z. Yu, W. Fong, and X. Lu (2013), Inertia-gravity waves in Antarctica: A case study using simultaneous lidar and radar measurements

at McMurdo/Scott Base (77.8°S, 166.7°E), *J. Geophys. Res. Atmos*., 118(7), 2794–2808, doi:10.1002/jgrd.50318.

[3] Chen, C., X. Chu, W. Fong, X. Lu, A. J. McDonald, D. Pautet, and M. Taylor (2016a), Antarctic Wave Dynamics Mystery Discovered by Lidar, Radar and Imager, in *Proceedings of the 27th International Laser Radar Conference*, edited by B. Gross, F. Moshary, and M. Arend, p. 13004, New York, NY.

[4] Chen, C., X. Chu, J. Zhao, B. R. Roberts, Z. Yu, W. Fong, X. Lu, and J. A. Smith (2016b), Lidar observations of persistent gravity waves with periods of 3-10 h in the Antarctic middle and upper atmosphere at McMurdo (77.83°S, 166.67°E), *J. Geophys. Res. Sp. Phys*., 121(2), 1483–1502, doi:10.1002/2015JA022127.

[5] Chen, C., and X. Chu (2016), Two-dimensional Morlet wavelet transform and its application to extracting two-dimensional wave packets from lidar observations in Antarctica, *J. Atmos. Sol.-Terr. Phys*., in revision.

[6] Chu, X., Z. Yu, C. S. Gardner, C. Chen, and W. Fong (2011), Lidar observations of neutral Fe layers and fast gravity waves in the thermosphere (110-155 km) at McMurdo (77.8°S, 166.7°E), Antarctica, *Geophys. Res. Lett*., 38(23), L23807, doi:10.1029/2011GL050016.

[7] Lu, X., C. Chen, W. Huang, J. A. Smith, X. Chu, T. Yuan, P.-D. Pautet, M. J. Taylor, J. Gong, and C. Y. Cullens (2015), A coordinated study of 1 h mesoscale gravity waves propagating from Logan to Boulder with CRRL Na Doppler lidars and temperature mapper, *J. Geophys. Res. Atmos*., 120(19), 10,006–10,021, doi:10.1002/2015JD023604.

[8] Fong, W., X. Chu, X. Lu, C. Chen, T. J. Fuller-Rowell, M. Codrescu, and A. D. Richmond (2015), Lidar and CTIPe model studies of the fast amplitude growth with altitude of the

diurnal temperature “tides” in the Antarctic winter lower thermosphere and dependence on geomagnetic activity, *Geophys. Res. Lett.*, 42(3), 697–704, doi:10.1002/2014GL062784.

[9] Lu, X., X. Chu, W. Fong, C. Chen, Z. Yu, B. R. Roberts, and A. J. McDonald (2015b), Vertical evolution of potential energy density and vertical wave number spectrum of Antarctic gravity waves from 35 to 105 km at McMurdo (77.8°S, 166.7°E), *J. Geophys. Res. Atmos.*, 120(7), 2719–2737, doi:10.1002/2014JD022751.

CHAPTER 2

Characterization of Fast Gravity Waves from 30 to 155 km by Lidar at McMurdo

2.1 Introduction

[*Chu et al*., 2011b] discovered neutral Fe layers with fast gravity wave signatures from 110 to 155 km in the thermosphere, using an Fe Boltzmann temperature lidar on 28 May 2011 at McMurdo (77.83°S, 166.66°E), Antarctica (see Figure 2.1). This is the first report of neutral Fe layers up to 155 km and also the first observations of gravity waves observed in metal layers at such thermospheric altitudes. After that, the neutral metal layers up to 180 km have been observed by Fe Boltzmann lidar at McMurdo, Antarctica and range-resolved temperature profile up to 170 km has already been demonstrated (see Figure 2.2) [*Chu et al*., 2013, 2016]. New discoveries in recent years have radically changed our view on the range limit of neutral metal layers and have opened a new door to observing the neutral polar thermosphere with ground-based instruments. The neutral metal layers provide an excellent tracer for resonance-fluorescence lidars to directly measure the neutral temperatures and winds in the thermosphere. Using these layers as tracers, *Chu et al*. [2011, 2013] have demonstrated that neutral atmosphere temperatures can be derived from ~30 to ~170 km by combining the Fe Boltzmann technique with the Rayleigh integration technique.

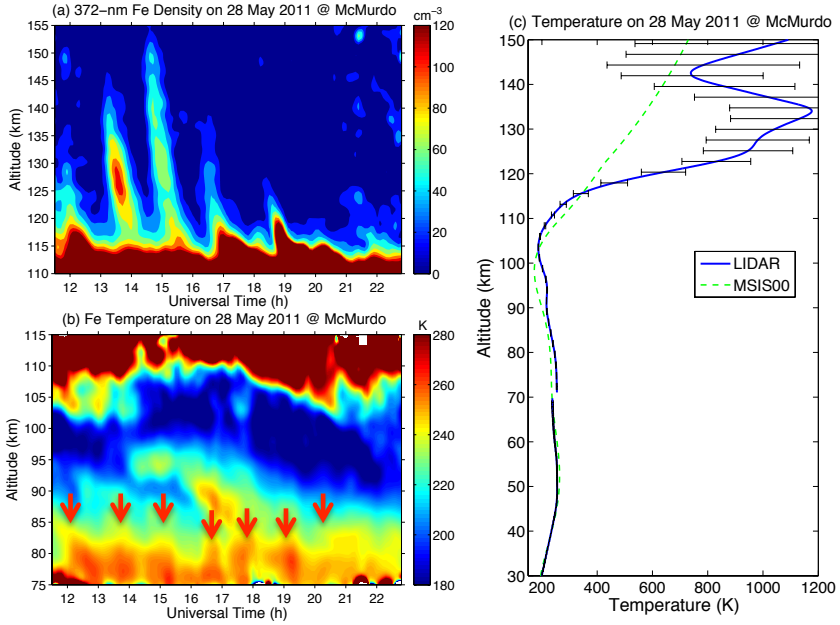

Figure 2.1. Fe lidar measurements on 28 May 2011 at McMurdo: (a) Thermospheric Fe density contour, (b) MLT temperature contour, and (c) temperature from 30 to 150 km [*Chu et al*., 2011b].

The Fe layers above 110 km in Figure 2.1 possess apparent wave features. The thermospheric Fe layer is clear at the beginning of the observation (11.5 UT) with a distinguishable layer up to 133 km. The layer descends with time and merges with the main layer at ~110 km around 13.5 UT. In the meantime, another Fe layer develops at ~145 km and then descends downward. The third and highest Fe layer occurs around 14.7 UT at 155 km and then descends with time. The wave-like features repeat four more times before the termination of the observations due to clouds, but the starting altitudes of the Fe layers become lower as time progresses. Fe temperatures plotted in Figure 2.1b for the main Fe layers show apparent wave perturbations as well. The dominant wave has a period of ~8 h and vertical phase velocity of ~0.7 m/s. Shorter-period waves of ~1.5 h are clearly visible below 90 km (denoted by the red arrows in Figure 2.1b). According to the theory originally proposed by *Chu et al*. [2011b] and later modeling studied by *Yu* [2014], *Yu and Chu*, [2014], *Chu et al*. [2016], and *Chu and Yu*

[2016], the observed neutral Fe layers with clear gravity wave signatures are formed through the neutralization of vertically converged Fe^+ ion layers, and the main neutralization channel is the direct electron-Fe^+ recombination. These Fe^+ ions are transported from their main deposition region (80–110 km) to the E–F regions by the polar electric field, and then vertically converged by gravity-wave-induced wind shears [*Yu*, 2014]. The converged Fe^+ layers possess very high Fe^+ ion densities and their recombination with electrons can produce the neutral Fe densities observed by the lidar. Wind shears descend with the downward phase velocities of the wave, thereby resulting in the downward transport of the Fe layers [*Chu and Yu*, 2016].

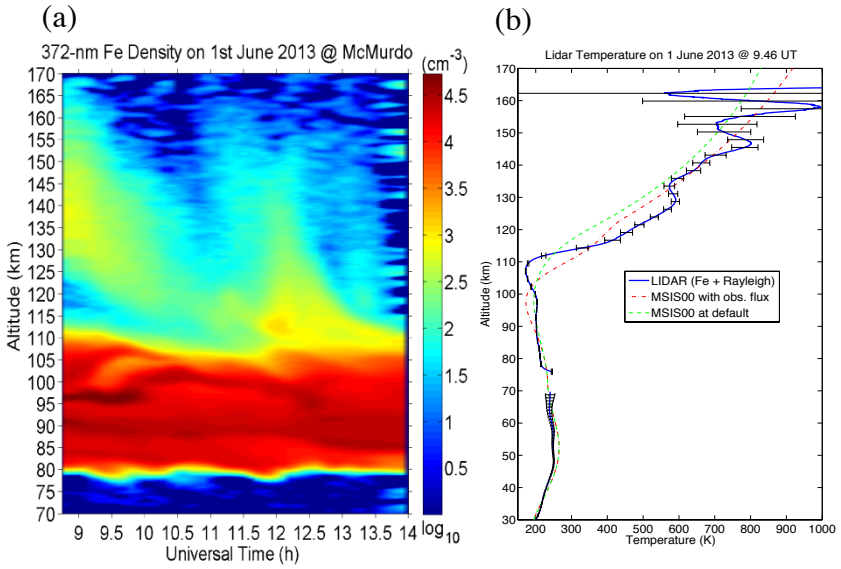

Figure 2.2. Measurements by an Fe Boltzmann temperature lidar at McMurdo, Antarctica have shown (a) neutral Fe layers extending as high as 170 km on 1 June 2013 and (b) the vertical profile from 30 to ~170 km of temperature at 9.46 UT [*Chu et al*. 2013].

Combining the Fe Boltzmann and Rayleigh integration techniques, temperatures are derived from 30 to 170 km using the Fe lidar (See Figure 2.1c and Figure 2.2b). Traditionally, very little is known about the neutral atmosphere in the altitude range of 100–200 km because observations of neutral winds, temperatures and densities in this region at any latitude are rare [*CEDAR: Strategic Vision*, 2011]. With the McMurdo Fe lidar observing Fe atoms, neutral Fe

temperatures and gravity waves well into the thermosphere, this issue is being addressed. The thermosphere Fe layers provide the potential tracers for modern Doppler lidars to measure neutral wind and temperature in the E-region between 100 km and at least 155 km. Furthermore, Fe atoms are the most abundant metal species in the Earth's upper atmosphere, while Fe^+ ions are a major component of sporadic E layers [*Plane*, 2003].

In order to accurately model such thermospheric Fe layers and validate the proposed generation mechanism, truthfully extracting the wave perturbations from the raw observation and derive the wave parameters are essential in providing a direct comparison and necessary model parameters. My contributions to this work are to analyze the fast gravity waves exhibited in these thermospheric gravity-wave-induced Fe layer events and to extract them from the neutral temperatures from the stratosphere through the MLT region to the thermosphere.

2.2 Characterization of the Fast Thermospheric Gravity Waves

To extract the fast gravity waves in the thermosphere, we use the case on 28 May 2011 as an example to demonstrate our wave analysis methods. First, we calculate the wave period profile in the thermospheric Fe layer by applying a Morlet wavelet transform [*Torrence and Compo*, 1998] to the Fe density data for each altitude (from 69 to 154 km) to get the dominant period profile. The errors of the periods are calculated from the standard deviations of the peak periods in the wavelet power spectra at single altitude. The period profile and its error bars are plotted in Figure 2.3b. The dominant periods of the gravity waves in the thermospheric Fe layer are ~1.5 h. We then draw two lines along the rising and falling edge of the third (the highest) Fe peak to mark the envelope of the center phase of the Fe layer. Between the two marked edges, we track the peak of the Fe thermosphere layer and calculate the downward descending speed, i.e., the vertical phase speed. The vertical wavelengths are then calculated by multiplying the

phase speeds with the dominant periods. The results for the vertical phase speeds and vertical wavelengths are shown in Figure 2.3c. Both the vertical phase speeds and vertical wavelengths increase rapidly with altitude, reaching ~13 m/s and ~80 km, respectively.

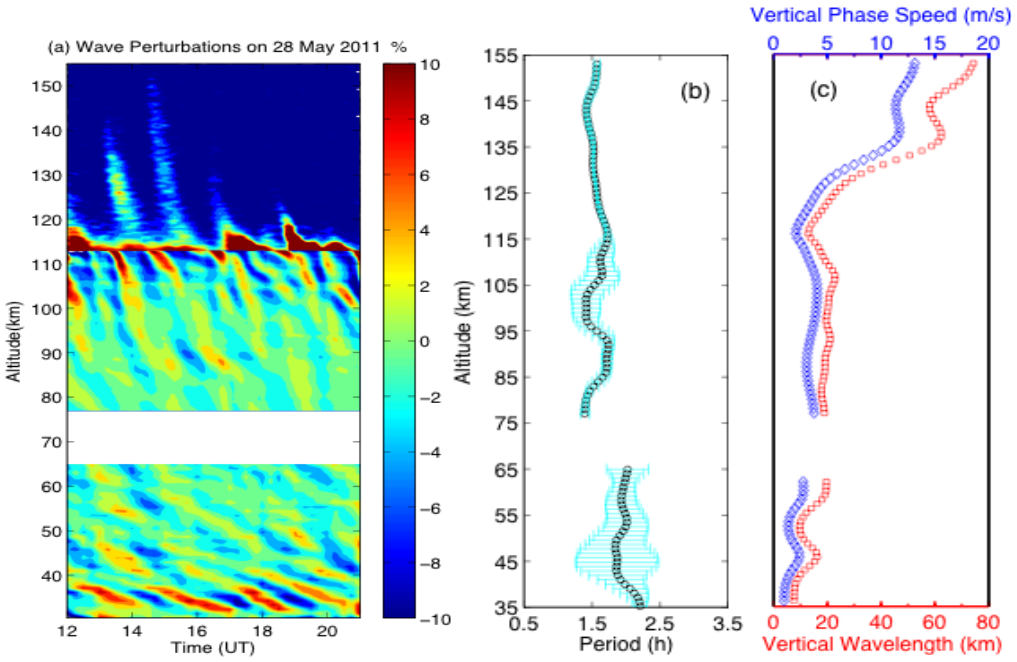

Figure 2.3. (a) Gravity wave perturbations in the Fe densities (112-155 km) and relative perturbations of Fe (78-112 km) and Rayleigh temperatures (33-65 km) on 28 May 2011 at McMurdo. (b) Derived wave period, (c) vertical wavelength and phase speed.

To reveal the 1.5 h wave in the MLT region, we should remove the dominant 8-h wave in the raw data (see Figure 2.1b). The method to remove the dominant wave is as follows. First, a Morlet wavelet analysis is applied to the time series at each altitude in the Fe temperature data and then the dominant period is determined. If the dominant period is longer than 3 h, a sinusoidal wave fit with the dominant period is performed then subtracted from the original data. The same process is then applied to the residual for several times until the dominant period determined from the Morlet wavelet analysis falls within the 3-h limit. Usually, five to six rounds of subtraction processes are sufficient to remove the dominant longer period waves from the Fe temperatures. After removing the dominant waves, a Morlet wavelet analysis is performed

at each altitude to obtain the dominant period of the residual fast gravity waves in the MLT region (results shown in Figure 2.3b). We derive the wave phases by fitting a sinusoidal wave with the dominant period determined above to the residual Fe temperatures at each altitude. Then based on the rate of the wave phase changing with altitude, the phase speeds and the corresponding vertical wavelengths are derived (results shown in Figures 2.3c).

In order to extract the fast gravity waves in the stratosphere, the same process of removing the dominant longer period wave is also applied to the Rayleigh temperature data. However, due to the existence of the downward propagating waves (with upward phase progression) in the stratosphere, an additional step is adopted to further remove the interference from undesired waves. To remove the downward propagating waves, we apply a two-dimensional (2-D) Fast Fourier Transform (FFT) to the Rayleigh temperature data, and then remove the first and the third quadrant, which represent the waves with upward phase progressions in a 2-D FFT spectrum. After that, we apply a 2-D Inverse FFT to reconstruct the Rayleigh temperature perturbations with only the second and the fourth quadrant of the 2-D FFT. Finally, the same procedures used for the temperature data in the MLT region are executed to derive the dominant periods, vertical phase speeds and vertical wavelengths from the reconstructed Rayleigh temperature data (results shown in Figures 2.3b and 2.3c).

Both the vertical phase speeds and vertical wavelengths of the fast gravity waves increase with altitude from the stratosphere to the thermosphere. This can be explained by the damping effect from the eddy and molecular diffusions and other wave dissipation mechanisms such as convective and dynamical instabilities. These processes can cause waves with slower vertical phase speeds and shorter vertical wavelengths to dissipate more rapidly than those with faster phase speeds and longer vertical wavelengths when propagating into the thermosphere.

Therefore, only the short period, long vertical wavelength waves that exhibit fast vertical phase speeds are able to propagate to the higher altitudes as we observed [*Vadas*, 2007]. This is the first time that a single instrument has been able to observe a wave over such a large altitude range. Waves generated in the lower atmosphere can propagate into the upper atmosphere and ionosphere, and produce significant disturbances in winds, temperature, constituents and electron densities [*Vadas and Liu*, 2009]. Our result provides a direct evidence of "wave communication" from the stratosphere, mesosphere to at least the F region in the ionosphere, showing that these regions are coupled through the propagation of the gravity waves. Although the wave source for the current observation is unknown, the region around McMurdo has been considered a gravity wave 'hotspot' [*Baumgaertner and McDonald*, 2007] because of enhanced orographic forcing of waves near the Trans-Antarctic Mountains [*Hertzog et al.*, 2008]. Many more cases of thermospheric gravity waves have been observed at McMurdo and the wave parameters are analyzed using similar methods.

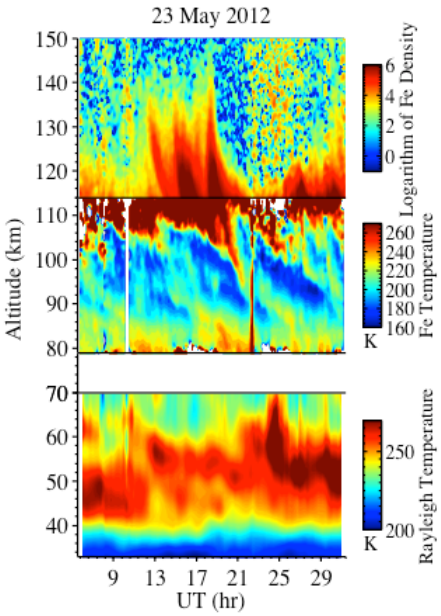

Figure 2.4. Lidar data on 23 May 2012 at McMurdo. Above 114 km, Fe density data are shown. Below 114 km, lidar temperature data are shown.

As another example, on 23 May 2012, a new case of thermospheric fast gravity wave is observed (see Figure 2.4). The first interesting feature of this case is that a long-period (~12 h) wave was observed in the thermospheric Fe layers. Diffusive neutral Fe layers are seen in the region between the main Fe layer and 150 km during the period of 6 UT to 9 UT, and then between 13 UT and 24 UT. Finally, another diffusive Fe layer reappeared after 25 UT. Superposed on the diffusive background between 13 and 24 UT, three highly concentrated Fe layers with period about 3 h were observed from 11 UT to 20 UT. These fast descending Fe layers were likely caused by gravity waves from the lower atmosphere as in the case observed on 28 May 2011. After removing the dominant wave using band-pass filters, the Fe density and neutral temperature perturbations, along with the derived periods, vertical phase speeds and wavelengths are shown in Figure 2.5. The 3-h wave is traced back from the thermosphere to the stratosphere. In general, the vertical phase speeds and vertical wavelengths are faster and longer respectively in the higher altitudes than the lower altitudes, except for the regions where signal-to-noise ratio is relatively lower.

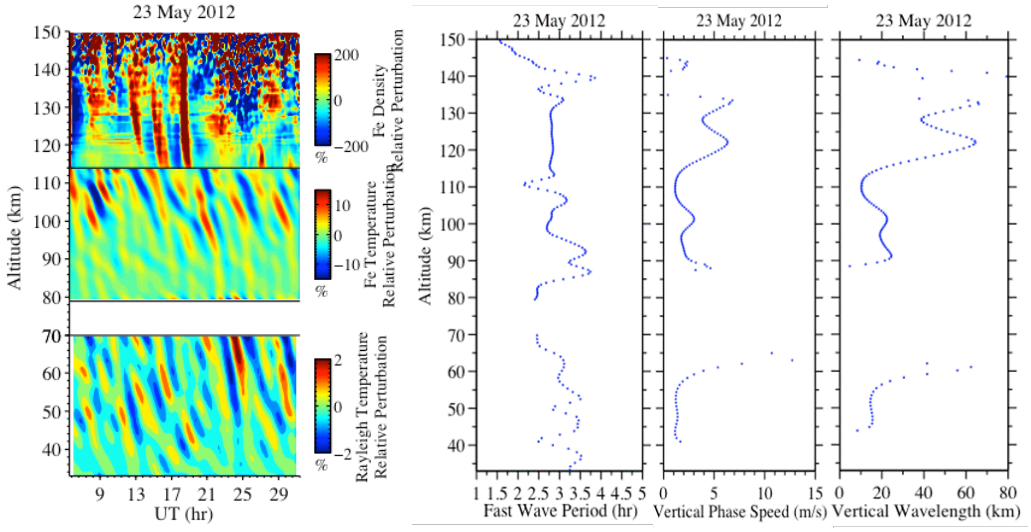

Figure 2.5. (Left) Relative perturbations of fast gravity wave on 23 May 2012 at McMurdo. (Right) Ground-based gravity wave period, vertical phase speeds and vertical wavelengths derived for the event on 23 May 2012 at McMurdo.

2.3 Conclusions and Outlook

The discovery of the thermospheric neutral Fe layers by lidar at McMurdo allows the measurements of neutral temperatures (and wind) and waves well into the thermosphere. These neutral metal layers provide a unique tracer to study waves in the thermosphere. Gravity waves with 1–3 h periods are seen in the converged Fe layers, and downward phase progression is seen to be continuous from the lower atmosphere indicating that the waves observed in the thermosphere appear to originate from the stratosphere or troposphere. The phase line shape, period, vertical phase speed and vertical wavelength of these waves are comparable to TIDs observed by Incoherent Scatter Radar (ISR). More and longer lidar observations in Antarctic winter are crucial to the better understanding of neutral temperatures and waves (GW and tide) from the stratosphere to the thermosphere. Characterizations of these waves are needed to better understand the behavior and sources of such waves.

CHAPTER 3

Discovery and Characteristics of Inertia-Gravity Waves in the Antarctic MLT with Simultaneous Lidar and Radar Observations

3.1 Introduction

Gravity waves are critically important in the middle and upper atmosphere because of their role in influencing the mean circulation, affecting thermal structure, and transporting energy, momentum and constituents [*Fritts and Alexander*, 2003]. Unfortunately, the gravity wave parameterizations used in global models are poorly constrained, and information on the range of intrinsic wave properties observed in the mesosphere and lower thermosphere (MLT) and on the sources of these waves is limited. Long-duration, large-altitude-range and high-resolution measurements of temperature and wind can be used to characterize the intrinsic properties of gravity waves, examine their propagation and infer the probable sources, thus providing important constraints for gravity wave parameterizations in global circulation models [*Alexander and Rosenlof*, 2003]. Here, we examine such temperature and wind perturbations that we believe are caused by inertia-gravity waves (IGWs). These waves have frequencies close to the inertial frequency and are affected by the rotation of the Earth. This class of gravity wave is often observed in the troposphere and lower stratosphere [*Cot and Barat*, 1986; *Sato*, 1994; *Sato et al*., 1997; *Thomas et al*., 1999; *Guest et al*., 2000; *Vincent and Alexander*, 2000; *Hoffmann et al*., 2006; *Nastrom and Eaton*, 2006; *Vaughan and Worthington*, 2007], but less frequently in the mesosphere and lower thermosphere [e.g., *Nakamura et al*., 1993; *Hall et al*., 1995; *Li et al*., 2007; *Lu et al*., 2009; *Nicolls et al*., 2010]. The infrequent occurrence of these waves in the MLT

region was believed to occur because of their small vertical wavelengths and small horizontal phase speeds, which make these waves susceptible to critical level filtering by background winds as they propagate upward [*Nicolls et al*., 2010].

Although they are thought to contribute less to momentum flux transport than smaller-scale waves [*Fritts and Vincent*, 1987], IGWs can play an important role in the Earth's atmosphere; for example, in constituent mixing via turbulence caused by convective and dynamical instability in the wave field [*Fritts and Rastogi*, 1985; *O'sullivan and Dunkerton*, 1995; *Xu et al*., 2000]. Recently, studies have shown that underestimated gravity wave drag (GWD), ascribed to both IGWs and higher-frequency gravity waves in the polar regions, may be responsible for the long-standing 'cold pole' problem in many general circulation and chemistry climate models [e.g., *Tan et al*., 2011; *McLandress et al*., 2012]. IGWs have been observed to induce the formation of polar stratospheric clouds (PSC), which can cause enhanced ozone depletion in the polar regions [*Dörnbrack et al*., 2002; *Shibata et al*., 2003; *McDonald et al*., 2009]. In the polar mesosphere, recent observations by *Chu et al*. [2011a] have shown that the cold phase of large temperature oscillations induced by IGWs facilitate the formation of polar mesospheric clouds (PMCs). In spite of playing such an important role in the polar regions, information concerning the sources and properties of these gravity waves is still limited as compared to mid- and low-latitudes [e.g., *Cot and Barat*, 1986; *Sato*, 1994; *Sato et al*., 1997; *Thomas et al*., 1999; *Guest et al*., 2000; *Vincent and Alexander*, 2000; *Hoffmann et al*., 2006; *Nastrom and Eaton*, 2006; *Vaughan and Worthington*, 2007; *Nakamura et al*., 1993; *Hall et al*., 1995; *Li et al*., 2007; *Lu et al*., 2009]. Therefore, investigations of IGWs in the mesopause region over the Antarctic are important, due to their potential influence on MLT temperatures and dynamics.

In the Antarctic MLT, there are a few observations of near-inertial frequency oscillations [e.g., *Collins et al*., 1992; *Hernandez et al*., 1992, 1993; *Fritts et al*., 1998]. Among these authors, *Hernandez et al*., [1993] have hinted these oscillations might be IGWs, while others indicate a tidal or planetary-wave origination. Characterization and climatology of the gravity wave motions observed in the Antarctic MLT were reported by *Collins et al*., [1994] and *Collins and Gardner*, [1995] using a sodium lidar, and by *Vincent* [1994] using an MF radar. However, the current report is the first study that derives the intrinsic properties of IGWs in the Antarctic MLT. A new lidar campaign at McMurdo, Antarctica, has begun to show an unexpectedly high occurrence of waves with periods of 4–9 h in the MLT temperatures [*Chu et al*., 2011a, 2011b], suggesting a significant gap in our understanding.

The University of Colorado lidar group deployed an Fe Boltzmann temperature lidar to Arrival Heights near McMurdo (77.8° S, 166.7° E) in December 2010, and has been collecting data since that time [*Chu et al*., 2011a, 2011b, 2012]. This lidar has full diurnal coverage, and is capable of measuring temperatures at altitudes between 30 and 110 km. The Scott Base Medium Frequency (MF) radar is co-located with the Fe lidar at Arrival Heights. It provides continuous measurements of zonal and meridional winds from 75 to 100 km [*Baumgaertner et al*., 2005]. The simultaneous MLT temperature and wind data provide a unique opportunity for studying IGWs and their intrinsic properties at this high southern latitude. In this paper, we present a case study of two IGWs propagating over Arrival Heights simultaneously, and apply filtering and hodograph analyses to determine their intrinsic properties. Our results show that these two IGWs are propagating in two different directions that are nearly perpendicular to one another.

3.2 Observations of IGW events on 29 June 2011

McMurdo and Scott Base are located on Ross Island, east of the Trans-Antarctic Mountains. The coordinated lidar-radar observations at Arrival Heights (77.83°S, 166.67°E) are a collaboration between the United States Antarctic Program (USAP) and Antarctica New Zealand (AntNZ). The Fe Boltzmann temperature lidar consists of two independent channels probing respectively the 372 and 374 nm absorption lines of neutral Fe atoms. Temperatures can be inferred from the signal ratios between these two channels by employing the Fe Boltzmann technique [*Gelbwachs*, 1994] in the MLT region with Fe distribution. Below the Fe layer and in the region free of aerosol scattering (usually between 30 and 70 km), temperatures are derived using the Rayleigh integration technique [*Hauchecorne and Chanin*, 1980]. Principles, capabilities and error analysis of the lidar are described in *Chu et al*., [2002], and its refurbishment and upgrade are discussed in *Wang et al*., [2012]. Plotted in Figure 3.1a are the temperatures measured by the Fe lidar from below 35 km to 107 km over 25 h on 29–30 June 2011 at McMurdo. The lidar signal levels between 67 and 81 km are insufficient for reliable temperature derivation at required resolutions of better than 1 h, thus a data gap exists in the temperatures as shown in Figure 3.1. The raw lidar data (photon counts) were recorded with resolutions of 1 min and 48 m. Above this gap, the original Fe temperatures in the MLT are derived in resolutions of 0.25 h and 0.5 km, with the sampling window shifted at steps of 0.1 h and 0.1 km. The data are then temporally and vertically smoothed with a Hamming window of 0.5 h and 1 km full-width-at-half-maximum (FWHM) to further reduce the temperature errors. Therefore, waves with periods longer than 1 h and vertical wavelengths longer than 2 km are resolved. Below this gap the Rayleigh temperatures have resolutions of 1 h and 1 km. Figure

3.1a shows that on the dataset average the stratopause is ~45–48 km and the mesopause is ~100 km.

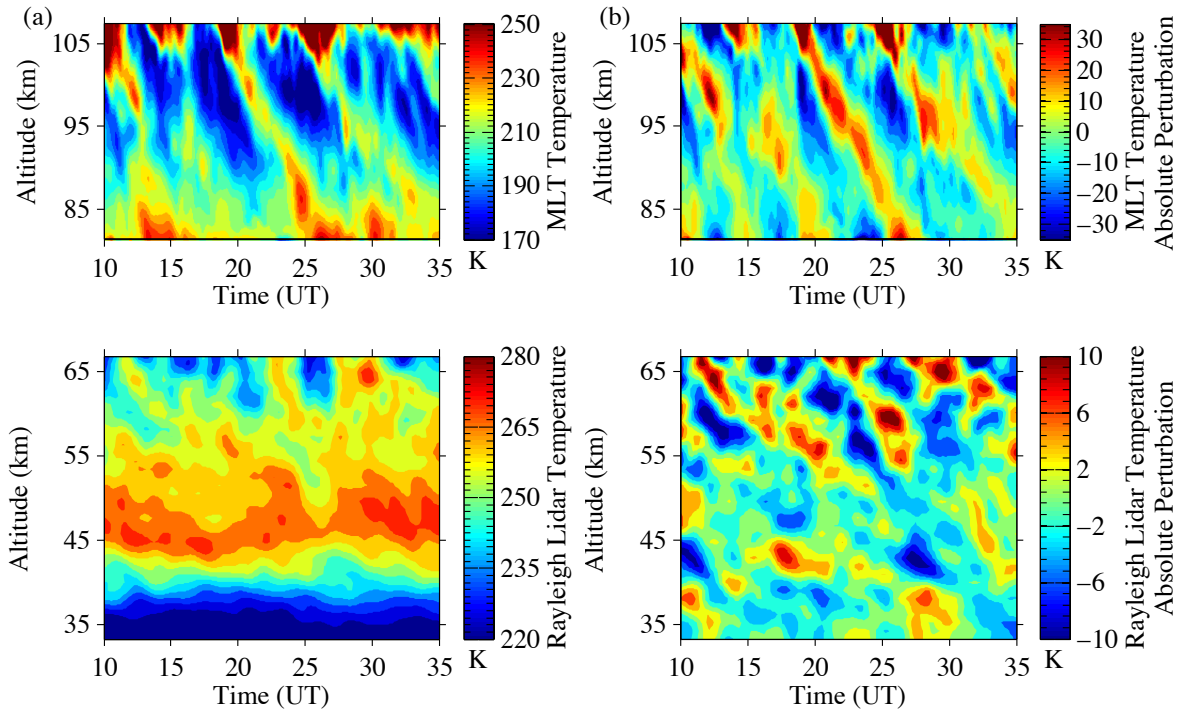

Figure 3.1. (a) Contours of raw temperature observations on 29–30 June 2011 at McMurdo by an Fe Boltzmann lidar in the MLT region (in the altitude range of 81–107 km), and from Rayleigh integration (in the altitude range of 33–67 km). The data gap between 67 and 81 km are due to insufficient signal levels for reliable temperature derivation at required resolutions of better than 1 h. (b) Contours of corresponding absolute temperature perturbations.

The temperature variations in Figure 3.1a are very large in the MLT region, and are also visible in the Rayleigh temperatures above 45 km. By subtracting the dataset-mean temperatures at each altitude, the temperature perturbations are derived and shown in Figure 3.1b, which exceed ±30 K in the MLT region around 100 km. Both Figures 3.1a and 3.1b exhibit clear wave structures with downward phase progression from the MLT to the lower mesosphere at ~50 km, indicating that the wave(s) is upward propagating. This implies that the wave source(s) is located in the lower atmosphere. In contrast to the lidar measurements of MLT temperatures at mid to

low latitudes that are commonly dominated by diurnal and semi-diurnal tides [e.g., *States and Gardner*, 2000; *She et al*., 2004; *Chu et al*., 2005; *Friedman and Chu*, 2007], the temperature variations at McMurdo in Figure 3.1a are dominated by wave oscillations with periods of 5–8 h during the entire observation period (~25 h) while diurnal or semi-diurnal tides are not apparent. Such wave oscillations with periods of 5–8 h are a common feature of the MLT temperatures at McMurdo. For example, Figure 4 in *Chu et al*., [2011a] exhibits a strong wave oscillation with a period of 6.5–7 h on 28–29 Jan 2011, while Figure 2 in *Chu et al*., [2011b] shows a strong wave oscillation with a period of ~8 h on 28 May 2011 at McMurdo. Therefore, it is intriguing to ask what causes such large-amplitude wave oscillations? We will argue in the rest of the paper that inertia-gravity waves are the most likely mechanism.

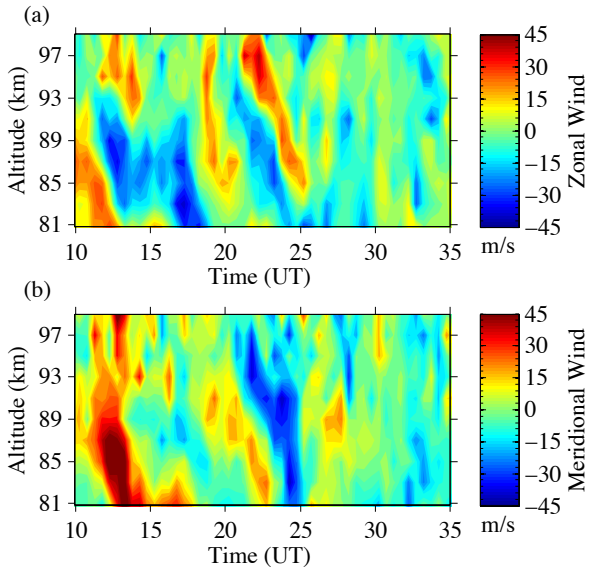

Figure 3.2. Contours of raw (a) zonal and (b) meridional wind observations on 29–30 June 2011 by the Scott Base MF radar in the MLT region (81–99 km). Data below 93 km may be considered reliable measurements of the neutral atmosphere wind.

To fully characterize gravity waves, simultaneous wind data are needed. Such wind data are obtained with the Scott Base MF radar whose receiver is co-located with the Fe lidar at Arrival Heights. This radar operates at 2.9 MHz with a FWHM field of view of 30°. It has near-

continuous temporal coverage, and has been collecting wind data at heights between 70 and 100 km since 1982 [*Fraser*, 1984]. The peak output power of the transmitter is 60 kW and the pulse repetition frequency is 8 Hz. By using the Full Correlation Analysis (FCA) technique, zonal and meridional winds can be calculated [*Baumgaertner et al*., 2005]. Illustrated in Figure 3.2 are the MF radar winds in zonal and meridional directions taken simultaneously with the lidar temperature measurements on 29–30 June 2011. The MF radar uses a pulse width of 30 μs, corresponding to a fundamental vertical resolution of 4.5 km, but the data are oversampled to have the display vertical resolution of 2 km in Figure 3.2. The temporal resolution of the MF radar wind is 0.5 h; therefore, the MF radar can resolve waves with periods longer than 1 h and vertical wavelengths longer than 9 km. In Figure 3.2, we see large wind perturbations in both the zonal and meridional directions; additionally, downward phase progression is clearly seen. The perturbation periods are shorter than diurnal or semi-diurnal tides, but are around 5–8 h, which is very similar to the wave periods deduced in the MLT temperatures measured by the lidar.

To combine the lidar and radar measurements for studies of the inertia-gravity waves, we derive the IGW-induced perturbations in the temperatures and winds by deriving relative temperature perturbations and absolute wind perturbations, in which the background temperatures/winds, and the perturbations induced by tides and planetary waves, are removed. Relative temperature perturbations are derived via subtracting the daily mean temperature at each altitude and then dividing by this mean. In order to minimize contamination of planetary wave oscillations, a linear trend in the time domain is removed from the original perturbations at each altitude, followed by a subtraction of a linear trend in the spatial domain as demonstrated in *Lu et al*., [2009]. To derive the wave-induced perturbations from the MF radar data, the tides are removed from the original wind observations by subtracting a temporal fitting of diurnal and

semi-diurnal period sinusoidal functions at each altitude. Figure 3.3 shows the derived wave perturbations in temperature, zonal and meridional winds, where the positive phase fronts of the waves are highlighted by black dotted-dashed lines. Clear downward phase progression is observed, implying upward propagation of gravity waves. Two different periods are seen in the perturbations. The wave perturbation with a period of ~5 h dominates the zonal wind and the first half of the temperature measurements, while the amplitude of the wave perturbation with a period of ~7–8 h is stronger in the meridional wind and in the second half of the temperature measurements. Figure 3.3 suggests that two inertia-gravity waves may have been observed at the same time over Arrival Heights. We perform detailed analyses in the next sections to confirm this hypothesis, and then derive the intrinsic properties of these two waves.

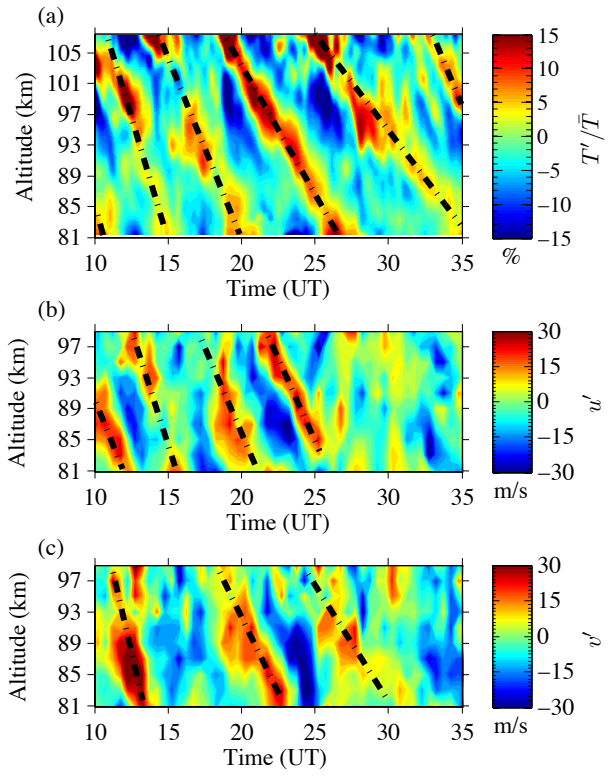

Figure 3.3. (a) Relative temperature perturbations (in the altitude range of 81–107 km), (b) zonal and (c) meridional wind perturbations (81–99 km) in the MLT region on 29–30 June 2011. Diurnal and semi-diurnal tides are removed from the raw perturbations. The black dashed-dotted lines highlight the positive phase fronts of the waves.

3.3 Wave Analysis Methodology

To verify whether two IGWs are present simultaneously, detailed spectral information on the waves is determined from the FFT spectra for the three fields, as shown in Figure 3.4. Large-amplitude ~8-h period peaks are seen in the temperature spectra at all altitudes, in the zonal wind spectra at z = 85–89 km km and in the meridional wind spectra at z = 83–91 km. Distinct ~5-h period peaks are also seen in the temperature spectra at most altitudes, in the zonal wind spectra at z = 81–97 km, and in the meridional wind spectra but with a smaller amplitude at z = 81–85 km. For each of the three fields and at each altitude, if a spectral peak is found in-between periods of 4–6 h or 6–10 h for one of the two waves, the period corresponding to this spectral peak is taken to represent the observed period of this wave at this altitude. The mean observed periods (τ) are obtained by averaging the results over all these altitudes; the results for both waves are summarized in all three fields in Table 1. In order to determine the errors in the period analysis, a nonlinear least-square fitting is applied to the time series using a sum-of-two-sine model; this is performed at each altitude and for each field of data. The model is written as follows,

$$x(t) = A\cos(\frac{2\pi}{\tau_1}t + \phi_1) + B\cos(\frac{2\pi}{\tau_2}t + \phi_2)\,, \tag{3.1}$$

where $x(t)$ represents the time series of the perturbation, A, τ_1 and ϕ_1 are the amplitude, apparent period and phase for the first wave, while B, τ_2 and ϕ_2 are the parameters for the second wave. The results of the fitted periods in the two sine functions (not shown here) are in accordance with the results obtained from the FFT analysis. The errors of the periods are then determined from the 95% confidence levels of the fitted periods at each altitude. The mean values of these errors for each wave are given in Table 1 and are used later in this paper to estimate the errors in the

intrinsic periods and other wave properties derived from the gravity wave dispersion and polarization relations. Since the temperatures have better temporal resolutions and smaller errors, the periods derived from the temperature data are taken as the observed periods of the waves. Hereinafter, whenever the information of observed period or its error is needed, we use the values derived from the temperatures. These two waves are referred to as 7.7-h wave and 5-h wave, respectively.

Table 3.1. Observed wave properties[1] for two IGWs derived from temperature and wind fields.

Wave	Data Field	τ (h)	λ_z (km)	c_z (m/s)	θ (deg)	$\bar{U}_h$ (m/s)	$\frac{d\bar{U}_h}{dz}$ (10^{-4} s^{-1})
7.7-h Wave	T	7.7 ± 0.2	22 ± 2	0.8 ± 0.1	11±5	2 ± 3	2±1
	u	7.9 ± 0.5					
	v	7.9 ± 0.4					
5-h Wave	T	5.0 ± 0.1	23 ± 2	1.2 ± 0.1	100±4	-2 ± 4	3±1
	u	4.9 ± 0.1					
	v	4.8 ± 0.2					

[1]Observed period (τ), vertical wavelength (λ_z), vertical phase speed (c_z), azimuth angle of the wave horizontal propagation direction (θ), horizontal background wind speed ($\bar{U}_h$) and its vertical shear ($\frac{d\bar{U}_h}{dz}$).

The two isolated spectral peaks shown in Figure 3.4 could be an indication of two independent waves propagating across the lidar/radar fields of view at the same time. Or, it could be due to a single wave that is Doppler-shifted from one period to another over time. To examine this, we use wavelet analysis that provides information about the time when each wave is present in the spectra. The Morlet wavelet spectra for each data field at two example altitudes of 85 and 87 km are shown in Figure 3.5. The cone of influence (COI) is denoted by the white dashed lines, outside of which is the region in the spectrum where the true peak magnitude is reduced,

and a false peak might appear [*Torrence and Compo*, 1998]. White crosses on the contours denote the local peak between the periods of 4 h and 10 h. Both the zonal and meridional wind wavelet spectra clearly show the 5-h wave and the 7.7-h wave present at the same time regardless of their location relative to the COI. This confirms that two independent waves were in the wind field at the same time. In the temperature wavelet spectrum, these two waves are clearly seen at the same time at 87 km. At 85 km, however, the two peaks almost merge together below the COI from 20~25 UT. Although two peaks are present above the COI at other times, they are subject to edge effects, and thus must be interpreted with care. We will come back to this issue after separating the two waves and investigating their intrinsic properties in Section 3.4.

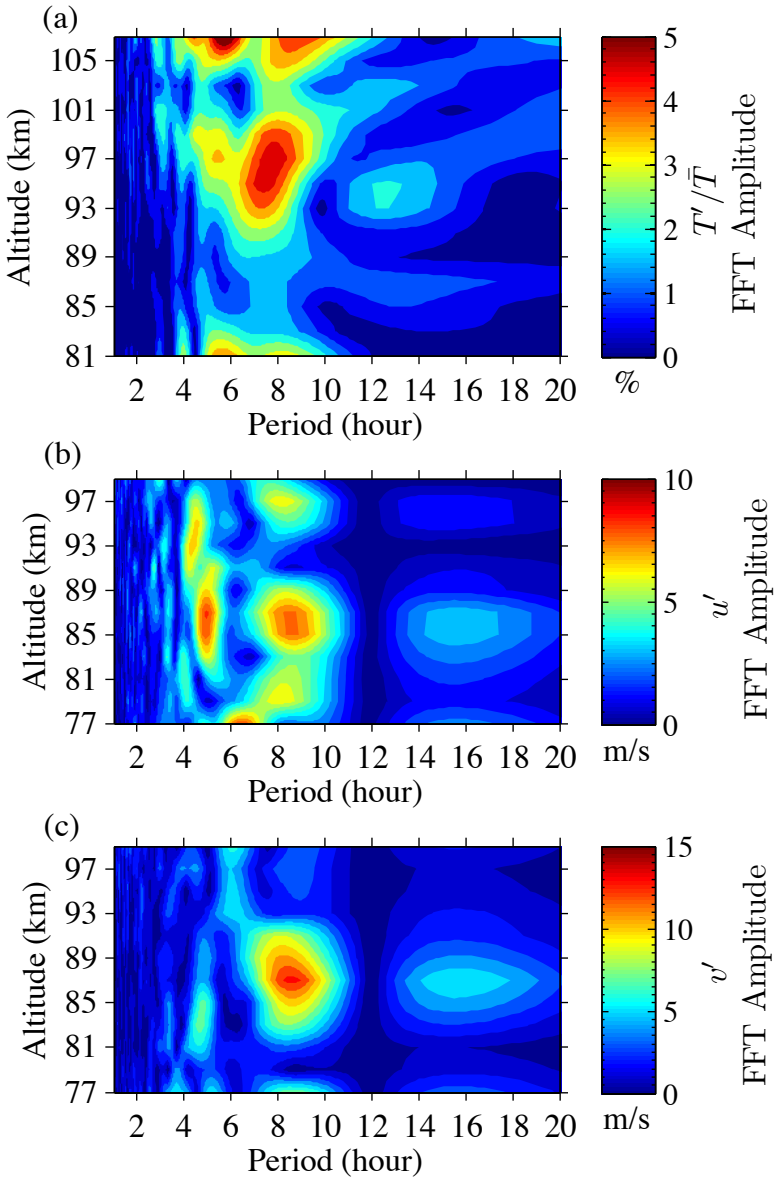

Figure 3.4. FFT amplitudes of (a) relative temperature perturbations (81–107 km), (b) zonal wind and (c) meridional wind perturbations (81–99 km) in the MLT region on 29–30 June 2011.

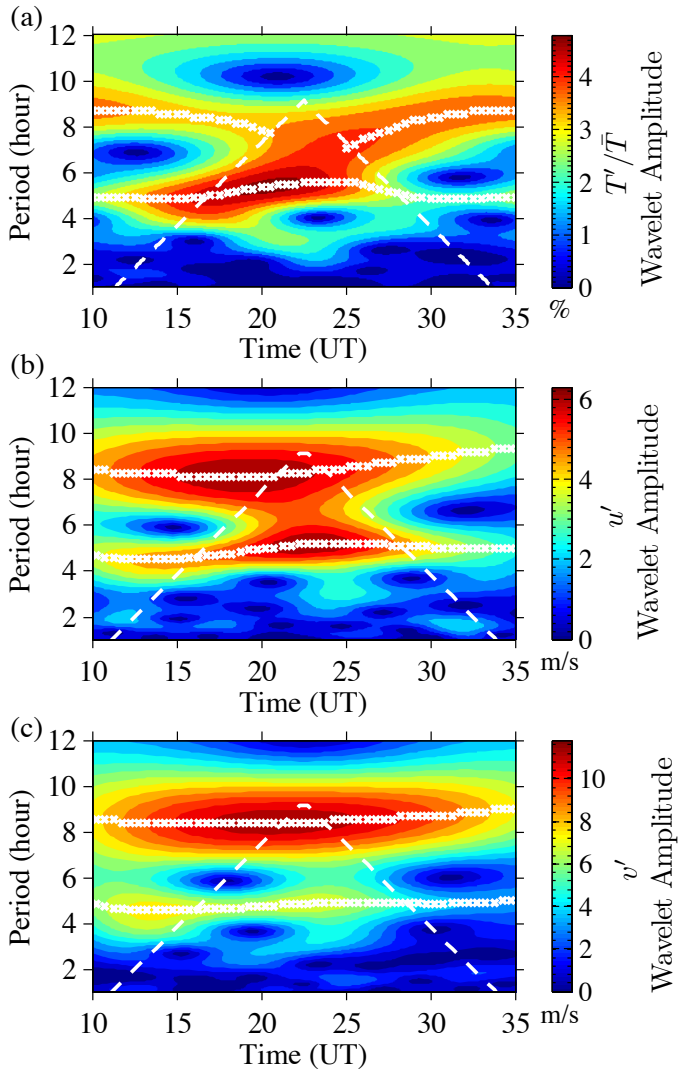

Figure 3.5. Amplitudes of the Morlet wavelet spectra for (a) relative temperature perturbations, (b) zonal and (c) meridional wind perturbations at 85 km on 29–30 June 2011. The white crosses denote the local maximum power in the wavelet spectra with periods between 4 and 10 h. The white dashed line in each contour denotes the cone of influence (COI) for the wavelet analysis.

3.3.1 Band-pass Filtering to Separate Two Waves

To separate these two waves, all three fields are band-pass filtered by a 6th-order Butterworth filter with pass bands at 6-10 h and 3.5-5.5 h for the 7.7-h wave and 5-h wave, respectively. The choice of the cutoff frequencies is a tradeoff between minimizing the interference from the other wave and ensuring that the desired wave is not attenuated too

severely. Since the 7.7-h wave is generally stronger, its final results are not very sensitive to the choice of its cutoff frequency; thus, the pass band of 6–10 h is a good compromise such that little energy is lost. In contrast, the 5-h wave suffers spectral leakage from the 7.7-h wave (which has the larger amplitude). For this wave, a passband of 3.5–5.5 h greatly reduces the spectral leakage from the 7.7-h wave, but does not severely attenuate the 5-h wave. Figure 3.6 shows the results for the passband of 6-10 h, and Figure 3.7 shows the results for the passband of 3.5–5.5 h. The filtered data for each field display clear downward phase progressions. Additionally, both waves are quasi-monochromatic. It is apparent in Figures 3.6 and 3.7 that the filtered 7.7-h and 5-h waves have larger or smaller amplitudes simultaneously in the wind field, which will not be the case if a single wave is Doppler-shifted from one period to another. It is also noted that Figures 3.6 and 3.7 show clear wave structures in the zonal and meridional winds after 30 UT, even though the amplitudes of both waves become smaller; however, the original wind perturbations (Figure 3.3) do not show such clear wave signatures. By reconstructing time series from these two filtered perturbations only and comparing them with the raw wind fields, we find that this phenomenon is caused by the destructive interference of these two waves after 30 UT. The results of Figures 3.6 and 3.7 support our hypothesis that two independent waves were propagating across our observational field of view simultaneously.

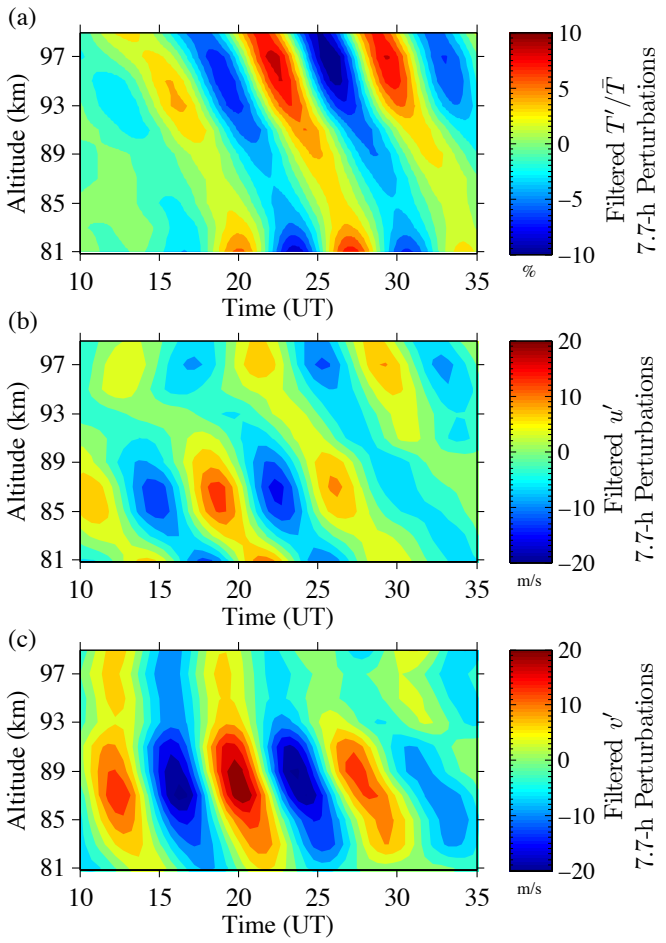

Figure 3.6. (a) Relative temperature perturbations, (b) zonal and (c) meridional wind perturbations filtered by a 6th-order band-pass Butterworth filter with lower and upper cut off frequencies at 1/10 and 1/6 h^{-1}, respectively.

The vertical wavelength (λ_z) of each wave is then determined from the filtered temperature data because of its higher vertical resolution and larger altitude coverage than the wind data. A linear least-square fit is first performed to the phase lines of the filtered temperature data to obtain the derivative of the altitude of the phase line with respect to time, i.e., the vertical phase speed (c_z). The vertical wavelength λ_z is then calculated by multiplying c_z with the observed period (τ). We obtain λ_z = 22±2 km for the 7.7-h wave and λ_z = 23±2 km for the 5-h wave. The uncertainties in λ_z and c_z are determined from the 95% confidence levels of the

fittings. The values and errors of λ_z and c_z are listed in Table 1. These results are generally comparable with the long-period oscillations observed by *Collins et al*. [1994] in the bottomside of the Na layer at the South Pole. They observed large-amplitude oscillations with periods around 5–12 h with a Na lidar. Their derived vertical wavelengths are close to 22 km for wave periods of 5 h, but are shorter (12–18 km) for periods of 7–8 h. Note that the IGW observed by *Nicolls et al*. [2010] in the Arctic had a long period of ~10.5 h, and a short vertical wavelength of ~4–10 km.

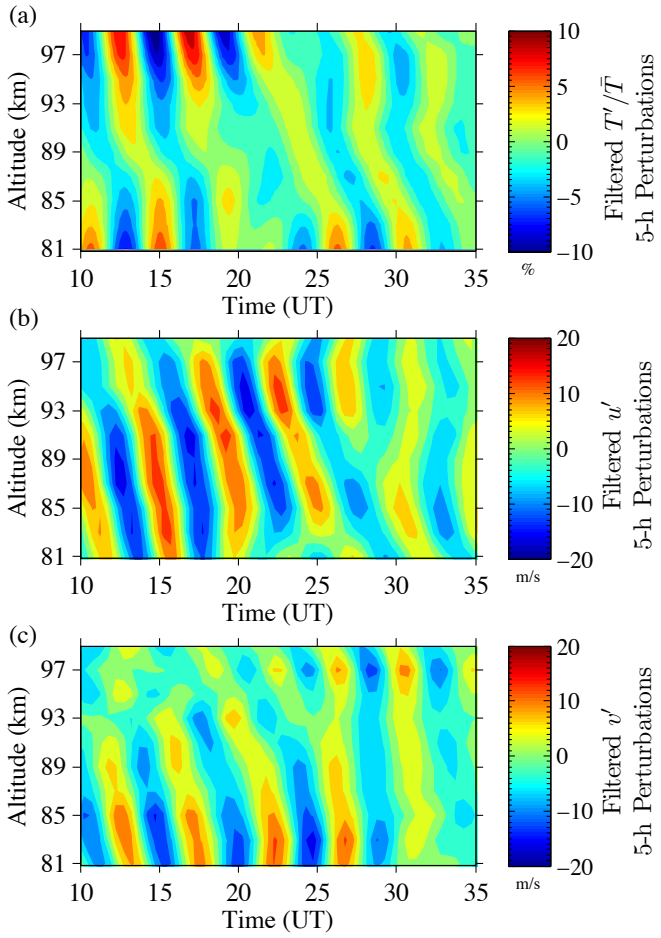

Figure 3.7. (a) Relative temperature perturbations, (b) zonal and (c) meridional wind perturbations filtered by a 6th-order band-pass frequency filter with lower and upper cut off frequencies at 1/5.5 and 1/3.5 h^{-1}, respectively.

3.3.2 Hodographs for Determining Wave Propagation Directions

We now treat each filtered wave as a quasi-monochromatic wave, and determine its propagation direction from a hodograph analysis. Hodograph analyses of wind data have been applied in altitude to study the intrinsic properties of gravity waves in the MLT [e.g., *Hu et al*., 2002; *Li et al*., 2007; *Lu et al*., 2009; *Nicolls et al*., 2010]. In this study, we choose to make temporal hodograph analyses of the MF radar wind. First, we do this because the overlapping range between the lidar and radar observations (less than 20 km between 80 and 100 km) is shorter than the vertical wavelengths of the waves (i.e., 22–23 km from the previous section. This is insufficient to accurately resolve the observed IGWs. Second, the vertical resolution (4.5 km) of the radar wind is too coarse to determine the orientation of the hodograph ellipse accurately. In contrast, the overlapping time between the lidar and radar observations is long (~25 h), so sufficient data are available to make the hodographs in the temporal domain. From a theoretical standpoint, hodograph analyses in the temporal or altitudinal domains are equivalent for a monochromatic wave in a constant background wind and temperature, in terms of determining the wave parameters (such as horizontal propagation direction).

The hodograph analysis is based on the IGW polarization relation [e.g., *Tsuda et al*., 1990; *Nakamura et al*., 1993]:

$$\widetilde{U}_{\parallel} = \mathrm{i}\frac{\hat{\omega}}{f}\widetilde{U}_{\perp} \tag{3.2}$$

where $\widetilde{U}_{\parallel}$ and $\widetilde{U}_{\perp}$ are the complex representations of the horizontal wind perturbations parallel and perpendicular to the wave horizontal propagation direction, respectively, $\hat{\omega}$ is the intrinsic frequency of the wave, and f is the Coriolis parameter. At McMurdo (77.8° S), the inertial period

is $2\pi/f$ = 12.24 h. In deriving equation (3.2), we assume that the perturbations are induced by a monochromatic wave, and thus $\tilde{U}_{\parallel}$ and $\tilde{U}_{\perp}$ are written as follows,

$$\tilde{U}_{\parallel} = \left|\tilde{U}_{\parallel}\right| \exp\left[\mathrm{i}(k_h x_h + mz - \omega t - \Phi_{\tilde{U}_{\parallel}}) + \frac{z}{2H}\right], \tag{3.3}$$

$$\tilde{U}_{\perp} = \left|\tilde{U}_{\perp}\right| \exp\left[\mathrm{i}(k_h x_h + mz - \omega t - \Phi_{\tilde{U}_{\perp}}) + \frac{z}{2H}\right], \tag{3.4}$$

respectively. Here k_h and x_h are the horizontal wavenumber and distance, respectively; m is the vertical wavenumber, and it is negative in the case of downward phase progression; ω is the observed (i.e., ground-based) frequency; $H = R\overline{T}/g$ is the density scale height, calculated from the observed mean temperature $\overline{T}$, the gas constant of dry air R, and the gravitational acceleration g; $\Phi_{\tilde{U}_{\parallel}}$ and $\Phi_{\tilde{U}_{\perp}}$ are the initial phases of $\tilde{U}_{\parallel}$ and $\tilde{U}_{\perp}$, respectively. Equation (3.2) neglects background shear terms [e.g., *Fritts and Alexander*, 2003]. This is applicable in our case, because such shear terms (calculated from the background wind) are sufficiently small (see Table 1). Equation (3.2) is also derived under the Boussinesq approximation, which assumes that the wave phase speed is much less than the sound speed, and that $\lambda_z << 4\pi H$ [*Kundu*, 1990]. According to equation (3.2), the gravity-wave-induced $\tilde{U}_{\parallel}$ and $\tilde{U}_{\perp}$ exhibit elliptical or circular polarization. The major axes of the ellipses point in the direction of wave propagation, although with a 180° ambiguity.

This 180° ambiguity in the propagation direction is resolved by making use of the lidar temperature data. We derive the polarization relation between the relative temperature perturbation $\tilde{T}$ and $\tilde{U}_{\parallel}$ for an IGW with $N >> \hat{\omega}$:

$$\tilde{T} = \frac{1}{g}(\mathrm{i}m + \frac{1}{2H})\frac{\hat{\omega}^2 - f^2}{\hat{\omega}\, k_h}\tilde{U}_{\parallel} \tag{3.5}$$

where $\tilde{T}$ is the complex representation of the relative temperature perturbation $T'/\overline{T}$ given by,

$$\tilde{T} = \left|\tilde{T}\right| \exp\left[\mathrm{i}(k_h x_h + mz - \omega t - \Phi_{\tilde{T}}) + \frac{z}{2H}\right]. \tag{3.6}$$

Here, $\Phi_{\tilde{T}}$ is the initial phase of $\tilde{T}$. Equation (3.5) agrees with [*Vadas*, 2013] (Equations (B8), (B9) and (B11)). The derivation of equation (3.5) assumes that H and the background winds are constant in time and in the horizontal plane *x*, *y*, *t*, but can vary slowly in altitude. The phase relation between $\tilde{T}$ and $\tilde{U}_{\parallel}$ can be derived from equation (3.5) as:

$$\Phi_{\tilde{U}_{\parallel}} - \Phi_{\tilde{T}} = \arctan(m \cdot 2H)\,. \tag{3.7}$$

Equation (3.7) poses a constraint on the wave propagation direction; only when $\tilde{U}_{\parallel}$ is along the correct propagation direction of the wave, is $\Phi_{\tilde{U}_{\parallel}} - \Phi_{\tilde{T}}$ (extracted from the wind and temperature observations) close to $\arctan(m \cdot 2H)$. The opposite direction of the wave leads to $\Phi_{\tilde{U}_{\parallel}} - \Phi_{\tilde{T}}$ approaching $\arctan(m \cdot 2H) \pm 180°$. Therefore, this extra constraint helps remove the 180° ambiguity.

The actual $\Phi_{\tilde{U}_{\parallel}} - \Phi_{\tilde{T}}$ are derived from the temperature and wind perturbations, in which we first project the zonal and meridional wind perturbations to one of the two directions along the major axis inferred from the hodograph analyses, and derive the corresponding horizontal wind perturbations ($\tilde{U}_{\parallel}'$). Then $\Phi_{\tilde{U}_{\parallel}}$ and $\Phi_{\tilde{T}}$ are extracted by performing a non-linear least square fitting to the wind and temperature perturbations using the real part of the monochromatic wave models as shown in equations (3.3) and (3.6). We then compare the derived $\Phi_{\tilde{U}_{\parallel}} - \Phi_{\tilde{T}}$ to $\arctan(m \cdot 2H)$. If $\Phi_{\tilde{U}_{\parallel}} - \Phi_{\tilde{T}}$ is close to $\arctan(m \cdot 2H)$, then the direction we chose is correct; otherwise, if $\Phi_{\tilde{U}_{\parallel}} - \Phi_{\tilde{T}}$ is close to $\arctan(m \cdot 2H) \pm 180°$, then the correct direction is 180° opposite

to the originally chosen direction. Thus, combining the wind and temperature data allows us to unambiguously identify the propagation directions from hodographs.

3.3.3 Derivations of Wave Intrinsic Properties

The absolute value of the intrinsic frequency $\hat{\omega}$ can be calculated from the amplitude ratio between $\tilde{U}_{\parallel}$ and $\tilde{U}_{\perp}$ using equation (3.2). This has been a common approach used to derive the intrinsic properties of IGWs [e.g., *Hu et al*., 2002; *Lu et al*., 2009]. For the 7.7-h wave, we find that the amplitude ratios of the fitted ellipses vary dramatically with altitude (in the range of 1.2–3.3, giving an estimate of an intrinsic period of 3.5–10 h from equation (3.2)); however, the major axes of these ellipses are oriented similarly. If we use this method to determine the intrinsic periods directly, large errors result. This likely occurs because there are two IGWs; although the filtering works well, some spectral leakage occurs and appears to greatly impact the amplitudes of the wind perturbations (and thus the ratios). Therefore, we take a different approach instead. Since the horizontal wave propagation direction has been unambiguously determined, and the apparent period and background winds are known, the intrinsic properties can be determined from the gravity wave dispersion relation and the definition of the intrinsic frequency [*Fritts and Alexander*, 2003]:

$$k_h^2 = \frac{\hat{\omega}^2 - f^2}{N^2}(m^2 + \frac{1}{4H^2}) \tag{3.8}$$

$$\hat{\omega} = \omega - k_h \bar{U}_h \tag{3.9}$$

where N is the buoyancy frequency computed from the dataset-mean lidar temperature profile $\bar{T}(z)$ as $N = \sqrt{\frac{g}{\bar{T}(z)}\left(\frac{\partial \bar{T}(z)}{\partial z} + \frac{g}{C_p}\right)}$. Note that equation (3.8) is a simplified form of equation

(3.24) in *Fritts and Alexander*, [2003], where we have used the fact that $N >> \hat{\omega}$ for IGWs. In deriving equation (3.8), it is also assumed that N is constant in x, y and t, but varies slowly in z. Additionally, we assume that the speed of sound c_s is much larger than the wave horizontal phase speed (i.e., the Boussinesq approximation [*Kundu*, 1990]). From equation (3.9), we have $k_h=(\omega-\hat{\omega})/\bar{U}_h$. Substituting k_h in equation (3.8) with this new expression, we obtain the following quadratic equations for $\hat{\omega}$:

$$\left(\frac{N^2}{\bar{U}_h^2}-m^2-\frac{1}{4H^2}\right)\hat{\omega}^2-\frac{2N^2\omega}{\bar{U}_h^2}\hat{\omega}+f^2\left(m^2+\frac{1}{4H^2}\right)+\frac{N^2\omega^2}{\bar{U}_h^2}=0\,. \tag{3.10}$$

Solving equation (3.10), we obtain the following solutions for $\hat{\omega}$:

$$\hat{\omega}=\frac{\dfrac{N^2\omega}{m^2+\dfrac{1}{4H^2}}\pm\sqrt{\left(\dfrac{N^2\omega}{m^2+\dfrac{1}{4H^2}}\right)^2-\left(\dfrac{N^2}{m^2+\dfrac{1}{4H^2}}-\bar{U}_h^2\right)\left(\dfrac{N^2\omega^2}{m^2+\dfrac{1}{4H^2}}+f^2\bar{U}_h^2\right)}}{\dfrac{N^2}{m^2+\dfrac{1}{4H^2}}-\bar{U}_h^2}\,. \tag{3.11}$$

The corresponding solutions for k_h are:

$$k_h=\frac{-\omega\bar{U}_h\mp\dfrac{\bar{U}_h}{|\bar{U}_h|}\sqrt{\left(\omega\bar{U}_h\right)^2+\left(\dfrac{N^2}{m^2+\dfrac{1}{4H^2}}-\bar{U}_h^2\right)\left(\omega^2-f^2\right)}}{\dfrac{N^2}{m^2+\dfrac{1}{4H^2}}-\bar{U}_h^2}\,. \tag{3.12}$$

These expressions are similar to those used by *Liu and Meriwether* [2004] and *Li et al*. [2007]. The intrinsic horizontal and vertical group velocities of the wave packet describe the energy propagation and they are derived by taking partial derivatives with respect to k_h and m on both sides of equation (3.8) [*Fritts and Alexander*, 2003]:

$$c_{gh} = \frac{\partial \hat{\omega}}{\partial k_h} = \frac{k_h (N^2 - \hat{\omega}^2)}{\hat{\omega}\left(k_h^2 + m^2 + \frac{1}{4H^2}\right)}, \tag{3.13}$$

$$c_{gz} = \frac{\partial \hat{\omega}}{\partial m} = -\frac{m(\hat{\omega}^2 - f^2)}{\hat{\omega}\left(k_h^2 + m^2 + \frac{1}{4H^2}\right)}. \tag{3.14}$$

We will utilize equations (3.11)–(3.14) to estimate the intrinsic properties of each wave.

3.4 Wave Analysis Results

3.4.1 The 7.7-h Inertia-Gravity Wave

As mentioned in Section 3.3.1, band-pass filters are used to extract two quasi-monochromatic waves. We plot the filtered zonal and meridional wind perturbations of the 7.7-h wave as hodographs in Figure 3.8a. Each plot in Figure 3.8a shows the hodograph for a given altitude between 83 and 91 km over the time range from 10 UT to 30 UT. These particular temporal and spatial ranges are chosen to coincide with when and where the wave amplitudes are large in the wind data and have the highest signal-to-noise ratio. The start and end times are denoted by stars and triangles, respectively. All five hodographs show an anti-clockwise rotation in time. A least mean square (LMS) ellipse fitting is performed on each hodograph and is indicated by the dotted-dashed ellipse. All of the ellipses are primarily elongated in the meridional direction with a slight variation in the major axis between the different altitudes. A red arrow is plotted along the major axis of each fitted ellipse, indicating a possible propagation direction of the wave, but with a 180° ambiguity.

To resolve the 180° ambiguity for the 7.7-h gravity wave, we first assume that the wave propagates in the direction indicated by the red arrow in each hodograph in Figure 3.8a. Then we

project the zonal and meridional wind perturbations along this direction, and derive the corresponding horizontal wind perturbations ($\tilde{U}_{\parallel}'$). After that, band-pass filtered perturbations $\tilde{U}_{\parallel}'$ and $T'/\overline{T}$ are fitted to the real part of the monochromatic wave models (see equations (3.3) and (3.6)). The deduced phase differences $\Phi_{\tilde{U}_{\parallel}} - \Phi_{\tilde{T}}$ are shown in Figure 3.9a as red crosses for the altitudes from 83 to 91 km. The theoretical value ($\arctan(m \cdot 2H)$) is shown as the solid vertical line, which in this case is 286±0.7°. The dashed vertical line shows the value of $\arctan(m \cdot 2H)$-180°. The uncertainties caused by errors in obtaining the phase information, deriving the ellipse orientation, and determining the wave period (with temporal variation), are estimated to be ±40° at the 95% confidence level (denoted by grey error bars). The discrepancies between the crosses and the solid vertical line mostly fall within the error bars (except at 91 km), implying that the orientation indicated by the red arrows is the correct propagation direction of this wave. Thus, we conclude that the 7.7-h wave is propagating slightly east of north at the azimuth angle of 11°±5°. Note that the larger biases seen at 91 km may be caused by spectral leakage from the shorter-period wave, because that is the altitude where the 7.7-h wave amplitude is smallest relative to the 5-h wave (see Figure 3.4). Therefore, we find that the hodograph method works well at those altitudes where spectral leakage from another significant wave is minimal; we also find this to be true for the 5-h wave, as discussed later.

To calculate the intrinsic wave properties from equations (3.9) and (3.10), we need to compute $\overline{U}_h$. We first low-pass filter the zonal and meridional winds to remove variations with periods shorter than or close to the wave being examined. The 6th-order Butterworth filters with a cut-off period of 7 h for the 5-h wave and of 10 h for the 7.7-h wave are used. The horizontal background winds along each wave's propagation direction are then determined by projecting

the background winds onto the coordinate system that has been rotated to be along the wave's propagation direction. $\bar{U}_h$ is then calculated as the dataset mean of the horizontal background winds at each altitude. The error of $\bar{U}_h$, $\Delta\bar{U}_h$, is calculated from the standard deviation of the horizontal background winds at each altitude. The mean values of $\bar{U}_h$ and $\Delta\bar{U}_h$ are given in Table 1. Notably, the mean background winds $\bar{U}_h$ are small for both waves, and their absolute values are ~2 m/s.

There are two pairs of solutions for $\hat{\omega}$ and k_h (see equations (3.11) and (3.12)). For the current case when the denominators of the right hand side of equations (3.11) and (3.12) are positive, i.e., $\bar{U}_h < U_{\lim} = N \Big/ \sqrt{m^2 + 1/4H^2}$, there exist two positive roots for $\hat{\omega}$ and one positive and one negative roots for k_h. Positive k_h means that the wave is propagating in the positive x-direction of our reference frame. We retain the pair of solutions for $k_h > 0$, because the horizontal axes of the ground-based reference frame have been rotated towards the wave propagation direction determined from the hodograph analysis. The resulting intrinsic period $\tau_I = 2\pi / \hat{\omega}$ and horizontal wavelength $\lambda_h = 2\pi/k_h$ of the 7.7-h wave are shown in Figure 3.10 a. We find the average values of $\tau_I \sim 7.9$ h and $\lambda_h \sim 2.2\times10^3$ km. The intrinsic frequency is red-shifted relative to the observed frequency; however, because the horizontal wavelength is large, the frequency shift is relatively small. The derived horizontal group velocity c_{gh} profile in Figure 3.10a has a mean of ~48 m/s, while the vertical group velocity c_{gz} has an average value of ~0.46 m/s, i.e., ~40 km/day in the vertical direction. The elevation angle of the wave propagation direction is calculated from the ratio of the vertical and horizontal group velocities, and is found to be very shallow: ~0.6° from the horizon. Profiles of other properties of the 7.7-h wave, such as the

intrinsic horizontal phase speed (c_{Ih}) and azimuth angle of propagation direction, are also shown in Figure 3.10a.

It is important to derive the errors of these intrinsic parameters using the error propagation law. The three major error sources are the uncertainties in the three observed variables: ω, m and $\bar{U}_h$. The error of each intrinsic parameter is obtained via taking derivatives of each intrinsic variable with respect to ω, m and $\bar{U}_h$, following the method developed by one of the authors Chu in [*Chu and Papen*, 2005] and in *Wang et al*., [2010] for lidar temperature and wind error analysis (see their equations (19) and (20)). Taking $\hat{\omega}$ as an example, its errors are derived as

$$\Delta\hat{\omega} = \frac{\partial\hat{\omega}}{\partial\omega}\Delta\omega + \frac{\partial\hat{\omega}}{\partial m}\Delta m + \frac{\partial\hat{\omega}}{\partial\bar{U}_h}\Delta\bar{U}_h \tag{3.15}$$

Because the three error terms of ω, m and $\bar{U}_h$ are not correlated, the final error is given by the square root of the sum of the squares of each derivative term. In the example of $\hat{\omega}$, the final error is given by

$$(\Delta\hat{\omega})_{rms} = \sqrt{\left(\frac{\partial\hat{\omega}}{\partial\omega}\Delta\omega\right)^2 + \left(\frac{\partial\hat{\omega}}{\partial m}\Delta m\right)^2 + \left(\frac{\partial\hat{\omega}}{\partial\bar{U}_h}\Delta\bar{U}_h\right)^2} \tag{3.16}$$

Similar error propagation equations are used for all of the intrinsic parameters we determine. Two approaches can be used to calculate the terms in equation (3.16). One is to take numerical derivatives, and the other is to employ a Monte Carlo method. For the latter, we compute the wave properties from equations (3.11)–(3.14) with varied input variables of $\bar{U}_h$, ω and m. The computation is done with a three-loop iteration. For each loop, each variable takes 10 evenly spaced values from the mean ω, m and $\bar{U}_h$ minus their errors to the means plus their errors. The final uncertainty for each calculated wave parameter is then determined by the

standard deviation of all the solutions in the iteration process. We have tried both approaches and obtained comparable results for each intrinsic parameter. The error bars derived from the Monte Carlo method are plotted in Figure 3.10a.

3.4.2 The 5-h Inertia-Gravity Wave

We investigate the intrinsic properties for the 5-h wave using the same procedure as the 7.7-h wave. The temporal hodographs for this wave are shown in Figure 3.8b for 89–93 km between 10 UT and 25 UT. Strong leakage from the 7.7-h wave at altitudes from 83 to 89 km (see Figure 3.4) makes it hard to obtain reliable results outside the limited spatial range of 89–93 km. Shown in Figure 3.9b are the calculated phase differences between the temperature and horizontal wind perturbations for z = 89, 91 and 93 km. The derived phase differences are close to the theoretical value. Therefore, we conclude that this wave propagates primarily from west to east with an average propagation azimuth angle of 100°±4° east of north, as illustrated by the red arrows in Figure 3.8b. The intrinsic properties for the 5-h wave are shown in Figure 3.10b. Notably, the average τ_I ~ 4.5 h, which is blue-shifted relative to the observed periods, and the average λ_h~1.1×10^3 km. For this 5-h wave, the mean c_{gh} is calculated to be ~58 m/s, and c_{gz} is ~1.1 m/s, i.e., 95 km/day in the vertical direction. The elevation angle of this wave is determined to be ~1.1° from the horizon.

The results from the hodograph analysis support our hypothesis that there are two independent IGWs observed in the temperature and wind perturbations, because these two filtered waves were found to propagate in two different directions that are nearly perpendicular to each other. This is different from an alternate hypothesis that an IGW source can excite waves with different parameters that arrive at the observation altitude at different times; in this case, a

single wave's period would steadily shift from one period to another over the 30-h observation window. Furthermore, the 5-h wave propagates at a steeper elevation angle than the 7.7-h wave, which means that the 5-h wave has a greater ability to induce vertical motions (and thus temperature oscillations) than the 7.7-h wave. This explains why the dominant periods in the temperature wavelet spectrum appear to transition from 5 h to 8 h in Figure 3.5. Since in the first half of the measurement the amplitude of the 5-h wave is comparable to that of the 7.7-h wave, the 5-h wave induces larger temperature oscillations than the 7.7-h wave. Thus, it would dominate the temperature wavelet spectrum in the first half of Figure 3.5. But as the 5-h wave amplitude reduces more quickly than the 7.7-h wave in the second half of the measurement (due, perhaps, to source changes in time), the 7.7-h wave would dominate the temperature spectrum during the second half of the measurement (see Figure 3.5).

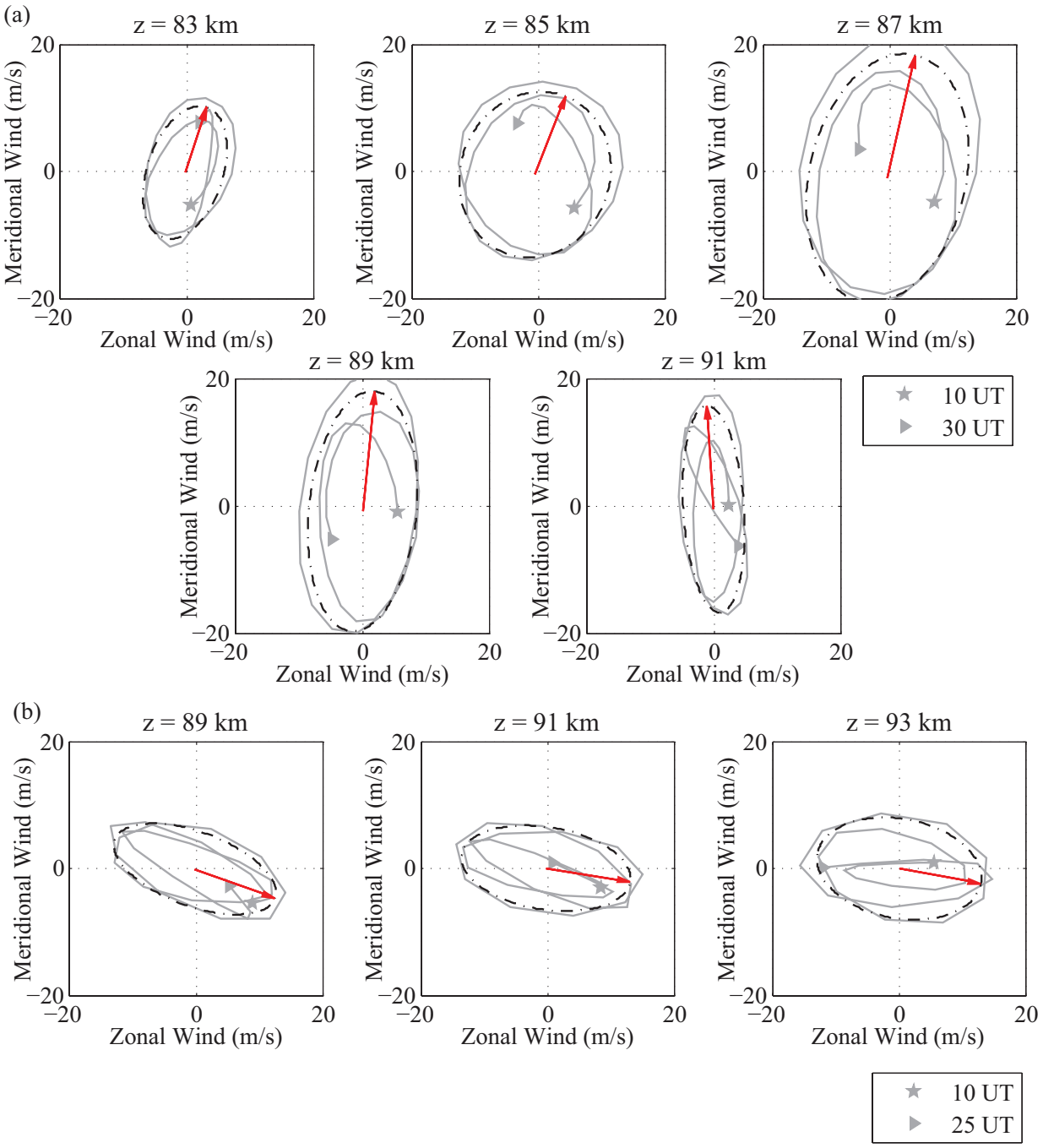

Figure 3.8. Temporal hodographs of zonal and meridional wind perturbations (a) for the 7.7-h wave in the altitude range of 83–91 km, and (b) for the 5-h wave in the altitude range of 89–93 km. Stars and triangles denote the start and the end times, respectively. The dotted-dashed ellipse on each plot shows the LMS elliptical fit of the hodograph. Red arrow is plotted along the major axis of each fitted ellipse, indicating the propagation direction of the wave.

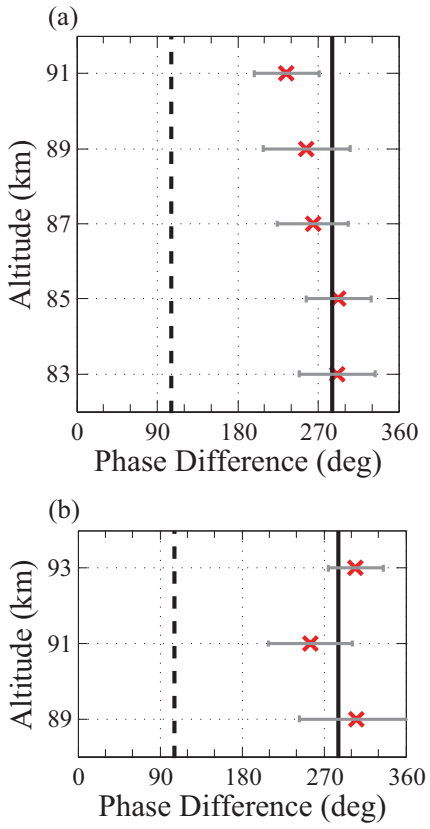

Figure 3.9. The deduced phase differences between $\tilde{U}_{\parallel}$ and $\tilde{T}$ (red crosses) for (a) the 7.7-h wave and (b) the 5-h wave. The solid vertical line identifies the value of $\arctan(m \cdot 2H) \sim 286^\circ$, while the dashed vertical line shows the value of $\arctan(m \cdot 2H) - 180^\circ \sim 106^\circ$. The grey horizontal bars denote the errors at the 95% confidence level.

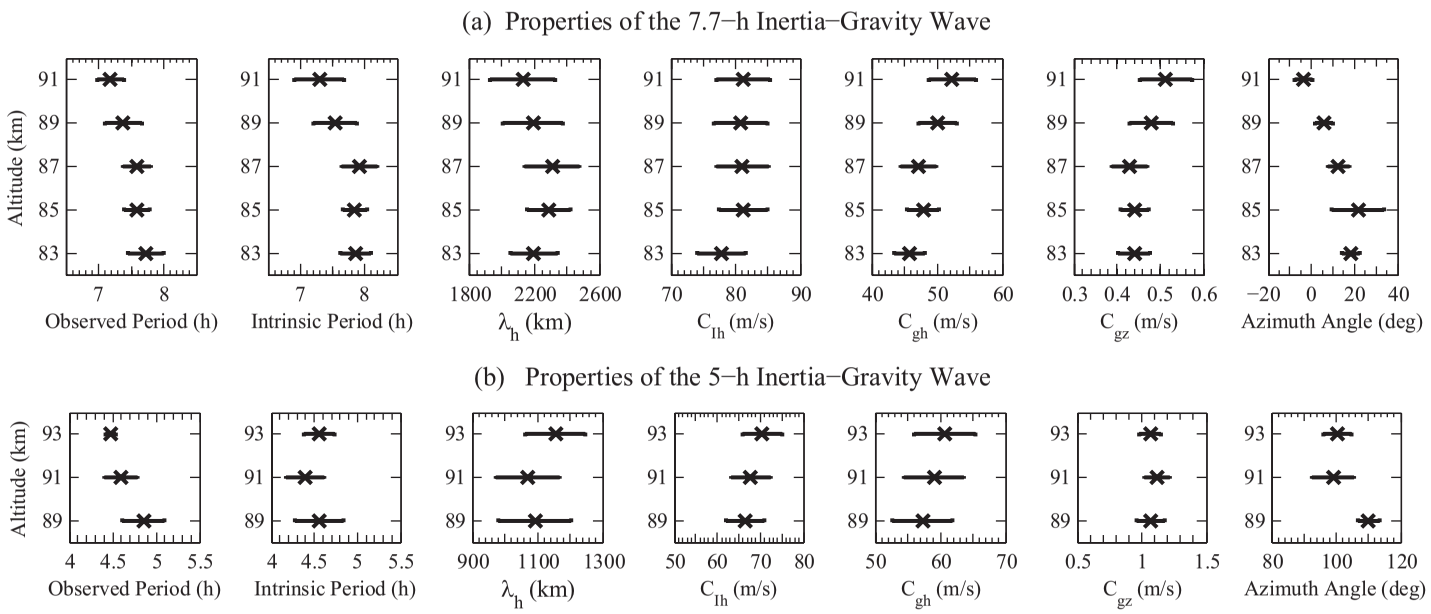

Figure 3.10. Wave properties (crosses) and corresponding errors (horizontal bars) for (a) the 7.7-h wave and (b) the 5-h wave. From left to right, the properties are observed period, intrinsic period, horizontal wavelength (λ_h), horizontal intrinsic phase speed (C_{Ih}), horizontal group velocity (C_{gh}), vertical group velocity (C_{gz}), and azimuth angle of the wave horizontal propagation direction.

3.5 Discussion

Although both waves are treated as IGWs in this paper, the 7.7-h and 5-h wave periods are close to that of the terdiurnal (8-h) tide and 4.8-h tide. However, the 7.7-h wave in our study is unlikely to be a terdiurnal tide for the following reasons. First, the vertical wavelengths of terdiurnal tides are generally much larger than that computed for the 7.7-h wave in our case. *Du and Ward* [2010] investigated the global structure of the terdiurnal tide, including migrating and 10 nonmigrating components, using the extended Canadian Middle Atmosphere Model (CMAM). Their study shows the vertical phase profile of the total terdiurnal tide superposed from the 11 components in June at 60°S, 130°E (Figure 6b in *Du and Ward*, [2010]), from which the vertical wavelength is inferred to be ~65 km, a factor of three greater than the observed value in our study. Model simulations of the migrating terdiurnal tide performed by *Smith and Ortland*, [2001] also support this point, since they indicate that the shortest vertical wavelength for all of the modes is 47 km, nearly twice as large as that in the current observation. Second, as shown in Figure 3.10, we observed large variations of the dominant periods with altitude, which does not satisfy the definition of a tidal wave, i.e., a harmonic of the Earth's rotation period. A notable feature of each wave is that the observed wave period decreases with increasing altitude. In Figure 3.10, the observed period of 7.7-h wave decreases from $\tau_1 = 7.7 \pm 0.3$ h at z = 83 km to $\tau_1 = 7.2 \pm 0.2$ h at z = 91 km, and the 5-h wave period decreases from $\tau_2 = 4.9 \pm 0.2$ h at z = 89 km to $\tau_2 = 4.5 \pm 0.1$ h at z = 93 km. According to *Nicolls et al*., [2010], such a feature can be explained by a spectrum of IGWs generated by a geostrophic adjustment of the jet stream. However, we note that these variations may be within our error bars. Third, modeling work by *Du and Ward* [2010] shows that the largest amplitude of the terdiurnal tides is given by the

migrating component. Examination of wind and temperature data from the MERRA reanalysis at the highest-pressure level (0.1 hPa, ~59 km) shows no evidence of a significant zonal wavenumber 3 pattern; this is also suggestive that the terdiurnal tide cannot explain the current observations.

Both the background temperature and winds play a role in wave propagation through the atmosphere, the latter typically being much more important in allowing (or disallowing) the gravity wave propagation. Unfortunately, the lack of extensive middle atmospheric wind and temperature measurements up to the MLT prohibit detailed studies involving ray tracing such slow waves through realistic atmosphere [e.g., *Nielsen et al*., 2012]. Such work is therefore outside the scope of this study. We now roughly identify the sources of the observed IGWs by making a number of simple assumptions. For both waves, the vertical group velocities (calculated above) are significantly slower than the horizontal group velocities. This implies that it would take ~1–2 days for each wave to propagate to the MLT (assuming that the vertical wind is negligible). Assuming that the horizontal background wind along the wave propagation path is also negligible, the wave would have propagated several thousands of kilometers in the horizontal plane prior to our observation. However, if the horizontal background winds at lower altitudes were opposite to the wave propagation direction, the horizontal distance and time taken to reach the mesopause would be shorter [*Nicolls et al*., 2010].

The 7.7-h wave propagates approximately northward, which suggests the wave source is located across the Antarctica continent. As *Nicolls et al*. [2010] argued in analyzing the IGWs observed in the Arctic, a possible mechanism of IGW generation is geostrophic adjustment of the jet stream. In general, any "bulk" change to the background wind (at any altitude) will excite gravity waves [*Zhu and Holton*, 1987; *Vadas and Fritts*, 2001]; if this change takes more than a

few hours and the horizontal scales are large, then IGWs will be excited. We can speculate (similar to *Nicolls et al*. [2010]) that the 7.7-h IGW observed at McMurdo was excited by geostrophic adjustment of the jet stream or unbalanced flow on the opposite side of the Antarctic continent. Work by *Sato et al*., [2012] utilized a high-resolution, middle-atmosphere, general circulation model to examine the gravity wave field in the Southern Hemisphere polar region. They found significant downward energy flux in the stratosphere during the winter. Their work suggests that at least some proportion of this field is linked to the in-situ production of waves within the stratosphere. The existence of in-situ wave sources in the stratosphere is also supported by *Sato and Yoshiki* [2008], *Yamashita et al*. [2009] and *Yamashita* [2011]. From intensive radiosonde observations performed at Syowa Station (69.0°S, 39.6°E), *Sato and Yoshiki* [2008] demonstrated that the IGWs observed in June were generated by spontaneous geostrophic adjustment of the unbalanced polar night jet located in the stratosphere. *Yamashita et al*. [2009] characterized gravity waves in the altitude range of 30–45 km at the South Pole (90°S) and Rothera (67.5°S, 68.0°W) with lidar data. They found that ~44% of the observed waves had upward phase progression, indicating downward wave propagation from the stratosphere or above. Using ECMWF data, *Yamashita* [2011] demonstrated that the wave excitation occurs in the stratosphere from in-situ energy sources.

Using a similar heuristic approach as in *Nicolls et al*. [2010] (that is, assuming constant horizontal and vertical group velocities and zero background wind), we can estimate approximate locations of the wave along its propagation path. We can then compare these locations with the structure of the background winds (at the appropriate locations and altitudes) from the MERRA reanalysis data. This will enable us to identify regions for which the background winds have significantly changed direction or speed in time over the period of 6–12

h and over scales of several hundreds of km. In such regions, the air likely goes out of geostrophic balance, leading to the generation of inertia-gravity waves [*Zhu and Holton*, 1987; *Fritts and Luo*, 1992; *Luo and Fritts*, 1993; *Vadas and Fritts*, 2001]. These waves are generated because the air in those regions strives to regain geostrophic balance. Therefore, identifying regions of significant wind changes in the MERRA data allows us to identify regions where the IGWs could have been generated. (The MERRA data are available from the GES DISC website.)

We examined the MERRA winds from 60 km (the approximate altitude of the highest MERRA pressure level output) to the surface at the times that the wave intersects that level. Inspection of the winds at the different altitude levels linked to the 7.7-h wave shows no features suggestive of unbalanced flow until the 0.7 and 1 hPa levels (43–46 km), as illustrated in Figure 3.11. In Figures 3.11a–3.11c, the stratospheric wind speeds are shown at 0.7 hPa (~46 km) on 28 June 2011 for 9, 12, and 15 UT, respectively. The open magenta circles show the estimated wave location of the 7.7-h wave at 12 UT. This location is ~(67ºS, 3ºE), a distance of ~3900 km from McMurdo. (Note that these magenta circles are in identical locations.) Figures 3.11d–3.11f show the stratospheric wind speeds at 1 hPa on 28 June 2011 for 6, 9, and 12 UT, respectively. Here, the open magenta circles show the estimated wave location for the earlier time of 9 UT and at the slightly lower altitude of ~43 km. This location is ~(65ºS, 2ºE), ~4100 km away from McMurdo. (Again, the magenta circles are in identical locations in Figures 3.11d–3.11f.) In the vicinity of each estimated wave position at the 0.7 and 1 hPa levels, we see what appears to be a jet stream exit region. In these regions and for both levels, the background winds change dramatically over a relatively short period of time. For 0.7 hPa, the background winds (u, v) are (74, 8) m/s at 9 UT on 28 June 2011, (79, 8) m/s at 12 UT, and then change significantly to (67, -13) m/s at 15 UT. The variations of the background winds are (Δu, Δv) = (–7, –21) m/s over a period of 6 h. At 1

hPa, the variations of the background winds are (Δu, Δv) = (28, –13) m/s over the same length of time (but from 6–12 UT on 28 June 2011). These relatively rapid changes in the background winds can be modeled as an external body force, which excites IGWs that propagate in most directions (except those perpendicular to the body force) [e.g., *Vadas and Fritts*, 2001]. Studies by *O'sullivan and Dunkerton* [1995] and *Thomas et al*. [1999] have also identified such regions as potential areas of active wave formation. Therefore, we hypothesize that the jet stream exit region at the level between 0.7 and 1 hPa, as indicated by the magenta open circles, may be the source of the 7.7-h wave. The large horizontal distance (~3900–4100 km) traveled by this wave is similar to that obtained by *Nicolls et al*. [2010] of ~4500–5500 km for the Arctic IGW. Note that the IGW observed by *Nicolls et al*. [2010] propagated southward over Alaska, and was traced back to northern Russia. Therefore, the IGW in their case likely propagated over the Arctic, which is comparable to our case that the IGW propagated across the Antarctic continent to reach McMurdo. It is worth pointing out that the IGW in the Arctic case may have originated from a jet stream adjustment at z ~ 10 km near the tropopause [*Nicolls et al*., 2010], while the stratosphere jet stream near 1 hPa (~43 km) is indicated in our Antarctic case as the wave source. Given the approximate north-south propagation direction of this 7.7-h wave, and that the southward component of the background wind along the wave propagation path was smaller than the wave's phase velocity (not shown), we believe that this wave could have originated from this altitude range, and could have followed this trajectory without being removed by critical level filtering.

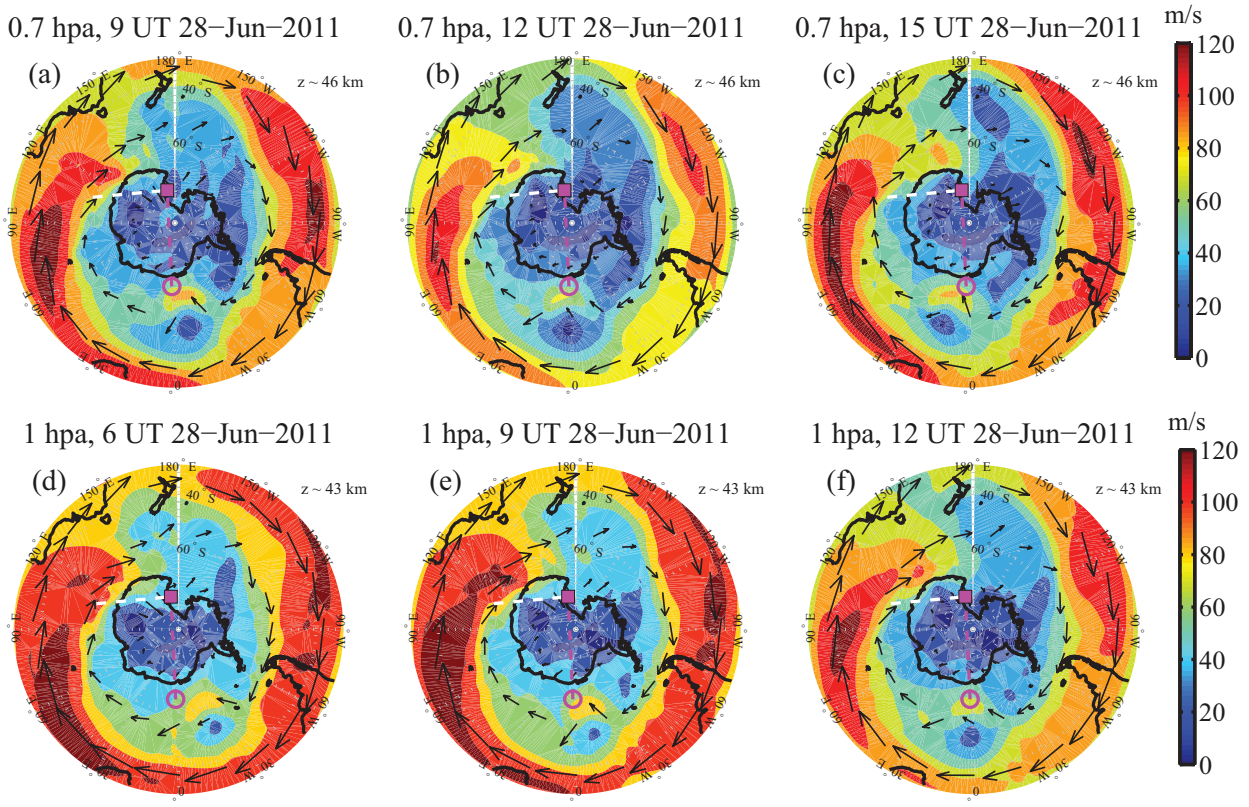

Figure 3.11. Horizontal winds over the Southern Hemisphere from the MERRA reanalysis data. Arrows are wind vectors; colors denote wind speeds. The magenta solid square indicates McMurdo. (b) The 0.7 hPa winds (~46 km) at 12 UT on 28 June. Open magenta circle shows the approximate source location for the 7.7-h wave. (a, c) Same as in (b), except for 3 h earlier and later, respectively. (e) The 1 hPa winds (~43 km) at 9 UT on 28 June. Open magenta circle shows the approximate source location for the 7.7-h wave. (d, f) Same as in (e), except for 3 h earlier and later, respectively. White dashed line shows the estimated horizontal trajectory of the 5-h wave.

The 5-h wave propagates nearly zonally from west to east. A similar analysis for the 5-h wave does not display a similarly convincing coincidence between the potential wave source and a region of unbalanced flow within the region observable by the MERRA reanalysis. However, given the zonal direction of wave propagation (denoted by white lines in Figure 3.11) and the high likelihood of critical level filtering, we suggest that its source was more likely above the upper boundary of MERRA (z~60 km).

3.6 Conclusions

Combined Fe lidar/MF radar measurements have shown the presence of two independent IGWs observed simultaneously above Arrival Heights during 29–30 June 2011 for over 20 h in the Antarctic MLT. The two IGWs have ground-based observed periods of 7.7±0.2 h and 5.0±0.1 h, respectively. Temporal filtering and hodograph analysis are applied to the temperature and wind data to determine the propagation directions of these IGWs. To resolve the ambiguity in the hodograph analysis, the phase difference between the temperature and horizontal wind perturbation (parallel to the horizontal wave propagation direction) is derived; this serves as a constraint for the extracted azimuth angle of the propagation direction. The analysis results show that the 7.7-h wave propagates approximately northward, while the 5-h wave propagates approximately eastward; these directions are approximately perpendicular to each other. The intrinsic frequency and horizontal wavenumber of each wave are calculated via solving a quadratic equation derived from the linear dispersion and polarization relations. The intrinsic periods are estimated to be 7.9±0.3 h and 4.5±0.3 h, and the corresponding horizontal wavelengths are $2.2\pm0.2\times10^3$ and $1.1\pm0.1\times10^3$ km, respectively. We have performed robust error analyses that have allowed us to derive the uncertainty in each IGW parameter.

To our knowledge, this is the first known observation of two simultaneous IGWs in the MLT at the same location. It is also the first report of the coincident observations of IGWs by an MF radar and lidar in the Antarctic MLT region. The intrinsic horizontal phase speeds are determined to be 80±4 and 68±5 m/s for the 7.7-h and 5-h waves, respectively. For the 7.7-h IGW, its horizontal and vertical group velocities are 48±3 and 0.5±0.1 m/s, respectively. For the 5-h IGW, the horizontal and vertical group velocities are 58±5 and 1.1±0.1 m/s, respectively. Therefore, both waves propagate with very shallow elevation angles from the horizon: ~0.6° and

1.1° for the longer- and shorter-period waves, respectively. This implies that it would take 1–2 days for the waves to propagate to the MLT after traveling several thousands of kilometers in the horizontal plane prior to our observations. This would have placed the source of the 7.7-h wave (propagating meridionally) on the opposite side of the Antarctic continent. As *Nicolls et al*. [2010] proposed, we speculate that both IGWs observed at McMurdo were generated from similar mechanisms, i.e., the geostrophic adjustments of the jet stream or unbalanced flow, but from different sources around Antarctica. A simple analysis of MERRA reanalysis data shows strong circumstantial evidence for the 7.7-h IGW to be associated with a source in the stratosphere linked to a region of unbalanced flow. A complete investigation of the wave sources and generation mechanisms is beyond the scope of this paper, but is a subject for future work. Observation of two simultaneous IGWs is unusual, but single IGW events have been frequently observed in the lidar temperatures at McMurdo. For example, an IGW event was identified with an intrinsic period of 7.5 h on 11 July 2011 at McMurdo [*Chen et al*., 2012] (This case study is included in Appendix A). The lidar campaign in the last two years has revealed an unexpectedly high occurrence of IGWs in the Antarctic MLT region. Due to the expected low likelihood of IGWs propagating to the MLT region, the observed high occurrence rate indicates that Antarctica may have favorable conditions for the upward propagation of IGWs. Statistical studies and numerical modeling are crucial for improving our understanding of the sources and impacts of IGWs on the polar middle and upper atmosphere.

CHAPTER 4

Lidar Observations of Persistent Inertia-Gravity Waves at McMurdo (77.83°S, 166.67°E)

4.1 Introduction

Owing to the high-resolution, long-duration, large-altitude-range temperature measurements provided by the Fe Boltzmann lidar at McMurdo [*Chu et al*., 2011a, 2011b; *Chen et al*., 2013], a new wave phenomenon in the Antarctic middle and upper atmosphere has been discovered. As illustrated in Figure 4.1, the raw temperature data from the stratosphere to the lower thermosphere (about 30–115 km) exhibit persistent, dominant, large-amplitude waves with non-tidal periods of ~3–10 h and vertical wavelengths of ~20–30 km. Here, the word "persistent" is used to describe the fact that these waves continue for a prolonged period, e.g., a single wave event (see Section 4.2) may last at least 10 h, and sometimes over 50 h, in the small field of view (FOV, 1 mrad) of the lidar beams. If we do not separate the observed wave variations into individual wave events with individual periods, but regard these waves as a group of waves with periods ranging between 3 and 10 h, then this wave group is perpetual. That is, these waves occur on every lidar run, spanning sufficient duration, and occur frequently enough as to appear endless and uninterrupted. There has not been any single lidar run that does not show the signature of this 3–10 h wave group during 5 years of lidar observations at McMurdo, and so far we have not seen any inactive wave gap epoch in observed temperature data. The word "dominant", as used above, is to describe the fact that the temperature variations in the mesosphere and lower thermosphere (MLT) are dominated by these non-tidal, short period

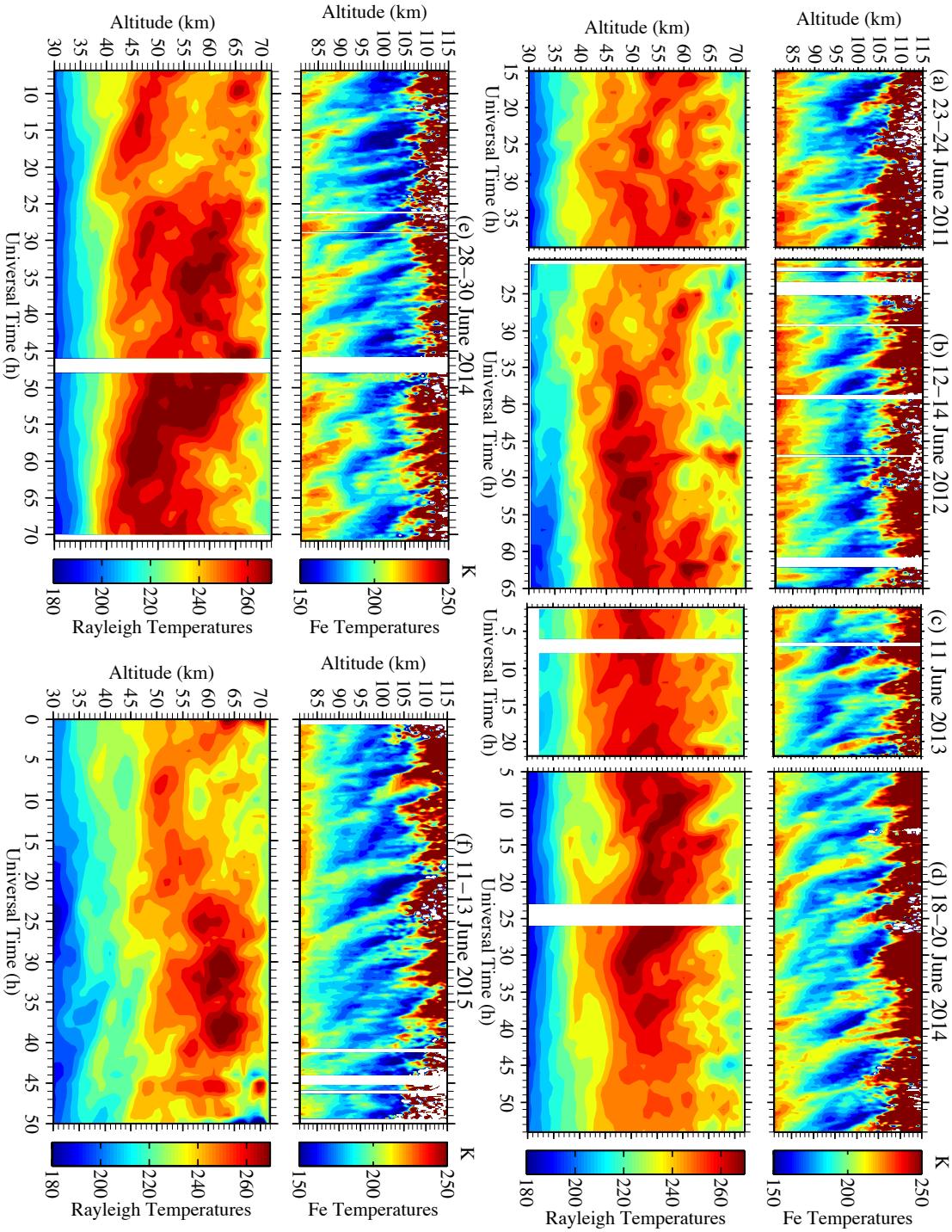

Figure 4.1. Contours of typical raw temperature observations in June from 2011 to 2015 at McMurdo by an Fe Boltzmann lidar in the MLT region (in the altitude range of 81– 115 km) and from Rayleigh integration (in the altitude range of 30–72 km).

waves, while the diurnal and semidiurnal tides in temperature are very minimal (up to 1–3 K amplitude) below 100 km [*Fong et al*., 2014, 2015]. Because planetary waves dominate the temperature variations in the polar winter stratosphere as studied by *Lu et al*. [2013], the 3–10 h waves are not as obvious in the stratosphere as in the MLT (Figure 4.1). Nevertheless, Figure 4.2 demonstrates that the 3–10 h waves are still persistent in the stratosphere and mesosphere once planetary waves are filtered out from the Rayleigh temperature perturbations.

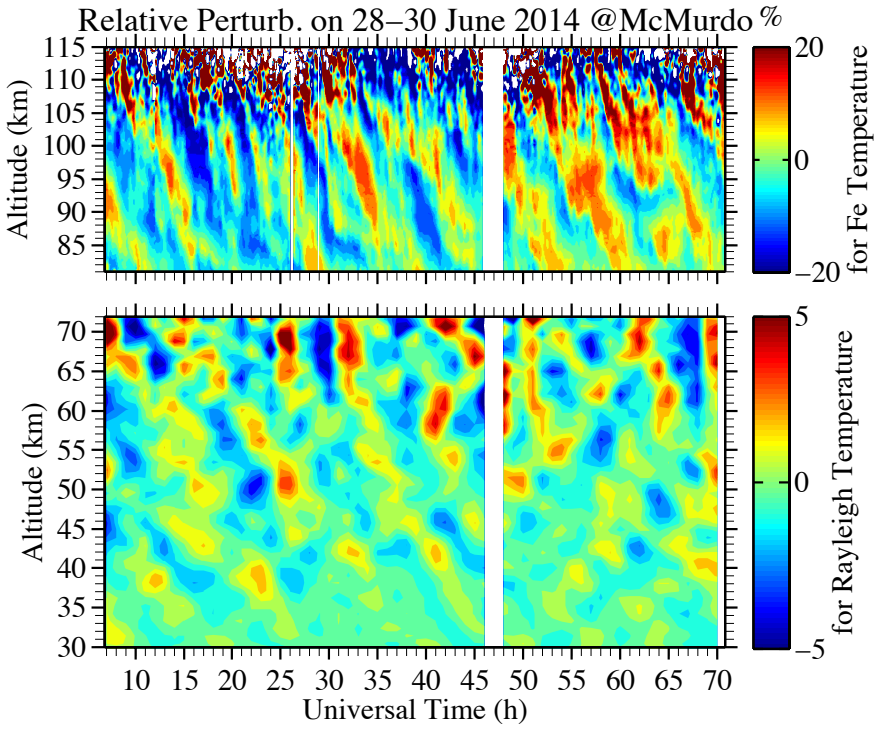

Figure 4.2. Relative temperature perturbations (unit: %) on 28–30 June 2014 at McMurdo. The Rayleigh temperature perturbations were high-pass filtered with a cutoff frequency of 1/12 h^{-1}, in order to reveal the waves with periods <12 h.

These persistent 3–10 h waves were unknown before the McMurdo lidar campaign started providing high-resolution, range-resolved temperature, though observations in the Antarctic middle and upper atmosphere can be traced back to the 1980s or even earlier [*Nomura et al*., 1987]. Horizontal wind observations using medium frequency (MF) or meteor radars have

been used to characterize diurnal and semidiurnal tides [e.g., *Forbes et al*., 1995; *Baumgaertner et al*., 2005; *Murphy et al*., 2006], planetary waves [e.g., *Dowdy*, 2004; *Espy et al*., 2005], gravity waves [e.g., *Vincent*, 1994; *Hibbins et al*., 2007] and lamb waves [e.g, *Forbes et al*., 1999; *Portnyagin et al*., 2000; *Kovalam and Vincent*, 2003]. However, none of these works noted the persistent 3–10 h waves, except *Forbes et al*., [1999] who described intradiurnal wave oscillations with periods of ~7.5–10.5 h. However, no information was provided on the vertical wavelengths. There have been observational studies of gravity waves, tides and planetary waves in Antarctica using OH airglow intensities by all sky imagers [e.g., *Espy et al*., 2006; *Suzuki et al*., 2011; *Nielsen et al*., 2012], wind and temperature measured by Michelson interferometers [e.g., *Sivjee and Walterscheid*, 1994; *Azeem and Sivjee*, 2009] and Fabry-Perot interferometers [e.g., *Hernandez et al*., 1992; *Wu et al*., 2005], but these instruments do not have vertical range resolution, and necessarily average over the altitude range of the emission. Na and Fe densities measured by broadband resonance fluorescence lidars were also used to observe wave dynamics in the Antarctic mesopause region [*Nomura et al*., 1987; *Collins and Gardner*, 1995; *Diettrich et al*., 2006], but none of them depicted persistent 3–10 h waves. Gravity waves and large-scale global waves such as tides and planetary waves in the Antarctic MLT have also been studied by satellite observations [e.g., *Iimura et al*., 2009; *Morris et al*., 2009; *McDonald et al*., 2010]. There are several explanations for the lack of evidence for persistent 3–10 h waves in the observations mentioned above: 1) Horizontal winds are usually dominated by tides, thereby obscuring these wave signatures; 2) non-range-resolved temperature, wind and airglow data would have easily mistaken these phenomena as tides because no vertical wavelength information was available; and 3) most observations in the past did not have sufficient temporal resolution or time span to reveal these waves deterministically. It is worth mentioning that an

Advanced Mesospheric Temperature Mapper (AMTM) operating at the South Pole in the same years as our observations at McMurdo has revealed wave oscillations in the OH layer temperatures with similar periods as the lidar findings (Mike Taylor, Utah State University, private communication).

It is surprising that these waves are so dominant and so strong in range-resolved temperature data, as shown in Figure 4.1. Temperature perturbations can easily reach ±10–30 K in the mesopause region, but tidal signatures are essentially invisible. This is very different from observations in sub-polar, mid- and low-latitude regions wherein tidal signatures usually dominate temperature variations while gravity wave perturbations are relatively minor [e.g., *States and Gardner*, 2000; *She et al*., 2004; *Chu et al*., 2005; *Friedman and Chu*, 2007]. *Chen et al*. [2013] conducted a case study for McMurdo waves on 29–30 June 2011, combining the Fe Boltzmann lidar temperature with MF radar horizontal wind data. Although tides are obvious in the winds, 3–10 h waves were found in the range-resolved wind data for the first time. Besides temperature and wind, the 372 and 374 nm Fe density data at McMurdo have also revealed these persistent 3–10 h waves. *Chu et al*. [2011a] presented such a case for summer in January 2011 (see their Figure 4). The downward phase progression in the density data is comparable to that in the temperature data and, interestingly, the cold phase of these waves helps polar mesospheric clouds to form in the summer, as demonstrated in *Chu et al*. [2011a]. A winter case is illustrated in Figure 4.3. The 3–10 h waves show nicely on the Fe density contours.

There are significant merits of studying these persistent 3–10 h waves. An intriguing question concerns wave sources and the generation mechanisms for such persistent, year-round waves. The waves would have a strong impact on composition and chemistry in the mesopause region because the large temperature perturbations induced by waves can alter the rates of

chemical reactions and, therefore, the concentrations of minor species in the region. Consequently, they are important to the correct modeling of metal layers, polar mesospheric clouds, and other species in the Antarctic middle and upper atmosphere. Because such strong waves cannot continue propagating upward forever, it is important to know where they break and how they impact the upper atmosphere. The implications of these waves on general circulation models (GCMs) and chemical climate models (CCMs) are also significant, particularly with regard to the "cold pole" problem. The "cold pole" problem refers to the cold bias in modeled winter temperatures in the southern polar stratosphere when compared to observations [*Garcia and Boville*, 1994; *Eyring et al*., 2006]. Numerical simulations have indicated missing wave drag in the southern stratosphere as a possible cause. Mountain waves generated by small islands around 60°S [*Alexander et al*., 2008; *McLandress et al*., 2012] or inertia-gravity waves (IGWs) [*Tan et al*., 2011] may provide the missing wave drag. However, the persistent occurrence of 3–10 h waves in the Antarctic mesopause region complicates the picture. If these IGWs survive into the mesopause, then it is unlikely that these waves break or severely dissipate in the stratosphere, so they may not produce sufficient wave drag in the stratosphere. On the other hand, could the unknown sources that persistently generate such waves be responsible for the missing wave drag?

None of the above questions can be answered before these 3–10 h waves are well characterized and documented in the Antarctic middle and upper atmosphere. Therefore, the major goals of this study are to establish the observational fact that the 3–10 h waves are persistent and dominant in the MLT region at McMurdo and to characterize the wave properties using the temperature perturbations. In addition to sophisticated analyses of an individual case demonstrating our new wave analysis methods, we perform a statistical study on the extensive

lidar data collected in June through five Antarctic winters from 2011 to 2015. Although these single-location observations cannot resolve the wave nature and source, they do provide the observational basis for future research on answering the important questions listed above.

4.2 Observations

Since December 2010, the McMurdo lidar observational campaign, conducted by the University of Colorado lidar group, has been in progress for 5 years as of this writing. The upgraded Fe Boltzmann/Rayleigh temperature lidar [*Chu et al*., 2002; *Wang et al*., 2012] has been operated at Arrival Heights observatory (77.83ºS, 166.67ºE) through a collaborative effort between the United States Antarctic Program (USAP) and Antarctica New Zealand (AntNZ). The observations are year round, weather permitting. Due to the Antarctic darkness, the winter lidar observations experience very low solar background. Combined with a higher Fe layer abundance in winter [*Yu et al*., 2012], the lidar data in winter months (i.e., May through August) provides the highest resolution and largest range of temperature measurements. Among the winter months, the data quantity is highest in June, primarily due to superior weather conditions. June data have been collected in five consecutive years, from 2011 to 2015. Therefore, this study focuses on the June data analysis, not only because very long datasets can be utilized to inspect wave activity, but also because good statistics can be achieved. These five years of data also allow investigation of year-to-year variability.

Several representative lidar runs are plotted in Figure 4.1 to illustrate the temperature data quality and length during the month of June. The temperatures in the MLT region (~80–115 km) are derived from the 372 and 374 nm channels of Fe lidar data using the Boltzmann technique [*Gelbwachs*, 1994; *Chu et al*., 2002], while the temperatures in the mesosphere and stratosphere (~28–73 km) are derived from the Rayleigh scattering obtained by the same Fe lidar with the

Rayleigh integration technique [*Hauchecorne and Chanin*, 1980]. Fe temperatures in the MLT are derived with resolutions of 0.25 h and 0.5 km and oversampled to 0.1 h and 0.1 km [*Chu et al*., 2011b]. The data are then temporally and vertically smoothed with a Hamming window of 0.5 h and 1 km full width at half maximum (FWHM) to further reduce the temperature error. The Rayleigh temperatures have resolutions of 1 h and 1 km and are plotted with steps of 1 h and 1 km. A gap exists between the Fe and Rayleigh temperature regions because the signals obtained from this gap region are too weak to derive reliable temperatures.

Chen et al. [2013] reported two simultaneous inertia-gravity wave events on 29–30 June 2011 at McMurdo, with apparent periods of 7.7±0.2 and 5.0±0.1 h and vertical wavelengths of 22±2 and 23±2 km, respectively. The data on 23–24 June 2011 are shown in Figure 4.1a, exhibiting similar wave patterns as those in *Chen et al*. [2013]. The case in 2012 covers nearly two days, while the case in 2013 is relatively short (~20 h). However, the wave patterns and periods are similar to each other and to the 2011 data. Two long datasets in 2014 are illustrated in Figure 4.1d and 4.1e, with ~50 and 65 h of data, respectively. The case in 2015 is again long, covering ~50 h. As mentioned above, weather conditions dictated the dataset lengths. Despite the differing lengths of the datasets in each year, the wave patterns, with periods falling between 3 and 10 h, are very similar in each case and similar to many cases that are not shown here. No obvious year-to-year variability is observed and, for this reason, such variability will not be a focus of this study. So far we have not seen any days of data without signatures of such 3–10 h waves. In fact, author Cao Chen was motivated to take nearly three days of continuous lidar data in 2014 to investigate whether these waves ever paused. Figures 4.1 and 4.2 clearly show that the 3–10 h waves were persistent for three entire days.

The 3–10 h wave signatures also show up clearly in all of the Fe density contours. An example is illustrated in Figure 4.3, where the Fe densities in 372-nm and 374-nm channels are plotted in direct comparison to the Fe temperatures for 28–30 June 2014. Note the large differences in the absolute Fe densities between two channels. These differences are determined by the Boltzmann distribution of populations on two different energy levels of atomic Fe, in which the 372 nm signals originate from the lowest ground state a^5D_4, and the 374 nm signals originate from a lower excited state a^5D_3. The Boltzmann distribution is temperature dependent and, therefore, the Fe temperatures are derived from the ratio of the signals from these two channels [*Gelbwachs*, 1994; *Chu et al*., 2002]. Figure 4.3 reveals periodic variations of Fe densities in both channels that are consistent with the Fe temperature variations through the three days of observations. As illustrated in the figure, eight white, dashed lines are overlaid with the downward-progressing phase lines of the local minimum of Fe density. The density phase lines closely match the cold temperature phase lines, especially when a nearly monochromatic wave dominates. The dashed line at around 20 UT marks a time when multiple waves were present in the Fe temperature contour with no dominant wave. Consequently, this phase line is an average. Though the 374-nm Fe density has the best phase match with Fe temperature, the phase match between the 372-nm Fe density and Fe temperature is reasonable as well. This is consistent with summer observational results by the same lidar at McMurdo (see Figure 4 in *Chu et al*. [2011a]). One implication of this observed phase correlation is that 3–10 h waves may be studied using the 372-nm Fe density data during the summer, when the Fe temperature data and 374-nm Fe density data are of lower quality.

For this study, we will only use the June Fe temperatures for wave analyses because of the very high quality of this data. Since the wind data from the MF radar at Scott Base and

Arrival Heights are not available for many days in June, we will focus on the lidar data, conducting a case study in Section 4.3 and then statistical studies in Section 4.4 to characterize the properties and occurrence rate of the 3–10 h waves.

4.3 Wave Analysis of a Case on 28–30 June 2014

Long, continuous lidar temperature data are essential for understanding these persistent 3–10 h waves. On 28–30 June 2014 (Figure 4.1e), about 65 h of high quality lidar data were taken—the longest winter-time observational run in all five years of this campaign. By subtracting the dataset-mean temperatures at each altitude and dividing by the mean, relative temperature perturbations in the MLT are derived and shown in Figure 4.2. Note that no filters are applied to the Fe temperature data. The perturbation data provides strong evidence for the persistency of these 3–10 h waves. During nearly 65 h of observations, clear wave structures with a downward phase progression persist in the MLT region, the amplitudes of which can exceed 25 K at 100 km. The temperature variations are dominated by wave oscillations with periods of 3–10 h throughout the observation while diurnal- and semidiurnal-period waves appear minor. In the lower mesosphere and stratosphere, after the long-period (>1 day) waves are high-pass filtered using a sixth-order Butterworth filter with a cutoff frequency of 1/12 h^{-1}, the 3–10 h waves are clearly shown. Several different periods emerge from analysis of the MLT perturbations apparent in Figure 4.2. We perform detailed wavelet analyses to characterize the properties of each wave packet.

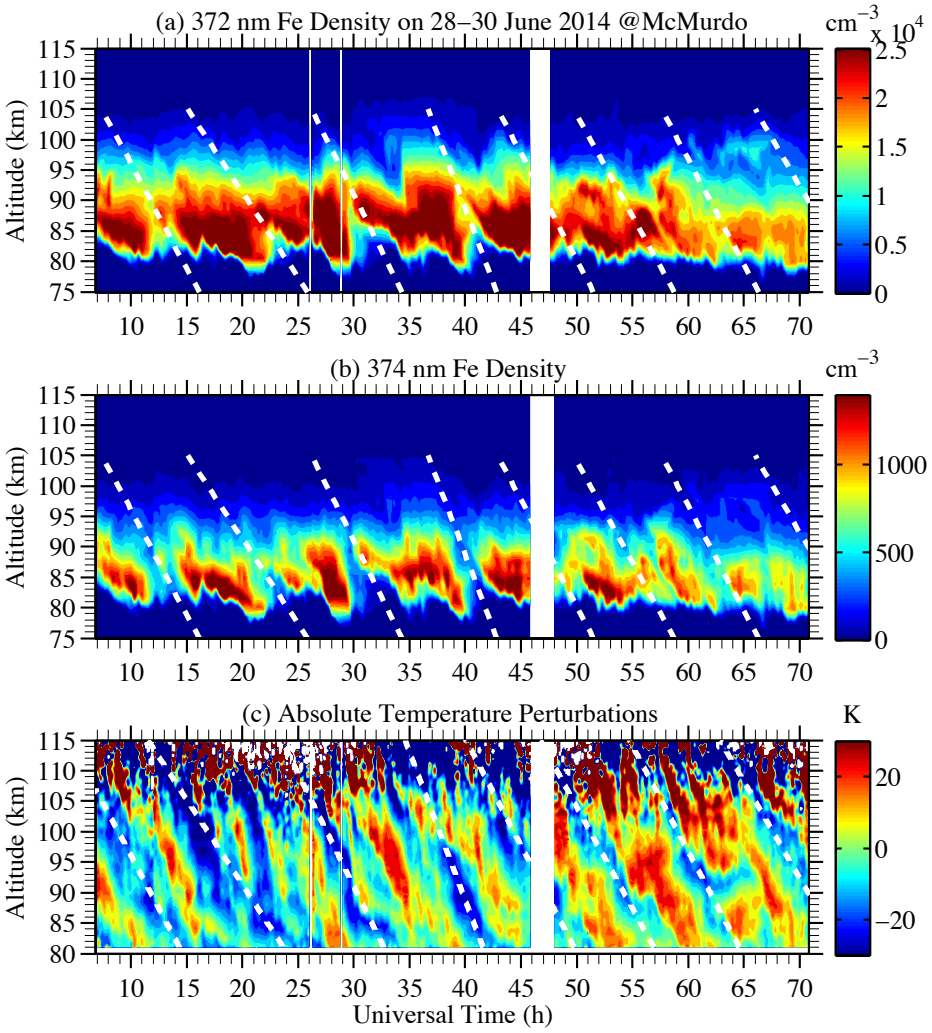

Figure 4.3. Wintertime Fe densities measured by the (a) 372 and (b) 374 nm channels along with the (c) Fe temperature perturbations (unit: K) in the MLT region on 28–30 June 2014 at McMurdo.

4.3.1 Wavelet Analysis Method

For separating each wave packet according to its dominant period, amplitude and life span, wavelet analysis is a very effective technique [*Nappo*, 2002]. By decomposing the time series into time–frequency space, wavelet analysis allows us to determine not only the dominant modes of variability, but also how those modes evolve with time [*Torrence and Compo*, 1998]. Many studies on gravity waves have used this technique to determine the locations of wave

events [*Sato and Yamada*, 1994; *Zhang et al*., 2001; *Wang et al*., 2006; *Lu et al*., 2015a] and to extract monochromatic wave packets [e.g., *Zink and Vincent*, 2001a, 2001b; *Werner et al*., 2007; *Murphy et al*., 2014]. The ability to analyze non-stationary signals gives the wavelet technique advantages over traditional Fourier spectrum analysis, which assumes constant amplitudes of oscillation over the data series.

In this study, we perform a wavelet analysis on the relative temperature perturbations. Since the wavelet transform prefers gap-less data, the original data gap between 46 UT and 48 UT was filled by means of a Lomb-Scargle (LS) periodogram, which is a method first proposed by *Scargle* [1989], and then described in detail by *Hocke and Kämpfer* [2009]. The power spectral density $P(\omega)$, amplitude $A_{FT}(\omega)$ and phase φ_{FT} of the LS periodogram were first calculated from the gapped data series using equations (3–10) in *Hocke and Kämpfer* [2009]. Then, the corresponding complex FFT vector $F(\omega)$ was calculated as

$$F(\omega) = A_{FT}(\omega)\exp(i\varphi_{FT}) \tag{4.1}$$

An inverse Fast Fourier transform was then applied to $F(\omega)$ to provide a non-gapped data series. Since the new data series shares the same LS spectrum with the gapped one, this method has the advantage of preserving the spectral features of the original gapped data series [*Hocke and Kämpfer*, 2009].

After the data gap was filled, we then applied a Morlet wavelet transform to the relative temperature perturbations and calculated their amplitude spectra $|W(t, T)|$ as a function of time (t) and period (T) following *Torrence and Compo* [1998]. It is known that wavelet power spectra calculated using the code provided by *Torrence and Compo* [1998] are distorted or biased in favor of large scales or low frequencies oscillations [see *Liu et al*., 2007]. To overcome the bias

of higher amplitudes for longer period waves, we constructed a new Morlet wavelet function that was modified from $\hat{\psi}(s\omega)$ given by equation (6) and Table 1 in *Torrence and Compo* [1998],

$$\hat{\psi}_{\mathrm{mod}}(s\omega) = \left(\frac{\delta t}{2\pi^{1/2} s}\right)^{1/2} \hat{\psi}(s\omega) = H(\omega) e^{-(s\omega-\omega_0)^2/2} \tag{4.2}$$

where s is the wavelet scale, which is almost equivalent to period T [*Torrence and Compo*, 1998], δt is the data sample interval, ω_0 is the nondimentional frequency, which is taken to be 6 [*Torrence and Compo*, 1998], and $H(\omega)$ is the Heaviside step function: $H(\omega)$=1 if ω>0, $H(\omega)$=0 otherwise. Using this "corrected" wavelet function, our forward-modeling tests show that the amplitude of the wavelet transform no longer biases towards the longer period features. This correction is very important for our purpose because it will prevent any bias towards the larger scale oscillations when extracting the dominant waves. Two more advantages of this corrected wavelet function are: First, the wavelet amplitude does not depend on the resolution of the data (δt) because δt has been cancelled out in Equation (4.2). This resolution independency allows comparison of the wavelet amplitude between data sets with different resolutions. Second, the wavelet amplitude is equivalent to the amplitude given by Fourier transform. Essentially, the new wavelet transform can give an accurate estimate of the wave amplitude. As an example, the wavelet amplitude spectra of the temperature relative perturbation time series at 90 km on 28–30 June 2014 are shown in Figure 4.4a. Several peaks are clearly shown: A dominant one with a period of 7.5 h and another two with periods of 6.5 h and 3.4 h. The value of each peak in the spectrum correctly represents the peak amplitude of each corresponding oscillation. The peak amplitude of the 7.5-h wave is 7.0%, while the peak amplitude of the 6.5-h and 3.4-h waves are 4.8% and 5.0%, respectively. It also demonstrates that the 6.5-h wave dominates in the first ~10 h of the temperature measurements, after which the 3.4-h wave dominates for the next ~20 h and

the 7.5-h wave becomes dominant for the remainder of the temperature measurements. This result agrees with the observations in Figure 4.2.

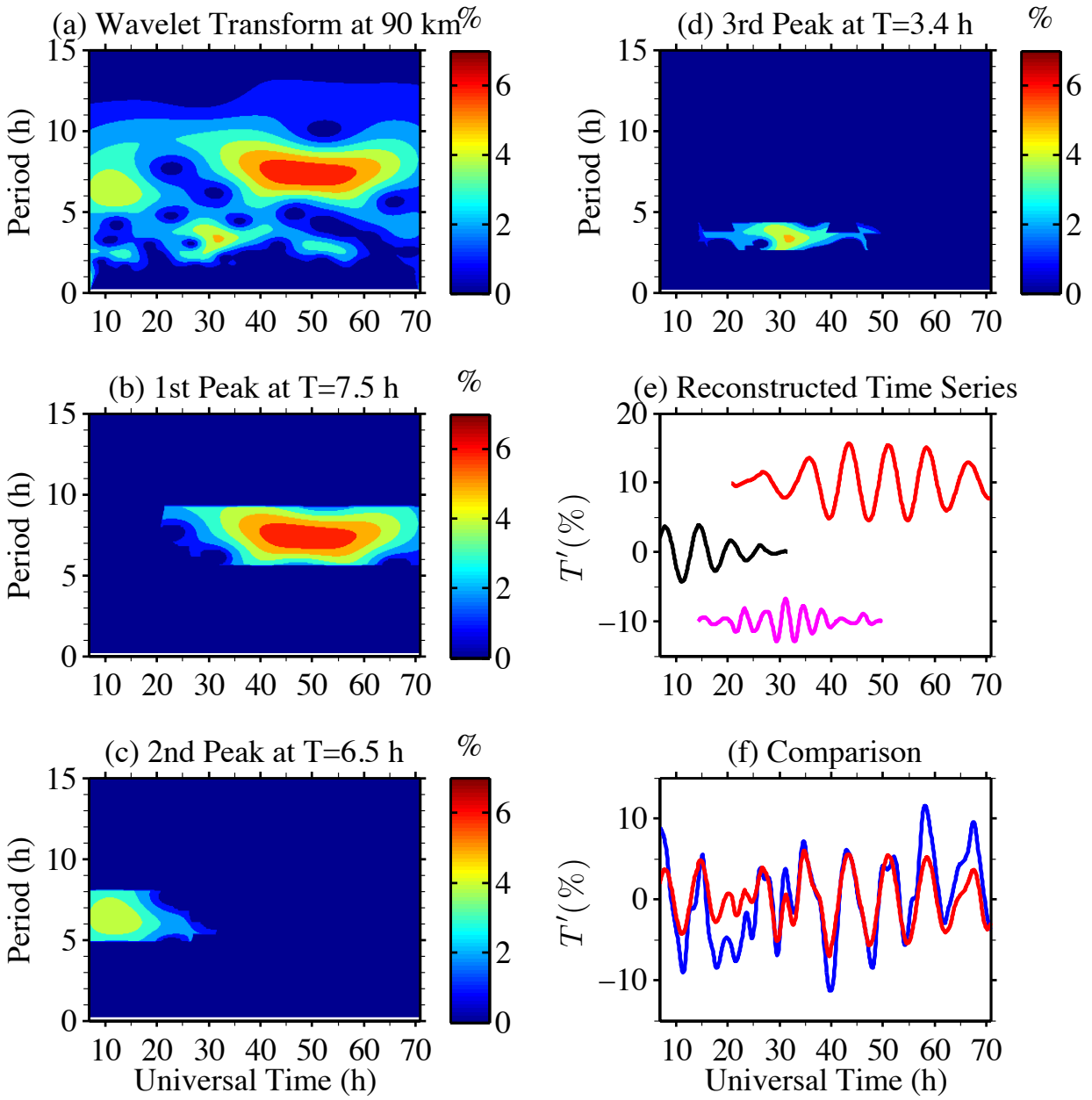

Figure 4.4. Example of the Morlet wavelet amplitude spectra of relative temperature perturbations at 90 km obtained on 28–30 June 2014 and extractions of wave packets. (a) Amplitude of wavelet spectrum. (b)-(d) Three identified peaks (at ~7.5, ~6.5, and ~3.4 h) and their extensions in the wavelet amplitude spectrum. (e) Reconstructed relative perturbations from each peak extensions around ~7.5 h (red), ~6.5 h (black), and ~3.4 h (magenta). Each line plot is

offset by 10%. (f) Comparison between the sum of three reconstructed perturbations (red) and the original temperature perturbation (blue).

To extract the perturbations induced by individual waves and characterize their wave parameters, we first search for local maxima $|W(t_{max}, T_{max})|$ in the amplitude spectrum. Then, for each of these maxima, we scan the surface of $|W(t, T)|$ around (t_{max}, T_{max}) to identify an extended region about the peak. This extended region about the peak is defined as the region in which the amplitude $|W(t,T)|$ monotonically descends from $|W(t_{max}, T_{max})|$ to where the amplitude either drops below a threshold (W_{th}) or begins to increase. For this study, we define a threshold of W_{th} = 2%. Using this method, the major peaks at periods T~7.5 h, T~6.5 h, and T~3.4 h and their corresponding extensions were identified in the wavelet amplitude spectrum, as shown in Figure 4.4b–4.4d. Then, the complex wavelet transform coefficients ($W(t_n,T_j)$) within each peak extension were recorded and reconstructed back to the time domain by summing the real part of the wavelet transform over all scales [*Torrence and Compo*, 1998]:

$$x_n = \frac{\delta j \delta t^{1/2}}{C_\delta \pi^{-1/4}} \sum_j \frac{\Re\{W(t_n, s_j)\}}{s_j^{1/2}}, \tag{4.3}$$

where x_n is the reconstructed time series at t_n, C_δ = 0.776 for Morlet (ω_0 = 6), and δj represents the sampling spacing of the scales. The reconstructed, relative temperature perturbations from each wavelet peak extension are shown in Figure 4.4e. As can be seen, each reconstructed time series is quasi-monochromatic, and their peak amplitudes agree well with the wavelet spectra. Another feature of the reconstructed time series is that they have wave packet-like shapes in the time domain, which matches a character of gravity waves, i.e., being intermittent. This will be further discussed in section 4.4.1. Finally, in order to further validate this method, these three reconstructed time-series are summed to compare with the original data in Figure 4.4f. The results show good agreement with the original time series in general, and better agreement can be

achieved if more peak extensions are included in the reconstruction (not shown here). These extra peak extensions include the 10.6-h wave shown in Figure 4.4a and Figure 4.5e and waves with periods longer than 15 h not shown in Figure 4.4a.

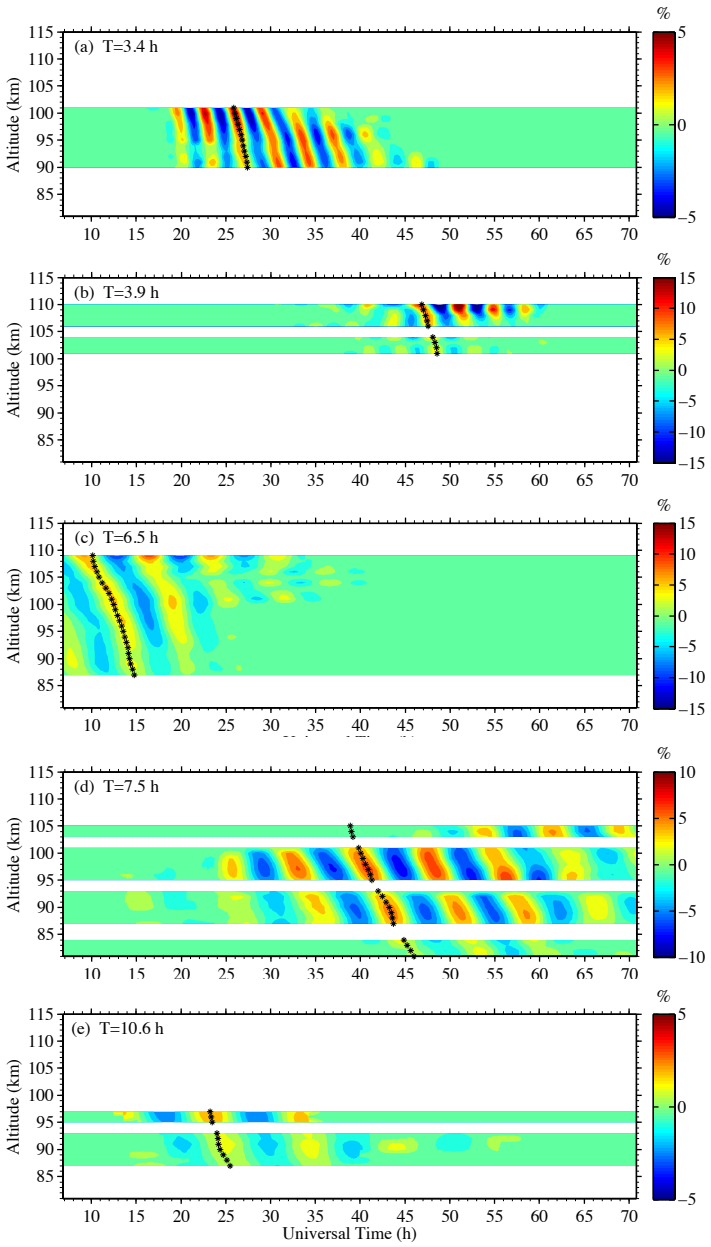

Figure 4.5. Wavelet reconstructed relative temperature perturbations of five wave events with periods of (a) 3.4 h, (b) 3.9 h, (c) 6.5 h, (d) 7.5 h, and (e) 10.6 h during 28–30 June 2014. Black asterisks on each contour plot mark the derived average hot phase line for each wave event.

4.3.2 Periods and Life Span of Five Wave Events

The above method can only be used to extract wave packets from a 1-D time series. However, since atmospheric waves propagate in both time and space, we need to extract the dominant waves in the 2-D (both time and altitude) domain. In order to do this, 1-D wave packets with similar periods (within ±0.5 h), but detected at different altitudes, are grouped into one 2-D wave packet. For each lidar observation, we can extract several dominant 2-D wave packets, each of which is called a "wave event". Only the wave events with vertical coverage larger than 4 km were selected for future analysis. We make this selection for the following two reasons. First, oscillations with no vertical coherence, perhaps due to noise or false detection by the wavelet transform, will be excluded from the analysis. This spatial scrutiny ensures that each wave event is a real atmospheric wave that travels in both time and space. Second, the spatial examination also helps us to study how wave characteristics change in a relatively large range of altitudes.

Using the above method, five wave events are identified for the ~65 h lidar run during 28–30 June 2014 and the extracted 2-D perturbations are shown in Figure 4.5. The mean period of each wave event is obtained by averaging the peak periods over the height range where the event is present. These five wave events have mean periods of T~7.5 h, T~6.5 h, T~3.4 h, T~10.6 h and T~3.9 h, respectively. Each wave event shows coherent, downward phase lines and a consistent period across altitude—the characteristics of quasi-monochromatic gravity waves. These wave events all show 'come-and-go' features (with a wave-packet-like 'envelope' of amplitudes), instead of constant amplitudes. Their occurrences also overlap with each other. As stated in Section 4.1, if we regard these wave events as a group of waves with periods ranging between 3 and 10 h, then this wave group is perpetual. The total life span of each major wave

event is defined as the span from the start of the appearance of the wave at any altitude until the last disappearance of the wave at any altitude. The results for the life spans of five wave events during this case are shown in Figure 4.6. The wave packet of period T~7.5 h is the most persistent wave event and its life span is nearly 60 hours in our observation, ~90% of the entire observation period. The other dominant wave events also last long (>30 h).

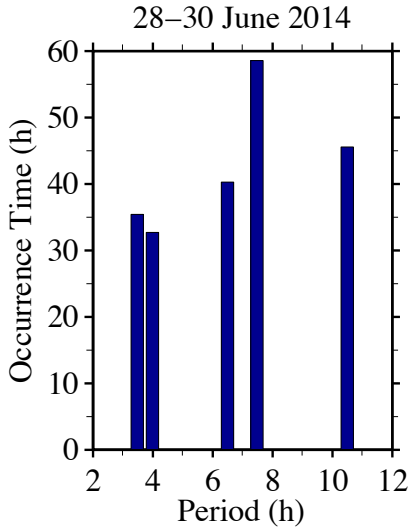

Figure 4.6. Life spans (in hours) of five wave packets identified from the wavelet analysis are plotted against their observed periods for 28–30 June 2014.

The presence of such persistent and long duration waves in the lidar data is astonishing. We may be able to make several inferences from this. Either the horizontal wavelengths of the waves are very long, or the sources producing these 3–10 h waves are persistent, or both. Future searches for wave sources should keep this observational fact in mind. Another interesting result is that four waves with periods of 7.5, 6.5, 3.4 and 10.6 h occur simultaneously around 20–30 UT in Figure 4.4a with comparable wave amplitudes. This explains why the second white dashed line from the left in Figure 4.3 does not follow any single wave, but is an average over multiple waves.

4.3.3 Phase, Vertical Wavelength and Vertical Phase Speed

Phases and vertical wavelengths are important for understanding the nature of waves. For example, if the waves are of tidal origin then they should have a relatively fixed phase. If the waves are normal modes, their vertical wavelengths may be very long. After wave events were identified, we derived phases and vertical wavelengths for each wave event using the method described by *Chu et al*. [2011b]. The mean phase is defined as the universal time of maximum temperature perturbation and the derived phase profile for each wave event is plotted on each contour in Figure 4.5 as black asterisks. The same phase profile, modulo 24 h, is shown in Figure 4.7a. The derived phases are quite smooth with the obvious downward progression. The phases of the five events occur at different local/universal times.

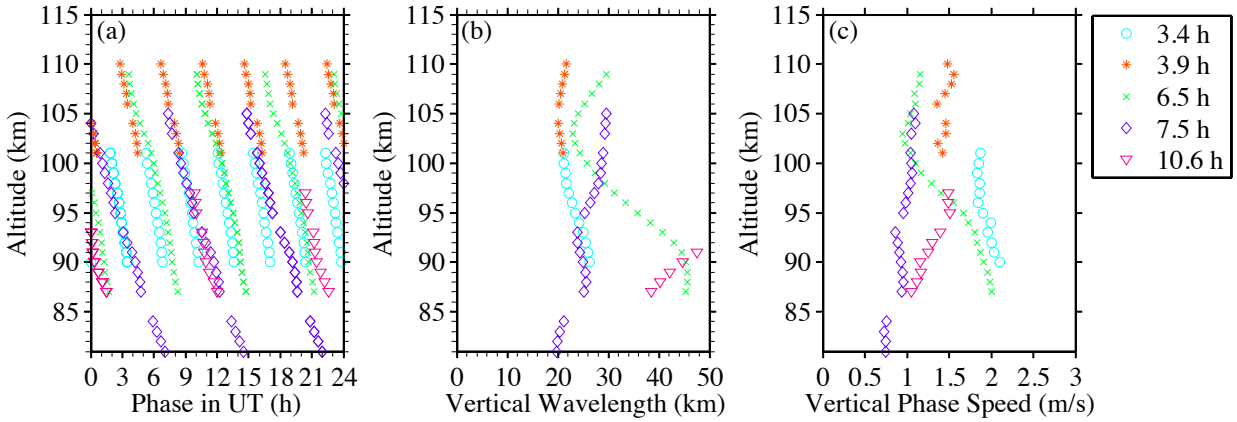

Figure 4.7. Vertical profiles of derived phase (a), vertical wavelength (b) and vertical phase speed (c) for each wave event on 28–30 June 2014. Results for each event are denoted in different colors and markers as indicated in the legend.

The vertical wavelength λ_z is derived as below

$$\lambda_z = T / (d\Phi / dz) \tag{4.4}$$

where T is the wave period, Φ is the phase expressed in universal time, and z is the altitude. Even though the periods of individual wave events are quite different, the vertical wavelengths,

as shown in Figure 4.7b, are mostly between 20–30 km, except at lower altitudes for the 6.5-h and 10.6-h waves. It appears that the 3–10 h waves in the MLT region exhibit a preference in vertical wavelength of 20–30 km. Such a result is surprising as we are not aware of any mechanisms that would limit, or select for, vertical wavelengths in the MLT region. The vertical phase speed (c_z) profiles derived from the wavelet analyses are shown in Figure 4.7c. The observed c_z of each wave is mostly around 1 m/s, comparable to the two IGWs studied by *Chen et al*. [2013] in which c_z=0.8 m/s and c_z=1.2 m/s for the 7.7-h and 5-h waves, respectively. This common c_z is also comparable to the summer case reported in *Chu et al*. [2011a] where the downward phase speed is ~0.7 m/s. We did not find any obvious or consistent trends in the c_z variations with altitude.

4.4 Statistical Studies of Wave Characteristics in June

Although several case studies have identified the 3–10 h waves as IGWs [*Chen et al*., 2012, 2013], case studies cannot provide an estimate on the occurrence frequency or representativeness of particular cases, and the results could be biased by sample selections. Moreover, it is quite difficult to make comparisons of case study results with other datasets, such as observations using different instruments at different locations and time, and with assimilated or forecast model data. Therefore, a statistical study is crucial to establish an observational basis of the properties of these 3–10 h waves that would serve as a foundation for future studies. In this section, the temperature data in June from 2011 to 2015 are used to derive several statistical wave properties. We select observation episodes longer than 12 h for the study because this allows us to accurately determine the wave periods. A total of ~323 hours of data are used in this study, and a list of the data is given in Table 4.1.

Table 4.1. Number of observations and hours of June data used in the analysis

Year	2011	2012	2013	2014	2015
Number of Observations	3	1	1	3	3
Hours	63	31.5	20.3	134.5	73.9

4.4.1 Statistical Results

Applying the same wave analysis technique as that described in Section 4.3 to the five years of June data, we identify a total of 35 wave events. Periods, life spans, phases, vertical wavelengths and phase speeds are calculated and recorded for all these wave events. We then categorize each wave event by its period. The proportion of time spans for identified wave events as a fraction of the complete observation time, plotted against the wave period, is shown in the histogram (Figure 4.8a). Figure 4.8a suggests that waves with periods of ~3.5, 5, 6, 6.5 and 7.5 h have the highest occurrence frequency, each occurring ~25–30% of the time in 323-h data examined. If we do not separate each wave event, but treat all of them as a group, the 3–10 h waves can be considered persistent. The percentage of the spectral power between periods of 3–10 h over the total spectral power was calculated. Then, the total time that this percentage exceeds 50% was counted. The results for altitudes from 80–110 km are shown in Figure 4.8b. Between 80–110 km, the 3–10 h waves have more than half of the entire spectral power for ~93% of the time. This result confirms our intuition that these waves are persistent and dominant and exhibit long lifetimes.

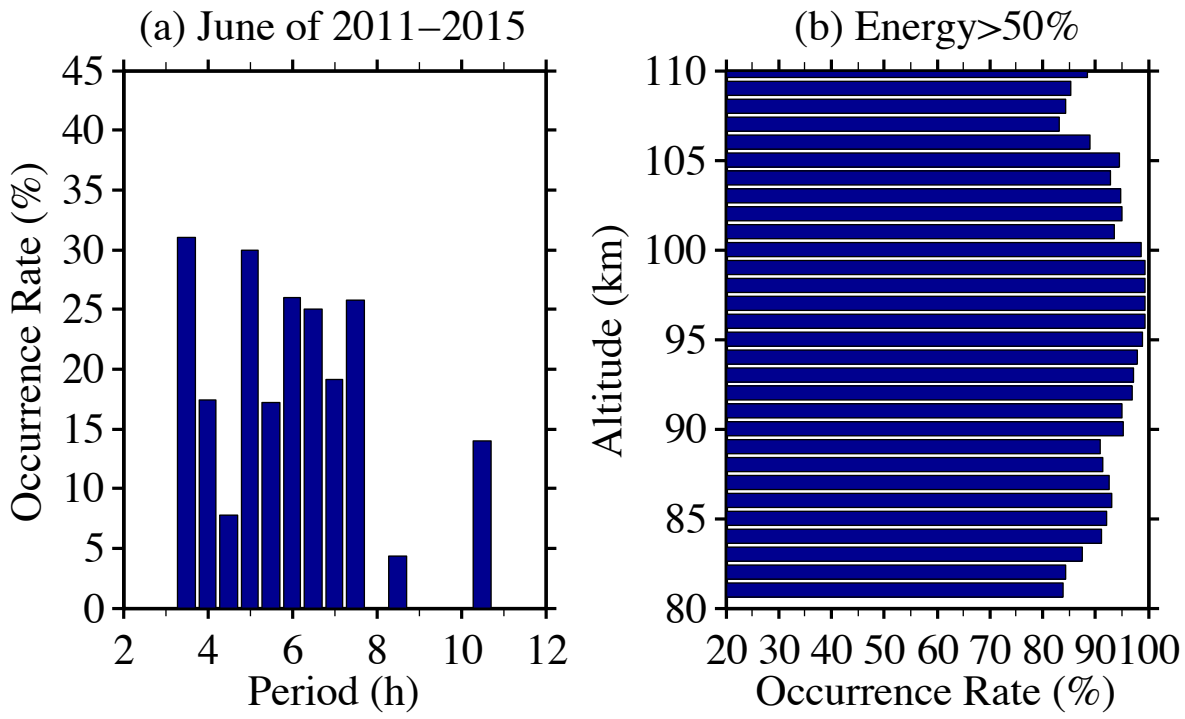

Figure 4.8. (a) Ratio of time span of a wave event over entire observation time (323.2 h) plotted against the wave period in June from 2011 to 2015. Each bin is 0.5 h wide. (b) Ratio of the time length over entire observation length when the spectral energy of the 3-10 h waves exceeds 50% of the total spectral energy. The results at different altitudes were shown. Each bin is 1 km wide.

It is worth pointing out that the persistence of these 3–10 h waves does not contradict a consensus that gravity waves are inherently intermittent. In the wave dynamics field, waves are considered to be intermittent when the amplitude of wave-induced disturbances is not constant, but varies with time scales comparable to those of the wave packets [*Hertzog et al*., 2012]. Many observational studies have shown that gravity waves are generally observed as wave packets [e.g., *Pfister et al*., 1993; *Alexander and Pfister*, 1995; *Eckermann and Preusse*, 1999; *Plougonven et al*., 2008]. This wave-packet behavior implies that the amplitudes of gravity waves vary in time and space, and that therefore, by nature, gravity waves are inherently (at least to some extent) intermittent [see *Fritts*, 1984; *Nappo*, 2002; *Vadas*, 2005; *Vadas and Fritts*, 2006; *Alexander et al*., 2010, *Hertzog et al*., 2012]. This concept of intermittency is not in

opposition to the definition of persistency in our analyses. Here, the persistency ignores variations in wave amplitude over time. In fact, our wavelet analysis and reconstruction have shown these waves to exhibit a packet-like shape in the time domain (see Figure 4.4 and 4.5 as examples), suggesting that the highly persistent 3–10 h waves we observed are intermittent as well.

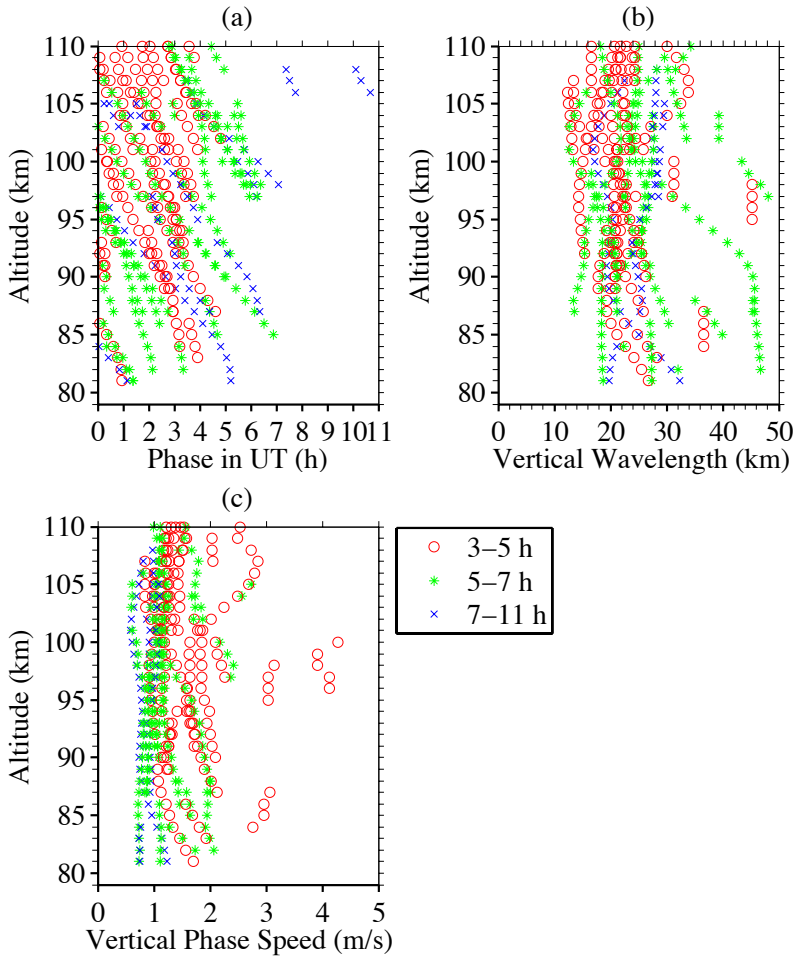

Figure 4.9. Vertical profiles of (a) phase, (b) vertical wavelength, and (c) vertical phase speed for each wave event in June from 2011 to 2015. The results are categorized in three different groups, i.e., 3–5 h, 5–7 h and 7–10 h, based on their mean wave periods, and are denoted in three different colors.

For each wave event, profiles of wave phases (defined as the UT time when the maximum temperature perturbations occurs at each altitude), vertical wavelengths and vertical

phase speeds are derived using the method described in Section 4.3.3. The wave phase modulo the corresponding wave period at each altitude is calculated and shown for five years of data in Figure 4.9a. The phases are categorized in three different groups, i.e., 3–5 h, 5–7 h and 7–10 h, based on their mean wave period, and are denoted in three different colors in order to show if there is any consistency within each group. These three groups of waves are chosen because their periods are close to some harmonics of Earth's rotational period (4, 6, and 8 h), which are also tidal wave periods. As can be seen from the figure, all of the extracted wave phases show a downward phase progression. Within each group, wave phases at each altitude are random. Figures 4.9b and 4.9c show the derived λ_z and c_z profiles, respectively. Even though the periods of the wave events are quite different, the vertical wavelengths λ_z remain around 20–30 km while the vertical phase speeds c_z remain around 0.8–2 m/s. Both λ_z and c_z profiles do not exhibit any obvious dependence on altitude, but are rather uniform throughout the MLT region. These statistical studies on the 3–10 h waves illustrate the randomness of the phases, yet uniform vertical wavelengths and phase speeds. Such information will be useful in studies of the nature of the waves and their possible sources.

4.4.2 Frequency Power Spectra and 2-D Wave Spectra of the MLT Temperatures

Even though there are numerous lidar studies on frequency power spectra in the MLT region based on Na densities [*Senft and Gardner*, 1991; *Beatty et al*., 1992; *Senft et al*., 1993; *Collins et al*., 1994, 1996; *Yang et al*., 2006], there are few studies based on temperature data in this region. One study that covers such a topic was performed by *Gardner and Yang* [1998] based on 65 hours (eight nights) of observations at a mid-latitude site in New Mexico. However, no information was given on how the spectra change with height and the length of each observation limited their study. To calculate the power spectral density (PSD), we first derive the

relative temperature perturbations from raw temperature data. Then, for each episode, the PSD is calculated at each altitude using a pre-whitening and post-coloring method. This method has been widely used and has been shown to reduce sidelobe leakage from the finite length of the rectangular window [e.g., *Tsuda et al*., 1990; *Nakamura et al*., 1993a; *Allen and Vincent*, 1995; *Dewan and Grossbard*, 2000; *Yang et al*., 2010]. However, all of the above studies have used the first-order autoregressive (AR) model (first-order differencing) with a fixed coefficient of ϕ=0.95 or ϕ=1. Among them, *Dewan and Grossbard* [2000] found the first order AR model sufficient for the data under consideration, but without giving any detailed comparison. There are many ways to pre-whiten data, all of which involve fitting an AR model to the data and transforming the signal to zero-mean white noise with a small variance and a small model estimation error [*Percival and Walden*, 1993]. In general, an *n*th-order AR model can be used to pre-whiten the relative temperature perturbations time series (*x(t)*).

$$w(t) = x(t) + \sum_{n} \phi_n x(t-n) \,, \tag{4.5}$$

where ϕ_n are estimated by solving the Yule-Walker equations, and *w(t)* is very close to white noise with variance σ_w^2 [*Brockwell and Davis*, 2013]. The order (*n*) of the AR model, which is proportional to the number of spectral peaks in the data, is chosen based on the final prediction error (FPE) criterion.

$$FPE = \sigma_w^2 \left(\frac{N+n}{N-n} \right), \tag{4.6}$$

where *N* is the length of the time series [*Brockwell and Davis*, 2013]. We have tested different orders (from first to seventh) of the AR model and found that the FPE decreases significantly from order 1 to order 4, but does not significantly decrease at higher orders. Therefore, we chose the fourth-order AR model to pre-whiten our data. The power spectral density ($PSD_w(\omega)$) of the

pre-whitened data is then calculated using the periodogram method [*Gardner and Voelz*, 1987; *Beatty et al*., 1992; *Dewan and Grossbard*, 2000].

$$PSD_w(\omega) = \frac{2\delta t}{N}\left|F_w(\omega)\right|^2 , \tag{4.7}$$

where $F_w(\omega)$ is the Fourier transform of $w(t)$. Periodogram of each episode must be calculated at the same frequency grids in order to average results of all episodes. However, each observation length is different in our datasets: the shortest length of all episodes is 12.7 h, while the longest is 64 h. Therefore, we zero-pad the shorter data to 64 h before calculating periodogram. To reduce the variability in the spectral slope estimation, *Dewan and Grossbard* [2000] suggest smoothing the raw $PSD_w(\omega)$. We use a Hamming window with FWHM of 0.25 h^{-1} to smooth $PSD_w(\omega)$. However, such smoothed spectra are not ideal for identifying spectral peaks. Therefore, in order for both peak identification and spectral slope estimation, both raw and smoothed $PSD_w(\omega)$ are post-colored to obtain the PSD of $x(t)$.

$$PSD(\omega) = \frac{PSD_w(\omega)}{\left|1 + \sum_{n=1}^{4} \phi_n \exp(-i\omega n\delta t)\right|^2} , \tag{4.8}$$

The PSD at each altitude was then vertically averaged every 5 km in order to reduce the variance in the spectra and improve accuracy [see *Gardner et al*., 1989; *Beatty et al*., 1992]. Finally, the results for each episode in June were weighted by their observation time lengths to obtain weighted-average frequency spectra. The mean raw and smoothed frequency spectra are plotted at increments of 5 km from 85–110 km for June in Figure 4.10a and 4.10b, respectively.

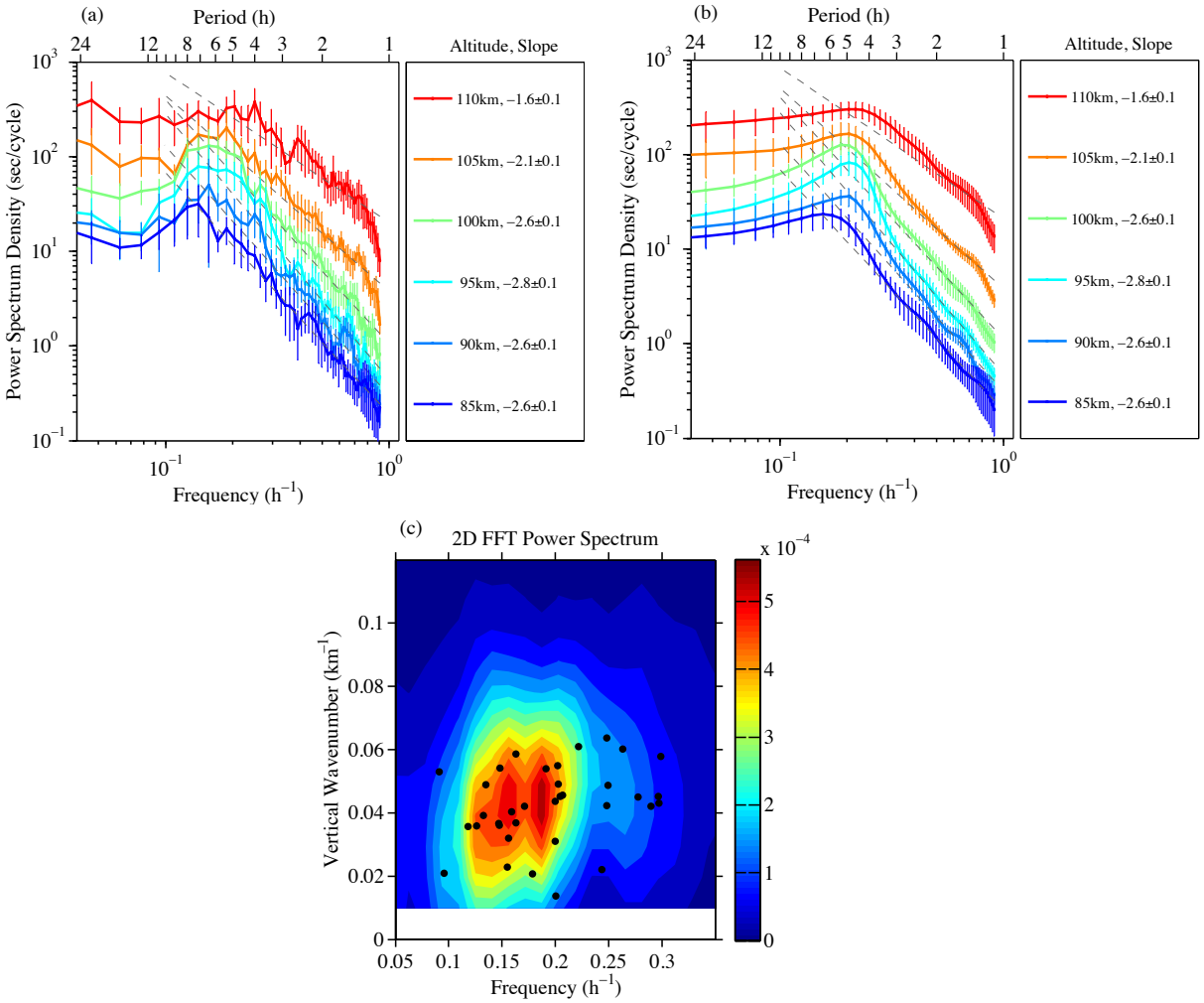

Figure 4.10. (a) Averaged raw frequency PSDs of relative temperature perturbations in June over the five years of 2011–2015 at different altitudes. Dotted lines are fittings of the power law shapes in the range of ~1–10 h. The fitted slopes are indicated in the legend. (b) Same as (a) but for smoothed frequency PSDs. (c) Averaged 2-D power spectrum of relative temperature perturbations (dimensionless) in June over the years of 2011–2015. Each black dot line on the contour marks the averaged vertical wavelength and period for each major wave event.

Results at different altitudes are denoted by different colors and are indicated in the legends of Figures 4.10a and 4.10b. In general, the magnitudes of the power spectra increase with increasing altitudes, with the PSD at 110 km being more than one order of magnitude larger than the PSD at 85 km. The absolute magnitudes of the PSDs are comparable to those in the study by *Gardner and Yang* [1998]. We mush be aware that the spectra at periods longer than the

total lengths of the original data are less reliable. Because the shortest dataset is 12.7 h, spectra longer than 12 h must be interpreted with caution. The raw spectra in Figure 4.10a show many peaks in the range of 3–10 h, but no consistent peaks at the same periods through 85–110 km. Even though the calculated spectra of the shorter data (<64 h) appear to have high frequency resolution (Δf = 1/64 h^{-1}), the true frequency resolution is lower and is limited by the shorter data length. Therefore, it is not meaningful to discuss these local peaks here. Least-square fittings of the power law spectral shape were done in the period range of 1–10 h, and dashed lines in Figures 4.10a and 4.10b denote the fitted spectra. The fitted slopes and their uncertainties at each altitude are also indicated in the legends. The fittings show the same slopes for the raw and smoothed spectra in Figures 4.10a and 4.10b, respectively. The slopes are all much steeper at lower altitudes around 85 to 100 km with an average of -2.7. However, from 95 km to 110 km, there is a clear trend in which the slopes gradually become shallower with altitude. At 110 km, the fitted slope becomes -1.6, comparable to the results in previous MLT region GW studies in which the slope was found to be either -5/3 or -2 [e.g., *Vincent*, 1984; *Senft and Gardner*, 1991; *Beatty et al*., 1992; *Nakamura et al*., 1993b; *Senft et al*., 1993; *Collins et al*., 1994, 1996; *Gao et al*., 1998; *Gardner and Yang*, 1998; *Yang et al*., 2006; *Sivakumar et al*., 2006]. However, below 110 km, the fitted slopes are significantly steeper than the results shown in previous MLT GW studies which means that, below 110 km, the 3–10 h waves at McMurdo have more excess energy than GWs of the same period band shown in other studies. Another interesting feature is that the transition frequency between the positive and negative slope regions, called the characteristic frequency ω^*, increases with increasing altitude. This trend is more obviously shown in Figure 4.10b. At 85 km, the corresponding transition period $T^* = 2\pi / \omega^*$ is ~6.7 h, gradually shifting to shorter periods with increasing altitude until T^* is ~4.5 h at 110 km. This

shift in T^* could be explained by atmospheric dissipation, since GWs with higher frequencies and, thus, larger vertical phase speeds (presuming vertical wavelengths are the same) are less susceptible to dissipation than those with the same vertical wavelengths, but lower frequencies [*Vadas and Fritts*, 2005; *Vadas*, 2007]. Processes such as wave-induced diffusion, molecular viscosity and thermal diffusion can all cause dissipation of GWs, and dissipation becomes even stronger when waves propagate above the turbopause (located at ~110 km) [*Weinstock*, 1990; *Vadas and Fritts*, 2005]. Therefore, the dominant periods of the waves become shorter as altitude increases. Finally, below ω^*, where PSD slopes are usually positive, the spectra gradually flatten as altitude increases. This is especially evident at and above 105 km in Figures 4.10a and 4.10b. Spectral leakage from the diurnal and semidiurnal "tides" with fast amplitude growth above 100 km caused by *in-situ* heating/cooling [see *Fong et al*., 2014, 2015] could have contributed to the flattening.

Vertical spatial spectra of GWs with λ_z<10 km in the MLT at McMurdo have been examined by *Lu et al*. [2015b]. They found that the spectra follow the power law for λ_z<10 km and that the mean spectral slope ($-p$) is approximately −2.26 in the winter MLT region at McMurdo. Since the 3–10 h waves tend to have longer vertical wavelengths ($\lambda_z \geq 20$ km), in order to study their vertical spatial spectra we focus on a larger vertical wavelength range. Furthermore, inspired by *Collins et al*., [1996], we examine the wavenumber and frequency dependence of the wave energy simultaneously by calculating the 2-D Fourier transform for each episode in June. The results for each episode are weighted by their observational time lengths and shown in Figure 4.10c. In order to average the spectra of episodes with different lengths and be consistent with the 1-D frequency spectra shown in Figures 4.10a and 4.10b, we use the same zero-padding method in the time domain so that padded data are 64-h long. Furthermore, for

sufficient spectral resolution in the long-wavelength part of the spectra, we also zero-pad the data to 1024 points in the vertical domain prior to the transform. Again, we must be aware that the long-wavelength parts (λ_z>35 km) of the spectra approach our vertical observation range (80-115 km). As can be seen in Figure 4.10c, generally, 2-D power spectrum has high powers at λ_z ~20–30 km across periods ~3.5–10 h. Two local peaks appear at T=5.3 h and T= 6.4 h; however, since frequency resolution of this averaged spectrum is limited by the shortest data, these peaks should be interpreted with caution. Each black dot on top of the 2-D power spectrum in Figure 4.10c is the averaged λ_z and period derived for each major wave event. Most of the derived individual wave parameters coincide well in the higher-power region of the 2-D spectrum. There is a weak positive correlation between period and λ_z, i.e., λ_z tends to increase with increasing period.

4.5 Discussion

Although several case studies, using simultaneous lidar and MF radar observations, identified some 3–10 h waves as IGWs [*Chen et al*., 2012, 2013], this is the first report to show that the 3–10 h waves are so persistent that they exist in all lidar observations, and that these waves occur year round at McMurdo. The vertical wavelengths of the 3–10 h waves we observed are quite close to that (~25 km) of the 'planetary-scale inertio gravity waves' generated by a Numerical Spectral Model [*Mayr*, 2003; *Mayr et al*., 2004]. These inertio gravity waves appear to have the largest amplitudes from late winter to spring in the polar MLT with periods between 9 and 11 h [*Mayr*, 2003; *Mayr et al*., 2004]. They are essentially the gravity mode (Class I) solutions to the classical Laplace tidal equations for the Earth's atmosphere, as discussed in the classical literature [*Longuet-Higgins*, 1968]. These simulated features capture some of the observed wave properties, but are not consistent with the larger period span (3–10 h) and all-

year-round occurrence at McMurdo. Possible identities of the 3–10 h waves, other than gravity waves, include short-period Atmospheric Normal Modes (ANMs), short-period tidal waves, and wave-wave interactions. ANMs, also called Lamb waves, were observed at the South Pole [see *Forbes et al*., 1999], and can have periods around 3–10 h and a long life span (up to several days) [*Lindzen and Blake*, 1972]. However, theoretically, ANMs have infinite λz in an isothermal atmosphere, or a long λz (at least ~80 km) in a simulated realistic atmosphere [see *Lindzen and Blake*, 1972; *Forbes et al*., 1999; *Kovalam and Vincent*, 2003]. As the predicted λz of ANMs are much longer than our observed results, the 3–10 h waves are unlikely to be ANMs. As for tidal waves, the vertical wavelengths of sub-diurnal tides are generally much larger than those of the 3–10 h waves. Theoretical calculations and model simulations performed by *Smith and Ortland* [2001] indicate that the 8-h tides have a long λz (>47 km). Other shorter-period (6-h, 4.8-h, etc.) tidal waves have an even longer λz [*Smith*, 2004]. Furthermore, from Figure 4.9a, there is no phase coherence among different wave events, indicating that the 3–10 h waves are not likely of tidal origin. The observed 3–10 h waves could be the result of wave-wave interactions. For example, based on the measurements from an array of instruments at northern high latitudes, *Wu et al*., [2002] presented revealing observations of a 10-h oscillation in the temperatures and winds in the MLT. By comparing the wave phases at different stations, a zonal wave number s = 5 was inferred. These wave properties led to the conclusion that nonlinear coupling between a semidiurnal tide and a 2-day planetary wave was likely the wave origin. However, without observations at different longitudes, we cannot explore the possibilities of such mechanisms.

As the observed 3–10 h waves are unlikely to be ANMs or tides, our current judgment is that they should be regarded as gravity waves, though we cannot rule out the possibility of wave-

wave interactions. A challenging question is then—what sources can generate such persistent gravity waves all year round? Although the winter cases may be attributed to unbalanced flow caused by the polar night jet, such a jet is unlikely to exist during the polar summer. *Mayr et al*. [2004] suggest that the planetary-scale inertio gravity waves are excited by instabilities that arise in the zonal mean circulation. Similarly, we may speculate the wave source to be an instability, but there are no clues as to the type of instability. Here we discuss what information on the source can be delineated from the statistical results.

Our frequency spectral analysis of the 3–10 h waves shows differences with the "canonical" wave spectrum, i.e., when waves are regarded as being fully damped or saturated, the PSD follows a form of m^{-p} (m is vertical wavenumber, p=3 usually) and ω^{-q} [e.g., *VanZandt*, 1982; *Dewan and Good*, 1986; *Smith et al*., 1987; *Gardner*, 1994]. Many different theories have been proposed to explain the universal wavenumber spectrum [e.g., *Dewan and Good*, 1986; *Weinstock*, 1990; *Hines*, 1991; *Gardner*, 1994], but fewer theories have been proposed to explain the universal frequency spectrum. Among these are saturated-cascade theory (SCT) [*Dewan*, 1994] and diffusive filtering theory (DFT) [*Gardner*, 1994]. Despite the differences in their mechanisms, SCT and DFT both agree that atmospheric dissipation processes, whether arising from molecular viscosity or eddy diffusion [*Weinstock*, 1990; *Gardner*, 1994], or instability and a turbulent cascade [*Dewan*, 1994], will transfer (diffuse) excess energy from the larger period waves to smaller temporal scale motions (either waves or turbulence). Therefore, it is expected that the slope of the frequency spectrum becomes shallower as it propagates away from the source region where the slope is steepest [*Gardner*, 1994]. When GWs are saturated, or fully damped, frequency spectra with a ω^{-2} or $\omega^{-5/3}$ trend are predicted from theory [*Dewan*, 1994; *Gardner*, 1994], which is supported by observations in the region where GWs were assumed

saturated or fully damped [e.g., *Senft and Gardner*, 1991; *Beatty et al*., 1992; *Senft et al*., 1993; *Gardner and Yang*, 1998]. On the other hand, a steeper slope implies that the observed wave spectrum still bears some resemblance to the source spectrum, which means that the dissipation effects have not yet changed the shape of the spectrum to a fully damped or saturated shape. This is likely the case for our data below 105 km. As the wave field propagates upward, atmospheric dissipation processes remove low frequency energy and, therefore, the observed spectrum becomes increasingly shallower than the source. This prediction matches our observation that the slopes gradually become shallower with increasing altitude. The phenomena observed at McMurdo imply that the wave source(s) of these 3–10 h wave may not be far from the MLT region, unlike at mid-low latitudes where major sources of the MLT gravity waves, such as convection, topography or tropospheric jet streams, are located in the troposphere [see *Fritts and Alexander*, 2003; *Alexander et al*., 2010]. Our results likely point to a wave source in the stratosphere, which is consistent with the speculation of the wave source for the 7.7-h wave (unbalanced flow in the polar vortex ~40 km) by *Chen et al*. [2013] in a case study. In fact, it is known that stratospheric sources are important for Antarctic gravity waves, as supported by many gravity wave studies [e.g., *Yoshiki and Sato*, 2000; *Sato and Yoshiki*, 2008; *Yamashita et al*., 2009; *Yamashita*, 2011; *Moffat-Griffin et al*., 2013; *Murphy et al*., 2014]

The universal peaks at λ_z ~20–30 km across periods ~3.5–10 h shown in the 2D-FFT results are "characteristic vertical wavelengths" that mark the transition between the source and the so-called "saturated" regimes of the spectrum [*Smith et al*., 1987]. These uniform, dominant vertical wavelengths could provide a hint as to the vertical scale of the sources because the strongest GW response tends to occur at a vertical wavelength about twice the depth of the forcing region [*Vadas and Fritts*, 2001; *Fritts and Alexander*, 2003; *Alexander and Holton*,

2004]. Using a similar heuristic argument as *Fritts and Alexander* [2003], we can estimate the approximate vertical scale of the wave sources. Since the vertical wavelength is inversely proportional to the buoyancy frequency N (equation (33) in *Fritts and Alexander*, 2003), and N in the Antarctic winter mesosphere is about 2/3 of its value in the stratosphere [*Lu et al*., 2015b], the λ_z of the 3–10 h wave in the stratosphere should, by the above argument, be ~2/3 of its MLT value, or ~16 km. Therefore, if it were a stratospheric source, the vertical scale of the forcing region might be ~8 km. This information might be useful in future studies on the wave source location, though we are aware that it is only a speculation for now.

4.6 Conclusions and Outlooks

To our knowledge, this study is the first to report the persistence of the 3–10 h gravity waves in the polar MLT region. During the last 5 years of lidar observations at McMurdo, the group of 3–10 h waves has been perpetual. That is, such waves occur on every lidar run spanning a sufficient duration, and so far we have not seen any inactive wave gap epoch in the lidar temperature data. In order to accurately quantify the lifetime and occurrence of these 3–10 h waves, we have demonstrated a new wave analysis method in a case study using ~65 h of lidar data from 28–30 June 2014 at McMurdo. A rectified wavelet function is used in a wavelet transform of relative temperature perturbations to give an accurate, unbiased estimate of the wave amplitudes for all periods in a 1-D time series. Dominant wave packets are identified through searching the amplitude contours on the wavelet power spectrum for each altitude. Vertical coherence of waves at multiple altitudes is then examined to determine the major wave events. Following this, the major wave perturbations are extracted using wavelet reconstruction. This improved wavelet function, in combination with the temporal wavelet reconstruction and some spatial scrutiny, enables us to quantify the life span, occurrence rate, and many other

properties of the waves in a systematic manner. Applying this new analysis method to all of the lidar data recorded during the month of June in the years of 2011–2015, the statistical results of wave properties, such as occurrence frequencies, periods, phases, vertical wavelengths, and vertical phase speeds, are obtained for McMurdo (77.8°S, 166.7°E), Antarctica. In general, these waves have periods of 3–10 h, vertical wavelengths of 20–30 km, and vertical phase speeds of ~0.8–2 m/s. These waves have dominant amplitudes in the MLT and extremely long lifetimes (sometimes ~60 h observed). The occurrence frequencies of these 3–10 h waves are high. Waves with periods of ~3.5, 5, 6–6.5 and 7.5 h, have the highest occurrence frequencies each occurring more than 25% of the time in 323-h of data examined. Furthermore, on average, 93% of time, the 3–10 h waves possess more than half of the spectral energy. The relatively slow vertical phase speeds and short vertical wavelengths make these 3–10 h waves very susceptible to damping in thermosphere diffusions. Therefore, the momentum flux, heat flux and atmospheric constituent flux associated with these waves have the potential to alter the mean flow, temperature structure and constituent concentrations in the Antarctic lower thermosphere.

The frequency spectra of these 3–10 h waves have also been examined using a rigorous method of "pre-whitening and post-coloring". To our knowledge, this study is the first to show how GW temperature frequency spectra evolve with altitude in the MLT region. By fitting the spectra with a power law spectral shape in the period range of 1–10 h, we find an interesting phenomenon for the 3–10 h waves at McMurdo. That is, the spectral slopes are unusually steep, with an averaged value of –2.7, below 100 km, gradually becoming shallower to –1.6 at 110 km. From this, we speculate that the source region is close to the MLT region, which points to a possible stratospheric source. The characteristic periods in the spectra show a clear trend towards shorter periods with increasing altitude. Such a variation is expected, considering that the effect

of atmospheric dissipations is to remove waves with longer periods, especially around the turbopause region. From the 2-D FFT spectra, these waves have peak powers at vertical wavelengths of ~20–30 km across periods of ~3.5–10 h. This uniform peak λ_z across the different periods might shed some light on the vertical scale of the wave sources. Many features of the 3–10 h waves challenge our understanding of gravity waves and demand deeper investigation into the sources and mechanisms for their generation, the reasons for their persistence, and their impacts on general circulation and chemical climate models. We cannot answer these important questions without further studying our Rayleigh lidar data and investigating the high-resolution global models and assimilated data sets.

CHAPTER 5

Development of Two-Dimensional Morlet Wavelet Transform Methods

5.1 Introduction

Observing and characterizing the field of atmospheric waves across various temporal and spatial scales has been, and continues to be, one of the most challenging tasks in atmospheric and space science research. Waves are the dominant mechanism for energy and momentum transport in the middle and upper atmosphere. Characterizing them is critically important to the understanding of circulation in Earth's atmosphere and ensuring the accuracy of numerical models that are used for climate prediction and weather forecasting. Advancements in remote sensing technologies in the last several decades have significantly improved observing capabilities, providing volumes of data with unprecedented coverage, precision, and temporal and spatial resolution. Efforts have been spent on analyzing the data to characterize the properties of various atmospheric waves, including gravity, tidal and planetary waves, by means of Fourier basis functions [e.g., *Manson and Meek*, 1986; *Gardner and Voelz*, 1987; *Nakamura et al*., 1993; *Harris*, 1994; *Sato*, 1994; *Forbes*, 1995; *She et al*., 2004; *Chu et al*., 2011b; *Lu et al*., 2015a]. However, because Fourier methods assume a time/space invariance of wave properties, more efforts are needed in the aspect of localization of these wave properties because, in reality, many waves are inherently intermittent and localized [*Teitelbaum and Vial*, 1991; *Sato and Yamada*, 1994; *Forbes et al*., 1995; *Alexander and Dunkerton*, 1999], i.e., wave properties such as amplitude, frequency and vertical wavenumber vary with both time and space as the wave propagates. Traditional Fourier analysis is not capable of resolving localized variations.

Windowed Fourier transforms are capable of localization, but use a fixed window width for all wave frequencies (or wavenumbers, same hereinafter) [*Daubechies*, 1992], which cannot dynamically adjust to lower or higher frequency phenomena. In contrast, the wavelet transform is able to adapt its window's temporal width to the wave spectrum, i.e., automatically narrowing at high frequencies and widening at low frequencies [*Chui*, 1992]. Therefore, wavelet analysis methods are more suitable than Fourier transform methods for analyzing real atmospheric wave phenomena.

Wavelets are a relatively new concept in applied mathematics but have gained fast development and diverse application. The term originated in the field of geophysics in the early 1980s [*Morlet et al*., 1982a, 1982b] to describe seismic signals. Since then, significant advances in wavelet theory have been made. Wavelets have been used in quantum physics [*Grossmann and Morlet*, 1984; *Paul*, 1984], applied mathematics [*Daubechies*, 1988; *Meyer and Salinger*, 1993], signal processing [*Mallat*, 1989], image compression [*Wickerhauser*, 1994], atmospheric turbulence [*Farge*, 1992], ocean wind waves [*Liu*, 1994] and many other fields. Their advantage, in addition to the localization capability, is the existence of many compactly supported orthonormal wavelet bases which allow signal decomposition into a minimal number of coefficients, enabling data compression [*Daubechies*, 1988; *Meyer*, 1989]. The 1-D wavelet has been popular for middle and upper atmospheric data analysis [e.g., *Sato and Yamada*, 1994; *Zhang et al*., 2001; *Zink and Vincent*, 2001b; *Pancheva et al*., 2002]. Recent lidar observations in Antarctica, assisted with the 1-D Morlet wavelet data analysis technique, have led to the discoveries of persistent gravity waves in the mesosphere and lower thermosphere (MLT) [*Chen et al*., 2016b]. These findings are significant, as they provide a rare insight into a poorly understood part of Earth's atmosphere.

While the 1-D wavelet analysis applied in *Chen et al*. [2016b] was instrumental in characterizing these persistent waves from time series at each individual altitude, discerning each wave feature across both the time and space domains had to be performed manually; a situation that is not desirable when handling large amounts of observational data. In addition, wave packets may travel "obliquely" and exist in different regions at different times. Such intrinsic features require spectral analyses of waves in more than one dimension simultaneously. Many remote sensing instruments deliver two-dimensional (2-D) data. For example, ground-based lidars and radars record range-resolved atmospheric data over time at a fix location, yielding 2-D data in the range-time domains. Ground-based imagers, and many satellite sensors, obtain 2-D spatial images. Unfortunately, extracting intermittent/localized 2-D wave packets is still a common technical challenge in analyzing atmospheric and space data. Therefore, the 2-D wavelet transform is recognized as an important tool for the autonomous processing of atmospheric data. Although some studies have used the 2-D wavelet transforms [*Farge et al*., 1990; *Kumar*, 1995; *Wang and Lu*, 2010; *Kaifler et al*., 2015], no 2-D Morlet wavelet code suitable for geophysical applications is publicly available, and the mathematical formalism to quantify the absolute power spectrum of the 2-D wavelet transforms is lacking due to arbitrary normalization.

The main goal of this study is to develop a 2-D wavelet transform methodology that can be made available to the public for the analysis of large amounts of atmospheric and space science datasets. The formalism of the 2-D wavelet transform is established with detailed mathematical derivations. During application of the 1-D wavelet technique in *Chen et al*. [2016b], problems were found in the publicly available 1-D wavelet code provided by *Torrence and Compo* [1998], i.e., wavelet power spectra are distorted or biased in favor of large scales or

low frequencies, as *Liu et al*. [2007] pointed out previously for atmosphere and ocean science applications. To overcome the issue, corrections were made to the code in *Chen et al*. [2016b], but no mathematical explanations were offered. In this study we provide the mathematical and physical basis for the correction to the 1-D wavelet in Section 5.2 to illustrate the procedure for constructing a wavelet mathematically and to offer physical meaning to the wavelet spectrum. We then expand this procedure to the development of 2-D wavelet transforms in Section 5.3. In order to apply the transform to real observational data, the continuous wavelet transforms must be discretized. This study provides equations for the discrete-time continuous wavelet transforms in Sections 5.2 and 5.3. Two-dimensional wavelet reconstruction, important in extracting wave packets, is given in Section 5.4. To demonstrate the appropriateness of 2-D wavelet methods in Section 5.5, we apply the 2-D wavelet transform to real lidar data taken during 28–30 June 2014 at McMurdo Station and compare our results to the 1-D results shown in *Chen et al*. [2016b]. Application of the 2-D wavelet transform to lidar data from May and July 2014 is shown to help in the characterization of persistent gravity waves in Antarctica. Finally, we conclude this study by highlighting the scientific utility of the 2-D wavelet transforms.

5.2 Correction for commonly used one-dimensional power spectrum

The 1-D Continuous Wavelet Transform (CWT) is commonly defined as [*Mallat*, 1999]

$$\begin{aligned} W_{f\psi}(s,t) &= \int_{-\infty}^{+\infty} f(t')\frac{1}{\sqrt{s}}\psi^*\left(\frac{t'-t}{s}\right)dt' \\ &= f(t)\otimes\frac{1}{\sqrt{s}}\psi^*\left(\frac{-t}{s}\right) \\ &= \frac{1}{2\pi}\int_{-\infty}^{+\infty}\hat{f}(\omega)\sqrt{s}\left[\hat{\psi}(s\omega)\right]^* e^{i\omega t}d\omega \end{aligned} \tag{5.1}$$

where $f(t)$ is the function of interest, $\psi(t)$ is a wavelet mother function, s is the wavelet scale (usually restricted to positive numbers), operator (*) denotes complex conjugate, operator ($\otimes$) denotes convolution, and operator ($\hat{}$) denotes Fourier transform, i.e., $\hat{f}(\omega) = \int_{-\infty}^{+\infty} f(t) e^{-i\omega t}\, dt$ and $\hat{\psi}(\omega) = \int_{-\infty}^{+\infty} \psi(t) e^{-i\omega t} dt$. The factor $1/\sqrt{s}$ is to ensure wavelets $\frac{1}{\sqrt{s}}\psi\left(\frac{t}{s}\right)$ are normalized, i.e., $\int_{-\infty}^{+\infty} \left|\frac{1}{\sqrt{s}}\psi\left(\frac{t}{s}\right)\right|^2 dt$ equals a constant and does not depend on s. Note that the second equality in Equation (5.1) is a result of the convolution theorem, i.e., the Fourier transform of a convolution is the pointwise product of Fourier transforms, applying the inverse Fourier transform $f \otimes g = F^{-1}\{F(f) \cdot F(g)\}$. Full derivation of Equation (5.1) is provided in Appendix B.1. The wavelet scale s is proportional to the window width in a dilated wavelet $\psi\left(\frac{t'-t}{s}\right)$. This property enables the wavelet "time-window" to dynamically adjust to higher or lower frequencies. The Morlet wavelet transform is provided to illustrate this feature and is defined as [*Farge*, 1992; *Meyers et al*., 1993; *Weng and Lau*, 1994],

$$\psi(t) = e^{i\omega_0 t} e^{-\frac{t^2}{2}}, \tag{5.2}$$

where $\omega_0 \geq 5$ in order to fulfill the "admissibility condition" that will be shown later in Equation (5.3) [*Farge*, 1992]. Note that some literatures include a normalization constant of $\pi^{-\frac{1}{4}}$ in their definition of Equation (5.2) in order that $\int_{-\infty}^{+\infty} |\psi(t)|^2 dt = 1$ (e.g., Kumar and Foufoula-Georgiou, 1997; Morlet et al., 1982b; Torrence and Compo, 1998). However, such constant is not a necessity in our definition here for two reasons. First, it is cancelled out if we do a forward

(Equation 5.1) and then an inverse wavelet transform (shown later in Equation (5.4)), so the value of this normalization constant will not affect the result of the reconstruction. Second, the effect of this constant to the forward wavelet transform will be accounted for later in our definition of wavelet power spectrum (Equation (5.11). Evaluating the wavelet transform given by Equation (5.1), we have $\psi^*\left(\frac{t'-t}{s}\right) = e^{-i\omega_0\left(\frac{t'-t}{s}\right)} e^{-\frac{(t'-t)^2}{2s^2}}$. The Gaussian "window" in the Morlet wavelet, $e^{-\frac{(t'-t)^2}{2s^2}}$, varies its width with the wavelet scale s, so it is adaptive to both low and high frequency waves for wave localization.

The only constraint imposed on a real wavelet function $\psi(t)$ is the so called "admissibility condition" [*Farge*, 1992],

$$C_\psi = \int_0^{+\infty} \frac{\left|\hat{\psi}(\omega)\right|^2}{\omega} d\omega < +\infty \,. \tag{5.3}$$

If $\psi(t)$ is admissible and real, the inverse wavelet transform, or wavelet synthesis, exists and is given by [Equation (4.38) in *Mallat*, 1999],

$$\begin{aligned} f(t) &= \frac{1}{C_\psi} \int_0^{+\infty} \int_{-\infty}^{+\infty} s^{-2} W_{f\psi}(s,t') \frac{1}{\sqrt{s}} \psi\left(\frac{t-t'}{s}\right) dt' ds \\ &= \frac{1}{C_\psi} \int_0^{+\infty} \int_{-\infty}^{+\infty} s^{-2} \int_{-\infty}^{+\infty} f(t'') \frac{1}{\sqrt{s}} \psi^*\left(\frac{t''-t'}{s}\right) dt'' \frac{1}{\sqrt{s}} \psi\left(\frac{t-t'}{s}\right) dt' ds \,. \end{aligned} \tag{5.4}$$

The derivation of Equation (5.4) is provided in Appendix B.2. If $\psi(t)$ is complex and $f(t)$ is real, e.g., Morlet wavelet, we should only take the real part of Equation (4) (See full derivations in Appendix B.3) [*Daubechies*, 1992]

$$f(t) = \frac{1}{C_\psi} \int_0^{+\infty} \int_{-\infty}^{+\infty} s^{-2} \Re\left[W_{f\psi}(s,t') \frac{1}{\sqrt{s}} \psi\left(\frac{t-t'}{s}\right) \right] dt' ds \,, \tag{5.5}$$

where the admissibility condition changes to

$$C_\psi = \int_0^{+\infty} \frac{\left|\hat{\psi}(\omega)\right|^2 + \left|\hat{\psi}(-\omega)\right|^2}{2\omega} d\omega = \int_{-\infty}^{+\infty} \frac{\left|\hat{\psi}(\omega)\right|^2}{2|\omega|} d\omega < +\infty \quad . \tag{5.6}$$

It is worth analyzing the physical meaning of the wavelet transform of Equation (5.1). If the variable t is time and ω is the corresponding angular frequency, then Parseval's theorem requires [*Mallat*, 1999]

$$\int_{-\infty}^{+\infty} |f(t)|^2 \, dt = \frac{1}{2\pi} \int_{-\infty}^{+\infty} \left|\hat{f}(\omega)\right|^2 d\omega \quad . \tag{5.7}$$

Equation (5.7) expresses the equality of the total energy of the signal in both time and spectral representations. Energy conservation applies to the wavelet transforms as well. The equivalent Parseval's theorem for the wavelet transform can be stated as (see full derivation in Appendix B.4)

$$\int_{-\infty}^{+\infty} |f(t)|^2 dt = \frac{1}{C_\psi} \int_0^{+\infty} \int_{-\infty}^{+\infty} \left|W_{f\psi}(s,t)\right|^2 \frac{1}{s} dt \frac{ds}{s} \quad . \tag{5.8}$$

Traditionally, the squared amplitude of the wavelet transform $|W_{f\psi}(s,t)|^2$ has been used to describe the wavelet power spectrum, as in *Torrence and Compo* [1998]. However, this definition is troublesome from a physical perspective, which can be shown in the following dimensional analysis. If the integrals in Equation (5.7) and Equation (5.8) are regarded as the total energy of signal $f(t)$, then $\left|f(t)\right|^2$ is the power, i.e., energy per unit time, while $\left|\hat{f}(\omega)\right|^2$ is the energy spectral density, i.e., energy per unit frequency. Because the right hand side of Equation (5.8) is a double-integral, $|W_{f\psi}(s,t)|^2$ is energy per unit time per unit frequency, which is power spectral density, equivalent to energy. Thus, $|W_{f\psi}(s,t)|^2$ does not represent the mean power of $f(t)$. The dimension of the signal's power ($\left|f(t)\right|^2$) equals the dimension of $|W_{f\psi}(s,t)|^2$ divided by the scale s. For a

periodic signal $f(t)$, we can show mathematically that the squared amplitude of the Morlet wavelet transform $|W_{f\psi}(s,t)|^2$ is proportional to s. Since $f(t)$ can be written as the sum of a series of cosine functions, $\hat{f}(\omega)$ can be written as a sum of Dirac delta functions.

$$\begin{aligned} f(t) &= \sum_{n=1}^{\infty} A_n \cos(\omega_n t + \varphi_n) \\ \hat{f}(\omega) &= \sum_{n=1}^{\infty} \pi A_n \left[\delta(\omega - \omega_n) e^{i\varphi_n} + \delta(\omega + \omega_n) e^{-i\varphi_n} \right] \end{aligned} \tag{5.9}$$

The squared amplitude of the Morlet wavelet transform for $f(t)$ is then

$$\begin{aligned} \left|W_{f\psi}(s,t)\right|^2 &= \left| \frac{1}{2\pi} \int_{-\infty}^{+\infty} \hat{f}(\omega) \sqrt{s} \left[\hat{\psi}(s\omega) \right]^* e^{i\omega t} d\omega \right|^2 \\ &= s \left| \frac{1}{2\pi} \int_{-\infty}^{+\infty} \hat{f}(\omega) \sqrt{2\pi} \cdot e^{\frac{-(s\omega-\omega_0)^2}{2}} e^{i\omega t} d\omega \right|^2 \\ &= s \left| \frac{1}{2\pi} \int_{-\infty}^{+\infty} \sum_{n=1}^{\infty} \pi A_n \left[\delta(\omega - \omega_n) e^{i\varphi_n} + \delta(\omega + \omega_n) e^{-i\varphi_n} \right] \sqrt{2\pi} \cdot e^{\frac{-(s\omega-\omega_0)^2}{2}} e^{i\omega t} d\omega \right|^2 \\ &= s \left| \frac{\sqrt{2\pi}}{2} \sum_{n=1}^{\infty} A_n \int_{-\infty}^{+\infty} \left[\delta(\omega - \omega_n) e^{i\varphi_n} + \delta(\omega + \omega_n) e^{-i\varphi_n} \right] \cdot e^{\frac{-(s\omega-\omega_0)^2}{2}} e^{i\omega t} \, d\omega \right|^2 \\ &= s \left| \frac{\sqrt{2\pi}}{2} \sum_{n=1}^{\infty} A_n \left[e^{\frac{-(s\omega_n-\omega_0)^2}{2}} e^{i\omega_n t} e^{i\varphi_n} + e^{\frac{-(s\omega_n+\omega_0)^2}{2}} e^{-i\omega_n t} e^{-i\varphi_n} \right] \right|^2 \end{aligned} \tag{5.10}$$

Equation (5.10) shows that $|W_{f\psi}(s,t)|^2$ is proportional to s multiplied by an oscillating term. This explains why the wavelet power calculated in *Torrence and Compo* [1998] is distorted and biased in favor of large scales or low-frequency oscillations, as pointed out by *Liu et al*. [2007] and *Chen et al*. [2016b]. To correct this bias, we divide $|W_{f\psi}(s,t)|^2$ by s and define an unbiased Morlet power spectrum as below,

$$
\begin{aligned}
P_f(s,t) &= \frac{1}{C_\psi'^2}\frac{\left|W_{f\psi}(s,t)\right|^2}{s} \\
&= \frac{1}{C_\psi'^2}\left|\frac{1}{2\pi}\int_{-\infty}^{+\infty}\hat{f}(\omega)\left[\hat{\psi}(s\omega)\right]^* e^{i\omega t}d\omega\right|^2 \\
&= \frac{1}{C_\psi'^2}\left|\frac{1}{\sqrt{2\pi}}\int_{-\infty}^{+\infty}\hat{f}(\omega)e^{\frac{-(s\omega-\omega_0)^2}{2}}e^{i\omega t}d\omega\right|^2
\end{aligned}
\tag{5.11}
$$

Note that this expression for the power spectrum was not rigorously derived from Equation (5.8). It is a practical expression that still has the dimension of power but does not exhibit bias towards large s. Following the methods of *Meyers et al*. [1993], the relationship between the equivalent Fourier period and the wavelet scale can be derived. By substituting $f(t)$ with a single cosine function $A_1\cos(\omega_1 t+\varphi_1)$ into Equation (11), we find that $P_f(s,t)$ in Equation (5.11) reaches its maximum at $s=\omega_0/\omega_1=\omega_0 T_1/2\pi$, where T_1 is the period of the cosine function (see full derivation in Appendix B.5). Therefore, $s=\omega_0/\omega_n$ describes the relationship between s and the Fourier frequency ω of the wave. Further, C_ψ' in Equation (5.11) can be chosen such that the wavelet power at $s=\omega_0/\omega_1$ equals the signal's mean power (averaged squared amplitude, $\frac{1}{T}\int_0^T|f(t)|^2dt=\frac{1}{2}A_1^2$). Therefore, we obtain $C_\psi'=\sqrt{\pi}$.

For application to a real world signal that is sampled at discrete times, the continuous wavelet transform of such a discrete signal becomes,

$$
\begin{aligned}
W_{f\psi}(s,n) &= \sum_{n'=0}^{N-1} f[n']\frac{1}{\sqrt{s}}\psi^*\left[\frac{n'-n}{s}\right]\Delta t \\
&= \frac{1}{N}\sum_{k=0}^{N-1}\hat{f}\left[\frac{2\pi k}{N\Delta t}\right]\sqrt{s}\left[\hat{\psi}[s\frac{2\pi k}{N\Delta t}]\right]^* e^{i\frac{2\pi kn}{N}}
\end{aligned}
\tag{5.12}
$$

The discretization of t and ω is as follows: $t = n\Delta t$, where n=0, 1, 2…N-1 and $\omega = 2\pi k/N\Delta t$, where k=0, 1, 2…N-1. Function $f[n]$ is $f(t)$ sampled at discrete times $t = n\Delta t$. (Note that the brackets used in this study denote the discrete functions.) Once the wavelet is selected, we choose a set of scales s. For convenience, we can write s at level j as base 2 exponentials [*Torrence and Compo*, 1998]:

$$s_j = s_0 2^{\frac{j}{J}}, \quad j = 0,1,2,3,4,... \tag{5.13}$$

where s_0 is the smallest resolvable scale, usually $2\Delta t$, j is an integer representing the level number, and J is the number of levels per octave. The discretized version of Equation (5.11) is

$$P_f(j,n) = \left| \frac{1}{N} \sum_{k=0}^{N-1} \hat{f}\left[\frac{2\pi k}{N\Delta t}\right] \sqrt{2} e^{\frac{-\left(2^{j/J} s_0 \frac{2\pi k}{N\Delta t} - \omega_0\right)^2}{2}} e^{\frac{2\pi i k n}{N}} \right|^2 \tag{5.14}$$

where the discrete Fourier transform is defined as $\hat{f}[k] = \sum_{n=0}^{N-1} f[n] \exp(-\frac{i2\pi nk}{N})$.

To demonstrate the improvements of our method, we compare the above defined wavelet power spectrum result with that using the method in Torrence and Compo (1998) and the Matlab wavelet toolbox program cwtft() using an arbitrary times. The input time series is a summation of three sine waves with same amplitude of 20 K but different periods (2 h, 8 h, 24 h, respectively). The input time series and the wavelet power spectra using different methods are shown in Figure 5.1. As a result, our method calculates the correct amplitude of 20 K for each wave without any bias. In contrast, Torrence and Compo's method and the MATLAB program produce similar results, which are both biased in favor of the longer period waves.

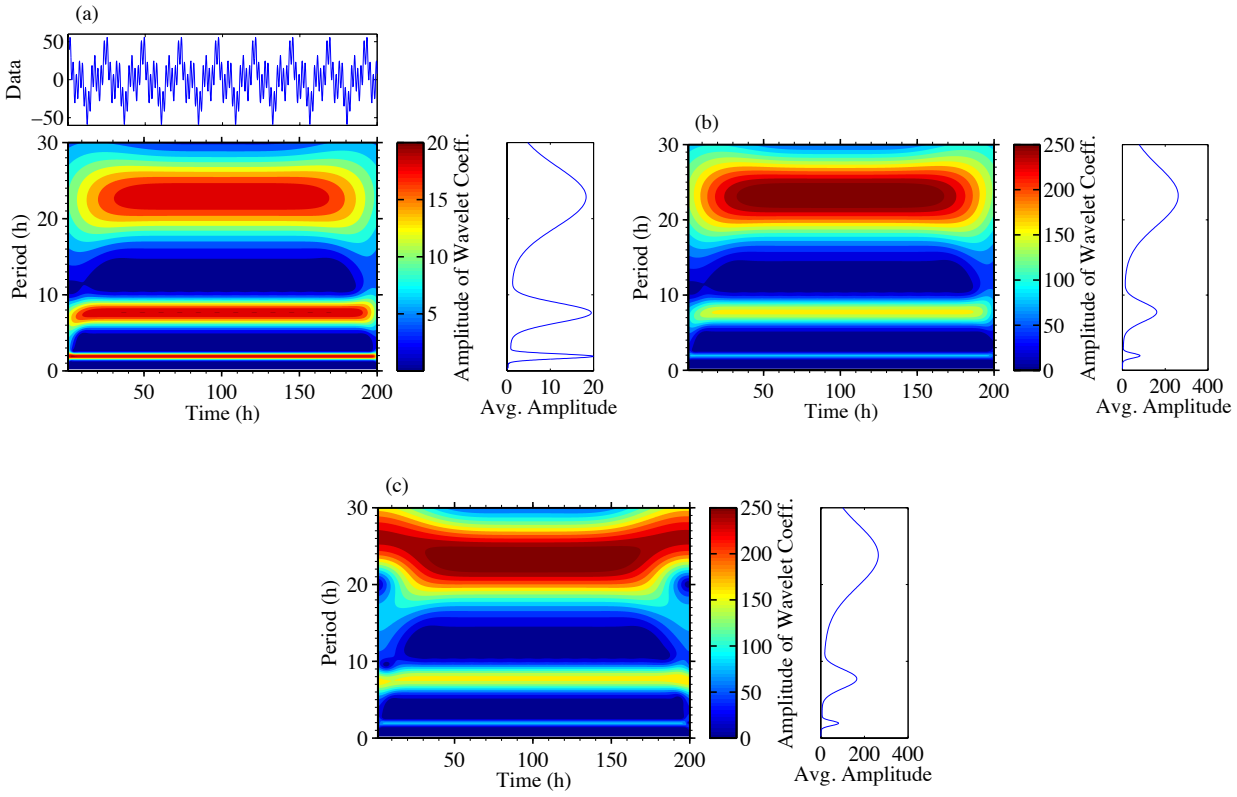

Figure 5.1. Wavelet power spectrum of an arbitrary time series using (a) the corrected wavelet power spectrum, (b) method in Torrence and Compo (1998), and (c) MATLAB program cftwt() in the wavelet toolbox. The input time series (shown in top panel of (a)) is the summation of three sine waves with same amplitude of 20 K but with different periods (2 h, 8 h, and 24 h respectively). For ease of comparison, time-averaged wavelet amplitudes are shown on the right of (a)–(c).

5.3 Two-dimensional Morlet wavelet power spectrum

The 1-D wavelet can be extended to two or more dimensions by rotation, dilation and translation [*Murenzi*, 1989]. The 2-D continuous wavelet transform is defined as

$$
\begin{aligned}
W_{f\psi}(s,\theta,\vec{t}) &= \int_{-\infty}^{+\infty}\int_{-\infty}^{+\infty} f(\vec{t}')\frac{1}{s}\psi^*\left(\mathbf{\Omega}_\theta^{-1}\,\frac{\vec{t}'-\vec{t}}{s}\right)d\vec{t}' \\
&= f(\vec{t})\otimes\frac{1}{s}\psi^*\left(\frac{-\mathbf{\Omega}_\theta^{-1}\vec{t}}{s}\right) \\
&= \frac{1}{4\pi^2}\int_{-\infty}^{+\infty}\int_{-\infty}^{+\infty} f(\vec{\omega})s\left[\psi(s\mathbf{\Omega}_\theta^{-1}\vec{\omega})\right]^* e^{i\vec{\omega}\cdot\vec{t}}\,d\vec{\omega}
\end{aligned}
\tag{5.15}
$$

where $\vec{t} = (t,z)$, with t and z representing time and spatial coordinates, $\vec{\omega} = (\omega,m)$, where ω is angular frequency and m is wavenumber. Note that $d\vec{t} = dtdz$ and $d\vec{\omega} = d\omega dm$, and operator ($\otimes$) denotes the 2-D convolution defined as $f(x,y) \otimes g(x,y) = \int_{-\infty}^{+\infty}\int_{-\infty}^{+\infty} f(x',y') \cdot g(x-x',y-y')dx'dy'$.

The rotation matrix $\mathbf{\Omega}_\theta$ is given below for a rotation parameter $\theta \in [0,2\pi]$

$$\mathbf{\Omega}_\theta = \begin{pmatrix} \cos\theta & -\sin\theta \\ \sin\theta & \cos\theta \end{pmatrix}. \tag{5.16}$$

Eqs. (5.15) and (5.16) indicate that, in addition to expanding the dilations and translations used in the 1-D wavelet, rotations of $\vec{t}$ and $\vec{\omega}$ are introduced in the 2-D wavelet and θ denotes the rotation angle. The 2-D Morlet wavelet function is defined as follows,

$$\psi(\vec{t}) = e^{i\vec{\omega}_0 \cdot \vec{t}} e^{-\frac{|\vec{t}|^2}{2}} \tag{5.17}$$

where $\vec{\omega}_0 = (\omega_0,0)$ and, we choose ω_0 = 6 for this implementation in order to fulfill the admissibility condition as in the 1-D case (Farge, 1992). $\vec{\omega}_0 \cdot \vec{t}$ is the dot product of two vectors and $|\vec{t}|^2 = t^2 + z^2$ is the squared vector magnitude. The Fourier transform $\hat{\psi}(\vec{\omega})$ is,

$$\hat{\psi}(\vec{\omega}) = 2\pi e^{-\frac{|\vec{\omega}-\vec{\omega}_0|^2}{2}} \tag{5.18}$$

If the 2-D wavelet function is admissible, then

$$C_\psi = \int_{-\infty}^{+\infty}\int_{-\infty}^{+\infty} \frac{\left|\hat{\psi}(\omega,m)\right|^2}{\omega^2 + m^2} d\omega\, dm < +\infty \tag{5.19}$$

.

The inverse 2-D wavelet transform is,

$$f(\vec{t}) = \frac{1}{C_\psi}\int_0^{2\pi}\int_0^{+\infty}\int_{-\infty}^{+\infty}\int_{-\infty}^{+\infty} s^{-3} W_{f\psi}(s,\theta,\vec{t}') \frac{1}{s}\psi(\mathbf{\Omega}_\theta^{-1}\frac{\vec{t}-\vec{t}'}{s}) d\vec{t}' ds d\theta \tag{5.20}$$

When $f(\vec{t})$ is real, we take the real part of Equation (5.19) and restrict $\theta \in [0,\pi]$:

$$f(\vec{t}) = \frac{1}{C_\psi} \int_0^{\pi} \int_0^{+\infty} \int_{-\infty}^{+\infty} \int_{-\infty}^{+\infty} s^{-3} \Re\left[W_{f\psi}(s,\theta,\vec{t}\,') \psi(\mathbf{\Omega}_\theta^{-1} \frac{\vec{t} - \vec{t}\,'}{s}) \right] \frac{1}{s} d\vec{t}\,' ds d\theta \tag{5.21}$$

where the admissibility condition becomes

$$C_\psi = \int_{-\infty}^{+\infty} \int_{-\infty}^{+\infty} \frac{\left|\hat{\psi}(\omega,m)\right|^2}{2(\omega^2 + m^2)} d\omega\, dm < +\infty \tag{5.22}$$

.

The derivations of Equation (5.20) and Equation (5.21) are provided in Appendices B.6 and B.7, respectively. The equivalent Parseval's theorem for the 2-D wavelet transform is (for derivation, see Appendix B.8),

$$\int_{-\infty}^{+\infty} \int_{-\infty}^{+\infty} \left| f(\vec{t}) \right|^2 d\vec{t} = \frac{1}{C_\psi} \int_0^{2\pi} \int_0^{+\infty} \int_0^{+\infty} \int_{-\infty}^{+\infty} \left| W_{f\psi}(s,\theta,\vec{t}) \right|^2 \frac{1}{s^2} d\vec{t}\, \frac{ds}{s} d\theta \tag{5.23}$$

.

Following the dimensional analysis of the 1-D case, we define the 2-D Morlet wavelet power spectrum as,

$$\begin{aligned} P_f(s,\theta,\vec{t}) &= \frac{1}{C'^2_\psi} \frac{\left| W_{f\psi}(s,\theta,\vec{t}) \right|^2}{s^2} \\ &= \frac{1}{C'^2_\psi} \frac{\left| \frac{1}{2\pi} \int_{-\infty}^{+\infty} \int_{-\infty}^{+\infty} f(\vec{\omega}) s \left[\psi(s\mathbf{\Omega}_\theta \vec{\omega}) \right]^* e^{i\vec{\omega}\cdot\vec{t}}\, d\vec{\omega} \right|^2}{s^2} \\ &= \frac{1}{C'^2_\psi} \left| \frac{1}{2\pi} \int_{-\infty}^{+\infty} \int_{-\infty}^{+\infty} f(\vec{\omega}) 2\pi e^{\frac{-\left|s\mathbf{\Omega}_\theta \vec{\omega} - \vec{\omega}_0\right|^2}{2}} e^{i\vec{\omega}\cdot\vec{t}}\, d\vec{\omega} \right|^2 \\ &= \frac{1}{C'^2_\psi} \left| \int_{-\infty}^{+\infty} \int_{-\infty}^{+\infty} f(\vec{\omega}) e^{\frac{-\left|s\vec{\omega} - \vec{\omega}'_0(\theta)\right|^2}{2}} e^{i\vec{\omega}\cdot\vec{t}}\, d\vec{\omega} \right|^2 \end{aligned} \tag{5.24}$$

where $\vec{\omega}'_0(\theta) = (\omega_0 \cos\theta, -\omega_0 \sin\theta)$. Analytical relationships between parameters s, θ and $\vec{\omega} = (\omega, m)$ of the Morlet wavelet can be derived using a similar method as for the 1-D case by

substituting $f(\vec{t})$ with a 2-D cosine functions $A_1\cos(\omega_1 t + m_1 z)$. The results show that $P_f(s,\theta,\vec{t})$ will reach its maximums where $s = \sqrt{\omega_0^2/(m_1^2+\omega_1^2)}$ and $\theta = \tan^{-1}(-m_1/\omega_1)$, which describe the analytical relationships between parameters (s, θ) and (ω, m) (See full derivation in Appendix B.9). We calculate the coefficient C'_ψ by ensuring that the result of the 2-D Morlet wavelet power at corresponding peak s and θ is equal to the signal's mean power $\frac{1}{2}A_n^2$. Doing so, we obtain $C'_\psi = \sqrt{2}\pi$ for this 2-D Morlet wavelet.

For practical application to a 2-D sampled, discrete signal, the continuous 2-D Morlet wavelet transform becomes,

$$\begin{aligned} W_{f\psi}[s,\theta,n_1,n_2] &= \sum_{n_1'=0}^{N_1-1}\sum_{n_2'=0}^{N_2-1}\left\{ f[n_1',n_2']\frac{1}{s}e^{\frac{-i\left[\omega_0\Delta t(n_1'-n_1)\cos\theta-\omega_0\Delta z(n_2'-n_2)\sin\theta\right]-\left[\Delta t(n_1'-n_1)\right]^2+\left[\Delta z(n_2'-n_2)\right]^2}{s \qquad 2s^2}}\Delta t\Delta z\right\} \\ &= \frac{2\pi}{N_1N_2}\sum_{k_1=0}^{N_1-1}\sum_{k_2=0}^{N_2-1}\left\{ \hat{f}\left[\frac{2\pi k_1}{N_1\Delta t},\frac{2\pi k_2}{N_2\Delta z}\right]se^{-\frac{\left(\frac{s2\pi k_1}{N_1\Delta t}-\omega_0\cos\theta\right)^2+\left(\frac{s2\pi k_2}{N_2\Delta z}+\omega_0\sin\theta\right)^2}{2}+2\pi i\left(\frac{k_1n_1}{N_1}+\frac{k_2n_2}{N_2}\right)}\right\} \end{aligned} \tag{5.25}$$

The discretization is as follows: $t = n_1\Delta t$, where $n_1 = 0, 1, 2\ldots N_1\text{-}1$, $z = n_2\Delta z$, where $n_2 = 0, 1, 2\ldots N_2\text{-}1$. $\omega = 2\pi k_1/N\Delta t$, where $k_1 = 0, 1, 2\ldots N_1\text{-}1$, and $m = 2\pi k_2/N\Delta z$, where $k_2 = 0, 1, 2\ldots N_2\text{-}1$. As with the 1-D wavelet, we need to choose a set of s and θ. For convenience, we use the same set of s as in the 1-D case but a uniform grid for θ as below

$$\begin{aligned} s_j &= s_0 2^{\frac{j}{J}}, \quad j = 0, 1, 2, \ldots \\ \theta_l &= l\pi/L, \quad l = 0, 1, 2, \ldots, L \end{aligned} \tag{5.26}$$

The discrete version of Equation (5.24) can now be written as

$$P_f[j,l,n_1,n_2]=\left|\frac{\sqrt{2}}{N_1N_2}\sum_{k_1=0}^{N_1-1}\sum_{k_2=0}^{N_2-1}\left\{\hat{f}[\frac{2\pi k_1}{N_1\Delta t},\frac{2\pi k_2}{N_2\Delta t}]e^{-\frac{\left(\frac{2^{\frac{j}{J}}s_0 2\pi k_1}{N_1\Delta t}-\omega_0\cos(\frac{l\pi}{L})\right)^2+\left(\frac{2^{\frac{j}{J}}s_0 2\pi k_2}{N_2\Delta t}+\omega_0\sin(\frac{l\pi}{L})\right)^2}{2}+2\pi i\left(\frac{k_1n_1}{N_1}+\frac{k_2n_2}{N_2}\right)}\right\}\right|^2 \tag{5.27}$$

5.4 Two-dimensional wavelet reconstruction

We can use the wavelet reconstruction to extract the original 2-D data within a desired frequency and wavenumber band. Reconstruction provides an opportunity to study the characteristics of a 2-D wave packet. Note that in mathematics the wavelet analysis and synthesis refer to the transform and inverse transform of wavelet, respectively. *Farge* [1992] has pointed out that the synthesizing wavelet function used in the inverse wavelet transform (the latter $\psi(t)$ in Equation (5.4)) could be very different from the analyzing wavelet function (the first $\psi^*(t)$ in Equation (5.4)). We can even choose a delta function $\delta(t)$ to reconstruct the signal. In order to do so, the constant C_ψ needs to be redefined. In a 1-D wavelet, if $f(t)$ is real and $\psi(t)$ is a Hermitian function (i.e., its complex conjugate is equal to the original function $\psi(t) = \psi^*(-t)$, as with the Morlet wavelet),

$$\begin{aligned} f(t) &= \frac{1}{C_\delta}\int_0^{+\infty}\int_{-\infty}^{+\infty} s^{-2}\Re\left[W_{f\psi}(s,u)\right]\frac{1}{\sqrt{s}}\delta\left(\frac{t-u}{s}\right)du\,ds \\ &= \frac{1}{C_\delta}\int_0^{+\infty}\Re\left[W_{f\psi}(s,t)\right]\frac{1}{\sqrt{s}}\frac{ds}{s} \end{aligned} \tag{5.28}$$

where

$$C_\delta = \int_{-\infty}^{+\infty} \frac{\hat{\psi}(\omega)}{2|\omega|} d\omega < +\infty \quad . \tag{5.29}$$

For a 2-D wavelet as a Hermitian function, such as the 2-D Morlet wavelet,

$$\begin{aligned} f(\vec{t}) &= \frac{1}{C_\delta} \int_0^{\pi} \int_0^{+\infty} \int_{-\infty}^{+\infty} \int_{-\infty}^{+\infty} s^{-3} \Re\left[W_{f\psi}(s,\theta,\vec{u})\right] \frac{1}{s} \delta\left(\mathbf{\Omega}_\theta^{-1} \frac{\vec{t}-\vec{u}}{s}\right) d\vec{u}\, ds\, d\theta \\ &= \frac{1}{C_\delta} \int_0^{\pi} \int_0^{+\infty} \Re\left[W_{f\psi}(s,\theta,t)\right] \frac{1}{s} \frac{ds}{s} d\theta \end{aligned} \tag{5.30}$$

where

$$C_\delta = \int_{-\infty}^{+\infty} \int_{-\infty}^{+\infty} \frac{\left|\hat{\psi}(\omega,k)\right|}{2\sqrt{\omega^2+k^2}} d\omega\, dk < +\infty \quad . \tag{5.31}$$

The discretized versions of the 1-D wavelet reconstruction Equation (5.28) and the 2-D wavelet reconstruction Equation (5.30) are

$$f[n] = \frac{1}{C_\delta} \sum_{j=0}^{J} \frac{\Re\left\{W_{f\psi}[j,n]\right\}}{2^{\frac{j}{2J}} \sqrt{s_0}} \cdot \frac{\ln 2}{J} \tag{5.32}$$

$$f[n_1,n_2] = \frac{1}{C_\delta} \sum_{l=0}^{L} \sum_{j=0}^{J} \frac{\Re\left\{W_{f\psi}[j,l,n_1,n_2]\right\}}{2^{\frac{j}{J}} s_0} \cdot \frac{\pi \ln 2}{JL} \tag{5.33}$$

To derive C_δ for a discrete wavelet function, *Torrence and Compo* [1998] substituted $f[n]$ in Equation (5.32) with a time series of a δ function, such that $\delta[n] = 1$ at $n = 0$. Since the Fourier transform of $\delta[n]$ has the uniform spectrum $\hat{\delta}[k] = 1$, we reconstruct Equation (5.32) at $n = 0$ to obtain C_δ for the 1-D wavelet reconstruction

$$C_\delta = \frac{1}{\delta[0]} \sum_{j=0}^{J} \frac{\Re\left\{W_{f\psi}[j,0]\right\}}{2^{\frac{j}{2J}}\sqrt{s_0}} \cdot \frac{\ln 2}{J} = \sum_{j=0}^{J} \Re\left[\frac{1}{N}\sum_{k=0}^{N-1} \sqrt{2\pi} e^{\frac{\left(2^{j/J} s_0 \frac{2\pi k}{N\Delta t} - \omega_0\right)^2}{2}}\right] \cdot \frac{\ln 2}{J} \tag{5.34}$$

By substituting a 2-D time series $f[n_1, n_2] = \delta[n_1, n_2]$ into Equation (5.33), we obtain C_δ for the 2-D wavelet reconstruction

$$C_\delta = \sum_{l=0}^{L}\sum_{j=0}^{J} \Re\left[\frac{1}{N_1 N_2}\sum_{k_1=0}^{N_1-1}\sum_{k_2=0}^{N_2-1} 2\pi e^{\frac{\left(\frac{2^{\frac{j}{J}} s_0 2\pi k_1}{N_1\Delta t} - \omega_0 \cos(\frac{l\pi}{L})\right)^2 + \left(\frac{2^{\frac{j}{J}} s_0 2\pi k_2}{N_2\Delta t} + \omega_0 \sin(\frac{l\pi}{L})\right)^2}{2}}\right] \cdot \frac{\pi \ln 2}{JL} \tag{5.35}$$

5.5 Applications to extracting two-dimensional wave packets from lidar data

In this section, we apply our two-dimensional wavelet analysis and synthesis methods to the lidar data collected from McMurdo, Antarctica. Besides the wavelet transform, inverse wavelet transform, and reconstruction methods discussed above, we will also demonstrate how to identify the major wave peaks and determine their extension from the 2-D wavelet analysis results, a key step to extracting wave packets. The data used here were taken by the University of Colorado lidar group during the McMurdo lidar observational campaign that has been active since December 2010. An upgraded Fe Boltzmann/Rayleigh temperature lidar [*Chu et al*., 2002; *Wang et al*., 2012] is operated from Arrival Heights Observatory (77.83ºS, 166.67ºE) through a joint effort between the United States Antarctic Program (USAP) and Antarctica New Zealand (AntNZ) [*Chu et al*., 2011a]. The observations are year-round, weather permitting. Because of the Antarctic darkness, the winter lidar data contain very little solar background [*Chu et al*., 2011b]. Combined with the highest Fe layer abundance in winter [*Yu et al*., 2012], the winter months (i.e., May through August) provide the highest resolution temperature measurements

with the largest altitude coverage [*Chu et al*., 2011b; *Chen et al*., 2013]. In this paper we select three cases to demonstrate our methods. One dataset spans 28–30 June 2014 and was studied in detail by *Chen et al*. [2016b] using the 1-D wavelet analysis methods. Here, this case is used as the baseline for the comparison of the 2-D and 1-D wavelet methods. The second and third cases are from 23–24 May 2014 and 16–18 July 2014, respectively.

The raw lidar data (photon counts) were recorded with resolutions of 1 min and 48 m, from which Fe temperatures in the MLT are derived at resolutions of 0.25 h and 0.5 km, with the sampling window shifted in steps of 0.1 h and 0.1 km. Relative temperature perturbations are calculated from the raw temperature data by subtracting the dataset-mean temperature at each altitude and dividing by the mean, such that slow varying background atmosphere is removed. We then apply the 2-D Morlet wavelet transform to the relative temperature perturbations and calculate their power spectra using Equation (5.25). The result of the 2-D wavelet power spectrum is a four-dimensional (4-D) array, representing scale s, rotation angle θ, time t and altitudes z, respectively. Recall that in Section 5.3, we have derived relationships between (s, θ) and (ω, m) for a monochromatic 2-D cosine wave $\cos(\omega t + mz)$, which are $s = \sqrt{\omega_0^2 / (m^2 + \omega^2)}$, $\theta = \tan^{-1}(-m/\omega)$ and ω_0 = 6. Thus, s and θ can be converted into period T and vertical wavelength λ_z using

$$\lambda_z = \frac{2\pi s}{\omega_0 \sin\theta} \tag{5.36}$$

$$T = \frac{2\pi s}{\omega_0 \cos\theta} \tag{5.37}$$

When the signs of T and λ_z are the same, the wave phase is downward progressing; when they are different, the wave phase is upward progressing. Since it is not possible to show the 4-D

array here, we fix one of the coordinates and present the resultant 3-D array in Figure 5.2. Figure 5.2a shows the power spectrum at λ_z = 25 km, where the 3-D data is sliced by three orthogonal planes at t = 55 h in Universal Time (UT), z = 90 km, and T = 7.6 h, respectively. Note that the unit of the color bar is $(\%)^2$. Three major wave packets with periods $T \sim 7.6$ h, $T \sim 6.5$ h and $T \sim 3.4$ h, respectively, can be identified in Figure 5.2a. Figure 5.2b shows the power spectrum at T = 7.6 h, where the 3-D data is sliced by three planes at t = 55 UT, z = 90 km, and λ_z = 25 km, respectively. The peak $\lambda_z \sim 25$ km is clearly shown in Figure 5.2b. Here spectral leakage from the 6.5-h wave into this 7.5-h power spectrum is visible due to their closeness in period, but these two waves are clearly separated in time in the 2-D wavelet spectrum. Figure 5.2c is the 2-D top view of Figure 5.2a, in the unit of wave amplitude (%) showing how the wave periods change with time at z = 90 km and λ_z = 25 km. This 2-D contour plot resembles the 1-D wavelet amplitude spectra shown in Figure 4a in *Chen et al*. [2016b], which is reproduced here in Figure 5.2d. Both plots exhibit quite similar patterns of wave period spectra at z = 90 km, which verifies the capability of the 2-D wavelet transform. The 2-D wavelet amplitude in Figure 5.2c is smaller than the 1-D wavelet amplitude in Figure 5.2d. This is because the amplitude of the 2-D wavelet spectrum represents only a finite vertical wavelength band (λ_z = 25 km), which is different from the 1-D wavelet spectrum that includes contributions from all vertical wavelengths. We use 71 levels for both scale s and rotation angle θ. More levels will yield higher resolution in period and vertical wavelength in the 2-D wavelet transform, but will increase computation time. Using 71 levels of s, 10 per octave scale, and 71 levels of θ (i.e., the maximum j = 70, J = 10, and L = 70 in Equation (5.26)), the resolutions in the wavelet period and vertical wavelength are respectively ~0.5 h and 2.5 km at $T \sim 7$ h and $\lambda_z \sim 22$ km.

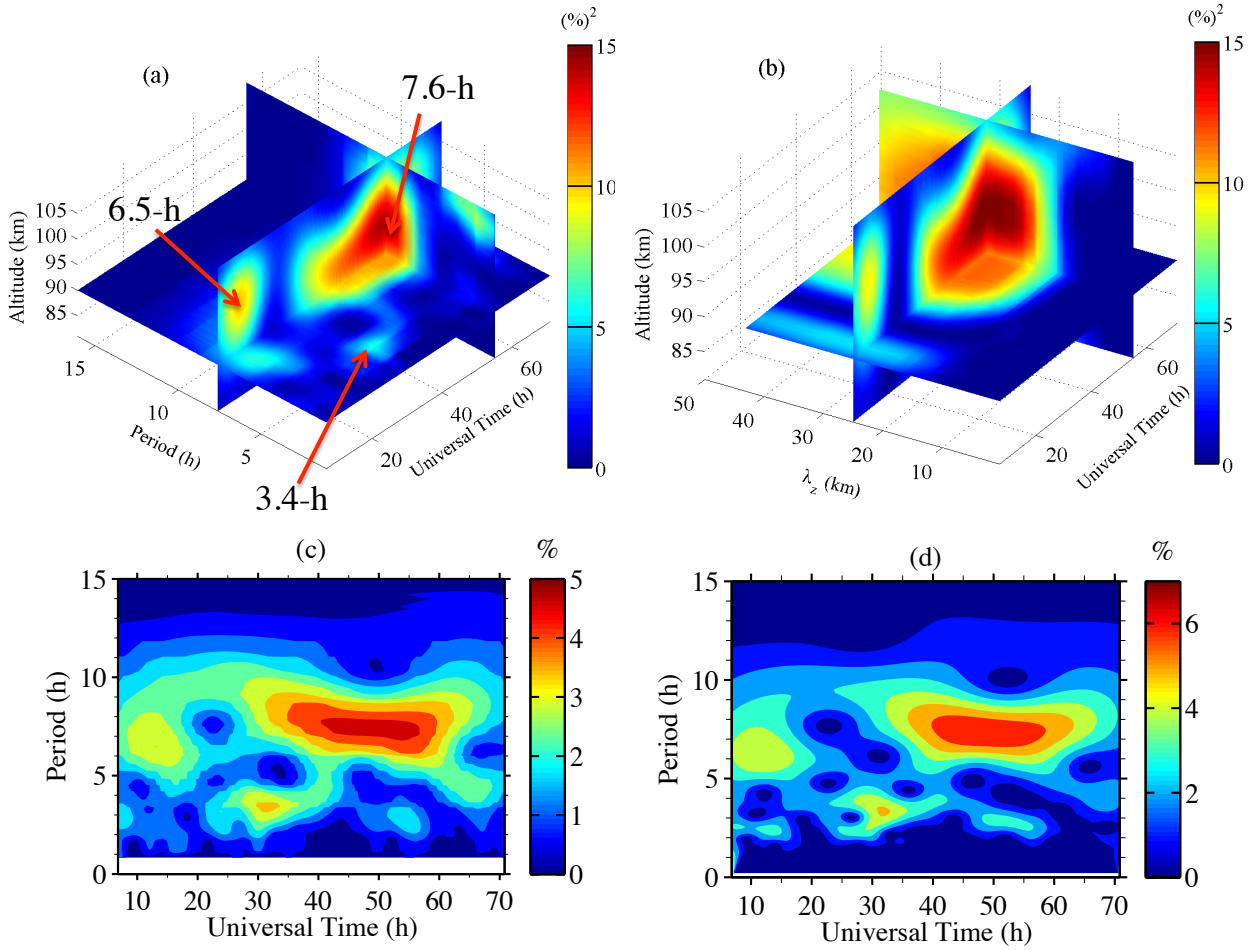

Figure 5.2. Three-dimensional illustration of the 2-D Morlet wavelet power spectrum of the relative temperature perturbations during 28–30 June 2014 at (a) λ_z = 25 km and (b) T = 7.6 h. Three slice planes in (a) are at t = 55 UT, z = 90 km, and T = 7.6 h, respectively. Locations of the three major wave packets with periods T ~ 7.6 h, T ~ 6.5 h and T ~ 3.4 h are marked with red arrows. Three slice planes in (b) are at t = 55 UT, z = 90 km, and λ_z = 25 km, respectively. (c) Two-dimensional top view of (a) showing how the wave period changes with time at z = 90 km and λ_z = 25 km. (d) One-dimensional Morlet wavelet power spectrum of the relative temperature perturbations during 28–30 June 2014 at z = 90 km (reproduced from Figure 4a in *Chen et al.* [2016b]).

We utilize a MATLAB program "imregionalmax()" in the MATLAB Image Processing Toolbox to search for regional maxima (local peaks), which have the highest value among their connected neighborhood elements. For such a 4-D array, we use 80-connected neighborhoods for the search. We sort the regional maxima according to their peak heights, then select the local peaks that have periods and vertical wavelengths within our range of interest. For this study,

these are downward phase progression waves (T and λ_z have the same sign) with periods of 3.15–12 h and vertical wavelengths of 5–100 km, respectively. We then set a threshold and select all of the local peaks that are above it. The threshold is set to one-fifth of the global maxima of the 4-D array. If two peaks occur in close proximity and have similar periods and vertical wavelengths, these two peaks are marked as one wave and their peak extensions will be combined later. After the selection of qualified local peaks in the 2-D wavelet spectrum, we then scan around those peaks for a contiguously extended region in all four dimensions that fully encapsulates the wave packet. This extended region about a peak is defined as the connected region in which the amplitude of the power spectrum monotonically descends from the peak to where the amplitude either drops below a threshold or begins to increase. In this study, we have used a threshold of 0.5% for the relative temperature perturbations. We confine each search within ±1/5 of each peak's period so that the connected peak extensions will be quasi-monochromatic in the frequency domain. After each search, the complex wavelet transform coefficients within each peak extension are recorded and this corresponding wave is removed from the next search so that the same wave element will not be recorded twice. The recorded wavelet coefficients of each peak extension are used to reconstruct the 2-D wave matrix using Equation (5.33). Several wave properties can be inferred from the wavelet coefficients of the peak extensions. First, the total lifespan can be obtained from the earliest appearance of the peak extension at any altitude to the latest appearance at any altitude. Second, the vertical wavelength and vertical phase speed can be derived as follows. We derive the vertical profile of the phase line directly from calculating the phase of complex wavelet coefficients within each peak extension. A phase of 2π corresponds to a hot phase in the relative temperature perturbations. This phase line is then tracked as a function of time and altitude. The derivatives of the phase

line in time with respect to altitude are then used to derive the vertical phase speeds and vertical wavelengths.

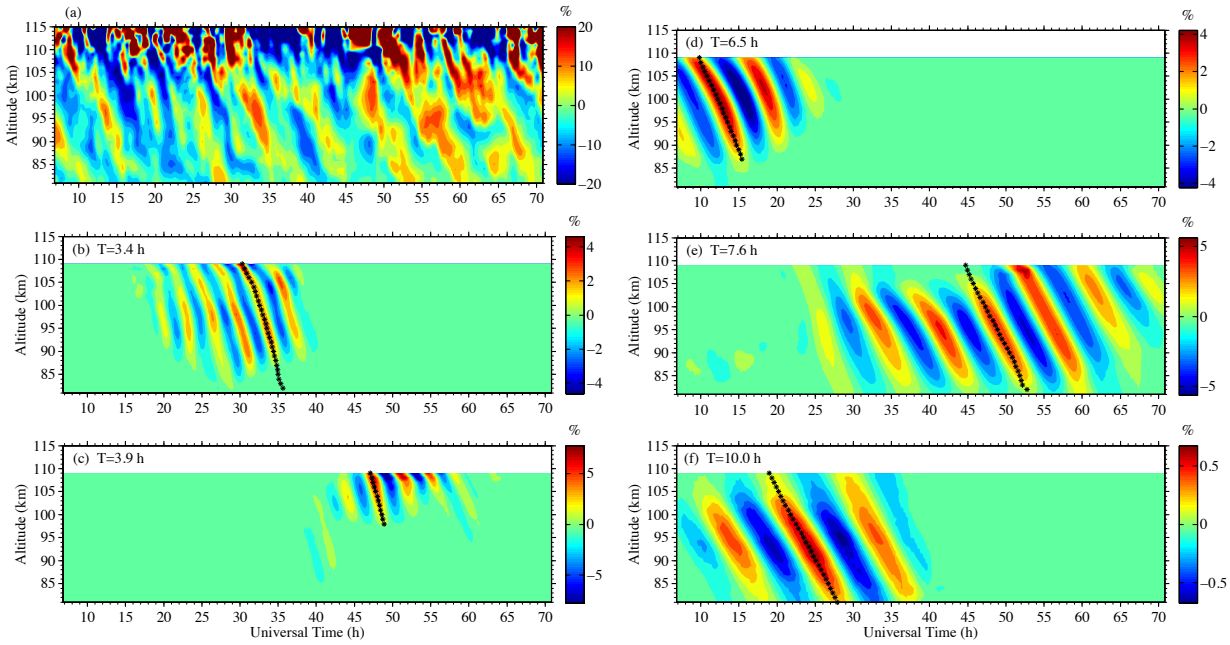

Figure 5.3. (a) Original relative temperature perturbations during 28–30 June 2014 and the 2-D Morlet wavelet reconstruction of five major wave events with periods of (b) 3.4 h, (c) 3.9 h, (d) 6.5 h, (e) 7.6 h and (f) 10.0 h.

We applied the above methods to automatically identify and reconstruct the dominant 2-D wave packets for a ~65 h lidar run from 28–30 June 2014 (raw perturbations shown in Figure 5.3a). Five wave events were identified, with the wave periods of ~3.4 h, 3.9 h, 6.5 h, 7.6 h, and 10.0 h, respectively. The reconstructed 2-D perturbations are shown in Figures 5.3b–5.3f. The phase lines of the reconstructed 2-D waves show good agreement with those of the original temperature perturbations, indicating that the reconstructions of the 2-D waves are based on real atmospheric waves. Each reconstructed 2-D wave is quasi-monochromatic in frequency and, within each wave, all of the phase lines are oriented in a similar direction. The quasi-monochromatic feature of gravity waves is common in the middle atmosphere and has been confirmed many times through observations with lidars and radars in the stratosphere [*Gardner*

et al., 1989b; *Sato*, 1994; *Sato et al*., 1997; *Zink and Vincent*, 2001a; *Nastrom and Eaton*, 2006; *Vaughan and Worthington*, 2007] and with lidars, radars and airglow imagers in the MLT [*Gardner and Voelz*, 1987; *Hall et al*., 1995; *Taylor et al*., 1995; *Collins et al*., 1996; *Walterscheid et al*., 1999; *Nicolls et al*., 2010; *Lu et al*., 2015a]. Therefore, 2-D wavelet methods are suitable for the identification of quasi-monochromatic atmospheric gravity waves in the middle atmosphere. The wave packet nature of these reconstructed waves (i.e., amplitudes varying with time) matches a key character of gravity waves, i.e., they are intermittent. Using the 2-D wavelet transform can help handle this intermittency and use it to differentiate wave packets.

Compared with the results of the 1-D wavelet in *Chen et al*. [2016b], the periods of major wave events were found to be nearly identical, except for a 10.6-h wave that was revised to 10.0 h. This difference is not critical, considering the resolution in the wavelet spectral analysis (> 0.5 at T = 10 h). The amplitude of each 2-D wave is smaller than its counterpart in the 1-D case because the 2-D wavelet is not only selective in the frequency domain, but also the spatial domain. Therefore, the amplitudes contained in the 2-D wavelet represent only a finite vertical wavelength band for the selected period band, unlike the 1-D wavelet reconstruction that includes contributions from all vertical wavelengths and even waves with an upward phase progression. The selectivity in the spatial domain is an advantage of the 2-D wavelet and yields a more accurate reconstruction of the 2-D wave packet. The lifespan of each 2-D wave is shown in Figure 5.4a. Compared to *Chen et al*. [2016b], the lifespans of the 3.9 h and 7.6 h waves in this analysis are slightly longer, while lifespans of the 3.4 h, 6.5 h and 10.0 h waves are found to be marginally shorter. Due to the 2-D wavelet method's selectivity in the spatial domain, we believe that the 2-D wavelet results are more accurate. Also, due to this selectivity, estimates of the vertical wavelengths are less biased than those from the 1-D case. The vertical wavelengths, as

shown in Figure 5.4b, range between 20 and 30 km, except for the 3.4 h wave at upper altitudes. Compared with the results in *Chen et al*. [2016b], the new results show significant improvement in the estimation of the vertical wavelengths for the 6.5 and 10.0 h waves. The vertical phase speeds shown in Figure 5.4c range mostly between 1–2 m/s, comparable to *Chen et al*. [2016b].

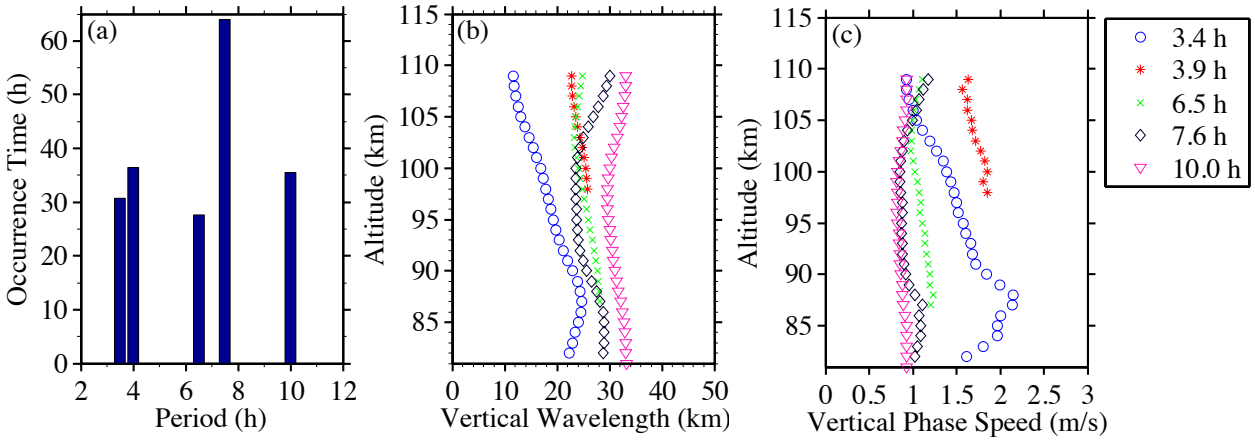

Figure 5.4. (a) Life span and vertical profile of (b) vertical wavelength and (c) vertical phase speed for each wave event on 28–30 June 2014 derived from the 2-D Morlet reconstruction. Results for each event are denoted in different colors and markers as indicated in the legend.

We also applied the 2-D wavelet analysis and reconstruction to the ~37 h and ~45 h lidar runs of 23–24 May 2014 and 16–18 July 2014 (raw relative temperature perturbations shown in Figures 5.5a and 5.7a, respectively). For both lidar datasets, three wave events were identified automatically and reconstructed using the above methods. Figures 5.5b–5.5d show the extracted wave packets of 23–24 May 2014, with periods of ~3.2 h, ~4.5 h and ~6.3 h, respectively. There are two types of temperature phase lines: two shorter-period (3.2-h and 4.5-h) waves show more vertical phase lines, while the 6.3-h wave shows more oblique phase lines. The derived lifespans, vertical wavelengths, and vertical phase speeds are shown in Figures 5.6a–5.6c. The vertical phase speed of the 6.3-h wave is < 0.5 m/s, indicating that it is more susceptible to atmospheric dissipation than the other two waves, which have shorter periods and faster phase speeds [*Vadas*

and Fritts, 2005; *Vadas*, 2007]. The phase speed of the 3.2-h wave exhibits a large variation with altitude, which could be the result of a more variable background wind condition. Figures 5.7b–5.7d show the extracted wave packets of 16–18 July 2014 with periods of ~3.6 h, ~4.8 h, and ~7.8 h, respectively. As with the May case, this case also shows two types of temperature phase lines, with the longer period wave exhibiting more oblique phase lines. The derived lifespans, vertical wavelengths, and vertical phase speeds for the July case are shown in Figures 5.8a–5.8c. The phase speeds, as with the June case, exhibit fewer variations with altitude. In both the May and July cases, the phase lines of the reconstructed 2-D waves generally show good agreement with the phase lines of the original temperature perturbations. May and July cases show more dynamical wave field structures than the June case. These results indicate that, even in the same winter season, there may be significant month-to-month variability in Antarctic MLT gravity wave activity.

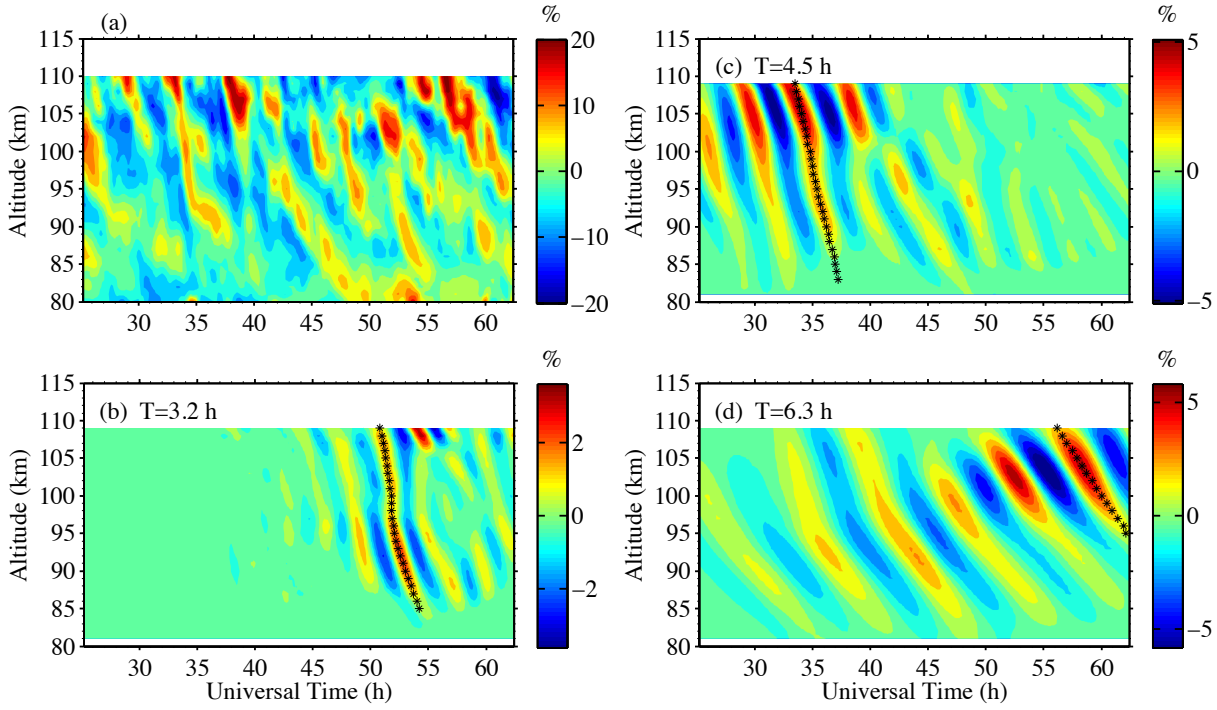

Figure 5.5. (a) Original relative temperature perturbations during 23–24 May 2014 and the 2-D wavelet reconstruction of three major wave events with periods of (b) 3.2 h, (c) 4.5 h, (d) 6.3 h.

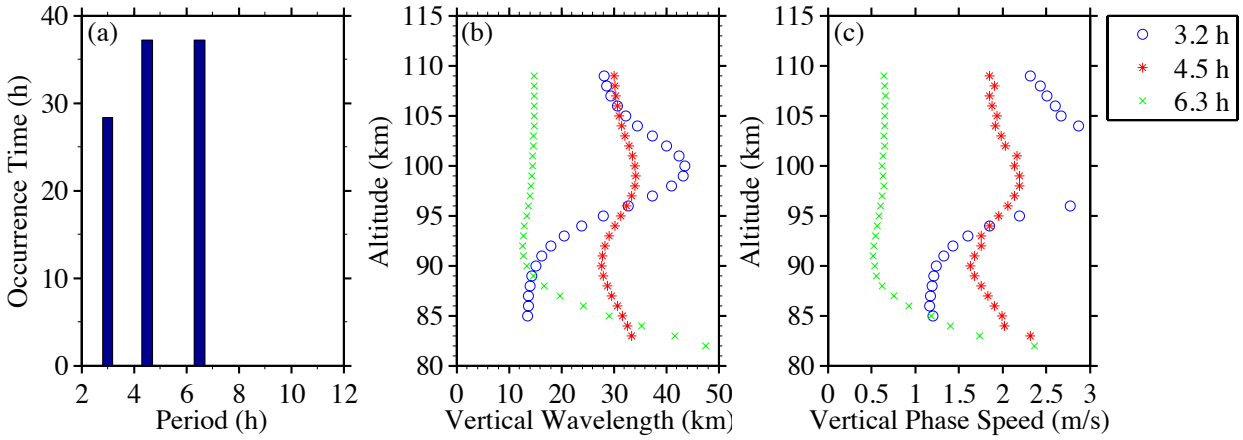

Figure 5.6. (a) Life span and vertical profile of (b) vertical wavelength and (c) vertical phase speed for each wave event on 23–24 May 2014 derived from the 2-D Morlet reconstruction. Results for each event are denoted in different colors and markers as indicated in the legend.

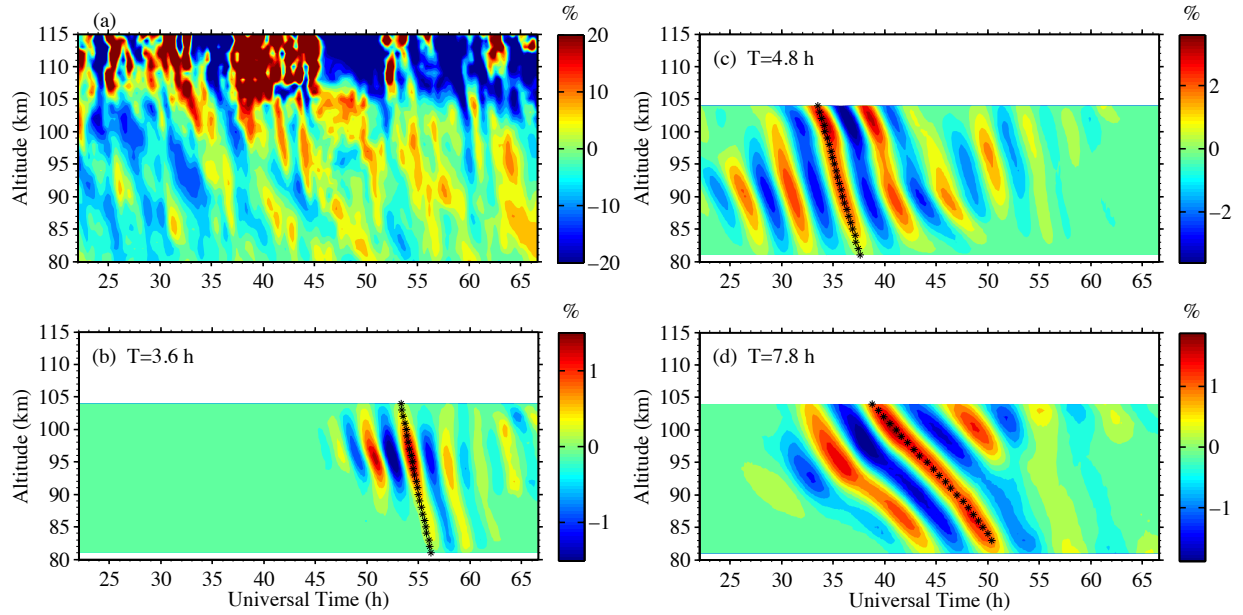

Figure 5.7. (a) Original relative temperature perturbations during 16–18 July 2014 and the 2-D wavelet reconstruction of three major wave events with periods of (b) 3.6 h, (c) 4.8 h, (d) 7.8 h.

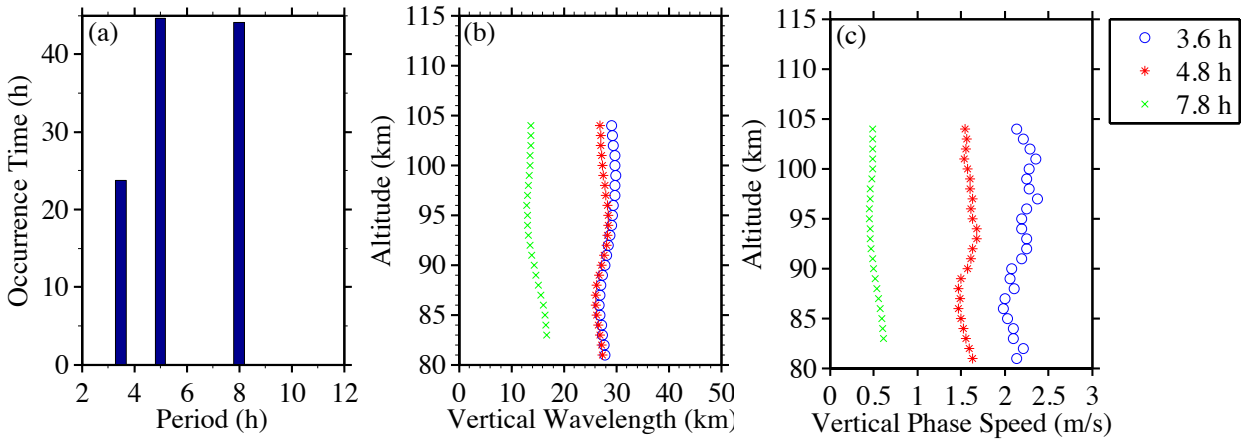

Figure 5.8. (a) Life span and vertical profile of (b) vertical wavelength and (c) vertical phase speed for each wave event on 16–18 July 2014 derived from the 2-D Morlet reconstruction. Results for each event are denoted in different colors and markers as indicated in the legend.

5.6 Conclusions and Outlook

We have developed a 2-D Morlet wavelet transform methodology for automatic extraction of quasi-monochromatic 2-D wave packets from 2-D datasets. The mathematical formalism of the 2-D Morlet wavelet analysis and synthesis is established with a detailed mathematical derivation. Discretization of the transform is provided so that the 2-D Morlet wavelet transform methodology can be realized in computer codes for applications to analyzing large amounts of atmospheric and space science data. The steps of the methodology are summarized as follows. The 2-D Morlet wavelet transform is applied to 2-D data by computing the wavelet convolution in the frequency domain, as in Equation (5.25). The amplitude of the transform is used to calculate the power spectrum, as in Equation (5.27). Local maxima in the power spectrum are then automatically identified and are selected based on their periods and vertical wavelengths. The transform coefficients that are the contagious extensions of the selected local peaks are used to reconstruct the 2-D wave packets, as in Eqs. (5.33) and (5.35). The time span of the contagious extension is the lifespan of the wave packet. Vertical

wavelengths and vertical phase speeds of each wave are derived from the phase, which is calculated from the complex wavelet transform coefficients.

The 2-D Morlet wavelet methods have been applied to three lidar datasets obtained in the winter of 2014 at McMurdo, Antarctica. The results in the June case are largely similar to those obtained using the 1-D wavelet transform in *Chen et al*. [2016b], but show significant improvement on the estimates of vertical wavelengths and phase speeds. This agreement verifies the validity and capability of the 2-D wavelet methods. The results in May and July provide additional evidence to confirm our conclusions in *Chen et al*. [2016b] that these inertia-gravity waves are persistent and dominant, and exhibit lifetimes of multiple days in winter. If we regard these wave events as a group of waves with periods ranging between 3 and 10 h, then this wave group is perpetual. The three cases in the same winter show different gravity wave features, suggesting the month-to-month variability in gravity wave activity in the Antarctic MLT. As a future work, the 2-D wavelet methods will be used to analyze large amounts of lidar data to further explore this month-to-month variability. Our results demonstrate that the 2-D Morlet wavelet analysis and reconstruction methods can faithfully extract wave packets with the desired quasi-monochromatic features. We have demonstrated the utility of 2-D wavelet methods to extracting gravity waves that are inherently intermittent. The advantage of using the Morlet wavelet, compared to other wavelets (such as the Halo and Mexican hat wavelets), lies in the straightforward relationship between s, θ and λ_z, T, and the capability of providing phase information that can be used to derive wave properties such as vertical wavelength and phase speed.

Despite the success of the 2-D wavelet transform and reconstruction as demonstrated above, there is still room for improvement. First, it is necessary to investigate the sensitivity of

the 2-D wavelet to measurement uncertainties. For example, when using Fe as a tracer to measure temperature, the errors are largest at the upper and lower boundaries of Fe layers due to the lower signal to noise ratio (SNR). Therefore, measurement uncertainties at upper and lower boundaries can cause false detection of a 2-D wave packet. One solution to this is to weight the raw data by the inverse of their errors prior to the wavelet transform. Nevertheless, effects induced by the measurement uncertainty are not significant since, in the current study, we have selected lidar data with high SNRs. Further efforts are also needed in the analysis regarding errors induced by the wavelet transform itself. The second issue with extracting atmospheric waves from the relative temperature perturbations using the 2-D wavelet transform is that it favors waves occurring at higher altitudes. The exponential decay of atmospheric density with altitude causes the atmospheric wave amplitude to increase with altitude. This feature makes the extraction of wave packets biased towards the waves at higher altitudes since their amplitudes are larger than those at lower altitudes. This bias can be resolved if the raw data are weighted by the square root of the atmospheric density at each altitude.

There are many more potential applications in various science topics and fields for the 2-D Morlet wavelet methods that we have developed. For example, such methods could be used to analyze satellite images [e.g., *Gong et al*., 2015; *Zhao et al*., 2015], or airglow imager or temperature mapper data to identify 2-D gravity wave packets and estimate their momentum flux [e.g., *Bossert et al*., 2015; *Pautet et al*., 2016; *Chen et al*., 2016a; *Yuan et al*., 2016]. Furthermore, the Morlet wavelet is anisotropic and is therefore suitable to identifying quasi-plane-wave packets. However, by implementing an isotropic wavelet function such as the Halo wavelet [e.g., *Wang and Lu*, 2010], 2-D wavelet analysis and reconstruction can be used to

identify and extract ring structures in concentric gravity waves (see details in *Yue et al*., 2009) on a horizontal 2-D dataset. This is left as future work.

CHAPTER 6

Exploration of the Possible Sources of the 3–10 h Waves

6.1 Introduction

In previous chapters we have qualitatively discussed the nature of the 3-10 h waves, and we conclude that these waves are most likely to be inertia-gravity waves. Besides inertia-gravity waves, there are other possibilities existing: tidal waves, atmospheric normal modes (Lamb waves), or the planetary scale inertio-gravity waves. Since different types of waves will usually have different types of generation mechanisms and wave sources, unraveling the nature of the persistent 3-10 h waves will guide us in searching the wave sources.

Large-scale waves such as tides, planetary waves, or atmospheric normal modes usually dominate and appear endless in the temperature and wind measurements the MLT region at mid- to low-latitudes. These waves are dominant because their wave sources are the strongest driven forces in the atmosphere such as solar radiation, instability and topography, or their modes are in resonance with Earth's atmosphere. The forcings of these large-scale waves are usually continuous and coherent, and therefore these waves often appear to be endless. On the other hand, for gravity waves (including inertia-gravity waves), since their driven forces are often smaller than those large-scale waves, their appearances are usually buried beneath their counterparts. However, our observations of the dominant and persistent gravity waves in the Antarctic MLT cause a mystery. What is the strong forcing that generates these dominant gravity waves? What are the inexhaustible wave sources for these persistent waves? These two questions are indeed mysteries if these waves are gravity waves. However, if they are not gravity waves,

then both of the previous questions are no longer mysterious. Therefore, a more fundamental question to ask is – what is the nature of these persistent 3-10 h waves? Therefore, we need to investigate how likely they can be tides, normal modes, or planetary-scale inertio gravity waves before exploring on the wave sources. We start by investigating such possibilities using an idealized atmospheric model based on classical theory. Then, we explore the wave sources by analyzing lidar temperature data, reanalysis and global circulation model data over McMurdo.

6.2 Investigation of the Wave Nature Based on the Classical Theory

Linear tidal theory begins with primitive equations in spherical coordinates that are linearized for perturbations in an isothermal atmosphere with no background winds. By assuming plane wave solutions to the primitive equations, two separated equations are deduced. One is vertical structure equation,

$$\begin{aligned} &\frac{d^2 G_n'}{dx^2} + \alpha^2 G_n' = F(x) \\ &\alpha^2 = \frac{\kappa H}{h_n} - \frac{1}{4} \end{aligned} \tag{6.1}$$

where h_n is called the equivalent depth which arises as the separation constant from the separation of variables, H is scale height, $\kappa = R/c_p \approx 7/2$, R is ideal gas constant and c_p is specific heat capacity at constant pressure. As the name implies, this equation controls the vertical structure of the wave. Note that all the symbols used hereinafter are in line with [*Forbes*, 1995] and details of the derivations are out of the scope of this thesis. $F(x)$ is the forcing term. When $F(x) \neq 0$, solutions to this equation are "forced" solutions, whose vertical wavelengths depend on h_n. When $F(x) = 0$, we obtain "free" solutions, where a single value of h_n is obtained for all free solutions.

The other equation is Laplace's tidal equation, which determines the latitudinal structure of the large-scale wave,

$$F_{s,\sigma}[\Theta_n] = \varepsilon_n \Theta_n \approx \frac{88\text{km}}{h_n}\Theta_n \tag{6.2}$$

For each wavenumber s, we can solve for h_n and frequency σ as the eigenvalues. The most popular approach is that outlined by *Chapman and Lindzen* [1970]. Those who are interested in solar and lunar tides often use this method. Basically, this method determines the equivalent depths as eigenvalues for a given forcing frequency [*Talaat*, 1999]. An opposite approach to Chapman and Lindzen's approach is to solve for frequencies after specifying a fixed h_n as presented by *Swarztrauber and Kasahara* [1985]. This is a more appropriate method for the 3-10 h wave since the 3-10 h waves' periods vary but they have similar 20–30 km vertical wavelengths. The code developed by Swarztrauber and Kasahara takes s and Lamb's parameter ε_n as input. We use the code (courtesy of Drs. Gustav Shved and Jeffrey M. Forbes) to calculate the eigenfrequencies of the Laplace's tidal equation as a function of Lamb's parameter ε_n and mode number n. Figures 6.1a–6.1c present the eigenfrequencies for zonal wavenumber s = 1, 2 and 6. The eigenfrequencies are separated in two directions (eastward and westward), which are represented by positive and negative values, respectively.

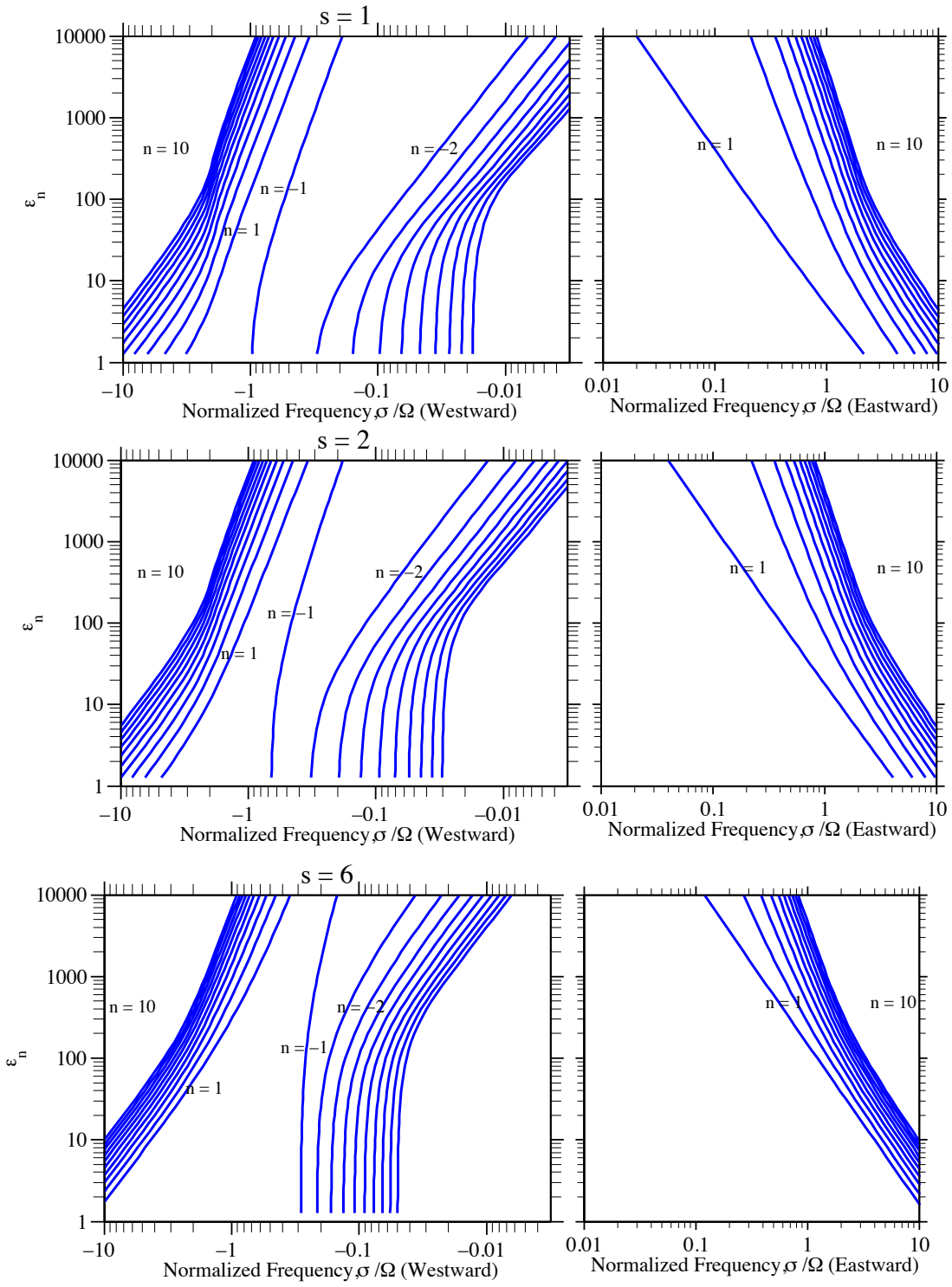

Figure 6.1. The first 10 modes ($|n|$ = 1–10) of normalized eigenfrequencies σ/Ω vs. Lamb's parameter ε_n ($\varepsilon_n > 1$) for (a) $s = 1$, (b) $s = 2$, (c) $s = 6$.

Normal modes are the free oscillation solutions of the atmosphere, which are the solutions for h_n = 10.5 km or ε_n = 8.4 of the classical Laplace tidal equations. When the period of the normal mode is shorter than diurnal period, it is often called Lamb wave. Under ideal conditions, Lamb waves have no phase change with height. However, after the effects of the nonisothermality, surface friction, eddy and molecular dissipation and ion drag are considered, *Lindzen* and *Blake* [1972] found that Lamb waves can have internal wave behavior, i.e., phase progression with height and finite lifetime (~4 days). Planetary scale inertio-gravity waves are gravity mode (Class I) solutions of the classical Laplace tidal equations. These waves propagate in both eastward and westward directions.

As we have discussed in previous chapter, the properties of the 3–10 h waves we observed are quite close to that (~25 km) of the 'planetary-scale inertio gravity waves' generated by a Numerical Spectral Model [*Mayr*, 2003; *Mayr et al*., 2004]. In their simulations, these inertio gravity waves appear to have the largest amplitudes from late winter to spring in the polar MLT with periods between 9 and 11 h, which are at the longer end of the period range of the 3–10 h waves. These waves are treated as the gravity mode solutions to the classical Laplace tidal equations. However, by carefully checking the solutions for λ_z = 20 to 30 km and periods of 3–10 h, we found that the 3–10 h waves are unlikely to have planetary scales. Figure 6.2 shows the solutions of the classical Laplace tidal equations with periods between 3–12 h, λ_z = 20 to 30 km (ε_n = ~110 to ~240), s =1 and s = 6. The solutions with such properties are all gravity mode solutions, which can propagate both eastward and westward. The period of the gravity mode decreases as the meridional wavenumber n increases and as s increases. Therefore, in order to yield a solution that has period ~6 h, high values of s (at least 6) and n (at least 20) are required.

The combination of high zonal and meridional wavenumbers hints that such gravity modes have localized scales rather than planetary scales (Dr. Jeffrey Forbes, private communication, 2015).

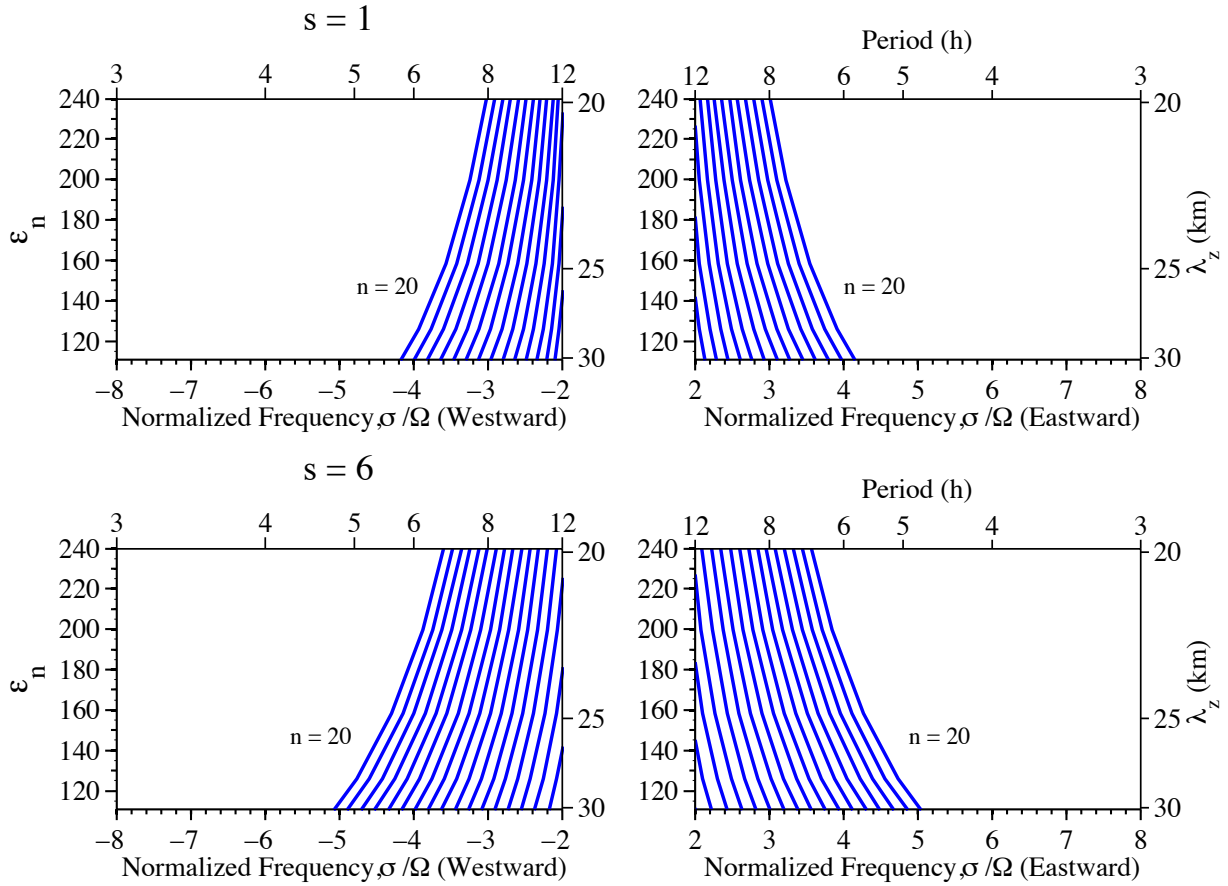

Figure 6.2. Normalized eigenfrequencies σ/Ω vs. Lamb's parameter ε_n, up to $n = 20$ with zonal wavenumber (a) $s = 1$, (b) $s = 6$.

Figure 6.3 shows the Hough functions of the gravity mode solution with period ~6–7 h, $\varepsilon_n = 156$ ($\lambda_z \sim 25$ km) and $n = 20$. The latitudinal structure suggests that the wave has larger amplitudes in temperature and winds at the Polar Regions. Since tides and normal modes are large-scale waves that are usually dominated by the lowest three or four modes (Dr. Jeffrey Forbes, private communication, 2015), our calculations using classical tidal theory have once again demonstrated that the wave nature of the 3–10 h waves is unlikely to be atmospheric tides or normal modes. The high wavenumber required to reproduce the wave properties of the 3–10 h

waves is also different from that of the planetary-scale inertio-gravity waves studied by Mayr et al.

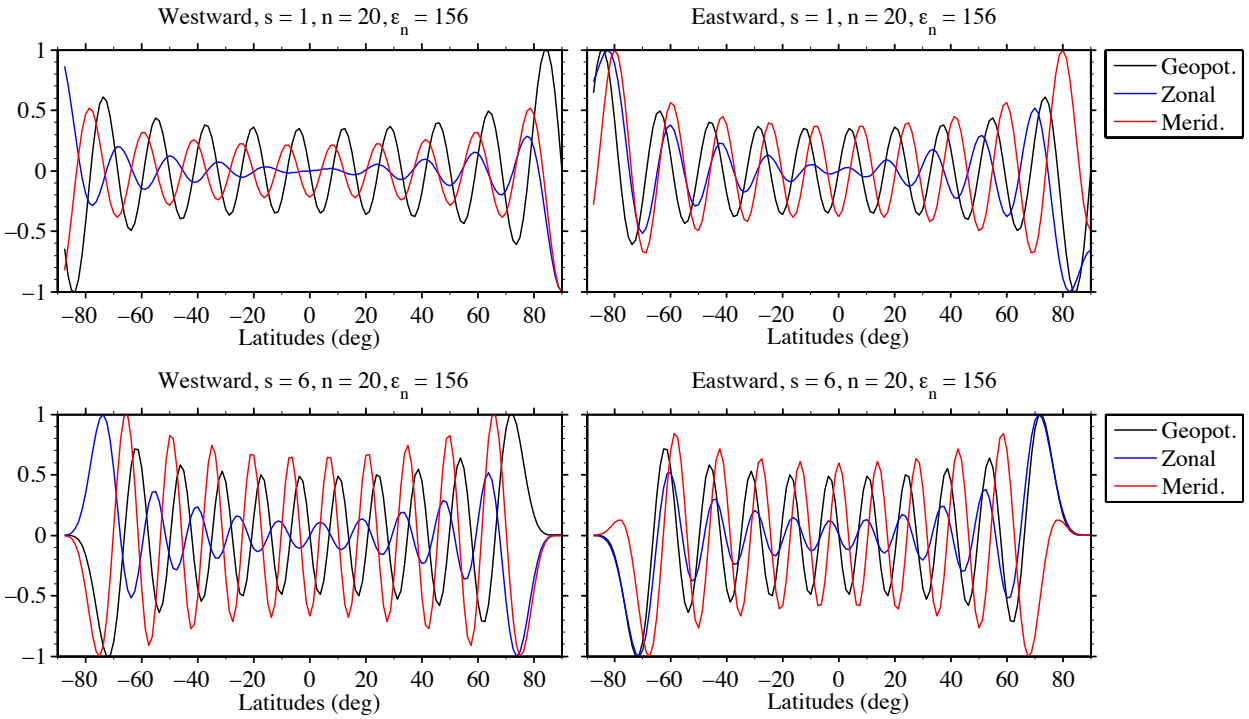

Figure 6.3. Hough functions for the geopotential (black), zonal wind (blue) and meridional wind (red) with $\varepsilon_n = 156$ ($\lambda_z \sim 25$ km) for (a) $s = 1$ (period ~7 h) and (b) $s = 6$ (period ~6 h).

6.3 Analysis of the wave sources

6.3.1 Wave propagation directions in lidar temperatures at McMurdo

The source region of the 3–10 h waves can be inferred from the vertical energy propagation direction of the wave. For an upward propagating wave, the vertical energy propagation direction is positive after it leaves the source region. However, below the source region, the same wave source generates downward propagating waves at the same time [*Vadas et al.*, 2003]. Therefore, from observational point of view, above a wave source region, the wave energy propagates upward, and below that, the wave energy propagates downward. Usually, the

energy propagation direction is hard to retrieve directly from observations. Such information is often inferred from the vertical phase progression direction of the wave since the direction of the phase is usually perpendicular to that of the energy propagation. Note that the relationship between the vertical phase progression and energy propagation is not valid if the intrinsic frequency of the wave is negative, which happens when the background horizontal wind speed is high and in the same direction as the horizontal wave propagation direction.

The 2-D FFT spectral analysis allows us to distinguish gravity waves with different directions of vertical phase progression. We then use it to infer the energy propagation directions and the altitude range of the wave source(s). Using the data on 16–18 June 2014 as an example, we first calculate the relative perturbations in the Rayleigh temperature data by first subtracting the temporal mean at each altitude and divided the mean (shown in Figure 6.4a). Since the atmospheric density decreases exponentially with height, the squared amplitude of the atmospheric waves also increases exponentially although often not as fast if there is dissipation. This feature makes the spectral analysis results biased towards the waves at higher altitudes since their amplitudes are larger than those at lower altitudes. To resolve this bias, we weight the relative perturbations at each altitude by their standard deviation at that altitude. Then 2-D FFT are performed to the weighted data within a sliding vertical window with a width of 10 km. The window was then shifted every 1 km. In the 2-D FFT spectra, positive periods correspond to downward phase progression waves while negative period represents upward phase progression. The total power of the waves with downward (upward) phase progression can be calculated by summing the 2-D spectral power falling in the positive (negative) period range. The ratio of the downward phase progression power to the total power integrated over the entire period and vertical wavelength range is then calculated. Since we are more interested in the period range of

3–10 h, only the power that falls in such period range is counted for both upward and downward phase progressions. Figure 6.4b shows downward phase ratio as a function of altitude. In general, the downward phase ratio is high, which is about 70–80%. Two local minima at ~ 40 km and ~50 km can be seen, which correspond to the heights where upward phase ratios are maximum. In a statistical sense, under the assumption of positive intrinsic frequencies these two heights have higher possibilities to be wave source regions. However, whether these regions are responsible for the 3-10 h waves observed in the MLT is still a question since atmospheric waves not only propagate vertically but also horizontally. The 2-D FFT spectrum calculated from the entire dataset is shown in Figure 6.4c. Note that a significant peak is seen at T = –30 h and λ_z = 30 km.

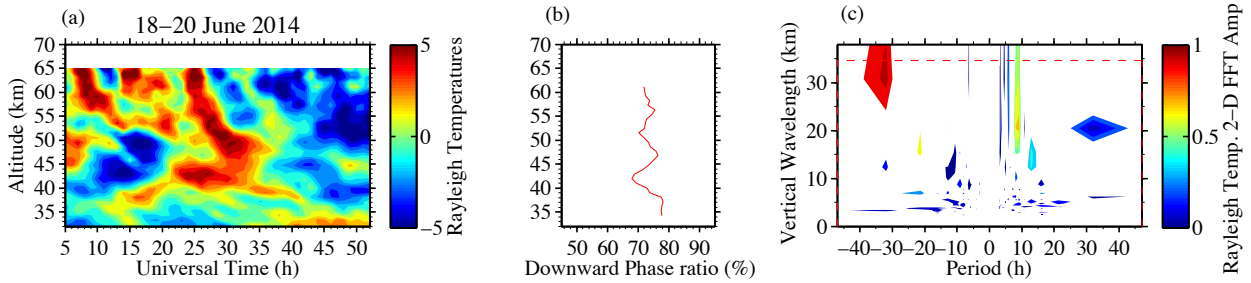

Figure 6.4. (a) Rayleigh temperatures observed at McMurdo on 16–18 June 2014. (b) Ratio of the downward phase progression to total (c) 2-D FFT spectrum of the Rayleigh temperatures.

We performed the analysis to the Rayleigh temperature data over McMurdo in the winter months (May to July) of 2011–2014. The results are then averaged and shown in Figure 6.5a. The minimum at 50–55 km suggests a potential wave source region over McMurdo. The downward phase ratios increase at above and below this region. Similar analyses are then applied to the high-resolution assimilated meteorological analyses from European Centre for Medium-Range Weather Forecasting (ECMWF) (data courtesy of Dr. Andreas Dörnbrack). We select the data over McMurdo in ECMWF data at the same time periods when there are lidar observations

to do the analysis. The data have 1-h temporal resolution and ~3 km vertical resolution at z = 50 km. Figure 6.5b shows the averaged result from the ECMWF data. While the general trend in the ECMWF result is similar to the lidar result at below 50 km. At above 50 km, the downward progression ratio continues to decrease with altitude, which is inconsistent with the lidar result. This is probably due to the sponge layer at the upper boundary of the ECMWF data.

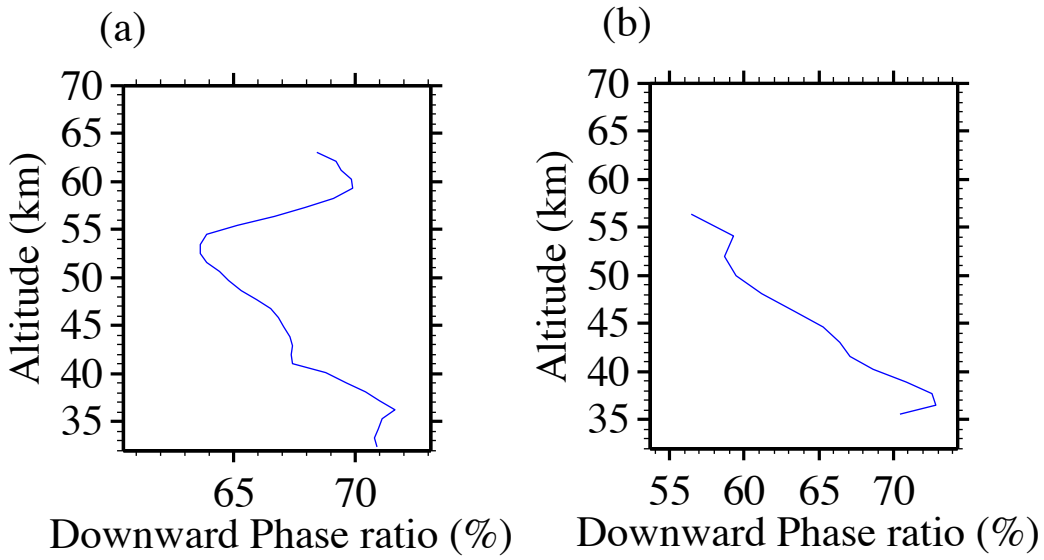

Figure 6.5. (a) Ratio of the downward phase progression to total in the Rayleigh temperatures in the winter months (May to July) of 2011–2014. (b) Results derived from the ECMWF reanalysis data.

6.3.2 Vertical Energy Flux directions in ECMWF at McMurdo

The sign of the vertical energy flux ($\overline{w'p'}$) directly determines the vertical energy propagation direction of the gravity waves, where p', w' are wave perturbations in pressure and vertical winds induced by gravity waves. Positive (negative) vertical energy flux means upward (downward) wave propagation, and increase (decrease) in the magnitude of the vertical energy flux over height suggests a possible wave source (sink). Using the high-resolution ECMWF data, we calculated the vertical energy flux over McMurdo from May through August in 2014. Results

are shown in Figure 6.6b, 6.7b, 6.8b, and 6.9b, respectively. The pressure and vertical wind perturbations are calculated by high-pass filtering pressures and vertical winds at each altitude with a cutoff period at 12 h. Resutls show siginificant increases in the vertical energy fluxes in all of these winter months at above 40 km. This suggests an active wave source region at above in the upper Antarctic stratosphere in winter months. On the other hand, zonal energy flux ($\overline{u'p'}$) determines the energy propagation in the zonal direction. Positive (negative) zonal energy flux means the wave propagate eastward (westward) relative to the background winds. Results of the zonal energy flux are shown in Figure 6.6a, 6.7a, 6.8a, and 6.9a, respectively. Similar to the calculation of the vertical energy flux. The perturbations are calculated by high-pass filtering pressures and zonal winds at each altitude with a cutoff period at 12 h.

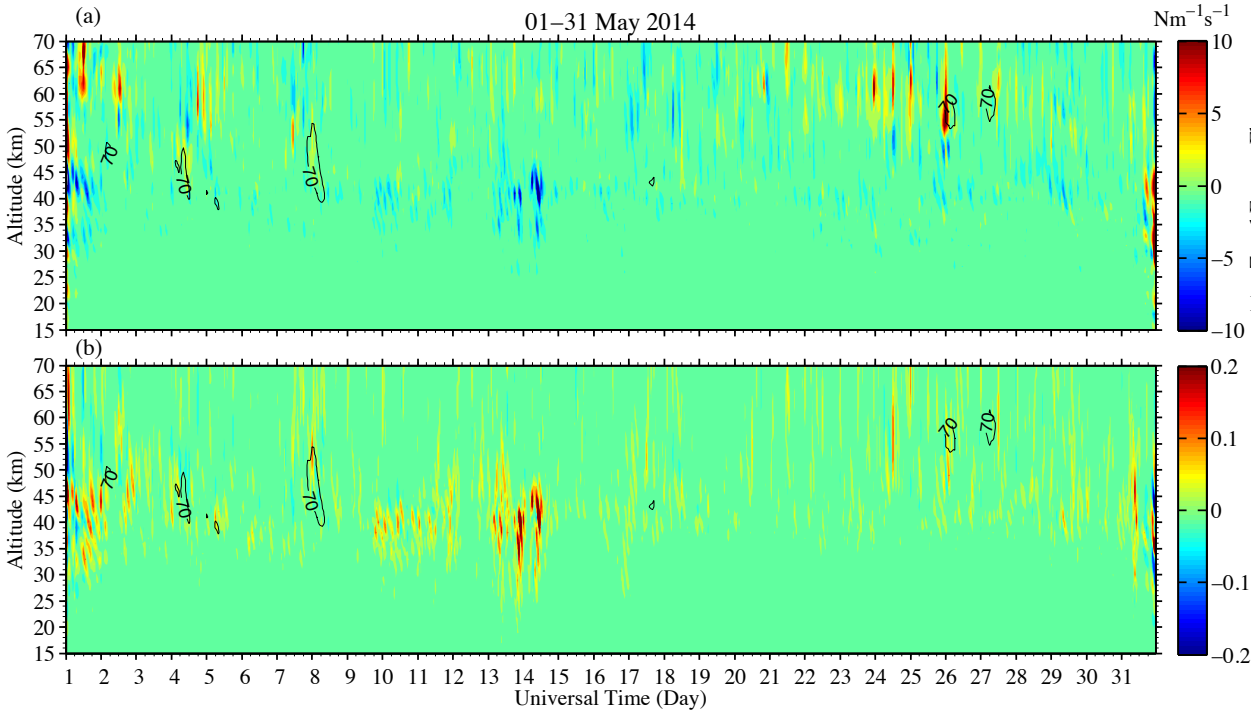

Figure 6.6. (a) Energy flux in zonal direction (b) Energy flux in vertical direction calculated using ECMWF data over McMurdo in May 2014.

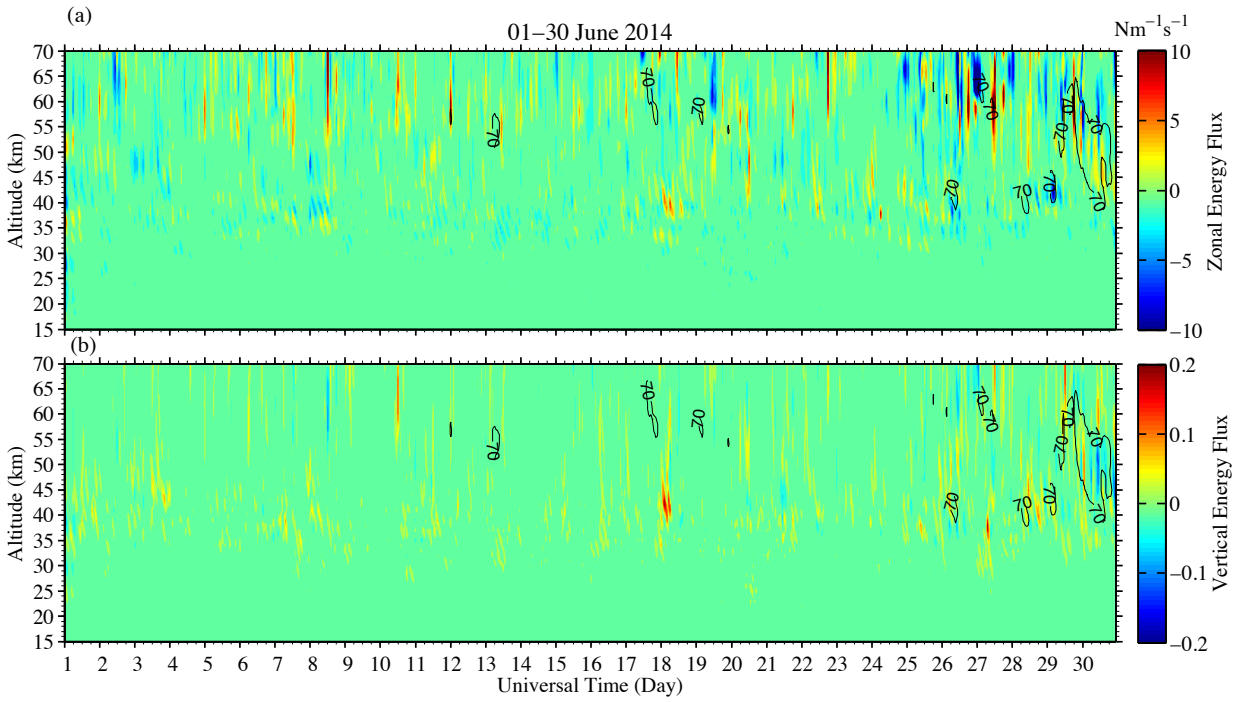

Figure 6.7. (a) Energy flux in zonal direction (b) Energy flux in vertical direction calculated using ECMWF data over McMurdo in June 2014.

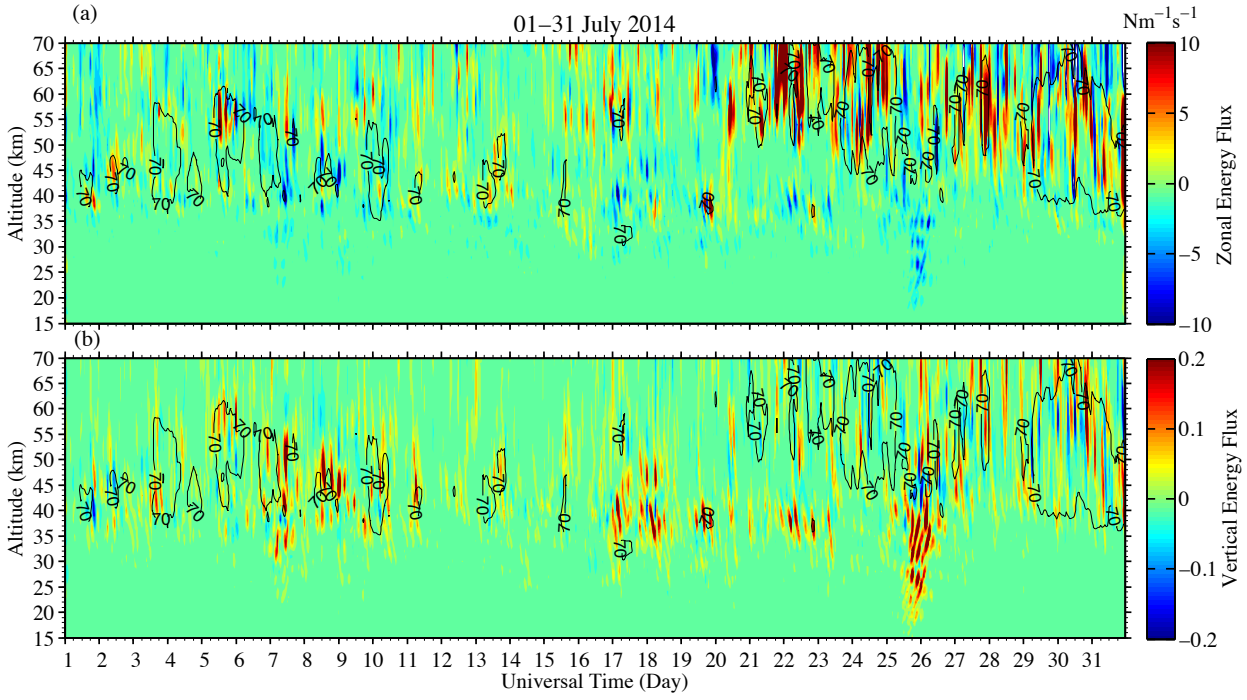

Figure 6.8. (a) Energy flux in zonal direction (b) Energy flux in vertical direction calculated using ECMWF data over McMurdo in July 2014.

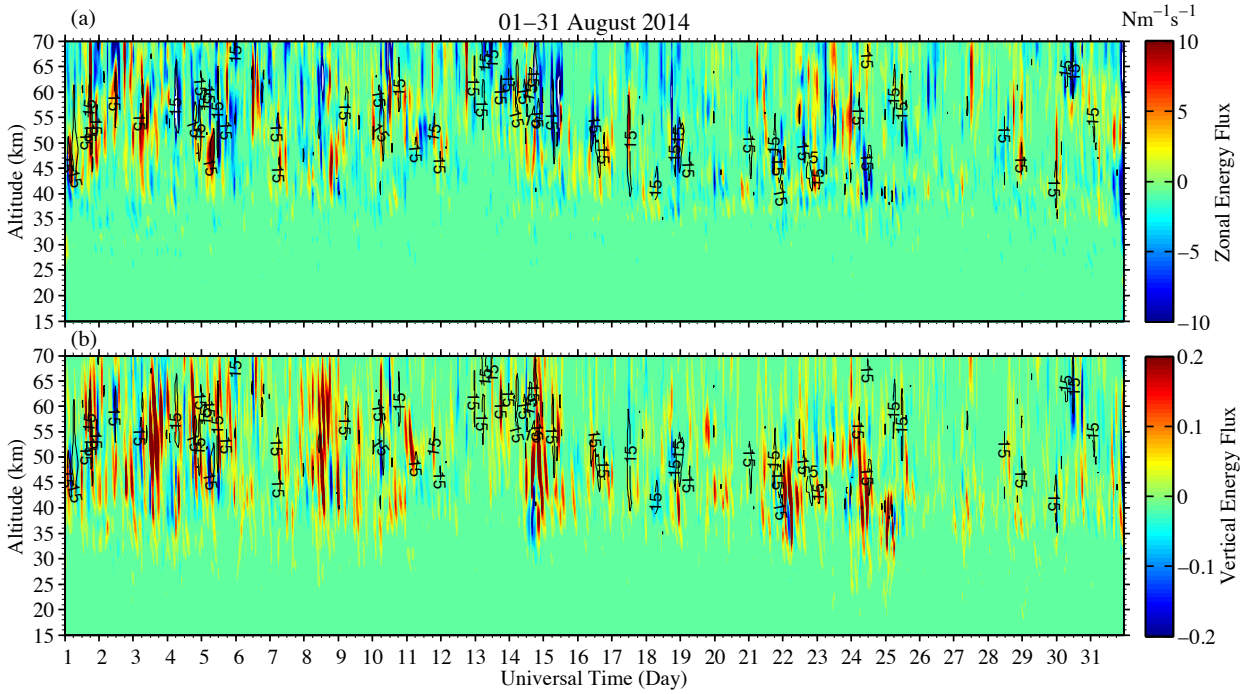

Figure 6.9. (a) Energy flux in zonal direction (b) Energy flux in vertical direction calculated using ECMWF data over McMurdo in August 2014.

6.4 Summary

By comparing the periods and vertical wavelengths of the solutions from the classical Laplace equations with those of the 3-10 h waves obtained from lidar observations, we show that in order for the theoretical solutions comparable to our observations, both the zonal wavenumbers s and meridional wavenumbers n of the waves need to be high ($s > 6$ and $n > 20$). The combination of high zonal and meridional wavenumbers hints that these waves are unlikely to be tides, normal modes or planetary-scale inertio gravity waves, supporting our inference of persistent inertia-gravity waves.

The statistical average of the ratio of downward phase progression power to the total power derived from the lidar Rayleigh temperatures shows a minimum at 50–55 km, which suggests a potential wave source region over McMurdo. Same ratio derived from ECMWF

reanalysis data is similar to that from lidar at below 50 km. However, at above 50 km, the downward progression ratio continues to decrease with altitude, which is inconsistent with lidar. This is probably due to the sponge layer at the upper boundary of the ECMWF data. The vertical energy flux over McMurdo is calculated from the ECMWF data from May through August in 2014. The upward vertical energy fluxes siginificantly increase at above 40 km in all of these winter months. This is a direct evidence of potential wave sources over McMurdo. However, whether these active source regions are linked to the persistent gravity waves cannot be unraveled before performing sophisticated ray-tracing analysis to identify the real wave sources. This is left as future work.

CHAPTER 7

Conclusions and Outlook

7.1 Conclusions

The McMurdo lidar campaign has led to intriguing new science discoveries and advanced our understandings of the polar space atmosphere interaction region (SAIR) where atmospheric neutral gases entwine with the dynamic plasma of space. The SAIR is one of the key factors enabling our Earth to harbor life. By absorbing extreme solar radiation, ablating meteoric materials, regulating gaseous escape, dissipating energetic particles and fields from space, while balancing influences from the planet itself in the form of wave transport and dissipation of energy and momentum, the fundamental processes in the Earth's SAIR are believed to be universal and applicable to the atmospheres of Earth-like planets throughout our galaxy. However, SAIR remains one of the least observed and understood regions. This thesis aims to advance the observations and characterizations of the atmospheric waves that are fundamental to shaping the SAIR. Currently, large-scale terrestrial atmospheric waves such as tides and planetary waves are reasonably well understood, and have been incorporated into global circulation models (GCMs). However, small-scale atmospheric waves, such as gravity waves, are difficult to observe but are essential to the modeling work of the global atmosphere because of their critical role in the momentum and energy transport through the whole atmosphere. At Polar Regions, there are many wind measurements that are typically dominated by tides, thereby obscuring gravity wave signatures. There are also a few non-range-resolved temperature, wind and airglow observations at Polar Regions but they cannot provide vertical wavelength

information, which is crucial in determining the wave nature. It was only until the Fe Boltzmann lidar at McMurdo provided high-resolution, long-duration, large-altitude-range temperature measurements, did we discover the mystery of the persistent inertia-gravity waves. This discovery provides a unique opportunity to study how different regions of the atmosphere "communicate" via gravity waves that have smaller scales but are more variable than the better understood tides, planetary waves and normal modes.

This thesis discovers a new wave phenomenon in the Antarctic middle and upper atmosphere, namely the persistent inertia-gravity waves with periods of 3-10 h. This group of waves is persistent and dominates the temperature perturbations from the stratosphere to the lower thermosphere (about 30-115 km). These waves occur on every lidar run, so frequently as to appear endless and uninterrupted. The large-amplitude perturbations caused by these waves certainly impact the composition, chemistry and thermodynamics of SAIR.

This thesis reports the first simultaneous lidar/radar observations of inertia-gravity waves in Antarctica. Two waves with periods of 5.0±0.1 h and 7.7±0.2 h are observed and characterized in the mesosphere and lower thermosphere. These waves have horizontal wavelengths of 1000–2000 km and horizontal group speeds of 50–60 m/s, and are roughly traced back to an unbalanced region in the polar night jet in the upper stratosphere.

This thesis establishes the observational facts that the 3–10 h waves are persistent and dominant in the MLT region at McMurdo. Then utilizing five years of lidar temperature data collected in June through five Antarctic winters from 2011 to 2015, this thesis characterizes the persistent wave properties for the first time. These waves exhibit a uniform dominant vertical wavelength of 20–30 km across periods of 3.5–10 h and vertical phase speeds of 0.8–2 m/s. These 3–10 h waves possess more than half of the spectral energy for ~93% of the time. A

detailed analysis of the 65-h lidar data on 28–30 June 2014 demonstrates multiple wave packets spanning as long as 60 h. The spectral slopes of these waves are unusually steep, with an averaged value of –2.7, below 100 km, gradually becoming shallower to –1.6 at 110 km. From this, we speculate that the source region is close to the MLT region, which points to a possible stratospheric source. This uniform peak λ_z (20–30 km) shown in the 2-D FFT spectrum across different periods might shed some light on the vertical scale of the wave sources.

Further analysis of May and July data with nearly automated methods confirm the persistence and dominance of these waves but reveal a month-to-month variability. While in the June case, all the waves show similar quasi-monochromatic and quasi-plane wave features, both May and July cases show two types of temperature phase lines, with the longer period wave exhibiting more oblique phase lines and shorter-period waves having more vertical phase lines. In general, May and July cases show more dynamical wave field structures than the June case, which could be a result of a more variable background wind condition during these two months.

The discovery of the thermospheric neutral Fe layers and fast gravity waves by *Chu et al*. [2011b] opens a new pathway to observing the neutral thermosphere with ground-based instruments, and also has triggered several observations of thermospheric events at other lidar stations. The contribution of this thesis to this discovery is to characterize the gravity waves from 30 km to 155 km. The fast gravity wave patterns are extracted from both the thermospheric Fe layers (110 to 155 km) and the Rayleigh and Fe temperatures (30 to 110 km). This work shows for the first time that a single instrument is able to "trace" gravity waves over such a large altitude range in the neutral atmosphere. It is a direct evidence of "wave communication" from the stratosphere, mesosphere to at least the F region in the ionosphere. The properties of the fast thermospheric gravity waves in these thermospheric Fe layers are derived.

As another major theme, this thesis develops a system of wave analysis methods. The methodologies include:

(1) Methods of repeatedly subtraction of the more dominant, longer-period waves to extraction of shorter-period fast gravity waves from the Rayleigh and Fe temperatures (30 to 110 km) and development of ridge tracking algorithm in the Fe layers at thermospheric altitudes (110-155 km) to extract the fast gravity waves. Using these methods, we show for the first time that a single instrument is able to "trace" gravity waves from ~30 km to 155 km in the neutral atmosphere.

(2) A temporal hodograph method is then developed to derive the intrinsic properties of inertia-gravity waves from lidar and radar data, in which lidar temperature helps remove the ambiguity of wave propagation direction. The resulting intrinsic properties of the waves are then used in tracing the wave source(s) using a simple ray tracing method.

(3) We discover a problem in the commonly used 1-D Morlet wavelet transform, and then provide the correction and establish the mathematic formalism of 1-D wavelet transform. Such improved 1-D Morlet transform is used to identify major wave events enabling us to quantify the life span, occurrence rate and many other properties of the waves in a systematic manner.

(4) A rigorous pre-whitening and post-coloring spectral analysis technique is introduced for the first investigation of how temperature frequency spectra of gravity waves evolve with altitude in the mesosphere and lower thermosphere.

(5) The reliance on human intervention of the 1-D wavelet method motivates our development of the 2-D Morlet wavelet analysis and synthesis methods for automated extraction of wave packets from two-dimensional data. We provide the detailed mathematical formalism of

the 2-D wavelet analysis and synthesis. The successful application to McMurdo lidar data demonstrates the utility of this 2-D wavelet transform in extracting gravity waves that are inherently intermittent. This 2-D wavelet method enables the automated analysis of large amounts of 2-D scientific data in a standardized manner.

Efforts are also spent on exploring the nature of the persistent waves and searching the wave source(s). By solving the classical Laplace equations and comparing the solutions of periods and vertical wavelengths with lidar observations, we conclude that these waves are unlikely to be tides, normal modes or planetary-scale inertio gravity waves, supporting our inference of persistent inertia-gravity waves. The lidar Rayleigh temperatures and European Centre for Medium-Range Weather Forecasting (ECMWF) reanalysis data are used to derive the statistical average of the ratio of downward phase progression power to the total power, and the results suggest an active wave source region existing above 40 km over McMurdo in winter. Follow-up studies are necessary in the future to investigate whether this region is linked to the persistent gravity waves and what generation mechanisms are in action. Sophisticated ray-tracing, in combination with automated 2-D wavelet analysis of lidar, radar, imager, ECMWF, and high-resolution general circulation model data, will likely provide new insight into the wave sources and their impacts on the whole atmosphere and space.

7.2 Outlook

In this thesis, we characterized the properties of the persistent inertia-gravity waves primarily in winter months. As a future work, it is necessary to characterize the wave properties of these persistent waves in other months in a year (especially in summer) and at all altitudes (30 to 110 km). This work will advance our understanding and help in the search of the wave source and generation mechanisms. In this thesis, we have attempted to explore the possible waves

sources of the persistent 3-10 h waves using the lidar and reanalysis data right over McMurdo. Since atmospheric waves propagate horizontally as well, further efforts are also needed in doing ray-tracing analysis of the waves in the high-resolution global models and assimilated data sets. Many features of the 3–10 h waves challenge our understanding of gravity waves and demand deeper investigation into the sources and mechanisms for their generation, the reasons for their persistence, and their impacts on general circulation and chemical climate models. We cannot answer these important questions without further investigating more ground-based data, high-resolution global models, and assimilated data sets.

The wave analysis methods developed in this thesis have many more potential applications in various science topics. In particular, the 2-D Morlet wavelet methods that we have developed could be used to detect and reconstruct quasi-plane wave structures in satellite images, airglow imager or temperature mapper data. By implementing an isotropic wavelet function such as the Halo wavelet such methods can be used to identify and extract ring structures in concentric gravity waves. Despite the success of the 2-D wavelet transform and reconstruction as demonstrated above, there is still room for improvement. For example, the error analysis on the 2-D wavelet method needs to be explored. Optimization on the algorithm should be implemented, which will improve the computing speed and facilitate the application of this method to large volume data. Such developments on automated pattern analysis, detection, recognition, tracking, and reconstruction techniques are greatly needed by the CEDAR community. The emerging technology breakthroughs in fields such as artificial intelligence, robotics, and autonomous vehicles will soon have an impact in the science field as well. In time, we will enter the era of the fourth industrial revolution.

Appendix A

Lidar and Radar Investigation of an Inertia Gravity Wave Event on 11 July 2011 at Mcmurdo, Antarctica

A.1 Introduction

Gravity waves have been recognized to be important because of their major impacts in driving the mean meridional circulations, affecting thermal structure and constituent transport. Long-duration, large-altitude-range and high-resolution measurements of gravity waves are essential to provide constraints for gravity wave parameterizations. The long-standing "cold pole" problem in many models can be attributed in large part to underestimated wave drag induced by IGWs or short period waves. IGWs are long-period waves that are influenced by the rotation of the Earth. They are often observed in the troposphere and stratosphere [e.g., *Sato et al*., 1997]. It has been demonstrated that the horizontal wavelengths of IGWs can be thousands of kilometers, while the vertical group velocity just a few centimeters per second. In the mesosphere and lower thermosphere (MLT) region, there have been observations of IGWs using lidars [e.g., *Li et al*., 2007; *Lu et al*., 2009]and incoherent scatter radar [4]. Similarly, large horizontal wavelengths were retrieved in these studies. Investigations of IGW in the mesopause region over Antarctica are rare yet important due to its potential influence on MLT temperatures and dynamics [e.g., *Nicolls et al*., 2010].

The University of Colorado lidar group deployed an Fe Boltzmann lidar to McMurdo since Dec 2010 [*Chu et al*., 2011a]. This lidar has full diurnal coverage and is capable of measuring temperatures at altitudes between 30 and 110 km [*Chu et al*., 2012]. The Scott Base

MF radar is co-located with the Fe lidar at Arrival Heights. This radar has near-continuous temporal coverage and has been collecting MLT wind data at heights between 70 and 100 km since 1982 [*Baumgaertner et al*., 2005]. The simultaneous MLT temperature and wind data provide a unique opportunity for studying the IGWs and their intrinsic properties at this high southern latitude.

A.2 Data Analysis

A.2.1 Derivation of Wave Perturbations

As shown in *Chu et al*. [2012], the temperatures in the McMurdo MLT observed by the lidar show strong wave activity. In particular, wave oscillations with periods of 5–8 h dominate the temperature variations, especially in the winter months. These dominant waves are likely inertia gravity waves.

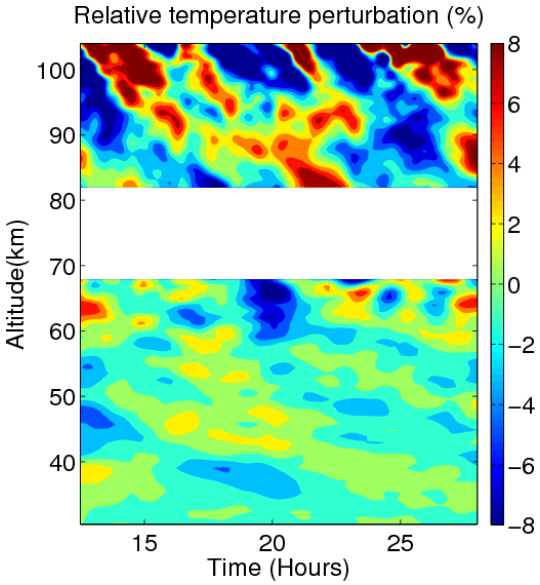

Figure A.1. Relative temperature perturbations after removing tides and high-frequency perturbations on 11 July 2011

The MLT temperature data we used have resolutions of 0.1 h and 0.1 km, and MF radar data have resolutions of 0.5 h and 2 km. The Fe lidar data were smoothed temporally and vertically with Hamming windows of 0.5 h and 1 km FWHM. Therefore, only the waves with periods longer than 1 h, and vertical wavelength λ_z longer than 2 km were resolved.

Relative temperature perturbations were derived by subtracting the mean temperature at each altitude and then divided by the mean. In order to minimize the contamination of tidal oscillations in the temperature perturbations, a linear trend in the time domain at each altitude is removed, followed by a subtraction of a linear trend in the spatial domain at each moment [*Lu et al*., 2009]. Figure A.1 shows the relative temperature perturbations from 35 to 105 km on 11 July 2011. A clear downward phase progression shows a vertical wavelength of 20 km around MLT region. To derive the gravity-wave-induced wind perturbations from MF radar data, the tidal effect was removed by subtracting a temporal fitting of diurnal and semi-diurnal–period sinusoidal functions at each altitude from the original wind observations.

A.2.2 Hodograph Method

Hodograph methods have been used to study gravity wave intrinsic properties in MLT regions by many analyses using wind and temperature data, such as in *Lu et al*. [2009]. Most of the studies apply hodograph analysis over height. However, for this study, we chose temporal hodograph instead for the following two main reasons. Firstly, the radar wind measurements only have a 2 km vertical resolution, so that there are usually not enough sequential height data to obtain a significant result, especially when the vertical wavelength is short. Secondly, the overlapping observation range between lidar and MF radar is usually confined to 20 km (from 80 to 100 km), which is not long enough to accurately resolve gravity waves with longer vertical wavelengths (≥20 km). The lidar measurements in the last 15 months have revealed that gravity

waves with such wavelengths are common at McMurdo. Therefore, the subsequent analysis will be restricted to temporal hodograph.

In-phase wind perturbation and quadrature-phase wind perturbation amplitude are related by the equation below,

$$\tilde{U} = \frac{i\hat{\omega}}{f}\tilde{V} \tag{A.1}$$

where $\tilde{U}$ is the in-phase wind perturbation, $\tilde{V}$ is the quadrature-phase wind perturbation, $\hat{\omega}$ is intrinsic frequency of the wave, and f is Coriolis parameter, corresponding to a 12.24-h inertial period at McMurdo (77.8° S). Equation (A.1) shows that gravity-wave-induced in-phase and quadrature-phase wind perturbations ($\tilde{U}$, $\tilde{V}$) exhibit elliptical polarization. In the Southern Hemisphere where $f < 0$, $\tilde{U}$ will lead $\tilde{V}$ and ($\tilde{U}$, $\tilde{V}$) will rotate counterclockwise with time if the wave propagates upward ($\hat{\omega} > 0$). The relation between temperature perturbation and the in-phase wind perturbation amplitudes is given as follows,

$$\tilde{T} = \frac{1}{g}\left(im + \frac{1}{2H}\right)\frac{\hat{\omega}^2 - f^2}{\hat{\omega}k_h}\tilde{U} \tag{A.2}$$

where m is the vertical wave number, k_h is the horizontal wave number, H is scale height, and $\tilde{T}$ is the relative temperature perturbation. Equation (A.2) shows that there is a fixed phase relationship between $\tilde{T}$ and $\tilde{U}$. Specifically, if we fit relative temperature perturbation and in-phase wind perturbation to the quasi-monochromatic gravity wave model given below,

$$\begin{aligned} \tilde{U} &= \left|\tilde{U}\right|\cos(\omega t + \Phi_U) \\ \tilde{T} &= \left|\tilde{T}\right|\cos(\omega t + \Phi_T) \end{aligned}, \tag{A.3}$$

the phase information deduced from the fitting will exhibit a relation as follows,

$$\Phi_U - \Phi_T = \tan^{-1}(m \cdot 2H) \tag{A.4}$$

Consequently, Equation (A.4) can be used to determine the wave propagation direction in the horizontal plane.

The intrinsic frequency $\hat{\omega}$ can be calculated from the amplitude ratio between $\tilde{U}$ and $\tilde{V}$ derived from the hodograph using Equation (A.1). However, our investigation shows that the amplitude ratio of the fitted ellipse varies dramatically with altitude but the major axis remains in similar directions. Therefore, we take a different approach that utilizes the major axis direction of the ellipse fitting, instead of amplitudes, to estimate intrinsic frequency. From the dispersion relationship, definition of intrinsic frequency, and by assuming small background wind shear [*Fritts and Alexander*, 2003],

$$\begin{cases} k_h^2 = \dfrac{\hat{\omega}^2 - f^2}{N^2 - \hat{\omega}^2}\left(m^2 + \dfrac{1}{4H^2} - \dfrac{\hat{\omega}^2}{c_s^2}\right) \\ \hat{\omega} = \omega - k_h \bar{U} \end{cases}, \tag{A.5}$$

Thus, $\hat{\omega}$ can be solved from the following equation:

$$\left(\frac{1}{c_s^2} - \frac{1}{\bar{U}^2}\right)\hat{\omega}^4 + \frac{2\omega}{\bar{U}^2}\hat{\omega}^3 + \left(\frac{N^2 - \hat{\omega}^2}{\bar{U}^2} - m^2 - \frac{1}{4H^2} - \frac{f}{c_s^2}\right)\hat{\omega}^2 - \frac{2N^2\omega}{\bar{U}^2}\hat{\omega} + f^2\left(m^2 + \frac{1}{4H^2}\right) + \frac{N^2\omega^2}{\bar{U}^2} = 0 \tag{A.6}$$

where c_s is speed of sound, $\bar{U}$ is the horizontal mean wind projected onto the wave propagation direction, N is the buoyancy frequency. Equation (A.6) has four roots, but only the meaningful solution will be selected. Details will be discussed in the next section.

A.3 Results and Discussion

On 11 July 2011, a coherent wave structure was observed in both lidar temperature and radar wind from 81 to 89 km as shown in Figure A.2, suggesting that these two instruments

observed the same gravity wave event. Therefore, temporal hodograph analysis was used to derive the intrinsic parameters.

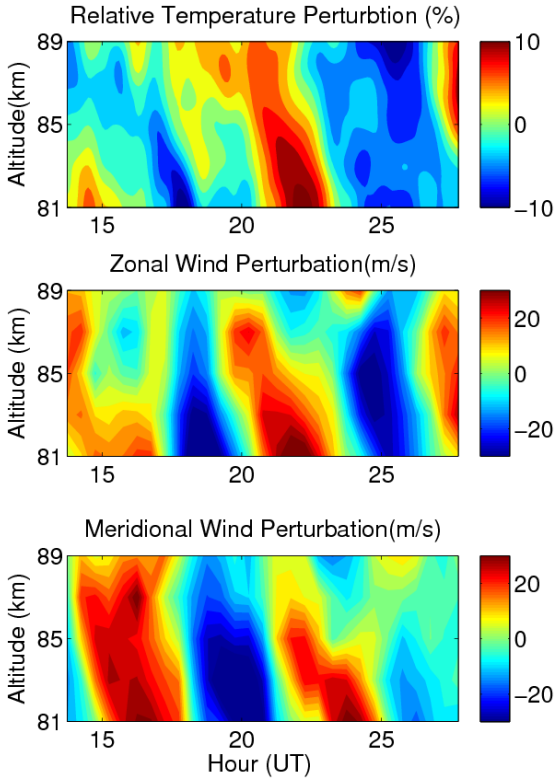

Figure A.2. From top to bottom, relative temperature, zonal wind, and meridional wind perturbations on 11 July 2011 at McMurdo, after tides and high-frequency waves are removed.

The procedure was to first determine the dominant observed period T_0 from the Lomb-Scargle spectrum analysis of the temperature, zonal wind, and meridional wind at each altitude. Then, all three datasets were band-pass filtered around the dominant observed frequency ω with cutoff periods at 10 and 5 h. The band-pass filtered wind perturbations were then plotted on a hodograph (see Figure A.3). As shown from the hodographs, all three ellipses at three altitudes are elongated in nearly northeast direction. The least mean square (LMS) fitting of all three ellipses showed that the azimuth angle was 62° or 62°+180°=242°. (The direction is defined to be 0°at north and increase clockwise). The 180° ambiguity was resolved by making use of

Equation (A.4). In doing so, we first chose the wave propagation direction as the bearing of the red arrow in Figure A.3. Zonal and meridional wind perturbations were then projected to the new x-axis to obtain the in-phase wind perturbations. Both in-phase wind perturbations and relative temperature perturbations were fitted to model Equation (A.3). The deduced phase difference $\Phi_U - \Phi_T$ is very close to the one calculated from Equation (A.4), with a discrepancy of ~-/5, which indicates that the wave was propagating in the direction as shown by the red arrow in Figure A.3, i.e., 62° east of north. The in-phase background wind ($\bar{U}$) was then derived by projecting horizontal wind onto the propagation direction and fitting a mean value plus a sinusoidal wave. The period of the sinusoidal wave is set equal to the period of the observed gravity wave. In this case, the projected mean wind was calculated to be 3.3±1 m/s by averaging the values in the altitude range.

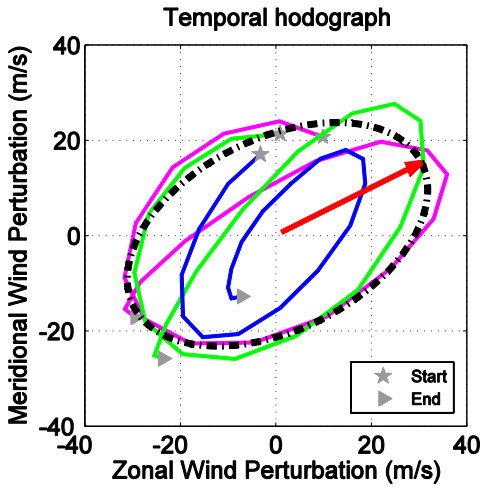

Figure A.3. Hodographs of zonal and meridional wind perturbations on 11 July 2011. Three hodographs (at 81, 83 and 85 km) are plotted together, where stars and triangles denote the beginning and end of the data.

Finally, the intrinsic frequency ($\hat{\omega}$) was solved from Equation (A.6). The calculated intrinsic periods are 7.47, 6.81, -0.09, and 0.09 h, corresponding solutions for horizontal wavelength are 1975, -1728, -1.1, and 1.08 km, respectively. The last two solutions are

unreasonable because the wavelengths are too small considering the MF radar field of view is ~30°. Since the propagation direction of the wave has been determined, only the positive wavelengths would be acceptable. Therefore, the first pair of solutions was selected so that intrinsic period of the wave is 7.47 h and the horizontal wavelength is 1975 km. The apparent horizontal phase speed is 76.7 m/s, while the intrinsic horizontal phase speed is 73.4 m/s. The group velocity was also calculated using Eqs. (A.7–A.8),

$$c_{gh} = \frac{\partial \hat{\omega}}{\partial k_h} = \frac{k_h (N^2 - \hat{\omega}^2)}{\hat{\omega}\left(k_h^2 + m^2 + \frac{1}{4H^2}\right)}, \tag{A.7}$$

$$c_{gz} = \frac{\partial \hat{\omega}}{\partial m} = -\frac{m(\hat{\omega}^2 - f^2)}{\hat{\omega}\left(k_h^2 + m^2 + \frac{1}{4H^2}\right)}. \tag{A.8}$$

Horizontal group velocity was found to be ~39 m/s, while the vertical group velocity was 0.44 m/s, i.e., 38 km/day in the vertical direction. The elevation angle of the energy propagation was ~0.6° from the horizon, which indicates that the wave source might be very far from the McMurdo station as discussed below.

The group velocities we calculated above indicate that the vertical group velocity was significantly slower than the horizontal group velocity. This implies that it would take ~1–2 days for the wave to propagate a vertical distance of ~40–80 km, if the vertical wind is negligible. During this period, the wave would have propagated ~5500 km in the horizontal plane, if we assume the background wind along the wave propagation path was negligible (although this may not be true). Certainly, if the background winds at lower altitudes were against the wave propagation direction, the horizontal distance and time needed to reach mesopause would be shorter [*Nicolls et al*., 2010].

The wave propagation direction derived from the hodograph is toward ~62° clockwise from the north. If we assume the wave propagating along this direction with nearly constant group velocity during the 1–2 days of period, the large horizontal propagation range would place the wave source on the opposite side of the Antarctic continent around 50–40°S and 55°E. This is close to the jet stream locations. As *Nicolls et al*. [2010] argued in analyzing the IGWs observed in the Arctic, a possible mechanism of generating IGWs is a geostrophic adjustment of the jet stream. Although the exact source location could not be pinpointed, Vadas' wave modeling demonstrated such a generation mechanism (Dr. Sharon Vadas, private communication, 2012). Similarly, we speculate the IGW observed at McMurdo could be excited by a geostrophic adjustment of the jet stream on the opposite side of the Antarctic continent, located 5000–6000 km away from McMurdo. The wave may have propagated for 1-2 days prior to our observations.

A.4 Conclusions

The hodograph analysis has been applied to the combined Fe lidar/ MF radar data of temperature and wind. A dominant inertia-gravity wave has been observed. This is the first time that a coincident observation of an inertia-gravity wave by an MF radar and lidar is reported in Antarctica. Our further analysis has also indicated another IGW event with an intrinsic period of 7.5 h on 29 June 2011 [*Chen et al*., 2013]. This suggests that there could be active wave sources generating these large-scale inertia-waves during winter. Our lidar measurements indicate that the IGWs have significant impacts on the MLT temperature at McMurdo. Therefore, it is crucial to evaluate the roles of IGWs in the polar region.

Whether the geostrophic adjustment of the jet stream is responsible for the observed IGWs deserves further investigations with wave modeling and ray-tracing test. Background wind

information is crucial in tracing the waves to their source regions. Our temporal hodograph method also needs validation against other approaches and assessment of the possible influence by the background wind shear.

Appendix B

Derivations of the Selected Equations in Chapter 5

B.1 Derivation of Equation (5.1)

Derivation of Equation (5.1) is as follows.

$$\begin{aligned} W_{f\psi}(s,t) &= \int_{-\infty}^{+\infty} f(t')\frac{1}{\sqrt{s}}\psi^*\left(\frac{t'-t}{s}\right)dt' = \frac{1}{\sqrt{s}} f(t)\otimes\psi^*\left(-\frac{t}{s}\right) \\ &= \frac{1}{2\pi}\frac{1}{\sqrt{s}}\int_{-\infty}^{+\infty}\hat{f}(\omega)\mathrm{FT}\left[\psi^*\left(-\frac{t}{s}\right)\right]e^{i\omega t}d\omega \end{aligned}, \tag{B.1}$$

where $\otimes$ denotes convolution, $f(t)\otimes h(t) = \int_{-\infty}^{+\infty} f(t')h(t-t')dt' = \frac{1}{2\pi}\int_{-\infty}^{+\infty}\hat{f}(\omega)\hat{h}(\omega)e^{i\omega t}d\omega$.

Operator (*) denotes complex conjugate, and both operator ($\hat{}$) and FT() denote the Fourier transform. Now we rewrite $\mathrm{FT}\left[\psi^*\left(-\frac{t}{s}\right)\right]$ as

$$\begin{aligned} \mathrm{FT}\left[\psi^*\left(-\frac{t}{s}\right)\right] &= \int_{-\infty}^{+\infty}\psi^*\left(-\frac{t}{s}\right)e^{-i\omega t}dt = \int_{-\infty}^{+\infty}\psi^*\left(-\frac{t}{s}\right)e^{-i(-s\omega)\left(-\frac{t}{s}\right)}dt \\ &= -s\int_{-\infty}^{+\infty}\psi^*\left(-\frac{t}{s}\right)\left[e^{-i(s\omega)\left(-\frac{t}{s}\right)}\right]^*\frac{dt}{-s} = s\int_{-\infty}^{+\infty}\left[\psi(t'')e^{-i(s\omega)t''}dt''\right]^* = s\left[\hat{\psi}(s\omega)\right]^* \end{aligned}, \tag{B.2}$$

By substituting (B.2) into Equation (B.1), we can prove Equation (5.1).

$$W_{f\psi}(s,t) = \frac{1}{2\pi}\frac{1}{\sqrt{s}}\int_{-\infty}^{+\infty}\hat{f}(\omega)s\left[\hat{\psi}(s\omega)\right]^* e^{i\omega t}d\omega = \frac{1}{2\pi}\int_{-\infty}^{+\infty}\hat{f}(\omega)\sqrt{s}\left[\hat{\psi}(s\omega)\right]^* e^{i\omega t}d\omega\,. \tag{B.3}$$

B.2 Derivation of Equation (5.4)

We prove Equation (5.4) by showing that the Fourier transforms of the both sides of the Equation (5.4) are equal. The Fourier transform of the left hand side (LHS) with regard to *t* is

$$\mathrm{FT}[\mathrm{LHS}] = \hat{f}(\omega), \tag{B.4}$$

The Fourier transform of the right hand side (RHS) with regard to *t* is

$$\begin{aligned}
\mathrm{FT}[\mathrm{RHS}] &= \frac{1}{C_\psi}\mathrm{FT}\left[\int_0^{+\infty}\int_{-\infty}^{+\infty}\frac{1}{s^2}W_{f\psi}(s,t')\frac{1}{\sqrt{s}}\psi\left(\frac{t-t'}{s}\right)dt'\,ds\right] \\
&= \frac{1}{C_\psi}\mathrm{FT}\left\{\int_0^{+\infty}\int_{-\infty}^{+\infty}\frac{1}{s^2}\left[\frac{1}{\sqrt{s}}f(t)\otimes\psi^*\left(\frac{-t}{s}\right)\right]\frac{1}{\sqrt{s}}\psi\left(\frac{t-t'}{s}\right)dt'\,ds\right\} \\
&= \frac{1}{C_\psi}\mathrm{FT}\left\{\int_0^{+\infty}\frac{1}{s^2}\left[\frac{1}{\sqrt{s}}f(t)\otimes\psi^*\left(\frac{-t}{s}\right)\right]\otimes\left[\frac{1}{\sqrt{s}}\psi\left(\frac{t}{s}\right)\right]ds\right\} \\
&= \frac{1}{C_\psi}\int_0^{+\infty}\frac{1}{s^3}\mathrm{FT}\left[f(t)\otimes\psi^*\left(\frac{-t}{s}\right)\otimes\psi\left(\frac{t}{s}\right)\right]ds \\
&= \frac{1}{C_\psi}\int_0^{+\infty}\frac{1}{s^3}\hat{f}(\omega)\mathrm{FT}\left[\psi^*\left(\frac{-t}{s}\right)\right]\mathrm{FT}\left[\psi\left(\frac{t}{s}\right)\right]ds
\end{aligned} \tag{B.5}$$

Now we rewrite $\mathrm{FT}\left[\psi\left(\frac{t}{s}\right)\right]$ as

$$\begin{aligned}
\mathrm{FT}\left[\psi\left(\frac{t}{s}\right)\right] &= \int_{-\infty}^{+\infty}\psi\left(\frac{t}{s}\right)e^{-i\omega t}dt = \int_{-\infty}^{+\infty}\psi\left(\frac{t}{s}\right)e^{-i(s\omega)\left(\frac{t}{s}\right)}dt \\
&= s\int_{-\infty}^{+\infty}\psi\left(\frac{t}{s}\right)e^{-i(s\omega)\left(\frac{t}{s}\right)}\frac{dt}{s} = s\int_{-\infty}^{+\infty}\psi(t'')e^{-i(s\omega)t''}dt'' = s\hat{\psi}(s\omega)
\end{aligned} \tag{B.6}$$

Substituting (B.2) and (B.6) into Equation (B.5), we obtain,

$$\begin{aligned}
\mathrm{FT}[\mathrm{RHS}] &= \frac{1}{C_\psi}\int_0^{+\infty}\frac{1}{s^3}\hat{f}(\omega)s\left[\hat{\psi}(s\omega)\right]^* s\hat{\psi}(s\omega)ds \\
&= \frac{\hat{f}(\omega)}{C_\psi}\int_0^{+\infty}\left|\hat{\psi}(s\omega)\right|^2\frac{ds}{s}
\end{aligned} \tag{B.7}$$

Equation (B.7) reduces to (B.4), if $C_\psi = \int_0^{+\infty} \left|\hat{\psi}(s\omega)\right|^2 \frac{ds}{s} < +\infty$. We only need to prove that this equation is essentially Equation (5.3) for any real wavelet function $\phi(t)$. Rewriting this equation, we have,

$$C_\psi = \int_0^{+\infty} \left|\hat{\psi}(s\omega)\right|^2 \frac{\omega ds}{s\omega} = \begin{cases} \int_0^{+\infty} \left|\hat{\psi}(\chi)\right|^2 \frac{d\chi}{\chi}, \text{ when } \omega \geq 0 \\ \int_0^{-\infty} \left|\hat{\psi}(\chi)\right|^2 \frac{d\chi}{\chi}, \text{ when } \omega < 0 \end{cases} = \begin{cases} \int_0^{+\infty} \left|\hat{\psi}(\chi)\right|^2 \frac{d\chi}{\chi}, \text{ when } \omega \geq 0 \\ \int_0^{+\infty} \left|\hat{\psi}(-\gamma)\right|^2 \frac{d\gamma}{\gamma}, \text{ when } \omega < 0 \end{cases} . \quad \text{(B.8)}$$

Since the wavelet function $\phi(t)$ is real, we have $\left|\hat{\psi}(\omega)\right|^2 = \left|\hat{\psi}(-\omega)\right|^2$. Then (B.6) becomes Equation (5.3),

$$C_\psi = \int_0^{+\infty} \frac{\left|\hat{\psi}(\omega)\right|^2}{\omega} d\omega < +\infty , \quad \text{(B.9)}$$

Under such condition, FT[LHS] = FT[RHS], and therefore we have proved Equation (5.4).

B.3 Derivation of Equation (5.5)

The derivation of Equation (5.5) is similar to that of (5.4), which is to show FT[LHS] = FT[RHS]. Again, we have,

$$\text{FT}[\text{LHS}] = \hat{f}(\omega) . \quad \text{(B.10)}$$

The Fourier transform of the right hand side (RHS) with regard to *t* is

$$
\begin{aligned}
\mathrm{FT}[\mathrm{RHS}] &= \frac{1}{C_\psi}\mathrm{FT}\left\{\int_0^{+\infty}\int_{-\infty}^{+\infty}\frac{1}{s^2}\Re\left[W_{f\psi}(s,t')\frac{1}{\sqrt{s}}\psi\left(\frac{t-t'}{s}\right)\right]dt'\,ds\right\} \\
&= \frac{1}{C_\psi}\mathrm{FT}\left\{\int_0^{+\infty}\frac{1}{s^2}\Re\left[\frac{1}{\sqrt{s}}f(t)\otimes\psi^*\left(\frac{-t}{s}\right)\otimes\frac{1}{\sqrt{s}}\psi\left(\frac{t}{s}\right)\right]ds\right\} \\
&= \frac{1}{C_\psi}\int_0^{+\infty}\frac{1}{2s^3}\mathrm{FT}\left\{f(t)\otimes\psi^*\left(\frac{-t}{s}\right)\otimes\psi\left(\frac{t}{s}\right)+f^*(t)\otimes\psi\left(\frac{-t}{s}\right)\otimes\psi^*\left(\frac{t}{s}\right)\right\}ds\ . \\
&= \frac{1}{C_\psi}\int_0^{+\infty}\frac{1}{2s^3}\left\{\hat{f}(\omega)s\left[\hat{\psi}(s\omega)\right]^* s\hat{\psi}(s\omega)+\hat{f}(\omega)s\hat{\psi}(-s\omega)s\left[\hat{\psi}(-s\omega)\right]^*\right\}ds \\
&= \frac{1}{C_\psi}\int_0^{+\infty}\frac{\hat{f}(\omega)}{2s}\left\{\left|\hat{\psi}(s\omega)\right|^2+\left|\hat{\psi}(-s\omega)\right|^2\right\}ds
\end{aligned}
\qquad \text{(B.11)}
$$

Equation (B.7) reduces to (B.11) if $C_\psi = \int_0^{+\infty}\frac{\left|\hat{\psi}(s\omega)\right|^2+\left|\hat{\psi}(-s\omega)\right|^2}{2s}ds < +\infty$. We rewrite C_ψ,

$$
\begin{aligned}
C_\psi &= \int_0^{+\infty}\left[\left|\hat{\psi}(s\omega)\right|^2+\left|\hat{\psi}(-s\omega)\right|^2\right]\frac{\omega ds}{2s\omega} = \int_0^{+\infty}\left[\left|\hat{\psi}(\chi)\right|^2+\left|\hat{\psi}(-\chi)\right|^2\right]\frac{d\chi}{2\chi} \\
&= \int_{-\infty}^{+\infty}\left[\left|\hat{\psi}(\chi)\right|^2\right]\frac{d\chi}{2|\chi|}
\end{aligned}
\qquad \text{(B.12)}
$$

which is Equation (5.6). Under such condition, FT[LHS]=FT[RHS], and thus we have proven Equation (5.5).

B.4 Derivation of Equation (5.8)

Now we derive Equation (5.8).

$$
\begin{aligned}
\mathrm{RHS} &= \frac{1}{C_\psi}\int_0^{+\infty}\int_{-\infty}^{+\infty}\left|W_{f\psi}(s,t)\right|^2\frac{1}{s}dt\frac{ds}{s} = \frac{1}{C_\psi}\int_0^{+\infty}\int_{-\infty}^{+\infty}\left|W_{f\psi}(s,t)\right|^2 dt\frac{ds}{s^2} \\
&= \frac{1}{2\pi C_\psi}\int_0^{+\infty}\int_{-\infty}^{+\infty}\left|\hat{W}_{f\psi}(s,\omega)\right|^2 d\omega\frac{ds}{s^2} = \frac{1}{2\pi C_\psi}\int_0^{+\infty}\int_{-\infty}^{+\infty}s\left|\hat{f}(\omega)\right|^2\left|\hat{\psi}(s\omega)\right|^2 d\omega\frac{ds}{s^2}. \\
&= \frac{1}{2\pi C_\psi}\int_{-\infty}^{+\infty}\left|\hat{f}(\omega)\right|^2\left[\int_0^{+\infty}\left|\hat{\psi}(s\omega)\right|^2\frac{ds}{s}\right]d\omega
\end{aligned}
\qquad \text{(B.13)}
$$

For a real wavelet function $\phi(t)$, we have proven that $C_\psi = \int_0^{+\infty} \left|\hat{\psi}(s\omega)\right|^2 \frac{ds}{s} < +\infty$. Therefore,

$\text{RHS} = \frac{1}{2\pi}\int_{-\infty}^{+\infty} \left|\hat{f}(\omega)\right|^2 d\omega = \int_{-\infty}^{+\infty} \left|f(t)\right|^2 dt = \text{LHS}$. In the case of a complex wavelet function $\phi(t)$ and a real $f(t)$, we have

$$\text{RHS} = \underbrace{\frac{1}{2\pi C_\psi}\left\{\int_0^{+\infty} \left|\hat{f}(\omega)\right|^2 \left[\int_0^{+\infty} \left|\hat{\psi}(s\omega)\right|^2 \frac{ds}{s}\right] d\omega\right\}}_{\text{(A.14)}} + \underbrace{\frac{1}{2\pi C_\psi}\left\{\int_{-\infty}^{0} \left|\hat{f}(\omega)\right|^2 \left[\int_0^{+\infty} \left|\hat{\psi}(s\omega)\right|^2 \frac{ds}{s}\right] d\omega\right\}}_{\text{(A.15)}}.$$

Since $\omega > 0$ in (B.14), by substituting $\chi = s\,\omega \geq 0$, we can rewrite (B.14) as

$$\frac{1}{2\pi C_\psi}\left\{\int_0^{+\infty} \left|\hat{f}(\omega)\right|^2 \left[\int_0^{+\infty} \left|\hat{\psi}(\chi)\right|^2 \frac{d\chi}{\chi}\right] d\omega\right\}. \tag{B.16}$$

However, $\omega < 0$ in (B.15), by substituting $\gamma = -s\,\omega \geq 0$ and $\zeta = -\omega$, we can rewrite (B.15) as

$$\frac{1}{2\pi C_\psi}\left\{\int_0^{+\infty} \left|\hat{f}(-\zeta)\right|^2 \left[\int_0^{+\infty} \left|\hat{\psi}(-\gamma)\right|^2 \frac{d\gamma}{\gamma}\right] d\zeta\right\}. \tag{B.17}$$

Utilizing $\left|\hat{f}(\omega)\right|^2 = \left|\hat{f}(-\omega)\right|^2$ for real $f(t)$, we have

$$\begin{aligned} \text{RHS} &= \frac{1}{2\pi C_\psi}\left[\int_0^{+\infty} \left|\hat{f}(\omega)\right|^2 d\omega\right]\left[\int_0^{+\infty} \left|\hat{\psi}(\chi)\right|^2 \frac{d\chi}{\chi} + \int_0^{+\infty} \left|\hat{\psi}(-\gamma)\right|^2 \frac{d\gamma}{\gamma}\right] \\ &= \frac{1}{2\pi C_\psi}\left[\int_0^{+\infty} \left|\hat{f}(\omega)\right|^2 d\omega\right]\left[\int_0^{+\infty} \frac{\left|\hat{\psi}(\chi)\right|^2 + \left|\hat{\psi}(-\chi)\right|^2}{\chi} d\chi\right] \end{aligned}. \tag{B.18}$$

Substituting $C_\psi = \int_0^{+\infty} \frac{\left|\hat{\psi}(\chi)\right|^2 + \left|\hat{\psi}(-\chi)\right|^2}{2\chi} d\chi$ from Equation (5.6) to (B.18) yields,

$$\text{RHS} = \frac{1}{2\pi}\left[2 \cdot \int_0^{+\infty} \left|\hat{f}(\omega)\right|^2 d\omega\right] = \frac{1}{2\pi}\left[\int_{-\infty}^{+\infty} \left|\hat{f}(\omega)\right|^2 d\omega\right] = \int_{-\infty}^{+\infty} \left|f(t)\right|^2 dt = \text{LHS}. \tag{B.19}$$

B.5 Wavelet Scales and Fourier Periods

Substitute a cosine function

$$\begin{aligned} f(t) &= A_1 \cos(\omega_1 t + \varphi_1) \\ \hat{f}(\omega) &= \pi A_1 \left[\delta(\omega - \omega_1) e^{i\varphi_1} + \delta(\omega + \omega_1) e^{-i\varphi_1} \right] \end{aligned} \tag{B.20}$$

into Equation (5.11).

$$\begin{aligned} P_f(s,t) &= \frac{1}{C_\psi'^2} \left| \frac{1}{\sqrt{2\pi}} \int_{-\infty}^{+\infty} \hat{f}(\omega) e^{\frac{-(s\omega-\omega_0)^2}{2}} e^{i\omega t} d\omega \right|^2 \\ &= \frac{1}{C_\psi'^2} \left| \frac{1}{\sqrt{2\pi}} \int_{-\infty}^{+\infty} \pi A_1 \left[\delta(\omega - \omega_1) e^{i\varphi_1} + \delta(\omega + \omega_1) e^{-i\varphi_1} \right] e^{\frac{-(s\omega-\omega_0)^2}{2}} e^{i\omega t} d\omega \right|^2 \\ &= \frac{\pi A_1^2}{2C_\psi'^2} \left| \left[e^{\frac{-(s\omega_1-\omega_0)^2}{2}} e^{i(\omega_1 t+\varphi_1)} + e^{\frac{-(s\omega_1+\omega_0)^2}{2}} e^{-i(\omega_1 t+\varphi_1)} \right] \right|^2 \end{aligned} \tag{B.21}$$

Since $s > 0$, $\omega_0 = 6$ and we can assume $\omega_1 > 0$ without losing generality, the second term on RHS can be neglected ($e^{\frac{-(s\omega_1+\omega_0)^2}{2}} < e^{-\frac{\omega_0^2}{2}} \sim 1.5\times10^{-8}$).

$$P_f(s,t) = \frac{\pi A_1^2}{2C_\psi'^2} e^{-(s\omega_1-\omega_0)^2} \tag{B.22}$$

To find the maximum value of $P_f(s,t)$, we set the derivative of (B.16) with respect to s to zero and obtain,

$$\frac{\partial P_f(s,t)}{\partial s} = -\frac{\pi A_1^2}{C_\psi'^2} (s\omega_1 - \omega_0) \omega_1 e^{-(s\omega_1-\omega_0)^2} = 0 \tag{B.23}$$

The only solution is $s = \omega_0/\omega_1 = \omega_0 T_1/2\pi$, where T_1 is the Fourier period. The maximum value $P_f(s,t)$ is then equal to $\pi A_1^2/2C_\psi'^2$. By setting this maxima equal to the signal's mean power ($A_1^2/2$), we obtain $C_\psi' = \sqrt{\pi}$.

B.6 Derivation of Equation (5.20)

Similar to the 1-D case, we prove Equation (5.20) by showing that the Fourier transforms of the both sides of the Equation (5.20) are equal. The Fourier transform of the LHS with regard to $\vec{t}$ is

$$\mathrm{FT}[\mathrm{LHS}] = \hat{f}(\vec{\omega}), \tag{B.24}$$

The Fourier transform of the RHS with regard to $\vec{t}$ is

$$\begin{aligned}
\mathrm{FT}[\mathrm{RHS}] &= \frac{1}{C_\psi}\mathrm{FT}\left[\int_0^{2\pi}\int_0^{+\infty}\int_{-\infty}^{+\infty}\int_{-\infty}^{+\infty}\frac{1}{s^3}W_{f\psi}(s,\theta,\vec{t}')\frac{1}{s}\psi\left(\Omega_\theta^{-1}\frac{\vec{t}-\vec{t}'}{s}\right)d\vec{t}'\,ds\,d\theta\right] \\
&= \frac{1}{C_\psi}\mathrm{FT}\left\{\int_0^{2\pi}\int_0^{+\infty}\frac{1}{s^3}\left[f(\vec{t})\otimes\frac{1}{s}\psi^*\left(\frac{-\Omega_\theta^{-1}\vec{t}}{s}\right)\right]\otimes\frac{1}{s}\psi\left(\frac{\Omega_\theta^{-1}\vec{t}}{s}\right)ds\,d\theta\right\}. \\
&= \frac{1}{C_\psi}\int_0^{2\pi}\int_0^{+\infty}\frac{1}{s^3}\hat{f}(\vec{\omega})\mathrm{FT}\left[\frac{1}{s}\psi^*\left(\frac{-\Omega_\theta^{-1}\vec{t}}{s}\right)\right]\mathrm{FT}\left[\frac{1}{s}\psi\left(\frac{\Omega_\theta^{-1}\vec{t}}{s}\right)\right]dsd\theta
\end{aligned} \tag{B.25}$$

Now we rewrite $\mathrm{FT}\left[\frac{1}{s}\psi^*\left(\frac{-\Omega_\theta^{-1}\vec{t}}{s}\right)\right]$ as

$$\mathrm{FT}\left[\frac{1}{s}\psi^*\left(\frac{-\Omega_\theta^{-1}\vec{t}}{s}\right)\right] = \int_{-\infty}^{+\infty}\int_{-\infty}^{+\infty}\frac{1}{s}\psi^*\left(-\frac{t\cos\theta+z\sin\theta}{s},-\frac{-t\sin\theta+z\cos\theta}{s}\right)e^{-i\omega t}e^{-imz}dtdz\,. \tag{B.26}$$

We change the variables (t, z) to a new set of variables (u, v),

$$\begin{aligned}
u &= -\frac{t\cos\theta+z\sin\theta}{s}, \\
v &= \frac{t\sin\theta-z\cos\theta}{s}
\end{aligned}. \tag{B.27}$$

Then, Equation (B.26) is rewritten as

$$
\begin{aligned}
\mathrm{FT}\left[\frac{1}{s}\psi^*\left(\frac{-\Omega_\theta^{-1}\vec{t}}{s}\right)\right] &= \int_{-\infty}^{+\infty}\int_{-\infty}^{+\infty}\frac{1}{s}\psi^*(u,v)e^{-is\omega(v\sin\theta-u\cos\theta)}e^{ism(u\sin\theta+v\cos\theta)}\left|\frac{\partial(t,z)}{\partial(u,v)}\right|dudv \\
&= \int_{-\infty}^{+\infty}\int_{-\infty}^{+\infty}\frac{1}{s}\psi^*(u,v)e^{is(\omega\cos\theta+m\sin\theta)u}e^{-is(\omega\sin\theta-m\cos\theta)v}s^2dudv \\
&= \int_{-\infty}^{+\infty}\int_{-\infty}^{+\infty}s\psi^*(u,v)e^{is(\omega\cos\theta+m\sin\theta)u}e^{-is(\omega\sin\theta-m\cos\theta)v}dudv \\
&= s\left[\int_{-\infty}^{+\infty}\int_{-\infty}^{+\infty}\psi(u,v)e^{-is(\omega\cos\theta+m\sin\theta)u}e^{-is(-\omega\sin\theta+m\cos\theta)v}dudv\right]^* \\
&= s\left[\hat{\psi}\left(s\omega\cos\theta+sm\sin\theta,-s\omega\sin\theta+sm\cos\theta\right)\right]^* \\
&= s\left[\hat{\psi}\left(s\Omega_\theta^{-1}\vec{\omega}\right)\right]^*
\end{aligned}
\quad , \qquad \text{(B.28)}
$$

where $\left|\frac{\partial(t,z)}{\partial(u,v)}\right|$ is the determinant of the Jacobian Matrix. Similarly, we have,

$$
\mathrm{FT}\left[\frac{1}{s}\psi\left(\frac{\Omega_\theta^{-1}\vec{t}}{s}\right)\right] = s\hat{\psi}\left(s\Omega_\theta^{-1}\vec{\omega}\right). \qquad \text{(B.29)}
$$

Substituting (B.28) and (B.29) into Equation (B.25), we obtain,

$$
\begin{aligned}
\mathrm{FT}[\mathrm{RHS}] &= \frac{1}{C_\psi}\int_0^{2\pi}\int_0^{+\infty}\frac{1}{s^3}\hat{f}(\vec{\omega})s^2\left|\hat{\psi}\left(s\Omega_\theta^{-1}\vec{\omega}\right)\right|^2 dsd\theta \\
&= \frac{1}{C_\psi}\int_0^{2\pi}\int_0^{+\infty}\hat{f}(\vec{\omega})\left|\hat{\psi}\left(s\Omega_\theta^{-1}\vec{\omega}\right)\right|^2\frac{ds}{s}d\theta
\end{aligned}
\quad . \qquad \text{(B.30)}
$$

Equation (B.30) reduces to (B.24), if $C_\psi = \int_0^{2\pi}\int_0^{+\infty}\left|\hat{\psi}\left(s\Omega_\theta^{-1}\vec{\omega}\right)\right|^2\frac{ds}{s}d\theta < +\infty$. We only need to prove that this condition is essentially same as Equation (5.20) for any 2-D wavelet function $\psi(\vec{t})$.

Rewriting the equation, by changing the variables (s, θ) to a new set of variables (x, y),

$$
\begin{aligned}
x &= s(\omega\cos\theta+m\sin\theta), \\
y &= s(-\omega\sin\theta+m\cos\theta)
\end{aligned}
\quad . \qquad \text{(B.31)}
$$

Or equivalently, the transform is

$$\begin{aligned} s &= \sqrt{\frac{x^2+y^2}{\omega^2+m^2}} \\ \theta &= \arctan(\frac{m}{\omega}) - \arctan(\frac{y}{x}) \end{aligned} \quad . \tag{B.32}$$

Changing the variables, we obtain

$$\begin{aligned} C_\psi &= \int_0^{2\pi}\int_0^{+\infty} \left|\hat{\psi}\left(s\Omega_\theta^{-1}\vec{\omega}\right)\right|^2 \frac{ds}{s} d\theta \\ &= \int_{-\infty}^{+\infty}\int_{-\infty}^{+\infty} \left|\hat{\psi}(x,y)\right|^2 \frac{1}{s}\left|\frac{\partial(s,\theta)}{\partial(x,y)}\right| dxdy \\ &= \int_{-\infty}^{+\infty}\int_{-\infty}^{+\infty} \left|\hat{\psi}(x,y)\right|^2 \frac{1}{s}\frac{1}{s|\omega|^2} dxdy \\ &= \int_{-\infty}^{+\infty}\int_{-\infty}^{+\infty} \frac{\left|\hat{\psi}(x,y)\right|^2}{x^2+y^2} dxdy \end{aligned} \quad . \tag{B.33}$$

Under condition $C_\psi = \int_{-\infty}^{+\infty}\int_{-\infty}^{+\infty} \frac{\left|\hat{\psi}(x,y)\right|^2}{x^2+y^2} dx\,dy < +\infty$, FT[LHS] = FT[RHS], and therefore we have proved Equation (5.20).

B.7 Derivation of Equation (5.21)

The Fourier transform of the LHS of Equation (5.21) with regard to $\vec{t}$ is $\hat{f}(\vec{\omega})$. The Fourier transform of the RHS with regard to $\vec{t}$ is

$$
\begin{aligned}
\mathrm{FT}[\mathrm{RHS}] &= \frac{1}{C_\psi}\mathrm{FT}\left[\int_0^{\pi}\int_0^{+\infty}\int_{-\infty}^{+\infty}\int_{-\infty}^{+\infty}\frac{1}{s^3}\Re\left[W_{f\psi}\left(s,\theta,\vec{t}'\right)\frac{1}{s}\psi\left(\Omega_\theta^{-1}\frac{\vec{t}-\vec{t}'}{s}\right)\right]d\vec{t}'\,ds\,d\theta\right] \\
&= \frac{1}{2C_\psi}\mathrm{FT}\left\{\int_0^{\pi}\int_0^{+\infty}\frac{1}{s^3}\left[f\left(\vec{t}\right)\otimes\frac{1}{s}\psi^*\left(\frac{-\Omega_\theta^{-1}\vec{t}}{s}\right)\otimes\frac{1}{s}\psi\left(\frac{\Omega_\theta^{-1}\vec{t}}{s}\right)\right.\right. \\
&\qquad\left.\left.+f\left(\vec{t}\right)\otimes\frac{1}{s}\psi\left(\frac{-\Omega_\theta^{-1}\vec{t}}{s}\right)\otimes\frac{1}{s}\psi^*\left(\frac{\Omega_\theta^{-1}\vec{t}}{s}\right)\right]ds\,d\theta\right\} \\
&= \frac{1}{2C_\psi}\int_0^{\pi}\int_0^{+\infty}\frac{1}{s^3}\left\{\hat{f}\left(\vec{\omega}\right)\mathrm{FT}\left[\frac{1}{s}\psi^*\left(\frac{-\Omega_\theta^{-1}\vec{t}}{s}\right)\right]\mathrm{FT}\left[\frac{1}{s}\psi\left(\frac{\Omega_\theta^{-1}\vec{t}}{s}\right)\right]\right. \\
&\qquad\left.+\hat{f}\left(\vec{\omega}\right)\mathrm{FT}\left[\frac{1}{s}\psi\left(\frac{-\Omega_\theta^{-1}\vec{t}}{s}\right)\right]\mathrm{FT}\left[\frac{1}{s}\psi^*\left(\frac{\Omega_\theta^{-1}\vec{t}}{s}\right)\right]\right\}ds\,d\theta \qquad \text{(B.34)} \\
&= \frac{1}{2C_\psi}\int_0^{\pi}\int_0^{+\infty}\frac{1}{s^3}\hat{f}\left(\vec{\omega}\right)\left[s\hat{\psi}^*\left(s\Omega_\theta^{-1}\vec{\omega}\right)\right]\left[s\hat{\psi}\left(s\Omega_\theta^{-1}\vec{\omega}\right)\right] \\
&\qquad+\hat{f}\left(\vec{\omega}\right)\left[s\hat{\psi}\left(-s\Omega_\theta^{-1}\vec{\omega}\right)\right]\left[s\hat{\psi}^*\left(-s\Omega_\theta^{-1}\vec{\omega}\right)\right]ds\,d\theta \\
&= \frac{\hat{f}\left(\vec{\omega}\right)}{C_\psi}\int_0^{\pi}\int_0^{+\infty}\left[\left|\hat{\psi}\left(s\Omega_\theta^{-1}\vec{\omega}\right)\right|^2+\left|\hat{\psi}\left(-s\Omega_\theta^{-1}\vec{\omega}\right)\right|^2\right]\frac{ds}{s}d\theta \\
&= \frac{\hat{f}\left(\vec{\omega}\right)}{2C_\psi}\int_0^{\pi}\int_0^{+\infty}\left|\hat{\psi}\left(s\Omega_\theta^{-1}\vec{\omega}\right)\right|^2\frac{ds}{s}d\theta+\int_{\pi}^{2\pi}\int_0^{+\infty}\left|\hat{\psi}\left(s\Omega_{\theta'}^{-1}\vec{\omega}\right)\right|^2\frac{ds}{s}d\theta' \\
&= \frac{\hat{f}\left(\vec{\omega}\right)}{2C_\psi}\int_0^{2\pi}\int_0^{+\infty}\left|\hat{\psi}\left(s\Omega_\theta^{-1}\vec{\omega}\right)\right|^2\frac{ds}{s}d\theta = \frac{\hat{f}\left(\vec{\omega}\right)}{2C_\psi}\int_{-\infty}^{+\infty}\int_{-\infty}^{+\infty}\frac{\left|\hat{\psi}(x,y)\right|^2}{x^2+y^2}dx\,dy
\end{aligned}
$$

Under condition $C_\psi = \int_{-\infty}^{+\infty}\int_{-\infty}^{+\infty}\frac{\left|\hat{\psi}(x,y)\right|^2}{2\left(x^2+y^2\right)}dx\,dy < +\infty$, FT[LHS] = FT[RHS], and therefore we have proved Equation (5.21).

B.8 Derivation of Equation (5.23)

Similar to the 1-D case, we rewrite the RHS of Equation (5.23) using the Parseval's theorem in two dimensions,

$$
\begin{aligned}
\text{RHS} &= \frac{1}{C_\psi}\int_0^{2\pi}\int_0^{+\infty}\int_{-\infty}^{+\infty}\int_{-\infty}^{+\infty}\left|W_{f\psi}(s,\theta,\vec{t})\right|^2\frac{1}{s^2}d\vec{t}\,\frac{ds}{s}d\theta \\
&= \frac{1}{C_\psi}\int_0^{2\pi}\int_0^{+\infty}\int_{-\infty}^{+\infty}\int_{-\infty}^{+\infty}\left|\hat{W}_{f\psi}(s,\theta,\vec{\omega})\right|^2\frac{1}{s^2}d\vec{\omega}\,\frac{ds}{s}d\theta \\
&= \frac{1}{C_\psi}\int_0^{2\pi}\int_0^{+\infty}\int_{-\infty}^{+\infty}\int_{-\infty}^{+\infty}\left|\hat{f}(\vec{\omega})s\hat{\psi}^*\left(s\Omega_\theta^{-1}\vec{\omega}\right)\right|^2\frac{1}{s^2}d\vec{\omega}\,\frac{ds}{s}d\theta \\
&= \int_0^{2\pi}\int_0^{+\infty}\int_{-\infty}^{+\infty}\int_{-\infty}^{+\infty}\left|\hat{f}(\vec{\omega})\right|^2\left|\hat{\psi}\left(s\Omega_\theta^{-1}\vec{\omega}\right)\right|^2 d\vec{\omega}\,\frac{ds}{s}d\theta \\
&= \int_{-\infty}^{+\infty}\int_{-\infty}^{+\infty}\left|\hat{f}(\vec{\omega})\right|^2\left[\int_0^{2\pi}\int_0^{+\infty}\frac{\left|\hat{\psi}\left(s\Omega_\theta^{-1}\vec{\omega}\right)\right|^2}{C_\psi}\frac{ds}{s}d\theta\right]d\vec{\omega} \\
&= \int_{-\infty}^{+\infty}\int_{-\infty}^{+\infty}\left|f(\vec{t})\right|^2 d\vec{t} = \text{LHS}
\end{aligned}
\tag{B.35}
$$

B.9 2-D Wavelet Angles and Scales vs. Fourier Frequencies and Vertical Wavenumbers

Substitute a cosine function

$$
\begin{aligned}
f(\vec{t}) &= A_1\cos(\omega_1 t + m_1 z) \\
\hat{f}(\vec{\omega}) &= 2\pi^2 A_1\left[\delta(\omega-\omega_1)\delta(m-m_1)+\delta(\omega+\omega_1)\delta(m+m_1)\right]
\end{aligned}
\tag{B.36}
$$

into Equation (5.24).

$$
\begin{aligned}
P_f(s,\theta,\vec{t}) &= \frac{1}{C_\psi'^2}\left|\frac{1}{2\pi}\int_{-\infty}^{+\infty}\int_{-\infty}^{+\infty} f(\vec{\omega})e^{\frac{-\left|s\vec{\omega}-\vec{\omega}_0'(\theta)\right|^2}{2}}e^{i\vec{\omega}\cdot\vec{t}}\,d\vec{\omega}\right|^2 \\
&= \frac{1}{C_\psi'^2}\left|\frac{1}{2\pi}\int_{-\infty}^{+\infty}\int_{-\infty}^{+\infty} 2\pi^2 A_1\left[\delta(\omega-\omega_1)\delta(m-m_1)+\delta(\omega+\omega_1)\delta(m+m_1)\right]e^{\frac{-\left|s\vec{\omega}-\vec{\omega}_0'(\theta)\right|^2}{2}}e^{i\vec{\omega}\cdot\vec{t}}\,d\vec{\omega}\right|^2 \\
&= \frac{\pi^2 A_1^2}{C_\psi'^2}e^{-\left[(s\omega_1-\omega_0\cos\theta)^2+(sm_1-\omega_0\sin\theta)^2\right]}
\end{aligned}
\tag{B.37}
$$

$P_f(s,\theta,\vec{t})$ reaches its maximum value $\pi^2 A_1^2 / C_\psi'^2$ at $s = \sqrt{\omega_0^2 / (m_1^2 + \omega_1^2)}$ and $\theta = \tan^{-1}(m_1 / \omega_1)$.

By setting this maxima equal to the signal's mean power ($A_1^2/2$), we obtain $C_\psi' = \sqrt{2}\pi$.

$$
\begin{aligned}
P\left(\sqrt{\frac{\omega_0^2}{m^2+\omega^2}}, \tan^{-1}\left(\frac{m}{\omega}\right), x, y\right) &= \frac{1}{C_\psi'^2}\left|\int_{-\infty}^{+\infty}\int_{-\infty}^{+\infty} A\cos(\omega u + mv)\frac{1}{s^2} e^{\frac{-i\omega_0[(u-x)\cos\theta+(v-y)\sin\theta]}{s}} e^{-\frac{(x-u)^2+(y-v)^2}{2s^2}} du dv\right|^2 \\
&= \frac{A^2}{C_\psi'^2}\left|\int_{-\infty}^{+\infty}\int_{-\infty}^{+\infty}\frac{1}{2}(e^{-i(\omega u+mv)} + e^{i(\omega u+mv)})\frac{1}{s^2} e^{-i[\omega(u-x)+m(v-y)]} e^{-\frac{(x-u)^2+(y-v)^2}{2s^2}} du\, dv\right|^2 \\
&= \frac{A^2}{4C_\psi'^2}\left|\int_{-\infty}^{+\infty}\int_{-\infty}^{+\infty} e^{-i[\omega(2u-x)+m(2v-y)]} e^{-\frac{(x-u)^2+(y-v)^2}{2s^2}} d(\frac{u}{s}) d(\frac{v}{s})\right. \\
&\qquad \left. + \int_{-\infty}^{+\infty}\int_{-\infty}^{+\infty} e^{i(\omega x+my)} e^{-\frac{(x-u)^2+(y-v)^2}{2s^2}} d(\frac{u}{s}) d(\frac{v}{s})\right|^2 \\
&\quad \frac{A^2}{4C_\psi'^2}\left|\int_{-\infty}^{+\infty}\int_{-\infty}^{+\infty} e^{-\frac{\left[u-\left(x-2is^2\omega\right)\right]^2+\left[v-\left(y-2is^2 m\right)\right]^2}{2s^2}} e^{-i(\omega x+my)-2s^2(\omega^2+m^2)} d(\frac{u}{s}) d(\frac{v}{s})\right. \\
&\qquad \left. + 2\pi e^{i(\omega x+my)}\right|^2 \\
&= \frac{A^2}{4C_\psi'^2}\left|2\pi e^{-i(\omega x+my)-2\omega_0^2} + 2\pi e^{i(\omega x+my)}\right|^2 \approx \frac{\pi^2 A^2}{C_\psi'^2} = \frac{A^2}{2}
\end{aligned}
\tag{B.38}
$$

Bibliography

Alexander, M. J., and T. J. Dunkerton (1999), A Spectral Parameterization of Mean-Flow Forcing due to Breaking Gravity Waves, *J. Atmos. Sci.*, *56*(24), 4167–4182, doi:10.1175/1520-0469(1999)056<4167:ASPOMF>2.0.CO;2.

Alexander, M. J., and J. R. Holton (2004), On the spectrum of vertically propagating gravity waves generated by a transient heat source, *Atmos. Chem. Phys.*, *4*(4), 923–932, doi:10.5194/acp-4-923-2004.

Alexander, M. J., and L. Pfister (1995), Gravity wave momentum flux in the lower stratosphere over convection, *Geophys. Res. Lett.*, *22*(15), 2029–2032, doi:10.1029/95GL01984.

Alexander, M. J., and H. K. Rosenlof (2003), Gravity-wave forcing in the stratosphere: Observational constraints from the Upper Atmosphere Research Satellite and implications for parameterization in global models, *J. Geophys. Res.*, *108*(D19), 4597, doi:10.1029/2003JD003373.

Alexander, M. J. et al. (2008), Global estimates of gravity wave momentum flux from High Resolution Dynamics Limb Sounder observations, *J. Geophys. Res. Atmos.*, *113*(D15), D15S18, doi:10.1029/2007JD008807.

Alexander, M. J. et al. (2010), Recent developments in gravity-wave effects in climate models and the global distribution of gravity-wave momentum flux from observations and models, *Q. J. R. Meteorol. Soc.*, 1103–1124, doi:10.1002/qj.637.

Allen, S. J., and R. A. Vincent (1995), Gravity wave activity in the lower atmosphere: Seasonal and latitudinal variations, *J. Geophys. Res.*, *100*(D1), 1327–1350, doi:10.1029/94JD02688.

Andrews, D. G., J. R. Holton, and C. B. Leovy (1987), *Middle Atmosphere Dynamics*, Academic Press, San Diego, CA.

Aso, T. (2003), An overview of the terdiurnal tide observed by polar radars and optics, *Adv. Polar Up. Atmos. Res.*, *17*, 167–176.

Azeem, S. M. I., and G. G. Sivjee (2009), Multiyear observations of tidal oscillations in OH M(3,1) rotational temperatures at South Pole, Antarctica, *J. Geophys. Res. Sp. Phys.*, *114*(A6), A06312, doi:10.1029/2008JA013976.

Baumgaertner, A. J. G., and A. J. McDonald (2007), A gravity wave climatology for Antarctica compiled from Challenging Minisatellite Payload/Global Positioning System (CHAMP/GPS) radio occultations, *J. Geophys. Res.*, *112*(D5), D05103, doi:10.1029/2006JD007504.

Baumgaertner, A. J. G., A. J. McDonald, G. J. Fraser, and G. E. Plank (2005), Long-term observations of mean winds and tides in the upper mesosphere and lower thermosphere

above Scott Base, Antarctica, *J. Atmos. Solar-Terrestrial Phys.*, *67*(16), 1480–1496, doi:10.1016/j.jastp.2005.07.018.

Beatty, T. J., C. A. Hostetler, and C. S. Gardner (1992), Lidar Observations of Gravity Waves and Their Spectra near the Mesopause and Stratopause at Arecibo, *J. Atmos. Sci.*, *49*(6), 477–496, doi:10.1175/1520-0469(1992)049<0477:LOOGWA>2.0.CO;2.

Bossert, K. et al. (2015), Momentum flux estimates accompanying multiscale gravity waves over Mount Cook, New Zealand, on 13 July 2014 during the DEEPWAVE campaign, *J. Geophys. Res. Atmos.*, *120*(18), 9323–9337, doi:10.1002/2015JD023197.

Brockwell, P. J., and R. A. Davis (2013), *Time Series: Theory and Methods*, Springer Science & Business Media, New York, NY.

Cadet, D., and H. Teitelbaum (1979), Observational Evidence of Internal Inertia-Gravity Waves in the Tropical Stratosphere, *J. Atmos. Sci.*, *36*(5), 892–907, doi:10.1175/1520-0469(1979)036<0892:OEOIIG>2.0.CO;2.

CEDAR: Strategic Vision (2011), *CEDAR: The New Dimension, Strategic Vision for the NSF Program on Coupling, Energetics and Dynamics of Atmospheric Regions*.

Chapman, S., and R. S. Lindzen (1970), *Atmospheric Tides*, D. Reidel Publishing Company, Dordrecht, Netherlands.

Chen, C., and X. Chu (2016), Two-dimensional Morlet wavelet transform and its application to extracting two-dimensional wave packets from lidar observations in Antarctica, *Submitt. to J. Atmos. Solar-Terrestrial Phys*.

Chen, C., X. Chu, Z. Yu, W. Fong, A. J. McDonald, X. Lu, and W. Huang (2012), Lidar and radar investigation of inertia gravity wave intrinsic properties at McMurdo, Antarctica, in *Proceedings of the 26th International Laser Radar Conference*, pp. 1057–1060, Porto Heli, Greece.

Chen, C., X. Chu, A. J. McDonald, S. L. Vadas, Z. Yu, W. Fong, and X. Lu (2013), Inertia-gravity waves in Antarctica: A case study using simultaneous lidar and radar measurements at McMurdo/Scott Base (77.8°S, 166.7°E), *J. Geophys. Res. Atmos.*, *118*(7), 2794–2808, doi:10.1002/jgrd.50318.

Chen, C., X. Chu, W. Fong, X. Lu, A. J. McDonald, D. Pautet, and M. Taylor (2016a), Antarctic Wave Dynamics Mystery Discovered by Lidar, Radar and Imager, in *Proceedings of the 27th International Laser Radar Conference*, edited by B. Gross, F. Moshary, and M. Arend, p. 13004, New York, NY.

Chen, C., X. Chu, J. Zhao, B. R. Roberts, Z. Yu, W. Fong, X. Lu, and J. A. Smith (2016b), Lidar observations of persistent gravity waves with periods of 3-10 h in the Antarctic middle and upper atmosphere at McMurdo (77.83°S, 166.67°E), *J. Geophys. Res. Sp. Phys.*, *121*(2), 1483–1502, doi:10.1002/2015JA022127.

Chu, X., and G. Papen (2005), Resonance Fluorescence Lidar for Measurements of the Middle and Upper Atmosphere, in *Laser Remote Sensing*, edited by T. Fukuchi and T. Fujii, pp. 179–432, CRC Press, Boca Raton, Fla.

Chu, X., and Z. Yu (2016), Formation mechanisms of neutral Fe layers in the thermosphere studied with a thermosphere-ionosphere Fe/Fe^+ (TIFe) model in Antarctica, *Manuscript in Preparation*.

Chu, X., W. Pan, G. C. Papen, C. S. Gardner, and J. A. Gelbwachs (2002), Fe Boltzmann Temperature Lidar: Design, Error Analysis, and Initial Results at the North and South Poles, *Appl. Opt.*, *41*(21), 4400–4410, doi:10.1364/AO.41.004400.

Chu, X., C. S. Gardner, and S. J. Franke (2005), Nocturnal thermal structure of the mesosphere and lower thermosphere region at Maui, Hawaii (20.7°N), and Starfire Optical Range, New Mexico (35°N), *J. Geophys. Res.*, *110*(D9), D09S03, doi:10.1029/2004JD004891.

Chu, X., W. Huang, W. Fong, Z. Yu, Z. Wang, J. A. Smith, and C. S. Gardner (2011a), First lidar observations of polar mesospheric clouds and Fe temperatures at McMurdo (77.8°S, 166.7°E), Antarctica, *Geophys. Res. Lett.*, *38*(16), L16810, doi:10.1029/2011GL048373.

Chu, X., Z. Yu, C. S. Gardner, C. Chen, and W. Fong (2011b), Lidar observations of neutral Fe layers and fast gravity waves in the thermosphere (110-155 km) at McMurdo (77.8°S, 166.7°E), Antarctica, *Geophys. Res. Lett.*, *38*(23), L23807, doi:10.1029/2011GL050016.

Chu, X., Z. Yu, C. Chen, F. Fong, W. Huang, C. S. Gardner, Z. Wang, B. Roberts, J. A. Smith, and W. Fong (2012), McMurdo lidar campaign: A new look into polar upper atmosphere, in *Proceedings of the 26th International Laser Radar Conference*, pp. 1019–1022, Porto Heli, Greece.

Chu, X., Z. Yu, W. Fong, C. Chen, W. Huang, X. Lu, C. S. Gardner, A. J. McDonald, T. J. Fuller-Rowell, and S. L. Vadas (2013), New Discoveries Resulted from Lidar Investigation of Middle and Upper Atmosphere Temperature, Composition, Chemistry and Dynamics at McMurdo, in *AGU Fall Meeting 2013*, San Francisco, CA, December 9–13.

Chu, X. et al. (2016), From Antarctica Lidar Discoveries to Oasis Exploration, in *Proceedings of the 27th International Laser Radar Conference*, edited by B. Gross, F. Moshary, and M. Arend, p. 12001, EDP Sciences.

Chui, C. K. (1992), *An Introduction to Wavelets*, Wavelet Analysis and Its Applications, edited by C. K. Chui, Academic Press, San Diego, CA.

Collins, R. ., and C. . Gardner (1995), Gravity wave activity in the stratosphere and mesosphere at the South Pole, *Adv. Sp. Res.*, *16*(5), 81–90, doi:10.1016/0273-1177(95)00175-E.

Collins, R. L., D. C. Senft, and C. S. Gardner (1992), Observations of a 12 H wave in the mesopause region at the South Pole, *Geophys. Res. Lett.*, *19*(1), 57–60, doi:10.1029/91GL02780.

Collins, R. L., A. Nomura, and C. S. Gardner (1994), Gravity waves in the upper mesosphere over Antarctica: Lidar observations at the South Pole and Syowa, *J. Geophys. Res.*, *99*(D3), 5475–5485, doi:10.1029/93JD03276.

Collins, R. L., X. Tao, and C. S. Gardner (1996), Gravity wave activity in the upper mesosphere over Urbana, Illinois: lidar observations and analysis of gravity wave propagation models, *J. Atmos. Terr. Phys.*, *58*(16), 1905–1926, doi:10.1016/0021-9169(96)00026-8.

Cornish, C. R., M. F. Larsen, C. R. Cornish, and M. F. Larsen (1988), Observations of Low-Frequency Inertia-Gravity Waves in the Lower Stratosphere over Arecibo, *J. Atmos. Sci.*, *46*(15), 2428–2439, doi:http://dx.doi.org/10.1175/1520-0469(1989)046<2428:OOLFIG>2.0.CO;2.

Cot, C., and J. Barat (1986), Wave-turbulence interaction in the stratosphere: A case study, *J. Geophys. Res.*, *91*(D2), 2749–2756, doi:10.1029/JD091iD02p02749.

Daubechies, I. (1988), Orthonormal bases of compactly supported wavelets, *Commun. Pure Appl. Math.*, *41*(7), 909–996, doi:10.1002/cpa.3160410705.

Daubechies, I. (1992), *Ten Lectures on Wavelets*, Society for Industrial and Applied Mathematics, Philadelphia, Pennsylvania.

Dewan, E. M. (1994), The saturated-cascade model for atmospheric gravity wave spectra, and the wavelength-period (W-P) relations, *Geophys. Res. Lett.*, *21*(9), 817–820, doi:10.1029/94GL00702.

Dewan, E. M., and R. E. Good (1986), Saturation and the "universal" spectrum for vertical profiles of horizontal scalar winds in the atmosphere, *J. Geophys. Res.*, *91*(D2), 2742–2748, doi:10.1029/JD091iD02p02742.

Dewan, E. M., and N. Grossbard (2000), Power spectral artifacts in published balloon data and implications regarding saturated gravity wave theories, *J. Geophys. Res.*, *105*(D4), 4667–4683, doi:10.1029/1999JD901108.

Diettrich, J. C., G. J. Nott, P. J. Espy, X. Chu, and D. Riggin (2006), Statistics of sporadic iron layers and relation to atmospheric dynamics, *J. Atmos. Solar-Terrestrial Phys.*, *68*(1), 102–113, doi:10.1016/j.jastp.2005.08.008.

Dörnbrack, A., T. Birner, A. Fix, H. Flentje, A. Meister, H. Schmid, E. V. Browell, and M. J. Mahoney (2002), Evidence for inertia gravity waves forming polar stratospheric clouds over Scandinavia, *J. Geophys. Res.*, *107*(D20), 8287, doi:10.1029/2001JD000452.

Dowdy, A. J. (2004), The large-scale dynamics of the mesosphere–lower thermosphere during the Southern Hemisphere stratospheric warming of 2002, *Geophys. Res. Lett.*, *31*(14), L14102, doi:10.1029/2004GL020282.

Du, J., and W. E. Ward (2010), Terdiurnal tide in the extended Canadian Middle Atmospheric Model (CMAM), *J. Geophys. Res.*, *115*(D24), D24106, doi:10.1029/2010JD014479.

Eckermann, S. D., and and P. Preusse (1999), Global Measurements of Stratospheric Mountain Waves from Space, *Science (80-.).*, *286*(5444), 1534–1537, doi:10.1126/science.286.5444.1534.

Espy, P. J., R. E. Hibbins, D. M. Riggin, and D. C. Fritts (2005), Mesospheric planetary waves over Antarctica during 2002, *Geophys. Res. Lett.*, *32*(21), L21804, doi:10.1029/2005GL023886.

Espy, P. J., R. E. Hibbins, G. R. Swenson, J. Tang, M. J. Taylor, D. M. Riggin, and D. C. Fritts (2006), Regional variations of mesospheric gravity-wave momentum flux over Antarctica, *Ann. Geophys.*, *24*(1), 81–88, doi:10.5194/angeo-24-81-2006.

van Eyken, A. P., P. J. S. Williams, S. C. Buchert, and M. Kunitake (2000), First measurements of tidal modes in the lower thermosphere by the EISCAT Svalbard radar, *Geophys. Res. Lett.*, *27*(7), 931–934, doi:10.1029/1999GL003687.

Farge, M. (1992), Wavelet Transforms and their Applications to Turbulence, *Annu. Rev. Fluid Mech.*, *24*, 395–457, doi:10.1146/annurev.fl.24.010192.002143.

Farge, M., M. Holschnerider, and J. F. Colonna (1990), Wavelet analysis of coherent structures in two-dimensional trubulent flows, in *Topological Fluid Mechanics*, edited by H. K. Moffatt and A. Tsinober, pp. 765–776, Cambridge University Press, Cambridge.

Fong, W., X. Lu, X. Chu, T. J. Fuller-Rowell, Z. Yu, B. R. Roberts, C. Chen, C. S. Gardner, and A. J. McDonald (2014), Winter temperature tides from 30 to 110 km at McMurdo (77.8°S, 166.7°E), Antarctica: Lidar observations and comparisons with WAM, *J. Geophys. Res. Atmos.*, *119*(6), 2846–2863, doi:10.1002/2013JD020784.

Fong, W., X. Chu, X. Lu, C. Chen, T. J. Fuller-Rowell, M. Codrescu, and A. D. Richmond (2015), Lidar and CTIPe model studies of the fast amplitude growth with altitude of the diurnal temperature “tides” in the Antarctic winter lower thermosphere and dependence on geomagnetic activity, *Geophys. Res. Lett.*, *42*(3), 697–704, doi:10.1002/2014GL062784.

Fong, W., X. Chu, X. Lu, T. J. Fuller-Rowell, M. Codrescu, A. D. Richmond, Z. Yu, B. R. Roberts, and C. Chen (2016), Winter temperature and tidal structures from 2011 to 2014 at mcmurdo station: observations from fe boltzmann temperature and rayleigh lidar, in *Proceedings of the 27th International Laser Radar Conference*, p. 12003, New York, NY.

Forbes, J. M. (1995), Tidal and Planetary Waves, in *The Upper Mesosphere and Lower Thermosphere: A Review of Experiment and Theory*, vol. 87, edited by R. M. Johnson and T. L. Killeen, pp. 67–87, American Geophysical Union, Washington, D. C.

Forbes, J. M., N. A. Makarov, and Y. I. Portnyagin (1995), First results from the meteor radar at South Pole: A large 12-hour oscillation with zonal wavenumber one, *Geophys. Res. Lett.*, *22*(23), 3247–3250, doi:10.1029/95GL03370.

Forbes, J. M., S. E. Palo, X. Zhang, Y. I. Portnyagin, N. A. Makarov, and E. G. Merzlyakov (1999), Lamb waves in the lower thermosphere: Observational evidence and global

consequences, *J. Geophys. Res.*, *104*(A8), 17107–17115, doi:10.1029/1999JA900044.

Fraser, G. J. (1984), Summer circulation in the Antarctic middle atmosphere, *J. Atmos. Terr. Phys.*, *46*(2), 143–146, doi:10.1016/0021-9169(84)90139-9.

Friedman, J. S., and X. Chu (2007), Nocturnal temperature structure in the mesopause region over the Arecibo Observatory (18.35°N, 66.75°W): Seasonal variations, *J. Geophys. Res.*, *112*(D14), D14107, doi:10.1029/2006JD008220.

Fritts, D. C. (1984), Gravity wave saturation in the middle atmosphere: A review of theory and observations, *Rev. Geophys.*, *22*(3), 275–308, doi:10.1029/RG022i003p00275.

Fritts, D. C., and M. J. Alexander (2003), Gravity wave dynamics and effects in the middle atmosphere, *Rev. Geophys.*, *41*(1), 1003, doi:10.1029/2001RG000106.

Fritts, D. C., and M. J. Alexander (2012), Correction to "Gravity wave dynamics and effects in the middle atmosphere," *Rev. Geophys.*, *50*(3), RG3004, doi:10.1029/2012RG000409.

Fritts, D. C., and Z. Luo (1992), Gravity Wave Excitation by Geostrophic Adjustment of the Jet Stream. Part I: Two-Dimensional Forcing, *J. Atmos. Sci.*, *49*(8), 681–697, doi:10.1175/1520-0469(1992)049<0681:GWEBGA>2.0.CO;2.

Fritts, D. C., and P. K. Rastogi (1985), Convective and dynamical instabilities due to gravity wave motions in the lower and middle atmosphere: Theory and observations, *Radio Sci.*, *20*(6), 1247–1277, doi:10.1029/RS020i006p01247.

Fritts, D. C., and R. A. Vincent (1987), Mesospheric Momentum Flux Studies at Adelaide, Australia: Observations and a Gravity Wave–Tidal Interaction Model, *J. Atmos. Sci.*, *44*(3), 605–619, doi:10.1175/1520-0469(1987)044<0605:MMFSAA>2.0.CO;2.

Fritts, D. C., D. M. Riggin, B. B. Balsley, and R. G. Stockwell (1998), Recent results with an MF radar at McMurdo, Antarctica: Characteristics and variability of motions near 12-hour period in the mesosphere, *Geophys. Res. Lett.*, *25*(3), 297–300, doi:10.1029/97GL03702.

Gao, X., J. W. Meriwether, V. B. Wickwar, T. D. Wilkerson, and S. Collins (1998), Rayleigh lidar measurements of the temporal frequency and vertical wavenumber spectra in the mesosphere over the Rocky Mountain region, *J. Geophys. Res.*, *103*(D6), 6405–6416, doi:10.1029/97JD03073.

Garcia, R. R., and B. A. Boville (1994), "Downward Control" of the Mean Meridional Circulation and Temperature Distribution of the Polar Winter Stratosphere, *J. Atmos. Sci.*, *51*(15), 2238–2245, doi:10.1175/1520-0469(1994)051<2238:COTMMC>2.0.CO;2.

Gardner, C. S. (1994), Diffusive filtering theory of gravity wave spectra in the atmosphere, *J. Geophys. Res.*, *99*(D10), 20601–20622, doi:10.1029/94JD00819.

Gardner, C. S., and D. G. Voelz (1987), Lidar studies of the nighttime sodium layer over Urbana, Illinois: 2. Gravity waves, *J. Geophys. Res.*, *92*(A5), 4673–4694,

doi:10.1029/JA092iA05p04673.

Gardner, C. S., and W. Yang (1998), Measurements of the dynamical cooling rate associated with the vertical transport of heat by dissipating gravity waves in the mesopause region at the Starfire Optical Range, New Mexico, *J. Geophys. Res.*, *103*(D14), 16909–16926, doi:10.1029/98JD00683.

Gardner, C. S., D. C. Senft, T. J. Beatty, R. E. Bills, and C. A. Hosteler (1989a), Rayleigh and sodium lidar techniques for measuring middle atmospheric density, temperature and wind perturbation and their spectra, in *World Ionsphere/Thermosphere Study Handbook*, edited by C. H. Liu and B. Edwards, pp. 148–187.

Gardner, C. S., M. S. Miller, and C. H. Liu (1989b), Rayleigh Lidar Observations of Gravity Wave Activity in the Upper Stratosphere at Urbana, Illinois, *J. Atmos. Sci.*, *46*(12), 1838–1854, doi:10.1175/1520-0469(1989)046<1838:RLOOGW>2.0.CO;2.

Gelbwachs, J. A. (1994), Iron Boltzmann factor LIDAR: proposed new remote-sensing technique for mesospheric temperature., *Appl. Opt.*, *33*(30), 7151–7156, doi:10.1364/AO.33.007151.

Gong, J., J. Yue, and D. L. Wu (2015), Global survey of concentric gravity waves in AIRS images and ECMWF analysis, *J. Geophys. Res. Atmos.*, *120*(6), 2210–2228, doi:10.1002/2014JD022527.

Grossmann, A., and J. Morlet (1984), Decomposition of Hardy Functions into Square Integrable Wavelets of Constant Shape, *SIAM J. Math. Anal.*, *15*(4), 723–736, doi:10.1137/0515056.

Guest, F. M., M. J. Reeder, C. J. Marks, and D. J. Karoly (2000), Inertia–Gravity Waves Observed in the Lower Stratosphere over Macquarie Island, *J. Atmos. Sci.*, *57*(5), 737–752, doi:10.1175/1520-0469(2000)057<0737:IGWOIT>2.0.CO;2.

Hall, C. M., A. H. Manson, and C. E. Meek (1998), Spectral characteristics of spring arctic mesosphere dynamics, *Ann. Geophys.*, *16*(12), 1607–1618, doi:10.1007/s00585-998-1607-3.

Hall, G. E., C. E. Meek, and A. H. Manson (1995), Hodograph analysis of mesopause region winds observed by three MF radars in the Canadian Prairies, *J. Geophys. Res.*, *100*(D4), 7411–7421, doi:10.1029/95JD00195.

Harris, T. J. (1994), A long-term study of the quasi-two-day wave in the middle atmosphere, *J. Atmos. Terr. Phys.*, *56*(5), 569–579, doi:10.1016/0021-9169(94)90098-1.

Hauchecorne, A., and M.-L. Chanin (1980), Density and temperature profiles obtained by lidar between 35 and 70 km, *Geophys. Res. Lett.*, *7*(8), 565–568, doi:10.1029/GL007i008p00565.

Hernandez, G., R. W. Smith, G. J. Fraser, and W. L. Jones (1992), Large-scale waves in the upper-mesosphere at Antarctic high-latitudes, *Geophys. Res. Lett.*, *19*(13), 1347–1350, doi:10.1029/92GL01281.

Hernandez, G., G. J. Fraser, and R. W. Smith (1993), Mesospheric 12-hour oscillation near South Pole, Antarctica, *Geophys. Res. Lett.*, *20*(17), 1787–1790, doi:10.1029/93GL01983.

Hertzog, A., G. Boccara, R. A. Vincent, F. Vial, and P. Cocquerez (2008), Estimation of Gravity Wave Momentum Flux and Phase Speeds from Quasi-Lagrangian Stratospheric Balloon Flights. Part II: Results from the Vorcore Campaign in Antarctica, *J. Atmos. Sci.*, *65*(10), 3056–3070, doi:10.1175/2008JAS2710.1.

Hibbins, R. E., P. J. Espy, M. J. Jarvis, D. M. Riggin, and D. C. Fritts (2007), A climatology of tides and gravity wave variance in the MLT above Rothera, Antarctica obtained by MF radar, *J. Atmos. Solar-Terrestrial Phys.*, *69*(4-5), 578–588, doi:10.1016/j.jastp.2006.10.009.

Hines, C. O. (1991), The Saturation of Gravity Waves in the Middle Atmosphere. Part II: Development Of Doppler-Spread Theory, *J. Atmos. Sci.*, *48*(11), 1361–1379, doi:10.1175/1520-0469(1991)048<1361:TSOGWI>2.0.CO;2.

Hirota, I., and T. Niki (1985), A Statistical Study of Inertia-Gravity Waves in the Middle Atmosphere, *J. Meteorol. Soc. Japan*, *63*(6), 1055–1065.

Hocke, K., and N. Kämpfer (2009), Gap filling and noise reduction of unevenly sampled data by means of the Lomb-Scargle periodogram, *Atmos. Chem. Phys.*, *9*(12), 4197–4206, doi:10.5194/acp-9-4197-2009.

Hocke, K., and K. Schlegel (1996), A review of atmospheric gravity waves and travelling ionospheric disturbances: 1982-1995, *Ann. Geophys.*, *14*(9), 917–940, doi:10.1007/s00585-996-0917-6.

Hoffmann, P., A. Serafimovich, D. Peters, P. Dalin, R. Goldberg, and R. Latteck (2006), Inertia gravity waves in the upper troposphere during the MaCWAVE winter campaign – Part I: Observations with collocated radars, *Ann. Geophys.*, *24*(11), 2851–2862, doi:10.5194/angeo-24-2851-2006.

Holton, J. R. (1983), The Influence of Gravity Wave Breaking on the General Circulation of the Middle Atmosphere, *J. Atmos. Sci.*, *40*(10), 2497–2507, doi:10.1175/1520-0469(1983)040<2497:TIOGWB>2.0.CO;2.

Hu, X., A. Z. Liu, C. S. Gardner, and G. R. Swenson (2002), Characteristics of quasi-monochromatic gravity waves observed with Na lidar in the mesopause region at Starfire Optical Range, NM, *Geophys. Res. Lett.*, *29*(24), 2169, doi:10.1029/2002GL014975.

Iimura, H., S. E. Palo, Q. Wu, T. L. Killeen, S. C. Solomon, and W. R. Skinner (2009), Structure of the nonmigrating semidiurnal tide above Antarctica observed from the TIMED Doppler Interferometer, *J. Geophys. Res.*, *114*(D11), D11102, doi:10.1029/2008JD010608.

Kaifler, B., N. Kaifler, B. Ehard, A. Dörnbrack, M. Rapp, and D. C. Fritts (2015), Influences of source conditions on mountain wave penetration into the stratosphere and mesosphere, *Geophys. Res. Lett.*, *42*(21), 9488–9494, doi:10.1002/2015GL066465.

Kovalam, S., and R. A. Vincent (2003), Intradiurnal wind variations in the midlatitude and high-latitude mesosphere and lower thermosphere, *J. Geophys. Res.*, *108*(D4), 4135, doi:10.1029/2002JD002500.

Kumar, P. (1995), A wavelet based methodology for scale-space anisotropic analysis, *Geophys. Res. Lett.*, *22*(20), 2777–2780, doi:10.1029/95GL02934.

Kumar, P., and E. Foufoula-Georgiou (1997), Wavelet analysis for geophysical applications, *Rev. Geophys.*, *35*(4), 385–412, doi:10.1029/97RG00427.

Kundu, P. K. (1990), *Fluid Mechanics*, Academic Press, San Diego, CA.

Li, T., C.-Y. She, H.-L. Liu, T. Leblanc, and I. S. McDermid (2007), Sodium lidar–observed strong inertia-gravity wave activities in the mesopause region over Fort Collins, Colorado (41°N, 105°W), *J. Geophys. Res.*, *112*(D22), D22104, doi:10.1029/2007JD008681.

Lindzen, R. S., and D. Blake (1972), Lamb waves in the presence of realistic distributions of temperature and dissipation, *J. Geophys. Res.*, *77*(12), 2166–2176, doi:10.1029/JC077i012p02166.

Liu, H.-L., and J. W. Meriwether (2004), Analysis of a temperature inversion event in the lower mesosphere, *J. Geophys. Res.*, *109*(D2), D02S07, doi:10.1029/2002JD003026.

Liu, P. C. (1994), Wavelet Spectrum Analysis and Ocean Wind Waves, in *Wavelet Analysis and Its Applications: Wavelets in Geophysics*, vol. 4, pp. 151–166, Academic Press, San Diego, CA.

Liu, Y., X. San Liang, and R. H. Weisberg (2007), Rectification of the Bias in the Wavelet Power Spectrum, *J. Atmos. Ocean. Technol.*, *24*(12), 2093–2102, doi:10.1175/2007JTECHO511.1.

Longuet-Higgins, M. S. (1968), The Eigenfunctions of Laplace's Tidal Equations over a Sphere, *Philos. Trans. R. Soc. A Math. Phys. Eng. Sci.*, *262*(1132), 511–607, doi:10.1098/rsta.1968.0003.

Lu, X., A. Z. Liu, G. R. Swenson, T. Li, T. Leblanc, and I. S. McDermid (2009), Gravity wave propagation and dissipation from the stratosphere to the lower thermosphere, *J. Geophys. Res.*, *114*(D11), D11101, doi:10.1029/2008JD010112.

Lu, X., X. Chu, T. Fuller-Rowell, L. Chang, W. Fong, and Z. Yu (2013), Eastward propagating planetary waves with periods of 1-5 days in the winter Antarctic stratosphere as revealed by MERRA and lidar, *J. Geophys. Res. Atmos.*, *118*(17), 9565–9578, doi:10.1002/jgrd.50717.

Lu, X., C. Chen, W. Huang, J. A. Smith, X. Chu, T. Yuan, P.-D. Pautet, M. J. Taylor, J. Gong, and C. Y. Cullens (2015a), A coordinated study of 1 h mesoscale gravity waves propagating from Logan to Boulder with CRRL Na Doppler lidars and temperature mapper, *J. Geophys. Res. Atmos.*, *120*(19), 10,006–10,021, doi:10.1002/2015JD023604.

Lu, X., X. Chu, W. Fong, C. Chen, Z. Yu, B. R. Roberts, and A. J. McDonald (2015b), Vertical evolution of potential energy density and vertical wave number spectrum of Antarctic gravity waves from 35 to 105 km at McMurdo (77.8°S, 166.7°E), *J. Geophys. Res. Atmos.*, *120*(7), 2719–2737, doi:10.1002/2014JD022751.

Luo, Z., and D. C. Fritts (1993), Gravity-Wave Excitation by Geostrophic Adjustment of the Jet Stream. Part II: Three-Dimensional Forcing, *J. Atmos. Sci.*, *50*(1), 104–115, doi:10.1175/1520-0469(1993)050<0104:GWEBGA>2.0.CO;2.

Mallat, S. (1989), A theory for multiresolution signal decomposition: the wavelet representation, *IEEE Trans. Pattern Anal. Mach. Intell.*, *11*(7), 674–693, doi:10.1109/34.192463.

Mallat, S. (1999), *A Wavelet Tour of Signal Processing*, 2nd ed., Elsevier, San Diego, CA.

Manson, A. ., and C. . Meek (1986), Dynamics of the middle atmosphere at Saskatoon (52°N, 107°W): a spectral study during 1981, 1982, *J. Atmos. Terr. Phys.*, *48*(11-12), 1039–1055, doi:10.1016/0021-9169(86)90025-5.

Manson, A. H., C. E. Meek, J. B. Gregory, and D. K. Chakrabarty (1982), Fluctuations in tidal (24-, 12-h) characteristics and oscillations (8-h-5-d) in the mesosphere and lower thermosphere (70–110 km): Saskatoon (52°N, 107°W), 1979–1981, *Planet. Space Sci.*, *30*(12), 1283–1294, doi:10.1016/0032-0633(82)90102-7.

Mayr, H. G. (2003), Planetary-scale inertio gravity waves in the Mesosphere, *Geophys. Res. Lett.*, *30*(23), 2228, doi:10.1029/2003GL018376.

Mayr, H. G., J. G. Mengel, E. R. Talaat, H. S. Porter, and K. L. Chan (2004), Properties of internal planetary-scale inertio gravity waves in the mesosphere, *Ann. Geophys.*, *22*(10), 3421–3435, doi:10.5194/angeo-22-3421-2004.

McDonald, A. J., S. E. George, and R. M. Woollands (2009), Can gravity waves significantly impact PSC occurrence in the Antarctic?, *Atmos. Chem. Phys.*, *9*(22), 8825–8840, doi:10.5194/acp-9-8825-2009.

McLandress, C., T. G. Shepherd, S. Polavarapu, and S. R. Beagley (2012), Is Missing Orographic Gravity Wave Drag near 60°S the Cause of the Stratospheric Zonal Wind Biases in Chemistry–Climate Models?, *J. Atmos. Sci.*, *69*(3), 802–818, doi:10.1175/JAS-D-11-0159.1.

Meyer, Y. (1989), Orthonormal Wavelets, in *Wavelets: Time-Frequency Methods and Phase Space*, edited by J.-M. Combes, A. Grossmann, and P. Tchamitchian, pp. 21–37, Springer Berlin Heidelberg, Berlin, Heidelberg.

Meyer, Y., and D. H. Salinger (1993), *Wavelets and Operators*, 1st ed., Cambridge University Press, Cambridge.

Meyers, S. D., B. G. Kelly, and J. J. O'Brien (1993), An Introduction to Wavelet Analysis in Oceanography and Meteorology: With Application to the Dispersion of Yanai Waves, *Mon.*

Weather Rev., *121*(10), 2858–2866, doi:10.1175/1520-0493(1993)121<2858:AITWAI>2.0.CO;2.

Moffat-Griffin, T., M. J. Jarvis, S. R. Colwell, A. J. Kavanagh, G. L. Manney, and W. H. Daffer (2013), Seasonal variations in lower stratospheric gravity wave energy above the Falkland Islands, *J. Geophys. Res. Atmos.*, *118*(19), 10,861–10,869, doi:10.1002/jgrd.50859.

Moore, T. E., and J. L. Horwitz (2007), Stellar ablation of planetary atmospheres, *Rev. Geophys.*, *45*(3), RG3002, doi:10.1029/2005RG000194.

Morlet, J., G. Arens, E. Fourgeau, and D. Giard (1982a), Wave propagation and sampling theory—Part I: Complex signal and scattering in multilayered media, *GEOPHYSICS*, *47*(2), 203–221, doi:10.1190/1.1441328.

Morlet, J., G. Arens, E. Fourgeau, and D. Giard (1982b), Wave propagation and sampling theory—Part II: Sampling theory and complex waves, *GEOPHYSICS*, *47*(2), 222–236, doi:10.1190/1.1441329.

Morris, R. J., A. R. Klekociuk, and D. A. Holdsworth (2009), Low latitude 2-day planetary wave impact on austral polar mesopause temperatures: revealed by a January diminution in PMSE above Davis, Antarctica, *Geophys. Res. Lett.*, *36*(11), L11807, doi:10.1029/2009GL037817.

Moudden, Y., and J. M. Forbes (2009), Mars W cloud: Evidence of nighttime ice depositions, *Geophys. Res. Lett.*, *36*(14), L14204, doi:10.1029/2009GL039061.

Moudden, Y., and J. M. Forbes (2013), A decade-long climatology of terdiurnal tides using TIMED/SABER observations, *J. Geophys. Res. Sp. Phys.*, *118*(7), 4534–4550, doi:10.1002/jgra.50273.

Murenzi, R. (1989), Wavelet Transforms Associated to the n-Dimensional Euclidean Group with Dilations: Signal in More Than One Dimension, in *Wavelets: Time-Frequency Methods and Phase Space*, edited by J.-M. Combes, A. Grossmann, and P. Tchamitchian, pp. 239–246, Springer Berlin Heidelberg, Berlin, Heidelberg.

Murphy, D. J. et al. (2006), A climatology of tides in the Antarctic mesosphere and lower thermosphere, *J. Geophys. Res.*, *111*(D23), D23104, doi:10.1029/2005JD006803.

Murphy, D. J., S. P. Alexander, A. R. Klekociuk, P. T. Love, and R. A. Vincent (2014), Radiosonde observations of gravity waves in the lower stratosphere over Davis, Antarctica, *J. Geophys. Res. Atmos.*, *119*(21), 11,973–11,996, doi:10.1002/2014JD022448.

Nakamura, T., T. Tsuda, M. Yamamoto, S. Fukao, and S. Kato (1993), Characteristics of gravity waves in the mesosphere observed with the middle and upper atmosphere radar: 2. Propagation direction, *J. Geophys. Res.*, *98*(D5), 8911–8923, doi:10.1029/92JD03030.

Nappo, C. J. (2002), *An introduction to atmospheric gravity waves*, Academic Press, San Diego, CA.

Nastrom, G. D., and F. D. Eaton (2006), Quasi-monochromatic inertia-gravity waves in the lower stratosphere from MST radar observations, *J. Geophys. Res.*, *111*(D19), D19103, doi:10.1029/2006JD007335.

National Research Council (2013), *Solar and Space Physics*, National Academies Press, Washington, D.C.

Nicolls, M. J., R. H. Varney, S. L. Vadas, P. A. Stamus, C. J. Heinselman, R. B. Cosgrove, and M. C. Kelley (2010), Influence of an inertia-gravity wave on mesospheric dynamics: A case study with the Poker Flat Incoherent Scatter Radar, *J. Geophys. Res.*, *115*(D3), D00N02, doi:10.1029/2010JD014042.

Nielsen, K., M. J. Taylor, R. E. Hibbins, M. J. Jarvis, and J. M. Russell (2012), On the nature of short-period mesospheric gravity wave propagation over Halley, Antarctica, *J. Geophys. Res.*, *117*(D5), D05124, doi:10.1029/2011JD016261.

Nomura, A., T. Kano, Y. Iwasaka, H. Fukunishi, T. Hirasawa, and S. Kawaguchi (1987), Lidar observations of the mesospheric sodium layer at Syowa Station, Antarctica, *Geophys. Res. Lett.*, *14*(7), 700–703, doi:10.1029/GL014i007p00700.

O'sullivan, D., and T. J. Dunkerton (1995), Generation of Inertia–Gravity Waves in a Simulated Life Cycle of Baroclinic Instability, *J. Atmos. Sci.*, *52*(21), 3695–3716, doi:10.1175/1520-0469(1995)052<3695:GOIWIA>2.0.CO;2.

OASIS (2014), *Exploring the interaction of Earth's atmosphere with space, Report to National Science Foundation*.

Oznovich, I., D. J. McEwen, G. G. Sivjee, and R. L. Walterscheid (1997), Tidal oscillations of the Arctic upper mesosphere and lower thermosphere in winter, *J. Geophys. Res.*, *102*(A3), 4511–4520, doi:10.1029/96JA03560.

Pancheva, D., N. Mitchell, R. R. Clark, J. Drobjeva, and J. Lastovicka (2002), Variability in the maximum height of the ionospheric F2-layer over Millstone Hill (September 1998–March 2000); influence from below and above, *Ann. Geophys.*, *20*(11), 1807–1819, doi:10.5194/angeo-20-1807-2002.

Paul, T. (1984), Functions analytic on the half-plane as quantum mechanical states, *J. Math. Phys.*, *25*(11), 3252–3263, doi:10.1063/1.526072.

Pautet, P.-D., M. J. Taylor, D. C. Fritts, K. Bossert, B. P. Williams, D. Broutman, J. Ma, S. D. Eckermann, and J. D. Doyle (2016), Large-amplitude mesospheric response to an orographic wave generated over the Southern Ocean Auckland Islands (50.7°S) during the DEEPWAVE project, *J. Geophys. Res. Atmos.*, *121*(4), 1431–1441, doi:10.1002/2015JD024336.

Percival, D. B., and A. T. Walden (1993), *Spectral Analysis for Physical Applications*, Cambridge University Press, Cambridge, UK.

Pfister, L., K. R. Chan, T. P. Bui, S. Bowen, M. Legg, B. Gary, K. Kelly, M. Proffitt, and W. Starr (1993), Gravity waves generated by a tropical cyclone during the STEP tropical field program: A case study, *J. Geophys. Res.*, *98*(D5), 8611–8638, doi:10.1029/92JD01679.

Plane, J. M. C. (2003), Atmospheric Chemistry of Meteoric Metals, *Chem. Rev.*, *103*(12), 4963–4984, doi:10.1021/cr0205309.

Plougonven, R., A. Hertzog, and H. Teitelbaum (2008), Observations and simulations of a large-amplitude mountain wave breaking over the Antarctic Peninsula, *J. Geophys. Res.*, *113*(D16), D16113, doi:10.1029/2007JD009739.

Portnyagin, Y. I., J. M. Forbes, E. G. Merzlyakov, N. A. Makarov, and S. E. Palo (2000), Intradiurnal wind variations observed in the lower thermosphere over the South Pole, *Ann. Geophys.*, *18*(5), 547–554, doi:10.1007/s00585-000-0547-3.

Rasool, S. I., and C. De Bergh (1970), The runaway greenhouse and the accumulation of CO2 in the Venus atmosphere., *Nature*, *226*(5250), 1037–1039, doi:10.1038/2261037a0.

Sato, K. (1994), A statistical study of the structure, saturation and sources of inertio-gravity waves in the lower stratosphere observed with the MU radar, *J. Atmos. Terr. Phys.*, *56*(6), 755–774, doi:10.1016/0021-9169(94)90131-7.

Sato, K., and M. Yamada (1994), Vertical structure of atmospheric gravity waves revealed by the wavelet analysis, *J. Geophys. Res.*, *99*(D10), 20623–20631, doi:10.1029/94JD01818.

Sato, K., and M. Yoshiki (2008), Gravity Wave Generation around the Polar Vortex in the Stratosphere Revealed by 3-Hourly Radiosonde Observations at Syowa Station, *J. Atmos. Sci.*, *65*(12), 3719–3735, doi:10.1175/2008JAS2539.1.

Sato, K., D. J. O'Sullivan, and T. J. Dunkerton (1997), Low-frequency inertia-gravity waves in the stratosphere revealed by three-week continuous observation with the MU radar, *Geophys. Res. Lett.*, *24*(14), 1739–1742, doi:10.1029/97GL01759.

Sato, K., S. Tateno, S. Watanabe, and Y. Kawatani (2012), Gravity Wave Characteristics in the Southern Hemisphere Revealed by a High-Resolution Middle-Atmosphere General Circulation Model, *J. Atmos. Sci.*, *69*(4), 1378–1396, doi:10.1175/JAS-D-11-0101.1.

Scargle, J. D. (1989), Studies in astronomical time series analysis. III - Fourier transforms, autocorrelation functions, and cross-correlation functions of unevenly spaced data, *Astrophys. J.*, *343*, 874, doi:10.1086/167757.

Senft, D. ., C. . Hostetler, and C. . Gardner (1993), Characteristics of gravity wave activity and spectra in the upper stratosphere and upper mesosphere at Arecibo during early April 1989, *J. Atmos. Terr. Phys.*, *55*(3), 425–439, doi:10.1016/0021-9169(93)90078-D.

Senft, D. C., and C. S. Gardner (1991), Seasonal variability of gravity wave activity and spectra in the mesopause region at Urbana, *J. Geophys. Res.*, *96*(D9), 17229–17264, doi:10.1029/91JD01662.

She, C. Y. et al. (2004), Tidal perturbations and variability in the mesopause region over Fort Collins, CO (41N, 105W): Continuous multi-day temperature and wind lidar observations, *Geophys. Res. Lett.*, *31*(24), L24111, doi:10.1029/2004GL021165.

Shibata, T., K. Sato, H. Kobayashi, M. Yabuki, and M. Shiobara (2003), Antarctic polar stratospheric clouds under temperature perturbation by nonorographic inertia gravity waves observed by micropulse lidar at Syowa Station, *J. Geophys. Res.*, *108*(D3), 4105, doi:10.1029/2002JD002713.

Sivakumar, V., P. B. Rao, and H. Bencherif (2006), Lidar observations of middle atmospheric gravity wave activity over a low-latitude site (Gadanki, 13.5° N, 79.2° E), *Ann. Geophys.*, *24*(3), 823–834, doi:10.5194/angeo-24-823-2006.

Sivjee, G. G., and R. L. Walterscheid (1994), Six-hour zonally symmetric tidal oscillations of the winter mesopause over the South Pole Station, *Planet. Space Sci.*, *42*(6), 447–453, doi:10.1016/0032-0633(94)00085-9.

Smith, A. K. (2004), Observations and modeling of the 6-hour tide in the upper mesosphere, *J. Geophys. Res.*, *109*(D10), D10105, doi:10.1029/2003JD004421.

Smith, A. K., and D. A. Ortland (2001), Modeling and Analysis of the Structure and Generation of the Terdiurnal Tide, *J. Atmos. Sci.*, *58*(21), 3116–3134, doi:10.1175/1520-0469(2001)058<3116:MAAOTS>2.0.CO;2.

Smith, S. A., D. C. Fritts, and T. E. Vanzandt (1987), Evidence for a Saturated Spectrum of Atmospheric Gravity Waves, *J. Atmos. Sci.*, *44*(10), 1404–1410, doi:10.1175/1520-0469(1987)044<1404:EFASSO>2.0.CO;2.

States, R. J., and C. S. Gardner (2000), Thermal Structure of the Mesopause Region (80–105 km) at 40°N Latitude. Part II: Diurnal Variations, *J. Atmos. Sci.*, *57*(1), 78–92, doi:10.1175/1520-0469(2000)057<0078:TSOTMR>2.0.CO;2.

Suzuki, S., M. Tsutsumi, S. E. Palo, Y. Ebihara, M. Taguchi, and M. Ejiri (2011), Short-period gravity waves and ripples in the South Pole mesosphere, *J. Geophys. Res.*, *116*(D19), D19109, doi:10.1029/2011JD015882.

Swarztrauber, P. N., and A. Kasahara (1985), The Vector Harmonic Analysis of Laplace's Tidal Equations, *SIAM J. Sci. Stat. Comput.*, *6*(2), 464–491, doi:10.1137/0906033.

Talaat, E. R. (1999), Nonmigrating tides in the mesophere and lower thermosphere., University of Michgan.

Tan, B., H.-L. Liu, and X. Chu (2011), Studying the "cold pole" problem in WACCM and comparison to lidar temperature morphology, in *AGU Fall Meeting 2011 (SA31B-1973)*, San Francisco, CA, December 7.

Taylor, M. J., Y. Y. Gu, X. Tao, C. S. Gardner, and M. B. Bishop (1995), An investigation of intrinsic gravity wave signatures using coordinated lidar and nightglow image

measurements, *Geophys. Res. Lett.*, *22*(20), 2853–2856, doi:10.1029/95GL02949.

Teitelbaum, H., and F. Vial (1991), On tidal variability induced by nonlinear interaction with planetary waves, *J. Geophys. Res.*, *96*(A8), 14169–14178, doi:10.1029/91JA01019.

Teitelbaum, H., F. Vial, A. H. Manson, R. Giraldez, and M. Massebeuf (1989), Non-linear interaction between the diurnal and semidiurnal tides: terdiurnal and diurnal secondary waves, *J. Atmos. Terr. Phys.*, *51*(7-8), 627–634, doi:10.1016/0021-9169(89)90061-5.

Theon, J. S., W. Nordberg, L. B. Katchen, and J. J. Horvath (1967), Some Observations on the Thermal Behavior of the Mesosphere, *J. Atmos. Sci.*, *24*(4), 428–438, doi:10.1175/1520-0469(1967)024<0428:SOOTTB>2.0.CO;2.

Thomas, L., R. M. Worthington, and A. J. McDonald (1999), Inertia-gravity waves in the troposphere and lower stratosphere associated with a jet stream exit region, *Ann. Geophys.*, *17*(1), 115–121, doi:10.1007/s00585-999-0115-4.

Torrence, C., and G. P. Compo (1998), A Practical Guide to Wavelet Analysis, *Bull. Am. Meteorol. Soc.*, *79*(1), 61–78, doi:10.1175/1520-0477(1998)079<0061:APGTWA>2.0.CO;2.

Tsuda, T., S. Kato, T. Yokoi, T. Inoue, M. Yamamoto, T. E. VanZandt, S. Fukao, and T. Sato (1990a), Gravity waves in the mesosphere observed with the middle and upper atmosphere radar, *Radio Sci.*, *25*(5), 1005–1018, doi:10.1029/RS025i005p01005.

Tsuda, T., Y. Murayama, M. Yamamoto, S. Kato, and S. Fukao (1990b), Seasonal variation of momentum flux in the mesosphere observed with the MU radar, *Geophys. Res. Lett.*, *17*(6), 725–728, doi:10.1029/GL017i006p00725.

Vadas, S. L. (2007), Horizontal and vertical propagation and dissipation of gravity waves in the thermosphere from lower atmospheric and thermospheric sources, *J. Geophys. Res.*, *112*(A6), A06305, doi:10.1029/2006JA011845.

Vadas, S. L. (2013), Compressible f-plane solutions to body forces, heatings, and coolings, and application to the primary and secondary gravity waves generated by a deep convective plume, *J. Geophys. Res. Sp. Phys.*, *118*(5), 2377–2397, doi:10.1002/jgra.50163.

Vadas, S. L., and D. C. Fritts (2001), Gravity Wave Radiation and Mean Responses to Local Body Forces in the Atmosphere, *J. Atmos. Sci.*, *58*(16), 2249–2279, doi:10.1175/1520-0469(2001)058<2249:GWRAMR>2.0.CO;2.

Vadas, S. L., and D. C. Fritts (2005), Thermospheric responses to gravity waves: Influences of increasing viscosity and thermal diffusivity, *J. Geophys. Res.*, *110*(D15), D15103, doi:10.1029/2004JD005574.

Vadas, S. L., and D. C. Fritts (2006), Influence of solar variability on gravity wave structure and dissipation in the thermosphere from tropospheric convection, *J. Geophys. Res.*, *111*(A10), A10S12, doi:10.1029/2005JA011510.

Vadas, S. L., and H. Liu (2009), Generation of large-scale gravity waves and neutral winds in the thermosphere from the dissipation of convectively generated gravity waves, *J. Geophys. Res.*, *114*(A10), A10310, doi:10.1029/2009JA014108.

Vadas, S. L., D. C. Fritts, and M. J. Alexander (2003), Mechanism for the Generation of Secondary Waves in Wave Breaking Regions, *J. Atmos. Sci.*, *60*(1), 194–214, doi:10.1175/1520-0469(2003)060<0194:MFTGOS>2.0.CO;2.

VanZandt, T. E. (1982), A universal spectrum of buoyancy waves in the atmosphere, *Geophys. Res. Lett.*, *9*(5), 575–578, doi:10.1029/GL009i005p00575.

Vaughan, G., and R. M. Worthington (2007), Inertia-gravity waves observed by the UK MST radar, *Q. J. R. Meteorol. Soc.*, *133*(S2), 179–188, doi:10.1002/qj.142.

Vial, F., and J. M. Forbes (1989), Recent progress in tidal modelling, *J. Atmos. Terr. Phys.*, *51*(7-8), 663–671, doi:10.1016/0021-9169(89)90064-0.

Vincent, R. A. (1984), Gravity-wave motions in the mesosphere, *J. Atmos. Terr. Phys.*, *46*(2), 119–128, doi:10.1016/0021-9169(84)90137-5.

Vincent, R. A. (1994), Gravity-wave motions in the mesosphere and lower thermosphere observed at Mawson, Antarctica, *J. Atmos. Terr. Phys.*, *56*(5), 593–602, doi:10.1016/0021-9169(94)90100-7.

Vincent, R. A., and M. J. Alexander (2000), Gravity waves in the tropical lower stratosphere: An observational study of seasonal and interannual variability, *J. Geophys. Res.*, *105*(D14), 17971–17982, doi:10.1029/2000JD900196.

Virdi, T. ., and P. J. . Williams (1993), Altitude variations in the amplitude and phase of tidal oscillations at high latitude, *J. Atmos. Terr. Phys.*, *55*(4-5), 697–717, doi:10.1016/0021-9169(93)90015-Q.

Walterscheid, R. L., J. H. Hecht, R. a. Vincent, I. m. Reid, J. Woithe, and M. P. Hickey (1999), Analysis and interpretation of airglow and radar observations of quasi-monochromatic gravity waves in the upper mesosphere and lower thermosphere over Adelaide, Australia (35°S, 138°E), *J. Atmos. Solar-Terrestrial Phys.*, *61*(6), 461–478, doi:10.1016/S1364-6826(99)00002-4.

Wang, L., D. C. Fritts, B. P. Williams, R. A. Goldberg, F. J. Schmidlin, and U. Blum (2006), Gravity waves in the middle atmosphere during the MaCWAVE winter campaign: evidence of mountain wave critical level encounters, *Ann. Geophys.*, *24*(4), 1209–1226, doi:10.5194/angeo-24-1209-2006.

Wang, N., and C. Lu (2010), Two-Dimensional Continuous Wavelet Analysis and Its Application to Meteorological Data, *J. Atmos. Ocean. Technol.*, *27*(4), 652–666, doi:10.1175/2009JTECHA1338.1.

Wang, Z., Z. Liu, L. Liu, S. Wu, B. Liu, Z. Li, and X. Chu (2010), Iodine-filter-based mobile

Doppler lidar to make continuous and full-azimuth-scanned wind measurements: data acquisition and analysis system, data retrieval methods, and error analysis., *Appl. Opt.*, *49*(36), 6960–6978.

Wang, Z., X. Chu, W. Huang, W. Fong, J. A. Smith, and B. Roberts (2012), Refurbishment and upgrade of Fe Boltzmann/Rayleigh temperature lidar at Boulder for McMurdo lidar campaign in Antarctica, in *Proceedings of the 26th International Laser Radar Conference*, pp. 207–210, Porto Heli, Greece.

Weinstock, J. (1990), Saturated and Unsaturated Spectra of Gravity Waves and Scale-Dependent Diffusion, *J. Atmos. Sci.*, *47*(18), 2211–2226, doi:10.1175/1520-0469(1990)047<2211:SAUSOG>2.0.CO;2.

Weng, H., and K.-M. Lau (1994), Wavelets, Period Doubling, and Time–Frequency Localization with Application to Organization of Convection over the Tropical Western Pacific, *J. Atmos. Sci.*, *51*(17), 2523–2541, doi:10.1175/1520-0469(1994)051<2523:WPDATL>2.0.CO;2.

Werner, R., K. Stebel, G. H. Hansen, U. Blum, U.-P. Hoppe, M. Gausa, and K.-H. Fricke (2007), Application of wavelet transformation to determine wavelengths and phase velocities of gravity waves observed by lidar measurements, *J. Atmos. Solar-Terrestrial Phys.*, *69*(17-18), 2249–2256, doi:10.1016/j.jastp.2007.05.013.

Wickerhauser, M. V. (1994), Comparison of picture compression methods: wavelet, wavelet packet, and loca cosine transform coding, in *Wavelets: Theory, Algorithms, and Applications*, vol. 5, edited by C. K. Chui, L. Montefusco, and L. Puccio, pp. 585–621, Academic Press, San Diego, CA.

Wu, Q., T. L. Killeen, D. McEwen, S. C. Solomon, W. Guo, G. G. Sivjee, and J. M. Reeves (2002), Observation of the mesospheric and lower thermospheric 10-hour wave in the northern polar region, *J. Geophys. Res.*, *107*(A6), 1082, doi:10.1029/2001JA000192.

Wu, Q., N. J. Mitchell, T. L. Killeen, S. C. Solomon, and P. T. Younger (2005), A high-latitude 8-hour wave in the mesosphere and lower thermosphere, *J. Geophys. Res.*, *110*(A9), A09301, doi:10.1029/2005JA011024.

Xu, J., A. K. Smith, and G. P. Brasseur (2000), The effects of gravity waves on distributions of chemically active constituents in the mesopause region, *J. Geophys. Res.*, *105*(D21), 26593–26602, doi:10.1029/2000JD900446.

Yamashita, C. (2011), Atmospheric Coupling Through Gravity Waves During Stratospheric Sudden Warmings: Gravity Wave Variations, Generation Mechanisms, and Impacts, University of Colorado Boulder.

Yamashita, C., X. Chu, H.-L. Liu, P. J. Espy, G. J. Nott, and W. Huang (2009), Stratospheric gravity wave characteristics and seasonal variations observed by lidar at the South Pole and Rothera, Antarctica, *J. Geophys. Res.*, *114*(D12), D12101, doi:10.1029/2008JD011472.

Yang, G., B. Clemesha, P. Batista, and D. Simonich (2006), Gravity wave parameters and their seasonal variations derived from Na lidar observations at 23°S, *J. Geophys. Res.*, *111*(D21), D21107, doi:10.1029/2005JD006900.

Yang, G., B. Clemesha, P. Batista, and D. Simonich (2010), Seasonal variations of gravity wave activity and spectra derived from sodium temperature lidar, *J. Geophys. Res.*, *115*(D18), D18104, doi:10.1029/2009JD012367.

Yiğit, E., and A. S. Medvedev (2010), Internal gravity waves in the thermosphere during low and high solar activity: Simulation study, *J. Geophys. Res. Sp. Phys.*, *115*(A8), A00G02, doi:10.1029/2009JA015106.

Yoshiki, M., and K. Sato (2000), A statistical study of gravity waves in the polar regions based on operational radiosonde data, *J. Geophys. Res.*, *105*(D14), 17995–18011, doi:10.1029/2000JD900204.

Younger, P. T. (2002), The 8-hour tide in the Arctic mesosphere and lower thermosphere, *J. Geophys. Res.*, *107*(A12), 1420, doi:10.1029/2001JA005086.

Yu, Z. (2014), Lidar Observations and Numerical Modeling Studies of Thermospheric Metal Layers and Solar Effects on Mesospheric Fe Layers, University of Colorado at Boulder.

Yu, Z., and X. Chu (2014), Roles played by electric field, vertical wind and aurora in the source, formation and evolution of thermospheric Fe/Fe+ layers at high latitudes, in *AGU Fall Meeting 2014*, San Francisco, CA, December 15–19.

Yu, Z., X. Chu, W. Huang, W. Fong, and B. R. Roberts (2012), Diurnal variations of the Fe layer in the mesosphere and lower thermosphere: Four season variability and solar effects on the layer bottomside at McMurdo (77.8°S, 166.7°E), Antarctica, *J. Geophys. Res. Atmos.*, *117*(D22), D22303, doi:10.1029/2012JD018079.

Yuan, T. et al. (2016), Evidence of dispersion and refraction of a spectrally broad gravity wave packet in the mesopause region observed by the Na lidar and Mesospheric Temperature Mapper above Logan, Utah, *J. Geophys. Res. Atmos.*, *121*(2), 579–594, doi:10.1002/2015JD023685.

Yue, J., S. L. Vadas, C.-Y. She, T. Nakamura, S. C. Reising, H.-L. Liu, P. Stamus, D. A. Krueger, W. Lyons, and T. Li (2009), Concentric gravity waves in the mesosphere generated by deep convective plumes in the lower atmosphere near Fort Collins, Colorado, *J. Geophys. Res.*, *114*(D6), D06104, doi:10.1029/2008JD011244.

Zhang, F. Q., S. E. Koch, C. A. Davis, and M. L. Kaplan (2001), Wavelet analysis and the governing dynamics of a large-amplitude mesoscale gravity-wave event along the East Coast of the United States, *Q. J. R. Meteorol. Soc.*, *127*(577), 2209–2245, doi:DOI 10.1002/qj.49712757702.

Zhao, Y., M. J. Taylor, C. E. Randall, J. D. Lumpe, D. E. Siskind, S. M. Bailey, and J. M. Russell (2015), Investigating seasonal gravity wave activity in the summer polar

mesosphere, *J. Atmos. Solar-Terrestrial Phys.*, *127*, 8–20, doi:10.1016/j.jastp.2015.03.008.

Zhu, X., and J. R. Holton (1987), Mean Fields Induced by Local Gravity-Wave Forcing in the Middle Atmosphere, *J. Atmos. Sci.*, *44*(3), 620–630, doi:10.1175/1520-0469(1987)044<0620:MFIBLG>2.0.CO;2.

Zink, F., and R. A. Vincent (2001a), Wavelet analysis of stratospheric gravity wave packets over Macquarie Island: 1. Wave parameters, *J. Geophys. Res.*, *106*(D10), 10275–10288, doi:10.1029/2000JD900847.

Zink, F., and R. A. Vincent (2001b), Wavelet analysis of stratospheric gravity wave packets over Macquarie Island: 2. Intermittency and mean-flow accelerations, *J. Geophys. Res. Atmos.*, *106*(D10), 10289–10297, doi:10.1029/2000JD900846.